Robust Control of a Quadrotor with a Suspended Payload

by

Cameron C. Taylor

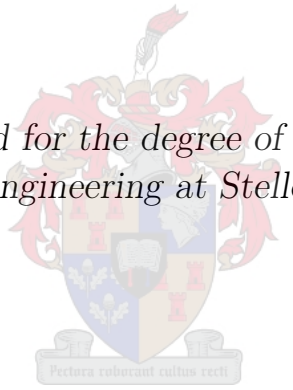

Dissertation presented for the degree of Doctor of Philosophy in the Faculty of Engineering at Stellenbosch University

Department of Electrical and Electronic Engineering,
University of Stellenbosch,
Private Bag X1, Matieland 7602, South Africa.

Dr J. A. A. Engelbrecht, Mr J. Treurnicht

March 2020

Declaration

By submitting this dissertation electronically, I declare that the entirety of the work contained therein is my own, original work, that I am the sole author thereof (save to the extent explicitly otherwise stated), that reproduction and publication thereof by Stellenbosch University will not infringe any third party rights and that I have not previously in its entirety or in part submitted it for obtaining any qualification.

Signature: .....
C. C. Taylor

Date: .....

Contents

Declaration i

Contents ii

List of Figures vii

List of Tables xvi

Abstract xvii

Uittreksel xviii

Acknowledgements xix

Nomenclature xx

1 Introduction 1

1.1 Project Background 1

1.2 Research Aims and Objectives 3

1.3 Contributions 4

1.4 Dissertation Overview 5

2 Background and Literature Review 7

2.1 Quadrotors and Suspended Payloads 7

2.1.1 Trajectory Generation 7

2.1.2 Suspended Payloads 9

2.1.3 Control of Quadrotors with Suspended Payloads 9

2.1.4 Robust Control of Quadrotors 12
2.1.5 Robust Control of Quadrotors with Suspended Payloads 14
2.2 Robust Control Methods 16
2.2.1 Outline of Available Techniques 16
2.2.2 H_∞ Techniques 17
2.3 Summary 19

3 The Quadrotor-Payload Model 21
3.1 Mathematical Model of the Quadrotor with a Suspended Payload 21
3.1.1 Quadrotor and Suspended Payload Point Mass Dynamics 22
3.1.2 Quadrotor Attitude Dynamics and Thrust 34
3.1.3 Model Uncertainty 37
3.1.4 Simulation Model 38
3.2 Linearised Models 45
3.2.1 Linearised Quadrotor and Suspended Payload Dynamics 46
3.2.2 Quadrotor Attitude 51
3.3 Summary 55

4 Cascade Control System Design 57
4.1 Control System Architecture 57
4.2 Quadrotor Attitude Control 58
4.2.1 Pitch Rate and Roll Rate Controller 58
4.2.2 Tilt Angle Controller 60
4.2.3 Simulation with Nonlinear Attitude Dynamics 64
4.2.4 Quadrotor Thrust Control 67
4.3 Quadrotor and Payload Translational Control 68
4.3.1 Overview 68
4.3.2 Quadrotor Vertical Velocity Control 69
4.3.3 Horizontal Velocity Control 72
4.3.4 Simulation Results with Benchmark Controller 81
4.4 Summary 85

5 H_∞ Robust Control Design **88**

5.1 Overview of H_∞ Loop Shaping Approach 88

5.2 Robust Control Theory 89

5.2.1 H_∞ Control 89

5.2.2 Uncertainty Descriptions 92

5.2.3 H_∞ Loop Shaping Design Theory 100

5.3 Quadrotor and Suspended Payload Translational Control: H_∞ Loop Shaping Design 107

5.3.1 Overview 107

5.3.2 Quadrotor Horizontal Velocity Control 108

5.3.3 Simulation Results with H_∞ Loop Shaping Controller . . 113

5.4 Summary 117

6 Extended H_∞ Loop Shaping Design **120**

6.1 Overview of the Extended H_∞ Loop Shaping Approach 120

6.2 Robust Stability Using the ν-gap Metric 121

6.2.1 Robust Stability Theorems 121

6.2.2 Robust Stability Analysis 122

6.3 Extended H_∞ Loop Shaping Design Theory 123

6.3.1 Theoretical Tools 124

6.3.2 Algorithm 126

6.4 Quadrotor and Payload Translational Control: Extended H_∞ Loop Shaping Design 129

6.4.1 Overview 130

6.4.2 Quadrotor Horizontal Velocity Control 130

6.4.3 Controller Performance with Nonlinear Model 136

6.5 Summary 140

7 Robust Trajectory Tracking **142**

7.1 Two-Degrees-of-Freedom H_∞ Loop Shaping 142

7.1.1 Overview 143

7.1.2 Problem Formulation 144

7.1.3 Quadrotor and Suspended Payload Translational Control: Two-degrees-of-freedom H_∞ Loop Shaping Design . 147
7.2 Extended Two-Degrees-of-Freedom H_∞ Loop Shaping 156
7.2.1 Overview 156
7.2.2 Problem Formulation 158
7.2.3 Quadrotor and Suspended Payload Translational Control: Two-degrees-of-freedom Extended H_∞ Loop Shaping Design 161
7.3 Input Shaping 170
7.3.1 Vibration Cancelling Impulses 171
7.3.2 Trajectory and Impulse Sequence Convolution 174
7.3.3 Input Shaper Design 175
7.4 Extended Loop Shaping Controller with Feedforward 178
7.4.1 Proposed Controller Architecture 179
7.4.2 Control System Performance with Nonlinear Model . . . 180
7.5 Summary 185

8 Conclusions and Recommendations 187
8.1 Summary 187
8.2 Future Work 189

Appendices 192

A H_∞ Control Concepts 193
A.1 Norms of Systems and Signals 193
A.1.1 Signal Spaces 193
A.1.2 Function Spaces 194
A.2 H_∞ Norm Optimization 195
A.2.1 Solution to H_∞ Sub-Optimal Control Problem 195

B Quadrotor and Suspended Payload Translational Model Coefficients 197

C Additional Modelling Information 198

References **200**

List of Figures

3.1 Quadrotor with suspended payload 23
3.2 Quadrotor with suspended payload 24
3.3 Quadrotor with suspended payload - relative payload position . . . 25
3.4 Relative payload velocities in the East-Down plane 26
3.5 Quadrotor with suspended payload - force balances 28
3.6 payload force balance under static conditions 29
3.7 Inertial and body frame orientation 34
3.8 SLADe quadrotor 38
3.9 Quadrotor drag force calculation 39
3.10 Data from flight tests using the SLADe quadrotor 41
3.11 SLADe quadrotor vehicle with suspended payload simulation 41
3.12 Simulated time history of payload angles when initialised to starting values of $\phi_L = 30$ degrees and $\theta_L = 7.5$ degrees. 42
3.13 Horizontal quadrotor velocity time history when suspended payload is initialised with payload angles of $\phi_L = 30$ degrees and $\theta_L = 7.5$ degrees. 43
3.14 Simulated time history of payload angles when initialised to starting values of $\phi_L = 7.5$ degrees and $\theta_L = 20$ degrees, with an input force applied to the quadrotor in the North direction 44
3.15 Horizontal quadrotor velocity time history when suspended payload is initialised with payload angles of $\phi_L = 7.5$ degrees and $\theta_L = 20$ degrees, with an input force applied to the quadrotor in the North direction 45
3.16 Pole-zero plot of P_{fpx} 49

3.17 Bode plot of P_{fpx}. Shown in blue is when the output matrix $\mathbf{C}_{fpx}$ is chosen to select the quadrotor velocity $\dot{x}$ as the system output. Shown in red is when the output matrix $\mathbf{C}_{fpx}$ is chosen to select the payload angle rate $\dot{\theta}_L$ as the system output. 52

4.1 Quadrotor Control System Architecture 58

4.2 Closed-loop pitch rate control system 59

4.3 Bode plot of open loop pitch rate system 60

4.4 Step response of closed loop pitch rate system T_Q, from input Q_R to pitch rate Q 61

4.5 Tilt Angle Controller 62

4.6 Tilt Angle Calculation 62

4.7 Tilt Angle Controller - simplified 63

4.8 Bode plot of open-loop tilt angle system (both compensated and uncompensated) 64

4.9 Step response of closed-loop tilt angle system $T_T(s)$, from tilt angle reference θ_R to tilt angle θ 65

4.10 Step response of tilt angle controllers to reference step force command in high-fidelity simulation 66

4.11 Step response of tilt angle controllers to reference step inertial force command in high-fidelity simulation 66

4.12 Step response of pitch angle in high-fidelity simulation 67

4.13 Benchmark controller implemented in high-fidelity simulation . . . 68

4.14 Linear quadrotor vertical velocity control system 69

4.15 Bode plot of linear floating point model P_{vz} and linear model with controller, $P_{vz}K_D$. 72

4.16 Step response of linear model P_{vz} with PI controller K_D. Also shown are the responses when the payload mass M_L and the thrust uncertainty T_t are varied. 73

4.17 Horizontal velocity controller architecture 73

4.18 Bode plot of linear floating point model P_{fpx}, tilt angle dynamics T_T, and combined model $P_{vx} = P_{fpx}T_T$. 74

4.19 Bode plot of open-loop uncompensated plant P_{vx}, the transfer function from y to u of the linear quadratic controller, which is denoted $\mathbf{K}_{lqi}(1,2)$, and the compensated system $P_{vx}\mathbf{K}_{lqi}(1,2)$. 79

4.20 Step response of closed-loop system with LQI controller to a horizontal velocity command 80

4.21 Poles and zeros of velocity control system with LQI controller. $\times$ is used to mark poles, and $\circ$ is used to mark zeros. Also shown are poles and zeros of the nominal open-loop system P_{vx}, shown in red. 81

4.22 Bode plot of open-loop system with LQI controller. Also shown are the responses with perturbed plants from the uncertainty set. . . . 82

4.23 Bode plot of closed-loop system with LQI controller. Also shown are the responses with perturbed plants from the uncertainty set. . 82

4.24 Response of quadrotor velocity $\dot{x}$ to a reference velocity command $\dot{x}_R$, with LQI controller. Also shown is the response of the linear model P_{vx} to the same reference input. 83

4.25 Response of payload angle θ_L to the same reference velocity command $\dot{x}_R$, with LQI controller. 84

4.26 Monte Carlo simulation of quadrotor velocity $\dot{x}$, with LQI controller, using high-fidelity simulation 84

4.27 Monte Carlo simulation of payload angle θ_L, with LQI controller, using high-fidelity simulation 85

4.28 Response of quadrotor velocity $\dot{\mathbf{p}}$ to a reference velocity command $\dot{\mathbf{p}}_R$, with LQI controller. In this simulation, the uncertain plant parameters are set to $M_L = 6$kg, $L = 1.7$m and $T_t = 1.2$. 86

4.29 Response of payload angle ϕ_L and θ_L to a reference velocity command $\dot{\mathbf{p}}_R$, with LQI controller. In this simulation, the uncertain plant parameters are set to $M_L = 6$kg, $L = 1.7$m and $T_t = 1.2$. . . . 87

5.1 General Control Configuration 89

5.2 General control configuration with performance bounds 91

5.3 Coprime factor Uncertainty. 93

5.4 $\mathbf{M\Delta}$ used for robust stability analysis 96

5.5 Coprime factor uncertainty. 97

5.6 Feedback system with left coprime factor uncertainty 102

5.7 Standard feedback configuration. 103

5.8 H_∞ loop shaping controller 107

5.9 H_∞ loop shaping controller used to control quadrotor velocity . . . 108

5.10 Bode plot of plant P_{vs}, shaped plant $P_s = P_{vs}W_1$, and shaping weight W_1. 110

5.11 Magnitude of $\rho(P_s, K)$ and $f(w) = \max_{P_{s-unc}} \Phi(P_s, P_{s-unc})(jw)$ . . 111

5.12 Bode plot of plant P_{vs}, shaped plant $P_s = P_{vs}W_1$, and shaped plant with H_∞ controller $P_sK = P_{vx}K_{LS}$. 111

5.13 Step response of closed-loop system with H_∞ loop shaping controller to a reference velocity command. 112

5.14 Poles and zeros of velocity control system with H_∞ loop shaping controller. $\times$ is used to mark poles, and $\circ$ is used to mark zeros. Also shown are poles and zeros of the nominal open-loop system P_{vx}, shown in red. 113

5.15 Bode plot of open-loop system with H_∞ loop shaping controller. Also shown are the responses with perturbed plants from the uncertainty set. 114

5.16 Bode plot of closed-loop system with H_∞ loop shaping controller. Also shown are the responses with perturbed plants from the uncertainty set 114

5.17 Response of quadrotor velocity $\dot{x}$ to a reference velocity command $\dot{x}_R$, with H_∞ loop shaping controller. 115

5.18 Response of payload angle θ_L to a reference velocity command $\dot{x}_R$, with H_∞ loop shaping controller. 116

5.19 Monte Carlo simulation of quadrotor velocity $\dot{x}$, with H_∞ loop shaping controller, using high-fidelity simulation 116

5.20 Monte Carlo simulation of payload angle θ_L, with H_∞ loop shaping controller, using high-fidelity simulation. 117

5.21 Response of quadrotor velocity $\dot{\mathbf{p}}$ to a reference velocity command $\dot{\mathbf{p}}_R$, with H_∞ loop shaping controller. In this simulation, the uncertain plant parameters are set to $M_L = 6$kg, $L = 1.7$m and $T = 1.2$. 118

5.22 Response of payload angle ϕ_L and θ_L to a reference velocity command $\dot{\mathbf{p}}_R$, with H_∞ loop shaping controller. In this simulation, the uncertain plant parameters are set to $M_L = 6$kg, $L = 1.7$m and $T = 1.2$. 119

6.1 Example frequency-by-frequency plot of $\bar{\sigma}(\Phi(\mathbf{P}_1, \mathbf{P}))(jw)$ and $\rho(\mathbf{P}, \mathbf{K})(jw)$.123

6.2 Magnitude of $\rho(P_s, K)$ and $f(w) = \max_{P_{s-unc}} \Phi(P_s, P_{s-unc})(jw)$ . . 124

6.3 Generalised plant for solving extended robust stabilisation 126

6.4 Feedback system with left coprime factor uncertainty 127

6.5 Feedback system with left coprime factor uncertainty cast into general configuration 127

6.6 Extended H_∞ loop shaping controller 130

6.7 Extended H_∞ loop shaping controller used to control quadrotor horizontal velocity 131

6.8 Magnitude of $\rho(P_s, K_\infty)$ and $\sin(\arcsin f(w) + \arcsin \alpha)$ 132

6.9 Bode plot of plant P_{vs}, shaped plant $P_s = P_{vs}W_1$, and shaped plant with extended H_∞ controller $P_sK_\infty = P_{vx}K_{ELS}$. 133

6.10 Bode plot of extended H_∞ controller $K_{ELS} = W_1K_\infty$. 134

6.11 Step response of closed-loop system with extended H_∞ loop shaping controller to a reference velocity command 135

6.12 Poles and zeros of velocity control system with extended H_∞ loop shaping controller. $\times$ is used to mark poles, and $\circ$ is used to mark zeros. Also shown are poles and zeros of the nominal open-loop system P_{vx}, shown in red. 135

6.13 Bode plot of open-loop system with extended H_∞ loop shaping controller. Also shown are the responses with perturbed plants from the uncertainty set. 136

6.14 Bode plot of closed-loop system with extended H_∞ loop shaping controller. Also shown are the responses with perturbed plants from the uncertainty set. 137

6.15 Response of quadrotor velocity $\dot{x}$ to a reference velocity command $\dot{x}_R$, with extended H_∞ loop shaping controller. 137

6.16 Response of payload angle θ_L to a reference velocity command $\dot{x}_R$, with extended H_∞ loop shaping controller. 138

6.17 Monte Carlo simulation of quadrotor velocity $\dot{x}$, extended with H_∞ loop shaping controller, using high-fidelity simulation 139

6.18 Monte Carlo simulation of payload angle θ_L, with extended H_∞ loop shaping controller, using high-fidelity simulation 139

6.19 Response of quadrotor velocity $\dot{\mathbf{p}}$ to a reference velocity command $\dot{\mathbf{p}}_R$, with extended H_∞ loop shaping controller. In this simulation, the uncertain plant parameters are set to $M_L = 6$kg, $L = 1.7$m and $T = 1.2$. 140

6.20 Response of payload angle ϕ_L and θ_L to a reference velocity command $\dot{\mathbf{p}}_R$, with extended H_∞ loop shaping controller. In this simulation, the uncertain plant parameters are set to $M_L = 6$kg, $L = 1.7$m and $T = 1.2$. 141

7.1 Two-degrees-of-freedom H_∞ loop shaping controller 143

7.2 Two-degrees-of-freedom H_∞ loop shaping problem 144

7.3 Two-degrees-of-freedom H_∞ loop shaping problem with controller $\mathbf{K}$ expanded 145

7.4 Quadrotor velocity control system with two-degrees-of-freedom H_∞ loop shaping controllers 147

7.5 Two-degree-of-freedom H_∞ loop shaping controller used to control horizontal quadrotor velocity. 148

7.6 Step response of reference system T_{ref} and step response of nominal plant P_{vx} with two-degrees-of-freedom H_∞ loop shaping controller. . 150

7.7 Bode plot of reference system T_{ref} and resulting closed-loop systems with two-degrees-of-freedom H_∞ loop shaping controller and two-degrees-of-freedom extended H_∞ loop shaping controller. 150

7.8 Step response of quadrotor velocity with two-degrees-of-freedom H_∞ loop shaping controller to a reference unit step, with perturbations present in the plant. 151

7.9 Poles and zeros of velocity control system with the two-degrees-of-freedom H_∞ loop shaping controller. $\times$ is used to mark poles, and $\circ$ is used to mark zeros. Also shown are poles and zeros of the nominal open-loop system P_{vx}, shown in red. 152

7.10 Bode plot of closed-loop system with the two-degrees-of-freedom H_∞ loop shaping controller. Also shown are the responses with perturbed plants from the uncertainty set. 153

7.11 Response of quadrotor velocity $\dot{x}$ to a reference velocity command $\dot{x}_R$, with extended H_∞ loop shaping controller. 154

7.12 Response of payload angle θ_L to a reference velocity command $\dot{x}_R$, with extended H_∞ loop shaping controller. 154

7.13 Monte Carlo simulation of quadrotor velocity $\dot{x}$, extended with H_∞ loop shaping controller, using full nonlinear simulation 155

7.14 Monte Carlo simulation of payload angle θ_L, with extended H_∞ loop shaping controller, using full nonlinear simulation 156

7.15 Response of quadrotor velocity $\dot{\mathbf{p}}$ to a reference velocity command $\dot{\mathbf{p}}_R$, with two-degrees-of-freedom H_∞ loop shaping controller. In this simulation, the uncertain plant parameters are set to $M_L =$ 6kg, $L = 1.7$m and $T = 1.2$. 157

7.16 Response of payload angle ϕ_L and θ_L to a reference velocity command $\dot{\mathbf{p}}_R$, with two-degrees-of-freedom H_∞ loop shaping controller. In this simulation, the uncertain plant parameters are set to $M_L =$ 6kg, $L = 1.7$m and $T = 1.2$. 158

7.17 Two-degree-of-freedom extended H_∞ loop shaping controller 158

7.18 Two-degrees-of-freedom H_∞ extended loop shaping problem 159

7.19 Simplified two-degrees-of-freedom H_∞ extended loop shaping problem 159

7.20 Generalised control configuration for two-degrees-of-freedom H_∞ extended loop shaping problem 160

7.21 Quadrotor velocity control system with two-degrees-of-freedom extended H_∞ loop shaping controllers 162

7.22 Two-degrees-of-freedom extended H_∞ loop shaping controller 162

7.23 Step response of quadrotor velocity with two-degrees-of-freedom extended H_∞ loop shaping controller to a reference unit step, with perturbations present in the plant. 164

7.24 Poles and zeros of velocity control system with the two-degrees-of-freedom extended H_∞ loop shaping controller. $\times$ is used to mark poles, and $\circ$ is used to mark zeros. Also shown are poles and zeros of the nominal open-loop system P_{vx}, shown in red. 165

7.25 Bode plot of closed-loop system with the two-degrees-of-freedom extended H_∞ loop shaping controller. Also shown are the responses with perturbed plants from the uncertainty set. 165

7.26 Response of quadrotor velocity $\dot{x}$ to a reference velocity command $\dot{x}_R$, with extended H_∞ loop shaping controller. 166

7.27 Response of payload angle θ_L to a reference velocity command $\dot{x}_R$, with extended H_∞ loop shaping controller. 167

7.28 Monte Carlo simulation of quadrotor velocity $\dot{x}$, with two-degrees-of-freedom extended H_∞ loop shaping controller, using full nonlinear simulation 168

7.29 Monte Carlo simulation of payload angle θ_L, with two-degrees-of-freedom extended H_∞ loop shaping controller, using full nonlinear simulation 168

7.30 Response of quadrotor velocity $\dot{\mathbf{p}}$ to a reference velocity command $\dot{\mathbf{p}}_R$, with two-degrees-of-freedom extended H_∞ loop shaping controller. In this simulation, the uncertain plant parameters are set to $M_L = 6$kg, $L = 1.7$m and $T = 1.2$. 169

7.31 Response of payload angles ϕ_L and θ_L to a reference velocity command $\dot{\mathbf{p}}_R$, with the two-degrees-of-freedom extended H_∞ loop shaping controller. In this simulation, the uncertain plant parameters were set to $M_L = 6$kg, $L = 1.7$m and $T = 1.2$. 170

7.32 Two-impulse sequence (ZV shaper) designed to have zero vibration at the expected system natural frequency w with a certain damping ratio ζ. 172

7.33 Residual vibrations as a function of normalised frequency w_{actual}/w. The ZV shaper is designed to have zero residual vibrations at $w_{actual} = w$. The ZVD shaper is designed to have zero residual vibration and zero residual vibration derivative at $w_{actual} = w$. . . . 174

7.34 Three-impulse sequence (ZVD shaper) designed to have zero vibration at the expected system natural frequency w with a certain damping ratio ζ. The impulses are also designed to ensure the residual vibration is less sensitive to changes in natural frequency and damping. 174

7.35 A arbitrary input being convolved with an impulse sequence to produce a shaped input 175

7.36 Pole-zero plot of P_{fpx} 176

7.37 An arbitrary input in the form of a reference force command in the inertial frame, $\boldsymbol{\tau}_{I_D}$. The input is shaped by a ZVD shaper to form a shaped input $\boldsymbol{\tau}_{I_R}$. 176

7.38 An arbitrary input in the form of a reference force command in the x direction, $\tau_{I_{R_x}}$. Also shown is the same input convolved with the ZVD shaper. 177

7.39 Quadrotor velocity response to arbitrary input, as well as to the shaped input. 178

7.40 Load angle response to arbitrary input, as well as to the shaped input. 179

7.41 Flight control system using input shaping and extended H_∞ loop shaping controller 180

7.42 Quadrotor velocity responses of many plants in uncertainty set to shaped input alone. 181

7.43 Load angle response of many plants in uncertainty set to shaped input alone. 182

7.44 Quadrotor velocity responses of many plants in uncertainty set to shaped input in conjunction with extended H_∞ loop shaping controller.
183

7.45 Load angle response of many plants in uncertainty set to shaped input in conjunction with extended H_∞ loop shaping controller . . 183

7.46 Quadrotor velocity response to shaped input with and without extended H_∞ loop shaping controller acting as a feedback controller. The quadrotor velocity receives a step disturbance 20 seconds into the simulation. 184

7.47 Load angle response to shaped input with and without extended H_∞ loop shaping controller acting as a feedback controller. The quadrotor velocity receives a step disturbance 20 seconds into the simulation. 185

A.1 General Control Configuration 195

C.1 Wind disturbance model 199

List of Tables

C.1 Plant Parameters 198
C.2 Gyroscope and GPS Measurement Noise Parameters in Simulation . 199

Abstract

Robust Control of a Quadrotor with a Suspended Payload

C. C. Taylor

Department of Electrical and Electronic Engineering,
University of Stellenbosch,
Private Bag X1, Matieland 7602, South Africa.

Dissertation: PhD

March 2020

This dissertation presents the design of a feedback control system for a quadrotor with a suspended payload, where the quadrotor-payload system contains significant uncertainties in the quadrotor thrust, the cable length, and the payload mass. The proposed controller provides robust stability with a guaranteed minimum stability margin for any plant in the uncertain set, and enables velocity reference tracking for the quadrotor vehicle, while adding damping to the payload swinging motion. The controller is designed using a novel modified H_∞ extended loop shaping design procedure that utilises H_∞ optimization and the ν-gap metric. The controller is used in a hybrid feedforward-feedback configuration whereby a robust Zero-Vibration-Derivative input shaper is used to generate shaped inputs that accomplish aggressive manoeuvres of the quadrotor, while cancelling residual oscillations of the suspended payload. The controller acts to correct deviations from the nominal trajectory, and ensures robust stability. The extended H_∞ loop shaping controller is compared to a benchmark LQR controller and a standard H_∞ loop shaping controller. The controller is verified in simulation using a validated simulation model of the SLADe quadrotor UAV. The results show that the new extended H_∞ loop shaping controller performs significantly better in terms of payload swing suppression, and provides robust stability for up to $\pm$ 20% thrust uncertainty, $\pm$ 25% cable length uncertainty, and $\pm$ 71% payload mass uncertainty.

Uittreksel

Robuuste Beheer van 'n Kwadrotor met 'n Hangende Vrag

C. C. Taylor

Departement Elektriese en Elektroniese Ingenieurswese,
Universiteit van Stellenbosch,
Privaatsak X1, Matieland 7602, Suid Afrika.

Proefskrif: PhD

Maart 2020

Hierdie proefskrif beskryf die ontwerp van 'n terugvoerbeheerstelsel vir 'n kwadrotor hommeltuig met 'n hangende vrag, waar die kwadrotor-vrag stelsel beduidende onsekerhede bevat in die stukrag van die rotors, die lengte van die kabel, en die massa van die vrag. Die voorgestelde beheerder verskaf robuuste stabiliteit met 'n gewaarborgde minimum veralgemeende stabiliteitsgrens vir enige aanleg in die onsekerheidversameling, en stel die kwadrotor in staat om snelheidsverwysings te volg terwyl dit die swaaibeweging van die hangende vrag demp. Die beheerder ontwerp word uitgevoer met 'n nuwe aangepaste uitgebreide H_∞ lusvorming ontwerp prosedure wat H_∞ optimisering en die ν-gap metriek gebruik. Die beheerder word gebruik in 'n hibriede vorentoevoer-terugvoer konfigurasie waarin 'n robuuste Zero-Vibrasie-Afgeleide intreevormer gebruik word om 'n gevormde intree te genereer om aggressiewe bewegings uit te voer met die kwadrotor, terwyl die residuele vibrasies in die hangende vrag gekanselleer word. Die terugvoerbeheerder tree dan op om afwykings van die nominale verwysingstrajek teen te werk, en verseker daarby robuuste stabiliteit. The beheerder is geverifieer in simulasie met 'n gevalideerde simulasiemodel van die SLADe kwadrotor onbemande hommeltuig. Die resultate wys dat die nuwe uitgebreide H_∞ lusvorming beheerder beduidend beter vaar in terme van die onderdrukking van die vrag se swaaibeweging, en dat dit robuuste stabiliteit verseker vir tot $\pm$ 20% stukrag onsekerheid, tot $\pm$ 25% onsekerheid in die lengte van die kabel, en tot $\pm$ 71% onsekerheid in die massa van die vrag.

Acknowledgements

I would like to thank the following people and organisations for their support and contributions towards this dissertation:

- My supervisors, Dr Japie Engelbrecht and Johann Treurnicht, for guiding me and motivating me throughout this project. Special thanks to Dr Japie Engelbrecht for his enthusiasm, patience, and encouragement over the last few years, and for being a guide into the world of research.
- My wife, Rebecca, for her love and support. Thank you for the sacrifices that you have made for me to complete my PhD, even though you were in the depths of completing your own PhD. Thank you for your understanding and willingness to encourage me when the task ahead seemed large.
- My daughter Liz, who has recently become aware of how much I time I spend sitting at my desk working. I look forward to telling you more about this season when you are older.
- My parents, Malcolm and Annette, for their support and for believing in me, and for always being willing to help Rebecca and I.
- My parents-in-law, Dave and Mimi, for the incredible support they have given Rebecca and I in this season.
- My siblings, Dean and Lauren, for your friendship over the last few years. Thank you for being interested in the progress of my PhD, and for giving Rebecca and I a sense of community in what was otherwise a very isolating time.
- DeltaV Aerospace, for the support they provided for me to complete my studies.

Nomenclature

Acronyms

ESL	Electronic Systems Laboratory
IDA-PBC	Interconnection and Damping Assignment Passivity-Based Control
lcf	Left coprime factorization
LMI	Linear Matrix Inequalities
LSDP	Loop Shaping Design Procedure
LSPI	Least Squares Policy Iteration
LTR	Loop Transfer Recovery
LQG	Linear Quadratic Gaussian
MAV	Micro-Aerial Vehicles
MPC	Model Predictive Control
NASA	National Aeronautics and Space Administration
RCAC	Retrospective Cost Adaptive Controller
rcf	Right coprime factorization
SMC	Sliding Mode Control
SQP	Sequential Quadratic Programming
ZV	Zero-Vibration
ZVD	Zero-Vibration-Derivative

Symbol Conventions

x	Scalar

$\mathbf{x}$	Vector
$\mathbf{X}$	Matrix

Constants

g	Gravitational acceleration

System Parameters

M_c	Quadrotor mass
d	Moment arm of thrust force
r_D	chord length where the rotor drag force is exerted
R_{LD}	Rotor's lift to drag ratio
M_L	Load mass
L	Cable length
τ	Rotor lag time constant

Aircraft Dynamics

L, M, N	Coordinates of moment vector in body axes (roll, pitch, and yaw moment)
I_{xx}, I_{yy}, I_{zz}	Principle moments of inertia of the quadrotor in body axis
P, Q, R	Coordinates of angular velocity vector in body axes (roll, pitch, and yaw rates)
δ_A, δ_E, δ_R	Virtual aileron, elevator and rudder control inputs. These map to individual rotor thrusts.
δ_{A_R}, δ_{E_R}, δ_{R_R}	Virtual aileron, elevator and rudder control input reference commands. These map to individual rotor thrust commands.
T_t	Total thrust force
T_i	Thrust force of rotor i
T_{i_R}	Thrust force command for rotor i
$\mathbf{p}$	Position vector in inertial axes (north, east and down position)

x, y, z	Coordinates of position vector in inertial axes (north, east and down position)
$\dot{\mathbf{p}}$	Velocity vector in inertial axes (north, east and down position)
$\dot{x}$,$\dot{y}$,$\dot{z}$	Coordinates of velocity vector in inertial axes (north, east and down position)
ϕ, θ, ψ	Euler 3-2-1 attitude parameters of body axis system relative to inertial axis system (roll, pitch, and yaw angle)

Load Dynamics

$\mathbf{p}_L$	Position vector in inertial axes (north, east and down position)
x_L, y_L, z_L	Coordinates of position vector in inertial axes (north, east and down position)
$\dot{\mathbf{p}}_L$	Velocity vector in inertial axes (north, east and down position)
$\dot{x}_L$,$\dot{y}_L$,$\dot{z}_L$	Coordinates of velocity vector in inertial axes (north, east and down position)
ϕ_L, θ_L	Angle of the load cable relative to Down direction, representing rotations around the North axis and the East axis respectively.
$\bar{v}$	Steady-state quadrotor and load velocity
$\phi_L^{\bar{v}}$, $\theta_L^{\bar{v}}$	Steady-state load swing angles at steady-state velocity

System Inputs

$\boldsymbol{\tau}_I$	Force vector in inertial coordinates, applied to quadrotor.
$\boldsymbol{\tau}_{I_R}$	Reference force vector in inertial coordinates, applied to quadrotor.

Aerodynamic Model

ρ	Density of air
C_D	Drag coefficient of the quadrotor
A_x, A_y, A_z	Drag force reference area of the quadrotor in the North, East, and Down direction respectively

A_L	Drag force reference area of the load in all directions
$\mathbf{D}_I$	Drag force vector acting on quadrotor, in inertial coordinates
D_x, D_y, D_z	Coordinates of drag force acting on quadrotor
$\mathbf{D}_{L_I}$	Drag force vector acting on load, in inertial coordinates
D_{L_x}, D_{L_y}, D_{L_z}	Coordinates of drag force acting on load

Linearised Floating Pendulum Model

$\mathbf{x}$	State vector
$\Delta\tau$	Control input vector
P_{fp}	Transfer function of linearised floating pendulum model in all three inertial directions
P_{fpx}	Transfer function of linearised floating pendulum model in one horizontal inertial direction, such as North.

Linearised Quadrotor Attitude Dynamics

P_Q	Transfer function of linearised pitch rate dynamics
P_P	Transfer function of linearised roll rate dynamics
P_R	Transfer function of linearised yaw rate dynamics

Quadrotor Attitude Control

Q_R	Pitch rate reference
K_Q	Pitch rate controller
T_Q	Transfer function representing closed loop system of pitch rate dynamics and pitch rate controller
$\hat{\boldsymbol{\tau}}_{I_R}$	Normalised force vector reference in inertial axis system
$\mathbf{k}_{\tau_B}$	Normalised force vector reference in body axis system
$\mathbf{k}_z$	Unit vector in body fixed z-axis
K_S	Tilt angle controller
S_R	Total tilt rate command

P_R, Q_R	Roll rate command and pitch rate command
P_T	Roll and pitch angle dynamics
T_T	Closed loop roll and pitch angle dynamics with feedback controller K_S.

Linear Quadratic Controller

P_{vx}	Transfer function representing linearised floating pendulum dynamics cascaded with closed loop tilt angle dynamics
P_{vxi}	Transfer function representing P_{vx} but with error integral states added
$\mathbf{Q}$, $\mathbf{R}$	State and control weighting matrices used in solving linear quadratic optimization
$\mathbf{F}_x$, F_I	State feedback gain and error integral state feedback gain
$\mathbf{L}$	Estimator gain
$\mathbf{K}_{lqi}$	Two-degrees-of-freedom linear-quadratic-integral controller
W_1	Transfer function representing one degree of freedom of the linear-quadratic-integral controller

H_∞ Control Theory

H_∞	The set of all real-rational, stable transfer functions (with bounded H_∞ norm)
L_∞	The set of all real-rational transfer functions with no poles on the imaginary axis (with bounded L_∞ norm)
$\bar{\sigma}()$	Maximum singular value
$\mathbf{W}_u$, $\mathbf{W}_p$	Performance weights on control input and error term
F_l	Lower linear fractional transformation
$\mathbf{G}$	Generalised plant
$\mathbf{\Delta}$	Transfer function representing uncertain dynamics. The system can have any phase angle or magnitude, and is usually bounded by some norm
$\mathbf{N}$, $\mathbf{M}$	Right coprime factors of a plant
$\bar{\mathbf{N}}$, $\bar{\mathbf{M}}$	Left coprime factors of a plant

$\eta()$	Open right half-plane poles
$\zeta()$	Open right half-plane zeros
wno()	Winding number
$\delta_\nu()$	ν-gap metric
$\Psi()$	Frequency-by-frequency magnitude of ν-gap metric if winding number condition is satisfied
b	Generalised stability margin
$\rho()$	Frequency-by-frequency magnitude of b if closed-loop system is stable
M_G	Gain margin
M_P	Phase margin

H_∞ Loop Shaping Design

$P_{vx-perturbed}$	Plant P_{vx} with uncertainties present
$\mathbf{W}_1$, $\mathbf{W}_2$	Pre- and post-compensating performance weights used to shape the nominal plant frequency response
P_s	Plant P_{vx} with performance weights added
P_{s-unc}	Uncertain plant $P_{vx-perturbed}$ with performance weights added
K	Controller synthesised in robust stabilisation step
K_{LS}	Robust stabilising controller with performance weights
$\Omega()$	Set of all plants satisfying a constraint on the ν-gap metric between the plants in the set and a nominal plant

Extended H_∞ Loop Shaping Design

$f(w)$	Frequency-by-frequency worst-case measurement of ν-gap metric between all the plants in the uncertainty set and the nominal plant
α	Residual stability margin guaranteed to all plants in uncertainty set
β	Minimum H_∞ norm of closed-loop system presenting a "shaped" generalised stability margin

W_δ	Real-rational transfer function approximating worst-case ν-gap metric between all the plants in the uncertainty set, with an added safety margin
$\mathbf{K}_\infty$	Controller minimizing β
$\mathbf{K}_{ELS}$	Extended H_∞ loop shaping controller. It is $\mathbf{K}_\infty$ cascaded with the compensating weights.

Two-degrees-of-Freedom Design

$\mathbf{K}$	Two-degrees-of-freedom H_∞ loop shaping controller
$\mathbf{K}_1$, $\mathbf{K}_2$	Pre-filter and standard H_∞ robust stabilizing controller
γ	Magnitude of error of model-matching, in the H_∞ norm sense
ρ	Scalar constant emphasising model-matching or robust stability
$\mathbf{T}_{ref}$	Reference system to use in model-matching
w_n	Natural frequency of reference system
ζ	Damping ratio of reference system
$\mathbf{W}_i$	Constant gain scaling steady-state gain of closed-loop system
$\mathbf{T}_{LS}$	Closed-loop system from reference inputs to outputs of two-degrees-of-freedom controller
$\mathbf{T}_{ES}$	Closed-loop system from reference inputs to outputs of two-degrees-of-freedom controller
T_{els}	Closed-loop system with extended H_∞ loop shaping controller as a feedback controller in the forward path. Used in inner loop in two-degrees-of-freedom extended H_∞ loop shaping controller

Input Shaping Design

w	Expected natural frequency of lightly damped mode in the system
w_{actual}	Actual natural frequency of lightly damped mode in the system

ζ	Damping ratio of lightly damped mode in the system
A_j	Amplitude of impulse j
t_j	Time that impulse j is applied
A_{amp}	Residual amplitude of vibrations from impulses
V_1, V_2	Terms contributing to amplitude of residual vibrations
K	Scalar used to determine amplitude of vibration cancelling impulses for a given system
ΔT	Time between impulses for a given system
$\boldsymbol{\tau}_{I_D}$	Arbitrary desired input reference inertial force
$\boldsymbol{\tau}_{I_S}$	Shaped desired input reference inertial force

Chapter 1

Introduction

1.1 Project Background

There is an increasing number of commercial opportunities for unmanned autonomous aircraft in business (aerial photography, speed courier services in cities), agriculture (surveying, crop inspection, crop dusting, farm security), industry and mining (power line inspection, prospecting), the emergency services (disaster monitoring, delivery of emergency supplies, firefighting) and in security services (surveillance, policing). An interesting application for UAVs is to collect, transport, and deliver different types of loads in urban environments. Example loads may include cargo to be loaded or unloaded, packages to be collected and delivered, and water buckets to be filled and emptied for aerial fire-fighting.

The flying characteristics of helicopter and multi-rotor UAVs enable them to carry suspended loads, where the payload is suspended below the vehicle with one or more cables. However, flying with a suspended payload is a challenging and hazardous task. The suspended payload significantly changes the flight dynamics of the vehicle, and the swinging motion of the suspended payload can result in loss of stability, or collisions with static or dynamic obstacles. Flying with a suspended payload becomes even more challenging when there are uncertainties in the vehicle model and/or the payload mass. The uncertainty in the vehicle model primarily originates from the uncertain rotor thrust characteristics and the uncertain vehicle aerodynamic model. The uncertainty in the payload mass may be because the payload mass is only approximately known (e.g. for aerial cargo transport), or may vary substantially during flight (e.g. for aerial fire-fighting vehicles). A need therefore exists for a flight control system for a quadrotor UAV with a suspended payload that enables reference trajectory tracking for the vehicle, while suppressing the swinging motion of the payload, and providing guaranteed robust stability in the presence of sig-

nificant uncertainties in the vehicle model and the payload mass.

Flight control systems are still predominantly designed in the aerospace industry using classical design and analysis techniques [1]. Many of these classical design and analysis techniques are from the 1950's, yet still find consistent use in place of more modern control techniques. On the one hand, this highlights the proven usefulness of classical control, but on the other hand, it indicates an underlying problem of an ever growing gap between the theory and application of robust control systems.

During the 1960's, research on optimal control resulted in *linear quadratic Gaussian* (LQG) control, coinciding with large space programmes in the United States and the former Soviet Union [2]. LQG control has proven to be a very powerful control technique, forming the basis of successful aerospace solutions. However, the application of LQG control in more widespread applications resulted in less successful solutions; once the problem of robustness became apparent, LQG seemed to have an Achilles heel.

John C. Doyle was the first to show that there are no guaranteed stability margins for an LQG system [3]. Skogestad et al. [2] show how there are guaranteed stability margins for an LQR (linear quadratic regular) controlled system, as well as guaranteed stability margins for an LQE (linear quadratic estimator or Kalman filter), but not for the two systems combined (LQG) due to interactions between the estimator and the controller. Loop transfer recovery (LTR) is a procedure designed to regain those guaranteed stability margins for the full system. However, even the concept of stability margins does not fully quantify the robustness of multi-input multi-output (MIMO) systems, because the classical single-input single-ouput (SISO) concepts of gain and phase margin are lost (or, need to be generalized) when moving to the MIMO case. Also, a key weakness of stability margins alone is that it can be difficult to determine the amount of margin necessary to accommodate a certain uncertainty condition, especially when multiple sources of uncertainty are considered.

This led to the development of robust control theory, starting in the late 1970's and reaching maturity in the early 2000's, when it was successfully applied to a number of aerospace control problems. However, Hyde [4] states that there is still a large gap between the theory developed for robust control, and its successful industrial applications.

In summary, unmanned aircraft with suspended payloads can offer economic and strategic benefits through various applications. However, adding a suspended payload to an aircraft has a generally negative effect on the aircraft dynamics. At the same time, for a system to be practically useful in industrial applications, a robust flight control system is critical to ensure safe and reliable operation of such a system. A need therefore exists for the development

of a robust flight control system for unmanned aerial vehicles with suspended loads, while acknowledging that there is currently a large gap between robust control theory and its practical application to aircraft control systems. In this study, advanced robust control techniques will be used to design a novel robust flight control system for a quadrotor UAV with a suspended payload.

1.2 Research Aims and Objectives

The aim of this research is to develop a robust flight control system for a quadrotor with a suspended payload, thereby contributing to the safe and reliable application of such systems. Furthermore, this research aims at closing the gap between theory and application of advanced robust control systems in an aerospace flight control situation. To this end, the objectives of this research are:

- Formulate a mathematical model of a quadrotor and suspended payload system
- Study the dynamics of a quadrotor with a suspended payload, including formulating a linearised model for analysis and design
- Apply linear-quadratic optimal control methods to design a stabilizing controller for the system. The control system must use only the feedback measurements available on standard quadrotors, and it should suppress the swinging motion of the payload. This will serve as a benchmark control system, as linear quadratic methods are commonly used in aerospace applications and therefore provide a good benchmark of controller performance. The performance of the linear-quadratic-integral controller when used with an uncertain model of the quadrotor and suspended payload must be analysed.
- Use robust control techniques to synthesise a robust flight control system that provides acceptable performance in terms of transient response, bandwidth, and steady-state tracking error. The robust flight control system must provide theoretically guaranteed robust stability when all uncertainties in the system are considered. The control system must use only the feedback measurements available on standard quadrotors, and it should suppress the swinging motion of the payload.
- Use advanced H_∞ control concepts and configurations in order to improve reference trajectory tracking performance of the robust control system.

- Provide a means of generating input reference trajectories to the quadrotor and suspended payload that result in minimal residual swinging of the payload.

1.3 Contributions

The original contributions of this work are:

- A Lagrangian mechanics approach to the modelling of a floating-pendulum is presented. This model represents the translational dynamics of a quadrotor and suspended payload, in a novel quadrotor and suspended payload modelling methodology whereby quadrotor rotational dynamics are treated separately from quadrotor and suspended payload translational dynamics. This method relies on the assumption that the payload cable is attached at the centre of gravity of the quadrotor.
- A novel force-based LQG controller for a quadrotor with a suspended payload is developed. The LQG controller is an adaptation of an earlier acceleration-based successive loop closure controller that was presented by Taylor and Engelbrecht [5].
- A novel algorithm to design a robust controller based on the ν-gap metric and H_∞ optimization is presented. This algorithm is a modified version of an extended H_∞ loop shaping algorithm originally presented by Vinnicombe [6], which is an algorithm that has found little practical application until this research. The resulting control system is theoretically guaranteed to be robustly stable for all the plants in the uncertainty set.
- A novel robust flight control system for a quadrotor with a suspended payload is presented. The proposed controller provides robust stability with a guaranteed minimum stability margin for any plant in the uncertain set, and enables velocity reference tracking. The robust controller is designed using the novel modified H_∞ extended loop shaping design procedure mentioned above.
- A novel two-degrees-of-freedom robust flight control system is presented. This control system uses the robust controller mentioned above, and combines it with a model-matching H_∞ optimization step to synthesise a pre-filter that improves reference tracking performance of the system.
- A robust trajectory tracking control system for a quadrotor with a suspended payload is proposed. The proposed system uses a robust hybrid

feedforward-feedback architecture with feedforward to improve the trajectory tracking and feedback to correct deviations from the planned nominal trajectory. The architecture uses a robust input shaper to eliminate residual oscillations of the swinging payload, and a robust extended H_∞ loop shaping controller to ensure disturbance rejection and trajectory tracking.

1.4 Dissertation Overview

Chapter 1 provided an introduction to the research presented in this dissertation. The background of the study was given, the research aims and objectives were stated, and the original contributions were enumerated. An overview of the dissertation is also provided.

Chapter 2 contains a review of the current state of literature pertaining to control of unmanned aircraft such as quadrotors, control of quadrotors with suspended payloads, trajectory generation methods for lightly damped mechanical systems, and robust control methods. The chapter highlights the absence of robust flight control systems for quadrotors with suspended payloads, and establishes the current state of the existing literature on robust control.

Chapter 3 presents the mathematical modelling of the quadrotor and suspended payload system. A Lagrangian mechanics approach is used to derive a floating-pendulum model for the point mass translational dynamics. The point mass translational model is then augmented with a model of the quadrotor attitude dynamics and thrust.

Chapter 4 presents the design of a novel force-based LQR controller for a quadrotor with a suspended payload. An inner-loop controller is used to control the attitude and the thrust of the quadrotor vehicle so that reference force commands can be tracked. An outer-loop LQR controller then uses the reference force commands to control the quadrotor velocity.

Chapter 5 establishes some theoretical concepts pertaining to H_∞-based robust control, and presents the motivation for using concepts such as H_∞ optimization, H_∞ loop shaping, and the ν-gap metric to design robust controllers. A controller is then designed for the quadrotor with suspended payload using the "standard" H_∞ loop shaping technique.

Chapter 6 presents the design of a novel robust controller for a quadrotor with suspended payload using a modified H_∞ extended loop shaping design technique that utilises H_∞ optimization and the ν-gap metric. The resulting controller provides guaranteed robust stability for all plants in the uncertainty set.

Chapter 7 presents a robust trajectory tracking control system for a quadrotor with a suspended payload. The robust controllers designed in Chapters 5 and 6 are transformed into two-degrees-of-freedom controllers to improve trajectory tracking while maintaining robust stability. A robust hybrid feedforward-feedback architecture is proposed that uses feedforward to improve the trajectory tracking and feedback to correct deviations from the planned nominal trajectory. Input shaping is used to generate reference trajectories that produce minimal residual swinging of the payload.

Chapter 2

Background and Literature Review

2.1 Quadrotors and Suspended Payloads

The problem of controlling quadrotors with suspended payloads is currently a very active research area. Both open-loop trajectory generation methods and closed-loop feedback control methods are being investigated. The open-loop methodologies have focused primarily on shaping the desired trajectories of the quadrotor and suspended payload system, in order to accomplish certain objectives. Due to the highly resonant nature of the system, a common objective is to reduce the swinging motion of the payload. However, other interesting objectives, such as navigation through cluttered environments, have also been pursued. The feedback methodologies have primarily focused on stabilisation and tracking, and often these open-loop and closed-loop methods are combined to form systems where feedback control ensures stability while trajectory generation methods provide inputs for the system that accomplish design objectives.

2.1.1 Trajectory Generation

Trajectory Generation for lightly damped mechanical systems

The design of trajectories that are specifically formulated to reduce vibrations has been investigated for many years, with some of the earliest work being by Smith [7] in 1957. He was the first to show that control inputs for a lightly damped system can be designed to reduce residual oscillations of lightly damped modes. Singer [8] developed the input shaping technique; that is, he showed that specifically timed impulses applied to a system can cancel

out residual oscillation of the lightly damped mode. The usefulness of this technique is that the desired impulses inputs can be convoluted with any other desired inputs to form "shaped" inputs that reduce residual oscillations. Singer also analysed the robustness of input shaping with regards to variations in damping and natural frequencies of the lightly damped modes of a system. He presented the original Zero-Vibration (ZV) damper, and then extended the results to include the more robust Zero-Vibration-Derivative (ZVD) damper.

Starr [9] was the first to show that a carefully controlled path can reduce residual swinging motion in suspended objects. Following these contributions, the two primary methods used to generate swing free trajectories were impulse convolution, such as input shaping, and parameter optimisation, such as sequential quadratic programming (SQP). In 2005, Starr et al. [10] presented dynamic programming as another effective solution. They provided arguments against the suitability of input shaping and parameter optimisation methods as solutions to the trajectory generation problem, and presented a deterministic solution using dynamic programming. They argued that input shaping can produce non-smooth profiles that may not be suitable for practical implementation. This is caused by the convolution of the original trajectory with the oscillation-cancelling impulses. For our study, using non-smooth inputs as reference commands are not a source of concern, and so input shaping remains a viable and attractive solution for the quadrotor with suspended payload application. Starr et al. also argued that problems of non-convexity plague parameter optimisation methods.

Trajectory Generation as an Optimal Control Problem

Today, optimal control theory and a variety of numerical solutions (nonlinear and linear programming) present a large body of available techniques for solving trajectory generation problems. Betts [11] presented a detailed survey of available numerical techniques for trajectory generation.

Historically, the two main methods to solve the optimal control problem were dynamic programming and calculus of variations [12], although in the last few decades, the so-called "direct methods" have gained significant popularity. Of these, sequential quadratic programming (SQP) has been found to be a reliable and efficient solution to optimisation problems with nonlinear constraints, and can handle relatively high-dimensional problems, unlike dynamic programming which suffers from the "curse of dimensionality" [13]. SQP is considered one of the most successful methods for nonlinearly constrained optimisation problems [14], into which the optimal control problem can be formulated. Successful implementations of trajectory generation (and control methodologies) for quadrotor and suspended payload systems will be presented in Section 2.1.3.

2.1.2 Suspended Payloads

From as early as 1930, the dynamics and stability of helicopters with suspended load systems have been extensively studied. Most of these studies have been concerned with developing conditions for stability, such as finding safe flight regions, analysis robustness to parameter variations (such as cable lengths), and analysing the effect of payload shapes on stability (in the case of non-hover flight). In 1992, a technical paper by NASA [15] presented equations of motion for a wide variety of suspended payload configurations attached to helicopters. This work was the culmination of decades of research in this area, with Cicolani et al. [15] and Bisgaard et al. [16] giving more thorough chronologies of the development of the research. Some of the latest work on the dynamics of suspended load aerial systems is presented by Bisgaard et al. [16], who formulated generic equations of motion based on the Udwadia-Kalaba equation. However, this research was once again focused primarily on modelling techniques for different configurations of suspended loads (such as number of cables or transporting vehicles) as well as an analysis of the stability of such systems. Furthermore, their research only considered helicopters as the vehicles that transport the suspended payload. Flight control of helicopters differs from flight control of quadrotors primarily in the manner of actuation. Therefore, although these papers provide good insight, a unique model specifically for a quadrotor with a suspended payload must be used when studying the dynamics of such a system. Lucassen et al. [17] and Fester et al. [18] also performed research on the dynamics of suspended loads.

The problem of automatic control of helicopters received significant attention in the 1970s with solutions to the problems being provided by several different researchers [19, 20, 21, 22, 23]. These solutions were designed with semi-automatic conditions in mind; they were designed for piloted helicopters with suspended payloads. In 1995, a robust control system for a unique helicopter and suspended payload was developed by Faille et al. [24]. However, until this point, there had been a distinct lack of research done on load transportation by fully autonomous unmanned aircraft.

2.1.3 Control of Quadrotors with Suspended Payloads

In the early 2000s, much research into the development and control of micro-aerial vehicles (MAV) had been completed. A fairly comprehensive report on the subject of MAV control (specifically for quadrotors), was compiled by Mahony et al. [25]. What followed was a natural progression of the solutions previously implemented on full-size semi-automatic helicopters being implemented on fully autonomous MAV systems with suspended payloads. Some of the earliest work was done by Bisgaard et al. [26], who focussed mainly on

small-size autonomous helicopters. By 2013, the attention had turned to the control of quadrotors with suspended payloads, as is evident from the research presented by Palunko [27]. This research was most likely fueled by intense interest in the quadrotor as a research and hobbyist platform, and their mechanical simplicity compared to small helicopters. From 2013, research activity on quadrotors with suspended payloads increased dramatically.

In 2011, Palunko first researched the problem of a quadrotor with changes in the position of its centre of gravity, without specific focus on a suspended payload, and used nonlinear adaptive control to stabilise the system [27]. Adaptive control was used to stabilise the attitude motion of the quadrotor if a payload was connected to a point that is a significant distance away from the centre of gravity of the quadrotor. However, the effects of variations in payload mass, cable length, and uncertainty in quadrotor thrust were not analysed.

Following this, Palunko submitted a paper [28] and her PhD thesis [29] on the quadrotor with suspended payload problem, dealing with specific issues such as trajectory generation, cooperative lifting, and changes in the centre of gravity. Three methods were compared to deal with the swing-free trajectory generation: input shaping, dynamic programming, and a method whereby a Taylor series expansion is combined with the Nelder-Mead algorithm or another machine learning algorithm to learn the parameters in the Taylor series expansion. The Nelder-Mead algorithm, as well as a least squares policy iteration (LSPI) method was applied to ensure trajectory tracking. The latter two methods can be cast into the "parameter optimisation" domain, while the former (input shaping) is, of course, within the impulse convolution domain. Palunko showed that input shaping is sensitive to variations in cable length. However, it appears that she only employed a ZV input shaper, and did not use more robust input shapers, such as the ZVD shaper. Palunko et al. also used reinforcement learning to learn swing-free trajectories in cluttered environments [30].

In 2012, Pounds et al. [31] studied the stability of MAV systems with suspended payload under proportional-integral-derivative (PID) control and determined stability bounds for the mass and inertia properties of the system. They focused more on analysing the system with a given set of linear PID controllers, instead of on the synthesis of stabilising controllers.

A subfield of control theory named geometric nonlinear control theory has been applied extensively to the quadrotor-payload problem. Geometric control theory explores the application of differential geometric techniques to systems control, and is attractive because it is globally defined, meaning globally attractive controllers can be designed instead of controllers attractive only near certain operating points [32]. Goodarzi et al. [33] used a geometric nonlinear controller to ensure stability when the cable between the payload and quadrotor is assumed to be flexible (or rather, the effects of its flexibility are

significant). This work was then extended in 2015 to include systems where multiple quadrotors are lifting the payload [34]. Farhad also used geometric control in a robust control type application, showing stability for systems with varying cable lengths [35], as will be discussed later. Cruz et al. [36] also used geometric control to control a quadrotor in various stages of lifting a payload. Here, the geometric properties of system dynamics in various stages of lifting the payload were used to design a geometric nonlinear controller.

Further examples of geometric control are those presented by Kotaru et al. [37], who used geometric control to track load trajectories instead of quadrotor trajectories and also considered the elastic properties of the suspending cable. Taeyoung Lee developed a geometric nonlinear PID control system that incorporates the nontrivial coupling between the payload, links, and quadrotors in an intrinsic fashion, for use in cooperative lifting situations [38].

The nonlinear nature of the quadrotor-payload system has prompted the application of other forms of nonlinear control as well. By treating the supporting aircraft as a point mass and neglecting all rotational dynamics of the aircraft, Klausen et al. [39] derived a model for the system and applied the backstepping nonlinear control technique to achieve trajectory tracking. They also used input shaping to achieve residual swing free transport. Sadr et al. [40] also used nonlinear methods to control a quadrotor with a swinging payload, again focussed specifically on reducing the payload swinging motion. Nicotra et al. [41] used nested saturation control, and Guerrero et al. [42] used interconnection and damping assignment passivity-based control (IDA-PBC). Another passivity-based control approach was presented by Weijers et al. [43]. Ailon also used nonlinear controllers in both open- and closed-loop form to achieve set-point control [44].

Although the overwhelming focus has been on the application of nonlinear control techniques, some linear techniques have been applied as well. Model predictive control was done by Praveen, who also compared it to linear quadratic regulator (LQR) control [45]. He showed how the model predictive controller he designed can be executed in real-time, and that it gives marginally better residual swing reduction than an LQR controller. LQR control was also used by Alothman et al. [46], [47], who then extended the work to use iterative LQR control (iterative linearisation of the non-linear dynamic model and cost function).

Although a few examples of trajectory generation for quadrotor and suspended payload systems have been presented along with a discussion of the control methodologies used in the research, it would be useful to present further examples. Geisert et al. present numerical optimal control solutions for a variety of quadrotor tasks and payload situations [48]. Although they did not study the nonlinear programmer explicitly, they mention that the solver is based on SQP, and provide arguments for the suitability of SQP for such a problem. An-

other example is the mixed-integer quadratic programming used by Mellinger et al. [49] to solve trajectory generation for teams of quadrotors.

While the nonlinear and linear control techniques described above have been successful both in providing basic stability and in executing more dynamic manoeuvres for quadrotors with suspended payloads, they have not considered uncertainties in the system in any comprehensive manner. There are examples where uncertainties have been addressed in a very limited manner, such as Palunko's treatment of an uncertain distance between the vehicles centre of gravity and the payload attachment point. However, the majority of the research reviewed so far has assumed ideal laboratory conditions and the use of very accurate external sensor systems to measure the state of the quadrotor and payload system.

2.1.4 Robust Control of Quadrotors

The flight control system for a quadrotor UAV, like any other feedback control system, is designed using a mathematical model of the system to be controlled. As with any mathematical model, the quadrotor model is an approximate representation of the real quadrotor, and contains model inaccuracies and uncertainties. The aerodynamic forces and moments acting on the quadrotor are difficult to model and the aerodynamic models typically contain significant uncertainty. The quadrotor actuators typically have nonlinear gains which may not be accurately calibrated, and also contain uncertainty in their actuator time constants. The quadrotor sensors and the state estimators may also introduce uncertainties. The quadrotor sensors may contain measurement noise, measurement errors, and measurement delays, while the state estimator that fuses the sensor measurements may introduce time delays. The quadrotor mass and moment of inertia properties may also contain uncertainties. This has naturally led to the application of robust control techniques to the design of flight control systems for quadrotor UAVs.

Raharijaona et al. [50] used linear matrix inequalities (LMI) to address the problem of changes in the centre of gravity and gyroscopic effects caused by accelerations of the propellers. They developed a robust controller for attitude control only, formulating the problem as a LMI subject to consequent convex optimisation. They obtained a stable controller for a quadrotor with a nominal mass of 0.2 kg, and mass variations between 0.1 and 0.3 kg (0.1 kg uncertainty), as well as up to 10 cm of variation in quadrotor's centre of gravity. Lee et al. used geometric nonlinear control to ensure stability for bounded uncertainties [51]. They defined the uncertainties as force and moment quantities acting on the quadrotor and presented stabilising controllers for attitude and position control. However, they defined the uncertainties as force and moment quantities and provided no explanation as to the origin of

the quantities, meaning the exact sources of uncertainty and their respective effects were abstracted away.

Quantitative feedback theory was used by Xu et al. [52] to achieve stable hovering and trajectory tracking in the presence of uncertainties. They provided a detailed description of a large number of uncertainties that they consider in parametric form. However, most of the uncertainties were defined to be relatively small (in the order of 25% or less).

Other forms of linear robust control have also been applied. H_∞ loop shaping was done by Rich et al. [53]. Rich et al. derived a full model of quadrotor system, and then used a combination of linear quadratic control as well as a controller designed using the H_∞ loop shaping design procedure to achieve step tracking control. However, they exploited the fact that H_∞ loop shaping does not require any specific knowledge of the uncertainty that is present. They did not model any uncertainties, nor did they show robustness to any kind of uncertainty. They presented only the response of the nominal system and assumed that the system would be fairly robust given the results of the H_∞ algorithm.[1]

Linear robust control methods were also appled by Satici et al [55]., who used an L_1 optimal controller and compared it to a nonlinear back-stepping controller, finding that the linear compensator performed better. The controllers were designed for the attitude control of the quadrotor, with Satici et al. stating that they believed this is where the most significant uncertainty in the system reside. They argued that uncertainty in the attitude dynamics of the quadrotor will have significant effects on the translational dynamics. However, they shied away from detailed descriptions of the uncertainty and used linear control techniques that guarantee good disturbance rejection.

It must be noted that the literature on robust control of quadrotors is, in comparison to the literature pertaining to nonlinear control, quite limited. The common theme present throughout the research described above is that rotational dynamics are usually the most sensitive to uncertainties. While uncertainties in the rotational dynamics of the quadrotor will have significant effects on the translational dynamics of the quadrotor, experience and intuition indicate that these effects are rarely significant enough to cause translational instability. However, the case may be considerably different if a suspended payload is introduced, meaning it is pertinent to consider uncertainties in the system dynamics when moving to the quadrotor with suspended payload control problem.

[1]The H_∞ algorithm presented by Glover et al. [54] results in a parameter b that has a stability margin interpretation, meaning some "rules of thumb" can be made about systems being robustly stable to general uncertainty if $b > c$, where c is some small positive constant.

2.1.5 Robust Control of Quadrotors with Suspended Payloads

There has been a noticeable lack of research done on the robust control of quadrotor and suspended payload systems. The dominant focus of research on quadrotors and quadrotors with suspended payloads has been on the application of nonlinear control methods. This can be attributed to the following factors:

1. The majority of research on quadrotors with suspended payloads has been done in laboratories. Sophisticated measurement systems such as Vicon [56] have been used to enable precise measurements of the quadrotor and payload states.

2. The attention of researchers quickly turned to the execution of complex tasks, such as cooperative lifting, lifting the payload off the ground, and aggressive maneouvres. This naturally steered the attention away from linear control techniques applied at certain operating conditions, to nonlinear control techniques aiming for greater effectiveness in incorporating the highly nonlinear nature of the dynamics of a quadrotor and suspended payload system.

By assuming full-state feedback, the controllers often require the measurement of system states that would require further development to achieve on-board, motivating the use of external sensor systems. Also, the robustness of the controllers is rarely considered, so practical applications outside of laboratories are limited. This has prompted some efforts to research and develop robust flight controllers for the quadrotor and suspended payload system.

Some of the earliest work in the robust control of quadrotors and payloads was done by Min et al. [57]. They used adaptive robust control for the altitude control of a quadrotor carrying an uncertain payload, and used Lyapunov stability theory to show stability for a range of mass and inertia uncertainties in the system. However, they did not consider the payload directly; they treated the payload as rigidly attached to the quadrotor body, with uncertainties in the payload simply changing the mass and inertia properties of the quadrotor.

Dai et al. considered the case of a quadrotor with a suspended payload, and used a retrospective cost adaptive controller (RCAC) to eliminate steady-state errors in the altitude control caused by payloads of uncertain mass [58]. A nonlinear proportional-derivative (PD) controller was used for trajectory tracking, and the RCAC was used to account for uncertain payload masses. However, their study focussed primarily on altitude control, and showed that the RCAC performed slightly better than PID control, where the integral term would account for steady-state errors instead of the RCAC. They did not consider the

system as a whole, and the effects of the payload on the quadrotor and on the stability of the system were not considered.

Lee et al. [59] used parameter-robust linear quadratic regulator (PR-LQR) control. They showed that it is difficult to achieve parameter robustness in more than one direction of flight by using PR-LQR. Also, the only form of uncertainty that they considered was payload mass uncertainty.

Raffo et al. [60] used nonlinear robust control (by synthesising a nonlinear H_∞ controller and using a Lyapunov redesign technique) to design a robust control system for a quadrotor and suspended payload system. However, the only uncertainty that they considered is uncertainty in the inertia tensor of the quadrotor, which would affect the quadrotors rotational dynamics only. They used a technique of separating the system into *actuated* and *unactuated* parts during their control design. They also assumed that there are no external disturbances on the system.

Goodarzi used nonlinear geometric control and a stability proof based on the Lyapunov theory to show stability in the presence of varying cable lengths [35]. However, he considered only uncertainty in the cable length, and did not consider any other uncertainties.

The latest work to directly address payload mass uncertainty is that of Zhou et al. [61], who used PD control, sliding mode control (SMC), and model predictive control (MPC), to achieve basic trajectory tracking for systems with uncertain payload masses. However, they treated the payload very simplistically, as an unknown disturbance on the quadrotor, and then just designed a control system that has good disturbance rejection. Also, they only dealt with the issue of stability, and compared the three different controllers in terms of stability bounds (they determined the maximum payload mass variations for which the system would still remain stable). Due to their modelling the payload as a disturbance acting on the quadrotor, they did not consider the dynamics of the complete system.

This literature review therefore reveals that there has been a lack of linear robust control techniques applied to the quadrotor with suspended payload system. A well-formulated robust flight controller that can achieve a guaranteed level of performance with multiple sources of uncertainty present has not been presented, and we therefore identify this as a clear research gap.

2.2 Robust Control Methods

2.2.1 Outline of Available Techniques

As mentioned in the introduction, robust control research began in order to address the shortcomings of LQG control to handle system uncertainties. Loop transfer recovery (LTR) is a procedure designed to improve the ability of LQG control to handle uncertainties, yet Skogestad et al. [2] argue that the practical applicability of LTR is somewhat limited. They argue that it has some critical shortcomings, such as the requirement of the plant to be minimum phase, and the tendency of high gains to be introduced which can excite unmodelled dynamics. Because the gains need to be kept lower, LTR is often not used at its limits (the individual loop transfer function stability margins are not fully recovered), and what remains is an abstract and unintuitive procedure at indirectly shaping the open-loop transfer function singular values. The H_∞ loop shaping technique, which will be described later, is a much more intuitive and appealing technique for loop shaping.

LTR forms part of a list of other well-established or currently-developing methodologies for dealing with uncertainty in control systems. Some of the common and emerging areas of robust control include:

- Adaptive control: methodologies to design controllers that can learn (by parameter convergence) to deal with uncertainties or changes in plant dynamics. They can suffer from problems with parameter convergence, and the changes in dynamic performance can be difficult to predict for sudden changes in the plant (parameters need to be "learnt").

- Fuzzy control: control systems that rely on fuzzy logic. Fuzzy control claims not to need detailed mathematical descriptions of the plant. While appropriate for some situations, it appears to be rejected by many control theorists.

- Linear matrix inequalities: sophisticated mathematical techniques that generally result in convex or quasiconvex optimisations of linear matrix inequalities. Occasionally, closed form solutions exist for certain well known LMIs [62]. LMI formulations are frequently encountered in H_∞ control.

- Lyapunov techniques: energy-based techniques that are often used for nonlinear systems. Through a Lyapunov stability analysis, one can show stability for a bounded range of conditions.

- Loop transfer recovery: progressed from LQG control, an attempt to obtain the guaranteed stability margins that a linear quadratic regulator

or Kalman filter (linear quadratic estimator) would have by themselves [2].

- H_∞ control: the first robust control methodology, and still today the most popular and well known. They are frequency-domain techniques that bound the H_∞ norms of systems.

- Quantitative feedback theory: another frequency-domain technique that relies on the Nichols chart to bound and specify performance objectives and plant uncertainties [63].

For this study, we will focus on H_∞ control as it is still the favoured methodology and because of the ease with which uncertainties can be translated into the frequency domain. These techniques allow the designer to specify performance requirements in the frequency domain, and along with frequency domain representations of uncertainty and frequency-domain stability conditions, holistic control solutions can be obtained. Also, robust H_∞ control systems do not rely on real-time parameter convergence (such as in adaptive control systems), so they can guarantee stability for sudden changes in the plant, as long as those changes are within the uncertainty bounds. Furthermore, linear robust H_∞ control methods can be formulated while considering system nonlinearities as uncertainty in the system. The control methods can then provide robustness against the potentially negative affects of assuming linear system behaviour.

Although some of the other methodologies of robust control may also provide elegant solutions for the quadrotor-suspended payload system, H_∞ control is still supported by the strongest body of literature in terms of uncertainty representations and robustness analyses. Therefore, it seems pertinent to consider these methodologies thoroughly and prior to any of the other methodologies, and hence the decision to focus primarily on them for this project.

2.2.2 H_∞ Techniques

H_∞ techniques are built upon the concept of the H_∞ norm of a system. The H comes from the fact that we are considering the ∞-norm in the Hardy space, which is simply the set of all stable and proper transfer functions. A discussion of systems norms relating to this study is presented in Appendix A. It is this system norm and its minimization that H_∞ algorithms seek to address, because the H_∞ norm of a system has direct consequences on the time-domain response of a system.

Some popular H_∞ control methods are:

1. Mixed-sensitivity H_∞ control

2. Signal-based H_∞ control
3. μ-analysis
4. μ-synthesis
5. H_∞ loop shaping design procedure

In H_∞ control, the most common and generally appealing method is the H_∞ loop shaping design procedure (LSDP), developed by Macfarlane [54]. The H_∞ loop shaping technique has been successfully applied to some complex aerospace solutions [64] [65], has potential for advanced forms of implementation (such as two-degrees-of-freedom controllers and observer-based controllers), and most often has closed-form solutions and does not need optimising iterations to solve the minimum H_∞ norm problem. Essentially, the method requires shaping the open-loop transfer function frequency response using pre- and post-compensating weights, followed by a "robustication" to a general form of uncertainty. The ability to shape the open-loop frequency response presents an intuitive and efficient technique at achieving closed-loop characteristics.

Some recent developments in H_∞ LSDP are the formulation of gain-scheduled H_∞ controllers: which are controllers that use self-scheduled parameters [66]. These controllers make use of the fact that H_∞ loop shaping controllers can be formulated in observer form. In other words, the separation principle between state estimation and feedback gain is exploited, allowing access to state estimates within the controller. These states estimates are then used to gain-schedule the estimator gain and the state feedback gain.

Also, optimisation of the pre- and post compensating weights used in the H_∞ LSDP has received some recent attention by researchers. Lanzon et al. present algorithms based upon formulating the weight optimisation problem in a linear matrix inequality (LMI) framework, suitable for convex optimisation [67, 68, 69]. The latest work [68], provides smoothness constraints on the frequency response of the weights (i.e. gradient constraints) to prevent pole-zero cancellations between the plant and loop shaping weights. Further examples of weight optimisation are given by Liu et al. [70].

Skogestad et al. [2] recommend that even if H_∞ loop shaping is used as a controller synthesis method, the μ-analysis method could still be used to perform robust stability and robust performance analyses. μ-analysis makes use of the generalised Nyquist criteria (and in particular the small-gain theorem) to check for stability in a system with bounded uncertainty. It does this by looking at a property known as the structured singular value μ. The structured singular value can be used to reduce conservatism in the modelling of uncertainties - the "structure" of the uncertainty is exploited to produce tighter bounds on the effects of the uncertainty on the nominal plant.

Another concept that closely relates to the H_∞ LSDP method is the ν-gap metric (and the closely associated gap metric). The ν-gap metric, derived by Vinnicombe [71], is a measure of the *distance* or *difference* between two plants, and can be used to obtain *a priori* information about the robustness that can be achieved with a certain plant. Salah [64] used the ν-gap metric to determine the effects of certain simplifying assumptions on the plant. Unlike the μ-analysis technique, the ν-gap metric is not a method to represent all the uncertainty in a system. The ν-gap metric simply represents the difference between two plants in the graph topology. Therefore, it is up to the designer to ensure that the greatest ν-gap for a particular set of plants is found. In other words, the designer must find the plant in the uncertainty set that is the furthest away (in terms of ν-gap) and design using this worst-case scenario.

The most prominent alternative H_∞ control method for robust controller synthesis is DK-iteration, or μ-synthesis. Skogestad et al. [2] argue that the effort and complexity involved in μ-synthesis is rarely worth the results that it produces. μ-synthesis is a controller synthesis algorithm that incorporates μ-analysis and H_∞ norm optimisation to produce a robust controller. The procedure offers enormous flexibility in the synthesis of controllers; the synthesis procedure factors in designer-chosen weighting functions as well as the actual structure of the controller. The procedure is built upon signal-based H_∞ control, which is itself a generalisation of mixed-sensitivity H_∞ control.

In a recent design example by Hyde [4], it is noted that currently, a gap exists between the theory and application of H_∞ robust control. This is evident by the small number of examples in industry of this control methodology. The reason for this is partly due to the high level of theoretical understanding required by the practicing control engineer to use these techniques. It is also partly due to the fact robust control tends to produce conservative control designs.

2.3 Summary

The quadrotor and suspended payload problem has received substantial attention over the last few years. However, the work done on robust control of the system, that is, on the development of flight control systems that can perform under a defined range of uncertainties, is still immature. The majority of methodologies presented so far have relied on external sensor systems to measure system states, as well as ideal laboratory conditions to achieve the predicted results. We can therefore identify a clear research gap as: *No solution to robust flight control of the quadrotor and suspended payload system, using only the measurements available on standard quadrotors, that can reduce residual oscillations of the payload swinging motion, and that can guarantee*

robust stability and performance, has yet been presented.

Of the robust control methodologies available, H_∞ control is the most popular. H_∞ loop shaping is generally the most favoured method, with a relatively straightforward design procedure being presented by Macfarlane [54]. H_∞ control is an area of ongoing research attention. However, the techniques are not widely used in industry due to their theoretical and mathematical complexity.

Furthermore, the application of optimal control for trajectory generation or the use of impulse convolution can ease the task of the controller by generating trajectories that already reduce payload swinging motion. Input shaping in particular is presented as a tool that can "shape" desired trajectories to reduce residual oscillations, while providing good levels of robustness.

Chapter 3

The Quadrotor-Payload Model

This chapter presents a mathematical model of a quadrotor with a suspended payload. This mathematical model will be used in a full nonlinear simulation of a quadrotor and suspended payload based on a validated model of the SLADe quadrotor UAV, which is also described in this chapter. Finally, this chapter presents linearised versions of the equations of motion of the system. The linear models will be used to design control systems for the quadrotor with a suspended payload in subsequent chapters.

3.1 Mathematical Model of the Quadrotor with a Suspended Payload

This section describes the mathematical model of the quadrotor with suspended payload that serves as the basis for controller design and simulation. We start with a model of the quadrotor and suspended payload translational dynamics. The quadrotor and suspended payload are initially each treated as point masses in inertial coordinates. The point-mass dynamics of the resulting floating pendulum are derived using Lagrangian mechanics. The quadrotor-payload model describes the motion of the vehicle and payload as point masses under the influence of a generalised force vector applied to the vehicle point mass. We then augment the quadrotor and payload point mass model with a model of the quadrotor attitude dynamics and thrust. The attitude of the quadrotor and the magnitude of the thrust are translated into the force vector that is applied to the quadrotor point mass. Also, we model and bound the uncertainties in the vehicle thrust magnitude, the cable length, and the payload mass. Finally, we provide an overview of the simulation environment that was used for the simulation verification.

3.1.1 Quadrotor and Suspended Payload Point Mass Dynamics

The floating pendulum model that describes the motion of the quadrotor and suspended payload is shown in Figure 3.1. The quadrotor is treated as a point mass moving in inertial coordinates, with a suspended payload that is assumed to be attached at the quadrotor's centre of gravity. Also, the cable is assumed to be massless and rigid. The rigidity assumption would be violated if the tension in the cable becomes less than zero at some point during flight, meaning that the payload enters free-fall. This is unlikely for manoeuvres that are not highly aggressive. The rigidity assumption also means that the effects of cable stretching are neglected. However, the effects of cable stretch are intrinsically handled in a simplistic manner by considering uncertainty in the cable length parameter.

The assumption of a massless cable is justified by the fact that very lightweight cables can be used to carry the payloads considered in this study (payload masses of $1kg$ to $6kg$), and the small mass of the cable can be accounted for by adding uncertainty on the payload mass and cable length.

The position of the quadrotor is represented by its coordinate vector $\mathbf{p} = (x, y, z)^T$ in the inertial frame, where x, y, and z are the North, East, and Down coordinates of the quadrotor's position relative to some reference point. The position of the suspended payload with respect to the quadrotor is parameterised using two payload swing angles, ϕ_L and θ_L. ϕ_L and θ_L are the swing angles of the payload around the North axis and the East axis of the inertial axis system, respectively.

M_c is the mass of the quadrotor, M_L is the mass of the payload, and L is the length of the cable. $\boldsymbol{\tau}_I$ is an inertial force vector that acts on the point mass representing the quadrotor. This inertial force vector is generated by the thrust of the quadrotor acting in a certain direction. In other words, the thrust force is aligned with the body-fixed z-axis, and will have coordinates in the inertial frame that are dependent on the attitude of the quadrotor. $\boldsymbol{\tau}_I$ is the control input for the floating pendulum system. The relationship between the force vector in inertial coordinates and the quadrotor attitude and thrust will be presented in Section 3.1.2.

3.1.1.1 The Lagrangian of a Floating Pendulum

The equations of motion for the quadrotor and payload point mass dynamics are now derived using the method of Lagrange. Lagrangian mechanics is well suited for this derivation, because the quadrotor with suspended payload is a multi-body system, and because the constraint forces in the cable do not have to be modelled explicitly.

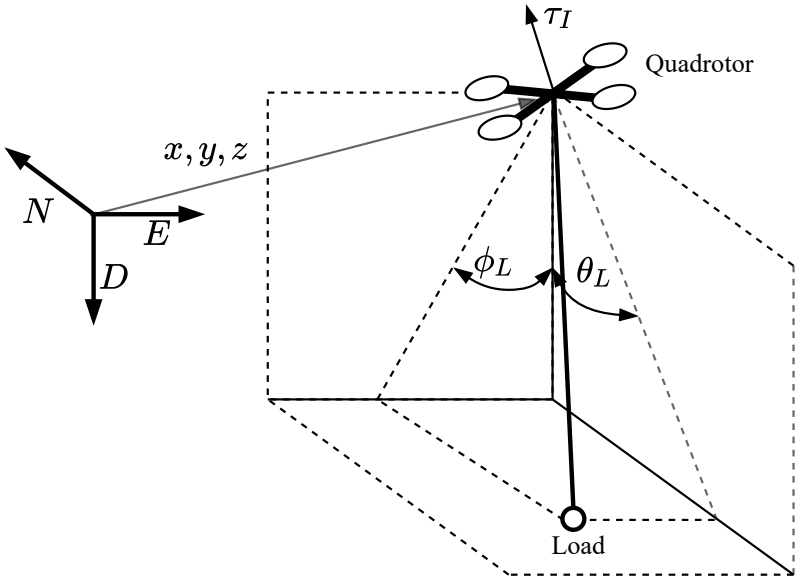

Figure 3.1: Quadrotor with suspended payload

The Euler-Lagrange equation is given by

$$\frac{d}{dt}\left(\frac{\partial L}{\partial \dot{q}_i}\right) - \frac{\partial L}{\partial q_i} = Q_i \tag{3.1.1}$$

with

$$L(\mathbf{q}, \dot{\mathbf{q}}, t) = T(\mathbf{q}, \dot{\mathbf{q}}, t) - V(\mathbf{q}) \tag{3.1.2}$$

where L is called the Lagrangian, q_i is an element of generalised coordinates $\mathbf{q}$, and Q_i is an element of generalised forces $\mathbf{Q}$. The term $T(\mathbf{q}, \dot{\mathbf{q}}, t)$ represents the total kinetic energy of the system, and the term $V(\mathbf{q})$ represents the total potential energy of the system. Note that $V(\mathbf{q})$ is not dependent on the rate of change of generalised coordinates $\dot{\mathbf{q}}$ nor on time t for mechanical systems. For example, gravitational potential energy is dependent on height only, not on rate of change of height nor on time. Substituting Equation 3.1.2 into Equation 3.1.1 gives:

$$\frac{d}{dt}\left(\frac{\partial T}{\partial \dot{q}_i}\right) - \frac{d}{dt}\left(\frac{\partial V}{\partial \dot{q}_i}\right) - \frac{\partial T}{\partial q_i} + \frac{\partial V}{\partial q_i} = Q_i, \tag{3.1.3}$$

which, considering that

$$\frac{d}{dt}\left(\frac{\partial V}{\partial \dot{q}_i}\right) = 0, \tag{3.1.4}$$

means that the expression simplifies to

$$\frac{d}{dt}\left(\frac{\partial T}{\partial \dot{q}_i}\right) - \frac{\partial T}{\partial q_i} + \frac{\partial V}{\partial q_i} = Q_i. \tag{3.1.5}$$

The generalised coordinates of the floating pendulum system are chosen to be $\mathbf{q} = [x, y, z, \phi_L, \theta_L]$.

Figure 3.2 shows the same as Figure 3.1, but with the quadrotor displayed as a point mass and with the direction of the two viewpoints, A_{ED} and A_{ND}, indicated.

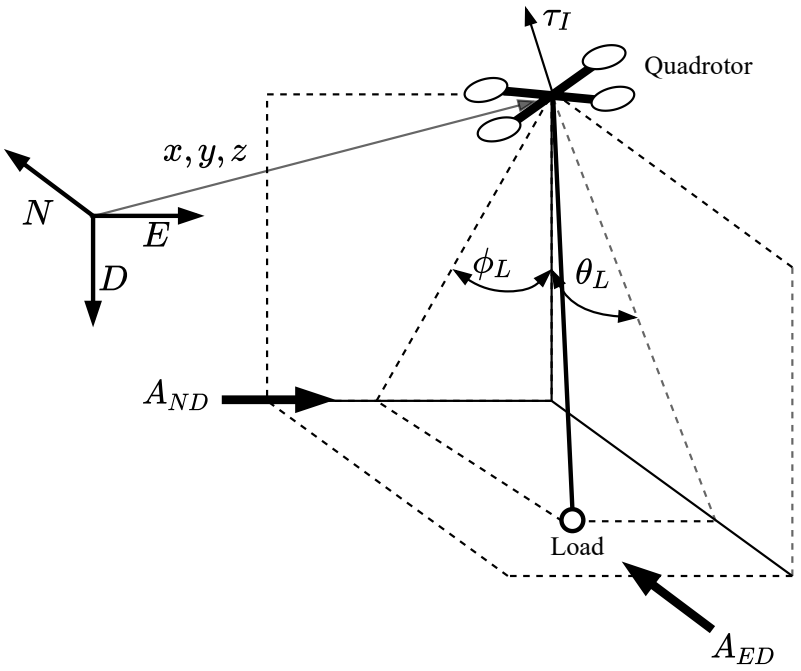

Figure 3.2: Quadrotor with suspended payload

In order to describe the position of the payload with respect to the quadrotor, we consider Figure 3.3, which shows the payload hanging straight down in position A and A', with $\theta_L = \phi_L = 0$. We first consider view A_{ED}. The change in payload position from A to B is caused by the rotation through the angle θ_L in the (N, D) plane, which would be perceived as coming out of the page. The payload then rotates through the angle ϕ_L in the (E, D) plane to move to position C. In view A_{ND}, a similar operation occurs, but with a rotation through the angle ϕ_L to move from A' to B', and then a rotation through θ_L to move to position C'. It should be clear from the figure that the payload position in the inertial frame, which we denote $\mathbf{p}_L = (x_L, y_L, z_L)^T$, can therefore be written as

$$\mathbf{p}_L = \begin{bmatrix} x_L \\ y_L \\ z_L \end{bmatrix} = \begin{bmatrix} x - L\cos\phi_L \sin\theta_L \\ y - L\cos\theta_L \sin\phi_L \\ z + L\cos\theta_L \cos\phi_L \end{bmatrix} \tag{3.1.6}$$

where x_L, y_L and z_L are the payload positions in the inertial frame corresponding to the North, East and Down directions, respectively.

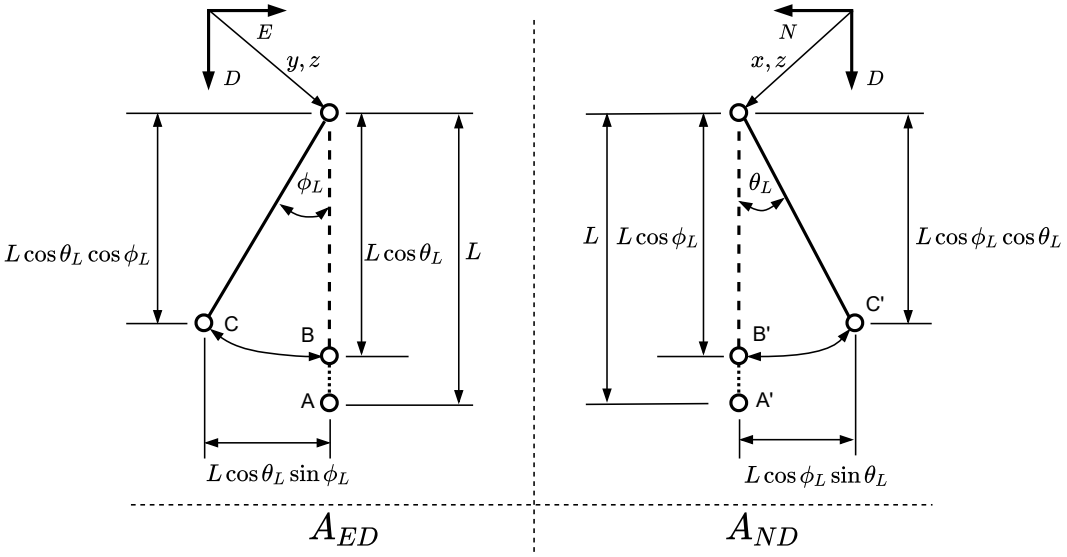

Figure 3.3: Quadrotor with suspended payload - relative payload position

In order to write expressions for the total kinetic energy of the system, we need to write expressions for the quadrotor velocity and the payload velocity in the inertial frame. In order to find the velocity of the payload in the inertial frame, denoted $\dot{\mathbf{p}}_L = (\dot{x}_L, \dot{y}_L, \dot{z}_L)^T$, we can differentiate the payload position in the inertial frame with respect to time:

$$\dot{\mathbf{p}}_L = \frac{d}{dt}\begin{bmatrix} x - L\cos\phi_L \sin\theta_L \\ y - L\cos\theta_L \sin\phi_L \\ z - L\cos\theta_L \cos\phi_L \end{bmatrix} = \begin{bmatrix} \dot{x} - \dot{\theta}_L L\cos\theta_L\cos\phi_L + \dot{\phi}_L L\sin\phi_L\sin\theta_L \\ \dot{y} - \dot{\phi}_L L\cos\theta_L\cos\phi_L + \dot{\theta}_L L\sin\phi_L\sin\theta_L \\ \dot{z} - \dot{\theta}_L L\sin\theta_L\cos\phi_L - \dot{\phi}_L L\sin\phi_L\cos\theta_L \end{bmatrix} \tag{3.1.7}$$

The payload velocities in the East-Down plane (corresponding to East and Down directions) are shown in Figure 3.4. The velocity $L\dot{\theta}_L \sin\theta_L$ is due to the payload swinging with angular velocity $\dot{\theta}_L$ in a direction that would be out of the page (in the North-Down plane). This would appear as a "shortening" of the payload cable in the East-Down plane, as the payload rotates through the angle θ_L in the North-Down plane. The velocity $L\cos\theta_L\dot{\phi}_L$ is from the payload swinging with angular velocity $\dot{\phi}_L$ in the East-Down plane. These

two velocities are then decomposed into their East and Down components as shown in the figure. A similar decomposition of the velocity components in the North-Down plane exists.

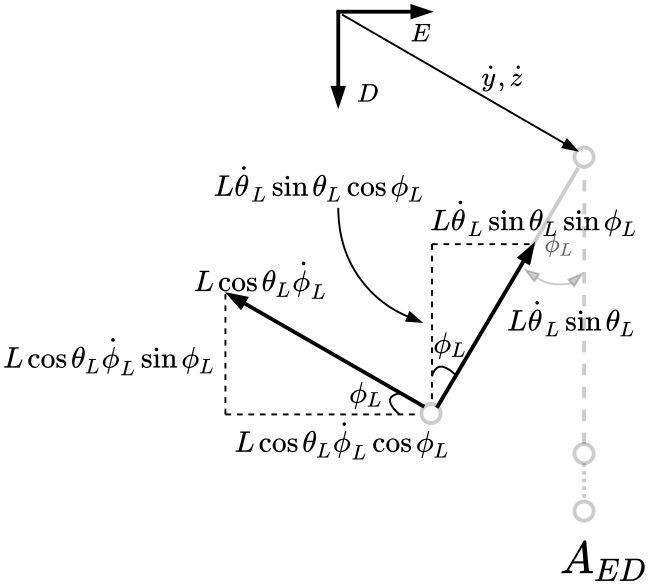

Figure 3.4: Relative payload velocities in the East-Down plane

Now, with the quadrotor and payload positions and velocities expressed in the inertial frame, we can write expressions for the total kinetic energy T and the total potential energy V in the system. The expressions for kinetic energy T and potential energy V are formed as follows:

$$T_c = \frac{1}{2}M_c||\dot{\mathbf{p}}||^2 = \frac{1}{2}M_c(\dot{x}+\dot{y}+\dot{z})^2, \tag{3.1.8}$$

$$\begin{aligned} T_L = \frac{1}{2}M_L||\dot{\mathbf{p}}_L||^2 = &\frac{1}{2}M_L(\dot{x} - \dot{\theta}_L L\cos\theta_L\cos\phi_L + \dot{\phi}_L L\sin\phi_L\sin\theta_L)^2 \\ &+\frac{1}{2}M_L(\dot{y} - \dot{\phi}_L L\cos\theta_L\cos\phi_L + \dot{\theta}_L L\sin\phi_L\sin\theta_L)^2 \\ &+\frac{1}{2}M_L(\dot{z} - \dot{\theta}_L L\sin\theta_L\cos\phi_L - \dot{\phi}_L L\sin\phi_L\cos\theta_L)^2 \end{aligned} \tag{3.1.9}$$

and $T = T_c + T_L$, where T_c and T_L are the kinetic energy of the quadrotor and payload respectively. The total potential energy of the system is

$$V = -M_c g z - M_L g z_L = -M_c g z - M_L g(z + L\cos\theta_L\cos\phi_L) \tag{3.1.10}$$

3.1.1.2 Non-conservative Force Definitions

Before using the expressions for the total kinetic and potential energy of the floating pendulum in Lagrange's equations of motion, the non-conservative forces (forces that remove energy from the system) are modelled. For this system, the primary non-conservative forces are friction due to aerodynamic drag forces, and the inertial force $\boldsymbol{\tau}_I$ which is due to the thrust of the quadrotor acting in a certain direction. The force $\boldsymbol{\tau}_I$ will be modelled more thoroughly in the next section, so we now focus on the aerodynamic drag forces.

Aerodynamic drag forces are considered in the point-mass model only; aerodynamic-induced moments on the quadrotor and payload are assumed to be zero. The motivation for such assumptions are that the model of the attitude dynamics of the SLADe quadrotor used in previous projects did not include aerodynamic-induced moments, yet still displayed good correlation with test flight data [72]. Further, the payload is assumed to be a sphere with the aerodynamic force acting on the centre of gravity of the payload. In summary, the aerodynamic centre of the quadrotor and the aerodynamic centre of the suspended payload are assumed to coincide with the centre of gravity of the quadrotor and centre of gravity of the payload, respectively.

The approach taken is to approximate the quadrotor as a flat plate moving through a fluid with an effective frontal area and drag area. This approximation has been used to design control systems for the SLADe quadrotor that allowed forward flight of up to 79 km/h in previous research [72]. Therefore, this approximation is sufficient for the simulation model used, as such high speeds are not the focus of this research.

The equation for the drag force acting on an object moving through a fluid is given by

$$F_D = \frac{1}{2}\rho C_D A v^2 \tag{3.1.11}$$

where ρ is the density of the fluid around the object, C_D is the drag coefficient, A is the reference area, and v is the linear velocity of the object relative to the fluid. The equation assumes that the object has a blunt form factor and that the fluid has a sufficiently high Reynolds number to produce turbulence behind the object. Also, skin friction drag is neglected.

The drag force on the quadrotor is modelled in the inertial frame as drag force in the three coordinates of motion; North, East and Down, as $\mathbf{D}_I = [D_x, D_y, D_z]^T$. The drag force components on the quadrotor are

$$\mathbf{D}_I = \begin{bmatrix} D_x \\ D_y \\ D_z \end{bmatrix} = \begin{bmatrix} \frac{1}{2}\rho A_x C_D \dot{x}^2 \\ \frac{1}{2}\rho A_y C_D \dot{y}^2 \\ \frac{1}{2}\rho A_z C_D \dot{z}^2 \end{bmatrix} \tag{3.1.12}$$

where A_i represents the reference area corresponding to the i coordinate. The drag force on the payload is also modelled using Equation 3.1.11. Because an actual payload has not been selected and a spherical payload shape is assumed, we also make the assumption that the payload presents an equal reference area in the direction of each inertial coordinate. In other words, the drag coefficients of the payload are equal in all three directions (which is certainly true for a sphere), so we have:

$$\mathbf{D}_{L_I} = \begin{bmatrix} D_{L_x} \\ D_{L_y} \\ D_{L_z} \end{bmatrix} = \begin{bmatrix} \frac{1}{2}\rho A_L C_D \dot{x_L}^2 \\ \frac{1}{2}\rho A_L C_D \dot{y_L}^2 \\ \frac{1}{2}\rho A_L C_D \dot{z_L}^2 \end{bmatrix} \tag{3.1.13}$$

where D_{L_i} is the drag force on the payload in the i direction, and A_L is the reference area for the payload.

An example force balance of the quadrotor and payload flying horizontally ($\dot{z} = 0$) with velocity $\dot{y}$ is shown in Figure 3.5. In this case the payload is at an angle ϕ_L, and has angular velocity $\dot{\phi}_L$.

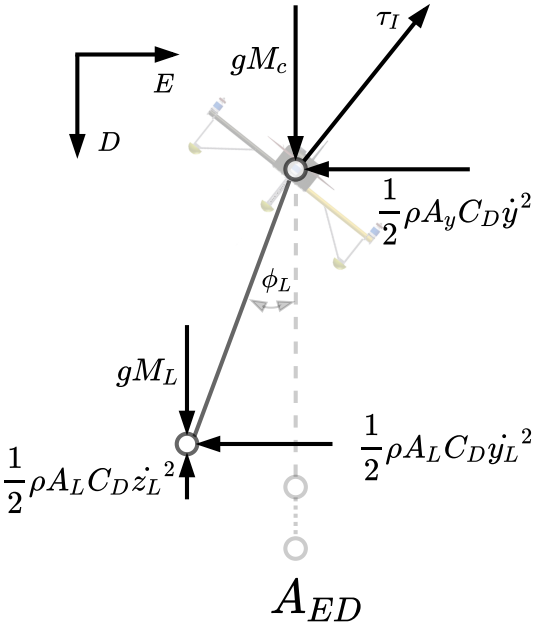

Figure 3.5: Quadrotor with suspended payload - force balances

For the static case, i.e. where the payload angular rate $\dot{\phi}_L = 0$, then $\dot{y}_L = \dot{y}$ and $\dot{z}_L = 0$. The static case will be used as a check to perform on the equations of motion by checking that moment balances around the quadrotor point mass hold. In steady-state horizontal flight in the East direction only with $\dot{\phi}_L = \dot{x} = \dot{z} = \theta_L = \dot{\theta}_L = 0$, the moment created by the gravity force on the payload should be equal to the moment created by the drag force on the payload. That is,

$$\frac{1}{2}\rho C_D A_L \dot{y}^2 L \cos\phi_L = M_L g L \sin\phi_L \tag{3.1.14}$$

as shown by Figure 3.6. From this, the steady-state value of ϕ_L at steady-state horizontal velocity $\dot{y} = \bar{v}$, denoted as $\phi_L^{\bar{v}}$, can be solved for as

$$\begin{aligned} \frac{1}{2}\rho C_D A_L \bar{v}^2 L \cos\phi_L^{\bar{v}} &= M_L g L \sin\phi_L^{\bar{v}} \\ \frac{\frac{1}{2}\rho C_D A_L \bar{v}^2 L}{M_L g L} &= \tan\phi_L^{\bar{v}} \\ \phi_L^{\bar{v}} &= \arctan\left[\left(\frac{\frac{1}{2}\rho C_D A_L}{M_L g}\right)\bar{v}^2\right] \end{aligned} \tag{3.1.15}$$

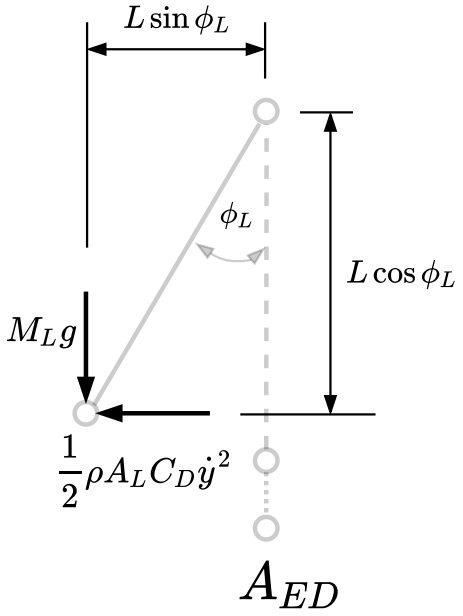

Figure 3.6: payload force balance under static conditions

With the drag forces defined, we can formulate the equations of motion of the floating-pendulum system that represents the translational dynamics of the quadrotor and suspended payload.

3.1.1.3 Equations of Motion

Evaluating Equation 3.1.5 for the generalised coordinate x results in

$$\begin{aligned} Q_x &= \frac{d}{dt}\left(\frac{\partial T}{\partial \dot{x}}\right) - \frac{\partial T}{\partial x} + \frac{\partial V}{\partial x} \\ &= (M_c + M_L)\ddot{x} + (LM_L \sin\theta_L \sin\phi_L)\ddot{\phi}_L - (LM_L \cos\theta_L \cos\phi_L)\ddot{\theta}_L \\ &+ (LM_L(\cos\theta_L \sin\phi_L \dot{\theta}_L + \cos\phi_L \sin\theta_L \dot{\phi}_L))\dot{\phi}_L \\ &+ (LM_L(\cos\theta_L \sin\phi_L \dot{\phi}_L + \cos\phi_L \sin\theta_L \dot{\theta}_L))\dot{\theta}_L \end{aligned}$$

The generalised forces that do virtual work in the x coordinate are the aerodynamic drag forces on the quadrotor and payload, as well as the component of the inertial force $\boldsymbol{\tau}_I$ in the x direction, denoted as τ_x. So,

$$\begin{aligned} Q_x &= \tau_x + D_x + D_{L_x} \\ &= \tau_x + \frac{1}{2}\rho A_x C_D \dot{x}^2 + \frac{1}{2}\rho A_L C_D \dot{x_L}^2 \\ &= \tau_x + \frac{1}{2}\rho A_x C_D \dot{x}^2 + \frac{1}{2}\rho A_L C_D (\dot{x} - \dot{\theta}_L L \cos\theta_L \cos\phi_L + \dot{\phi}_L L \sin\phi_L \sin\theta_L)^2 \end{aligned}$$

Similarly, for the y coordinate we have that:

$$\begin{aligned} Q_y &= \frac{d}{dt}\left(\frac{\partial T}{\partial \dot{y}}\right) - \frac{\partial T}{\partial y} + \frac{\partial V}{\partial y} \\ &= (M_c + M_L)\ddot{y} + (LM_L \sin\theta_L \sin\phi_L)\ddot{\theta}_L - (LM_L \cos\theta_L \cos\phi_L)\ddot{\phi}_L \\ &+ (LM_L(\cos\theta_L \sin\phi_L \dot{\phi}_L + \cos\phi_L \sin\theta_L \dot{\theta}_L))\dot{\theta}_L \\ &+ (LM_L(\cos\theta_L \sin\phi_L \dot{\theta}_L + \cos\phi_L \sin\theta_L \dot{\phi}_L))\dot{\phi}_L \end{aligned}$$

with

$$\begin{aligned} Q_y &= \tau_y + D_y + D_{L_y} \\ &= \tau_y + \frac{1}{2}\rho A_y C_D \dot{y}^2 + \frac{1}{2}\rho A_L C_D \dot{y_L}^2 \\ &= \tau_y + \frac{1}{2}\rho A_y C_D \dot{y}^2 + \frac{1}{2}\rho A_L C_D (\dot{y} - \dot{\phi}_L L \cos\theta_L \cos\phi_L + \dot{\theta}_L L \sin\phi_L \sin\theta_L)^2 \end{aligned}$$

Notice the symmetry between the equations of motion between the x and y coordinate; this is to be expected. For the z coordinate, we have

$$\begin{aligned}
Q_z &= \frac{d}{dt}\left(\frac{\partial T}{\partial \dot{z}}\right) - \frac{\partial T}{\partial z} + \frac{\partial V}{\partial z} \\
&= (M_c + M_L)\ddot{z} - (LM_L \cos\theta_L \sin\phi_L)\ddot{\phi}_L - (LM_L \cos\phi_L \sin\theta_L)\ddot{\theta}_L \\
&- (LM_L(\cos\theta_L \cos\phi_L \dot{\phi}_L + \sin\phi_L \sin\theta_L \dot{\theta}_L))\dot{\phi}_L \\
&+ (LM_L(\sin\theta_L \sin\phi_L \dot{\phi}_L + \cos\phi_L \cos\theta_L \dot{\theta}_L))\dot{\theta}_L
\end{aligned}$$

with

$$\begin{aligned}
Q_z &= \tau_z + D_z + D_{L_z} \\
&= \tau_z + \frac{1}{2}\rho A_z C_D \dot{z}^2 + \frac{1}{2}\rho A_L C_D {\dot{z}_L}^2 \\
&= \tau_z + \frac{1}{2}\rho A_z C_D \dot{z}^2 + \frac{1}{2}\rho A_L C_D (\dot{z} - \dot{\theta}_L L \sin\theta_L \cos\phi_L - \dot{\phi}_L L \sin\phi_L \cos\theta_L)^2
\end{aligned}$$

For the ϕ_L coordinate, we have

$$\begin{aligned}
Q_{\phi_L} &= \frac{d}{dt}\left(\frac{\partial T}{\partial \dot{\phi}_L}\right) - \frac{\partial T}{\partial \phi_L} + \frac{\partial V}{\partial \phi_L} \\
&= (LM_L \sin\theta_L \sin\phi_L)\ddot{x} - (LM_L \cos\theta_L \cos\phi_L)\ddot{y} - (LM_L \cos\theta_L \sin\phi_L)\ddot{z} \\
&+ L^2 M_L(\cos^2\theta_L \cos^2\phi_L + \sin^2\phi_L)\ddot{\phi}_L - (\frac{1}{4}L^2 M_L \sin 2\theta_L \sin 2\phi_L)\ddot{\theta}_L \\
&+ \frac{1}{2}L^2 M_L(\sin^2\theta_L \sin 2\phi_L \dot{\phi}_L - \sin 2\theta_L \cos^2\phi_L \dot{\theta}_L)\dot{\phi}_L \\
&+ \frac{1}{2}L^2 M_L(\sin^2\theta_L \sin 2\phi_L \dot{\theta}_L - \sin 2\theta_L \cos^2\phi_L \dot{\phi}_L)\dot{\theta}_L
\end{aligned}$$

The generalised force that does virtual work in the ϕ_L coordinate is only the moment created by drag forces on the payload, which, from Figure 3.5, is

$$\begin{aligned}
Q_{\phi_L} &= -D_{L_y} \cos\phi_L - D_{L_z} \sin\phi_L \\
&= -\frac{1}{2}\rho A_L C_D {\dot{y}_L}^2 \cos\phi_L - \frac{1}{2}\rho A_L C_D {\dot{z}_L}^2 \sin\phi_L \\
&= -\frac{1}{2}\rho A_L C_D (\dot{y} - \dot{\phi} L \cos\theta \cos\phi + \dot{\theta} L \sin\phi \sin\theta)^2 \cos\phi_L \\
&- \frac{1}{2}\rho A_L C_D (\dot{z} - \dot{\theta} L \sin\theta \cos\phi - \dot{\phi} L \sin\phi \cos\theta)^2 \sin\phi_L
\end{aligned}$$

Finally, we have for the θ_L coordinate:

$$
\begin{aligned}
Q_{\theta_L} &= \frac{d}{dt}\left(\frac{\partial T}{\partial \dot{\theta}_L}\right) - \frac{\partial T}{\partial \theta_L} + \frac{\partial V}{\partial \theta_L} \\
&= -(LM_L \cos\theta_L \cos\phi_L)\ddot{x} + (LM_L \sin\theta_L \sin\phi_L)\ddot{y} - (LM_L \cos\phi_L \sin\theta_L)\ddot{z} \\
&+ -(\frac{1}{4}L^2 M_L \sin 2\theta_L \sin 2\phi_L)\ddot{\phi}_L + L^2 M_L(\cos^2\theta_L \cos^2\phi_L + \sin^2\phi_L)\ddot{\phi}_L - \\
&+ \frac{1}{2}L^2 M_L(\sin^2\theta_L \sin 2\phi_L \dot{\phi}_L - \sin 2\theta_L \cos^2\phi_L \dot{\theta}_L)\dot{\phi}_L \\
&+ \frac{1}{2}L^2 M_L(\sin^2\theta_L \sin 2\phi_L \dot{\theta}_L - \sin 2\phi_L \cos^2\theta_L \dot{\phi}_L)\dot{\theta}_L
\end{aligned}
$$

where,

$$
\begin{aligned}
Q_{\theta_L} &= -D_{L_x}\cos\theta_L - D_{L_z}\sin\theta_L \\
&= -\frac{1}{2}\rho A_L C_D \dot{x_L}^2 \cos\theta_L - \frac{1}{2}\rho A_L C_D \dot{z_L}^2 \sin\theta_L \\
&= -\frac{1}{2}\rho A_L C_D(\dot{x} - \dot{\theta}_L L\cos\theta_L\cos\phi_L + \dot{\phi}_L L\sin\phi_L\sin\theta_L)^2\cos\theta_L \\
&- \frac{1}{2}\rho A_L C_D(\dot{z} - \dot{\theta}L\sin\theta\cos\phi - \dot{\phi}L\sin\phi\cos\theta)^2\sin\theta_L
\end{aligned}
$$

Again we notice the symmetry between the equations for ϕ_L and θ_L.

We can now write the equations of motion in a more convenient form as

$$
\begin{aligned}
\dot{\mathbf{n}} &= \mathbf{v} \\
\mathbf{M}(\mathbf{n})\dot{\mathbf{v}} + \mathbf{C}(\mathbf{n},\mathbf{v})\mathbf{v} + \mathbf{G}(\mathbf{n}) + \mathbf{D}(\mathbf{n},\mathbf{v}) &= \mathbf{T}_I
\end{aligned} \tag{3.1.16}
$$

where the state vector $\mathbf{n} = [x, y, z, \phi_L, \theta_L]$ represents the position of the vehicle and the swing angles of the suspended payload, the state vector derivative $\mathbf{v} = [\dot{x}, \dot{y}, \dot{z}, \dot{\phi}_L, \dot{\theta}_L]^T$ represents the velocity of the vehicle and the swing rates of the suspended payload, and the force vector $\mathbf{T}_I = [\tau_x, \tau_y, \tau_z, 0, 0]^T = [\boldsymbol{\tau}_I, 0, 0]^T$ contains the input force vector $\boldsymbol{\tau}_I$ acting on the quadrotor point mass coordinated in the inertial frame. This force vector is generated by the thrust of the quadrotor, and its orientation is determined by the attitude of the quadrotor.

This form is commonly used when dealing with robotic manipulators as it is a compact form that is convenient for simulation and analysis. The matrix $\mathbf{M}(\mathbf{n})$ represents the mass and moment of inertia of the quadrotor and payload, the matrix $\mathbf{C(n,v)}$ represents the centripetal forces and moments produced by the swinging motion of the payload, the matrix $\mathbf{G}(\mathbf{n})$ represents

the gravitational forces and moments, and the matrix $\mathbf{D}(\mathbf{n}, \mathbf{v})$ represents the aerodynamic damping forces and moments due to the quadrotor velocity and the payload angular rate. The input force vector $\mathbf{T}_I$ is the vector sum of the thrust force $\boldsymbol{\tau}_I = [\tau_x, \tau_y, \tau_z]^T$ and any external disturbance forces acting on the quadrotor vehicle. Note that $\mathbf{T}_I$ excludes the gravitational and aerodynamic forces, since they are already included in $\mathbf{G}(\mathbf{n})$ and $\mathbf{D}(\mathbf{n}, \mathbf{v})$, respectively. Also note that equation 3.1.19 describes only the point mass translational dynamics of the quadrotor and the payload, and does not include the quadrotor attitude dynamics. In Section 3.1.2 will show how the quadrotor attitude dynamics and thrust are modelled, and how the quadrotor attitude and thrust are translated into the thrust vector $\boldsymbol{\tau}_I$ coordinated in the inertial frame. The matrices $\mathbf{M}(\mathbf{n})$, $\mathbf{C}(\mathbf{n}, \mathbf{v})$, $\mathbf{G}(\mathbf{n})$, and $\mathbf{D}(\mathbf{n}, \mathbf{v})$ are determined to be

$$\mathbf{M} = \begin{pmatrix} M_c + M_L & 0 & 0 & LM_L\mathrm{s}\theta_L\mathrm{s}\phi_L & -LM_L\mathrm{c}\theta_L\mathrm{c}\phi_L \\ 0 & M_c + M_L & 0 & -LM_L\mathrm{c}\phi_L\mathrm{c}\theta_L & LM_L\mathrm{s}\phi_L\mathrm{s}\theta_L \\ 0 & 0 & M_c + M_L & -LM_L\mathrm{c}\theta_L\mathrm{s}\phi_L & -LM_L\mathrm{c}\phi_L\mathrm{s}\theta_L \\ LM_L\mathrm{s}\theta_L\mathrm{s}\phi_L & -LM_L\mathrm{c}\phi_L\mathrm{c}\theta_L & -LM_L\mathrm{c}\theta_L\mathrm{s}\phi_L & K(\mathrm{c}^2\theta_L\mathrm{c}^2\phi_L + \mathrm{s}^2\phi_L) & -\frac{1}{4}K\mathrm{s}(2\theta_L)\mathrm{s}(2\phi_L) \\ -LM_L\mathrm{c}\theta_L\mathrm{c}\phi_L & LM_L\mathrm{s}\phi_L\mathrm{s}\theta_L & -LM_L\mathrm{c}\phi_L\mathrm{s}\theta_L & -\frac{1}{4}K\mathrm{s}(2\theta_L)\mathrm{s}(2\phi_L) & K(\mathrm{c}^2\theta_L\mathrm{c}^2\phi_L + \mathrm{s}^2\theta_L) \end{pmatrix}$$

$$\mathbf{C} = \begin{pmatrix} 0 & 0 & 0 & LM_L(\mathrm{c}\theta_L\mathrm{s}\phi_L\dot{\theta}_L + \mathrm{c}\phi_L\mathrm{s}\theta_L\dot{\phi}_L) & LM_L(\mathrm{c}\theta_L\mathrm{s}\phi_L\dot{\phi}_L + \mathrm{c}\phi_L\mathrm{s}\theta_L\dot{\theta}_L) \\ 0 & 0 & 0 & LM_L\left(\mathrm{c}\theta_L\mathrm{s}\phi_L\dot{\phi}_L + \mathrm{c}\phi_L\mathrm{s}\theta_L\dot{\theta}_L\right) & LM_L\left(\mathrm{c}\phi_L\mathrm{s}\theta_L\dot{\phi}_L + \mathrm{c}\theta_L\mathrm{s}\phi_L\dot{\theta}_L\right) \\ 0 & 0 & 0 & -LM_L\left(\mathrm{c}\phi_L\mathrm{c}\theta_L\dot{\phi}_L - \mathrm{s}\phi_L\mathrm{s}\theta_L\dot{\theta}_L\right) & -LM_L\left(-\mathrm{s}\phi_L\mathrm{s}\theta_L\dot{\phi}_L + \mathrm{c}\phi_L\mathrm{c}\theta_L\dot{\theta}_L\right) \\ 0 & 0 & 0 & \frac{1}{2}L^2M_L(\mathrm{s}^2\theta_L\mathrm{s}(2\phi_L)\dot{\phi}_L - \mathrm{s}(2\theta_L)\mathrm{c}^2\phi_L\dot{\theta}_L) & \frac{1}{2}L^2M_L(\mathrm{s}^2\theta_L\mathrm{s}(2\phi_L)\dot{\theta}_L - \mathrm{s}(2\theta_L)\mathrm{c}^2\phi_L\dot{\phi}_L) \\ 0 & 0 & 0 & \frac{1}{2}L^2M_L(\mathrm{s}(2\theta_L)\mathrm{s}^2\phi_L\dot{\phi}_L - \mathrm{c}^2\theta_L\mathrm{s}(2\phi_L)\dot{\theta}_L) & \frac{1}{2}L^2M_L(\mathrm{s}(2\theta_L)\mathrm{s}^2\phi_L\dot{\theta}_L - \mathrm{c}^2\theta_L\mathrm{s}(2\phi_L)\dot{\phi}_L) \end{pmatrix}$$

$$\mathbf{G}(\mathbf{n}) = \begin{pmatrix} 0 \\ 0 \\ -g(M_c + M_L) \\ gLM_L\mathrm{c}\theta_L\mathrm{s}\phi_L \\ gLM_L\mathrm{c}\phi_L\mathrm{s}\theta_L \end{pmatrix}$$

$$\mathbf{D} = \begin{pmatrix} C_q\dot{x} + C_lv_{xx} & 0 & 0 & C_lv_{xp} & C_lv_{xt} \\ 0 & C_q\dot{y} + C_lv_{yy} & 0 & C_lv_{yp} & C_lv_{yt} \\ 0 & 0 & C_q\dot{z} + C_lv_{zz} & C_lv_{zp} & C_lv_{zt} \\ 0 & -C_lv_{yy}L\mathrm{c}\phi_L & -C_lv_{zz}L\mathrm{c}\phi_L & (-C_lv_{yp} - C_lv_{zp})L\mathrm{c}\phi_L & (-C_lv_{yt} - C_lv_{zp})L\mathrm{c}\phi_L \\ -C_lv_{xx}L\mathrm{c}\theta_L & 0 & -C_lv_{zz}L\mathrm{c}\theta_L & (-C_lv_{xp} - C_lv_{zp})L\mathrm{c}\theta_L & (-C_lv_{xt} - C_lv_{zt})L\mathrm{c}\theta_L \end{pmatrix}$$

with

$$K = L^2M_L \tag{3.1.17}$$

$$C_l = \frac{1}{2}\rho A_L C_D \tag{3.1.18}$$

$$C_q = \frac{1}{2}\rho A_x C_D \tag{3.1.19}$$

and where cx is shorthand for $\cos x$, and sx is shorthand $\sin x$. Note, $A_x = A_y = A_z$, as per Appendix C. The variables v_{xx}, v_{xp}, v_{xt}, v_{yy}, v_{yp}, v_{yt}, v_{zz}, v_{zp}, and v_{zt} are coefficients that relate $\dot{x}_L^2$, $\dot{y}_L^2$, and $\dot{z}_L^2$ to $\dot{x}$, $\dot{y}$, $\dot{z}$, ϕ_L, and $\dot{\theta}_L$, as follows

$$\dot{x}_L^2 = v_{xx}\dot{x} + v_{xp}\dot{\phi}_L + v_{xt}\dot{\theta}_L \tag{3.1.20}$$

$$\dot{y}_L^2 = v_{yy}\dot{y} + v_{yp}\dot{\phi}_L + v_{yt}\dot{\theta}_L \tag{3.1.21}$$

$$\dot{z}_L^2 = v_{zz}\dot{z} + v_{zp}\dot{\phi}_L + v_{zt}\dot{\theta}_L \tag{3.1.22}$$

The formulas for these coefficients are not shown here for the sake of brevity, but can be found in Appendix B.

3.1.2 Quadrotor Attitude Dynamics and Thrust

A body-fixed axis is used to describe the attitude of the quadrotor relative to the inertial frame. The standard Euler 3-2-1 parameterisation is used, shown in Figure 3.7.

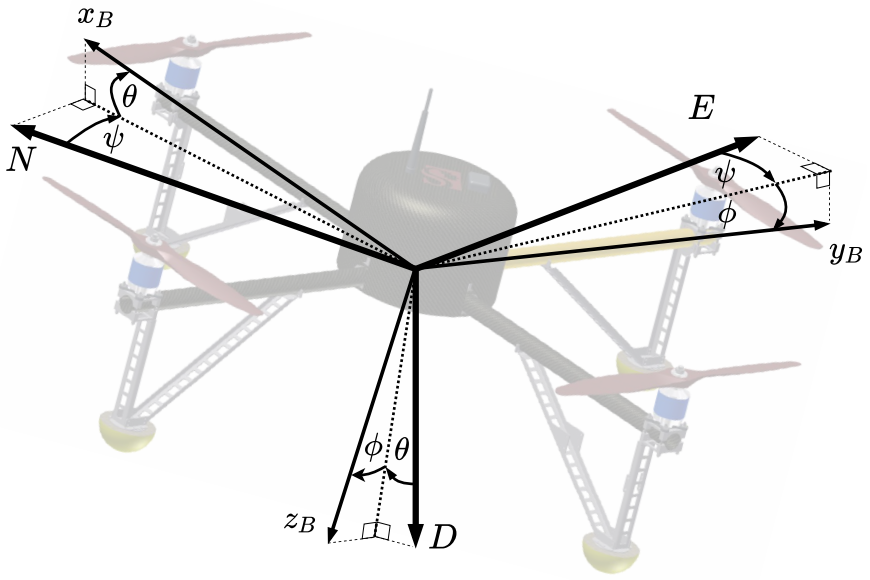

Figure 3.7: Inertial and body frame orientation

The quadrotor rotational dynamics and attitude kinematics are described by the following well-known rotational equations of motion

$$\begin{aligned} L &= I_{xx}\dot{P} + QR(I_{zz} - I_{yy}) \\ M &= I_{yy}\dot{Q} + PR(I_{xx} - I_{zz}) \\ N &= I_{zz}\dot{R} + PQ(I_{yy} - I_{xx}) \end{aligned} \tag{3.1.23}$$

$$\begin{bmatrix} \dot{\phi} \\ \dot{\theta} \\ \dot{\psi} \end{bmatrix} = \begin{bmatrix} 1 & \sin\phi\tan\theta & \cos\phi\tan\theta \\ 0 & \cos\phi & -\sin\phi \\ 0 & \sin\phi\sec\theta & \cos\phi\sec\theta \end{bmatrix} \begin{bmatrix} P \\ Q \\ R \end{bmatrix} \tag{3.1.24}$$

where I_{xx}, I_{yy}, I_{zz} are the principal moments of inertia of the quadrotor in body axes, P, Q, R are the coordinates of the quadrotor angular velocity in body axes, L, M, N are the coordinates of the moment applied to the quadrotor in body axes, and ϕ, θ, ψ are the roll, pitch, and yaw angles that represent the orientation of the quadrotor body axes relative to the inertial axes. We assume that roll and pitch angles will remain less than 90 degrees, thereby avoiding the singularity of $\sec pi/2$.

These equations assume that the quadrotor is a rigid body in atmospheric flight; the effects of the spinning rotors are neglected, and a point on the Earth is assumed to be the origin of the inertial reference frame.

The total thrust T_t and the moment $[L, M, N]^T$ applied to the quadrotor body are the result of the combination of the individual thrust forces T_1, T_2, T_3, and T_4 produced by each of the four rotors. The relationship between the applied moment and the individual rotor thrust forces is given by

$$\begin{aligned} L &= d(T_4 - T_2) \\ M &= d(T_1 - T_3) \\ N &= r_D(-T_1 + T_2 - T_3 + T_4)/R_{LD} \end{aligned} \tag{3.1.25}$$

where d is the moment arm of the thrust force (the distance between the quadrotor center of gravity, and the rotor's line of thrust), r_D is the chord length where the rotor drag force is exerted, and R_{LD} is the rotor's lift to drag ratio. The value $r_D T_i/R_{LD}$ represents the yawing moment of rotor i. Therefore, to produce zero net moment, rotors 1 and 3 rotate in the opposite directions to rotors 2 and 4. Rotor numbers are assigned clockwise, with rotor 1 being aligned with the body-fixed x_B axis.

The relationship between the total thrust T_t and the individual rotor thrust forces is given by

$$T_t = T_1 + T_2 + T_3 + T_4 \tag{3.1.26}$$

The rotor lag dynamics for each individual rotor can be included as a first-order transient response from the commanded thrust T_{i_R} to the instantaneous thrust T_i

$$\dot{T}_i = (-T_i + T_{i_R})/\tau \tag{3.1.27}$$

where i is the index of the rotor, and τ is the time constant of the first-order response. At this point, we introduce virtual actuators that produce thrust, rolling moment, pitching moment and yawing moment by commanding the rotors to produce collective and differential thrust, as follows:

$$\begin{aligned} \delta_T &= T_1 + T_2 + T_3 + T_4 \\ \delta_A &= T_4 - T_2 \\ \delta_E &= T_1 - T_3 \\ \delta_R &= -T_1 + T_2 - T_3 + T_4 \end{aligned} \tag{3.1.28}$$

Virtual actuators are used to simplify the mathematical model of the forces, allowing the use of thrust, rudder, aileron, and elevator commands and resulting forces instead of individual thrust forces. By differentiating (3.1.28) with respect to time and substituting it into (3.1.27), we can see that if the thrust lag dynamics are linear, then the virtual actuator dynamics are linear too. We wish to be able to determine individual thrust reference points, so by inverting (3.1.28) we determine the mixing matrix as

$$\begin{bmatrix} T_{1_R} \\ T_{2_R} \\ T_{3_R} \\ T_{4_R} \end{bmatrix} = \begin{bmatrix} 0.25 & 0 & 0.5 & -0.25 \\ 0.25 & -0.5 & 0 & 0.25 \\ 0.25 & 0 & -0.5 & -0.25 \\ 0.25 & 0.5 & 0 & 0.25 \end{bmatrix} \begin{bmatrix} \delta_T \\ \delta_A \\ \delta_E \\ \delta_R \end{bmatrix} \tag{3.1.29}$$

The control inputs into the system are therefore the four virtual actuator commands, which are then mapped to individual rotor thrust commands, T_{i_R}.

The quadrotor attitude ϕ, θ, ψ and the total thrust T_t that are output by the quadrotor attitude dynamics and thrust model are converted to the thrust vector $\boldsymbol{\tau_I}$ coordinated in the inertial frame to serve as the input signal for the quadrotor and payload point mass dynamics. The conversion from thrust in body axes to thrust in inertial axes is calculated using the following equations

$$\boldsymbol{\tau}_I = \begin{bmatrix} \tau_x \\ \tau_y \\ \tau_z \end{bmatrix} = \boldsymbol{R}(\phi, \theta, \psi) \begin{bmatrix} 0 \\ 0 \\ -T_t \end{bmatrix} \tag{3.1.30}$$

with

$$\boldsymbol{R}(\phi,\theta,\psi) = \begin{bmatrix} C_\psi C_\theta & C_\psi S_\theta S_\phi - S_\psi C_\phi & C_\psi S_\theta C_\phi + S_\psi S_\phi \\ S_\psi C_\theta & S_\psi S_\theta S_\phi + C_\psi C_\theta & S_\psi S_\theta C_\phi - C_\psi S_\phi \\ -S_\theta & C_\theta S_\phi & C_\theta C_\phi \end{bmatrix} \tag{3.1.31}$$

where the thrust vector $[0, 0, -T_t]^T$ coordinated in body axes is transformed into the thrust vector $[\tau_x, \tau_y, \tau_z]^T$ coordinated in inertial axes using the inverse direction cosine matrix $\boldsymbol{R}$ obtained from the quadrotor attitude expressed as the Euler angles ϕ, θ, ψ.

3.1.3 Model Uncertainty

In order to encapsulate some major sources of uncertainty that could be present in a practical flight system, the model of the quadrotor with suspended payload is allowed significant uncertainties in the quadrotor thrust magnitude, in the suspended payload mass, and in the cable length between the quadrotor and the payload. These uncertainties are modelled and bounded as follows:

- Thrust magnitude uncertainty: The actual thrust magnitude produced by the rotors is not directly measured and is instead assumed to be related to the rotor speed. The quadrotor therefore actuates the rotor speed and assumes that the corresponding thrust is produced. However, the aerodynamic thrust coefficient of the rotors may contain significant uncertainty, and the produced thrust may also vary with air density. The quadrotor total thrust T_t is therefore modelled to have a gain uncertainty of ΔT_t. This also translates into a ΔT_t uncertainty in the value of the input force $\boldsymbol{\tau}_I$.

- Payload mass uncertainty: The quadrotor vehicle may be expected to carry a number of different payloads with a large range of payload masses. Also, the payload mass may be only approximately known (e.g. for aerial cargo transport), or may vary substantially during flight (e.g. for aerial fire-fighting vehicles). The payload mass M_L is therefore modelled to vary between $M_{L_{\min}}$ and $M_{L_{\max}}$.

- Cable length uncertainty: The length of the cable connecting the suspended payload may also contain uncertainty. The payload cable may be adjusted to accommodate different payload sizes, or the centre of gravity of the payload may not be exactly known, changing the effective cable length. Also, cable length uncertainty can account for the possible effects of the cable stretching.

The uncertainties in the quadrotor thrust and the payload mass are modelled with the following equations

$$T_t = (1 + \Delta T_t) T_{t\text{cmd}} \tag{3.1.32}$$
$$M_L \in \{M_{L\text{min}}, M_{L\text{max}}\} \tag{3.1.33}$$
$$L \in \{L_{\text{min}}, L_{\text{max}}\} \tag{3.1.34}$$

where $T_{t\text{cmd}}$ is the expected thrust, T_t is the produced thrust, ΔT_t is the thrust gain uncertainty, $M_{L\text{min}}$ is the minimum payload mass, $M_{L\text{max}}$ is the maximum payload mass, L_{min} is the minimum cable length, and L_{max} is the maximum cable length.

3.1.4 Simulation Model

The quadrotor-payload simulation model is based on the SLADe quadrotor vehicle developed at the Electronic Systems Laboratory in the Department of Electrical and Electronic Engineering of Stellenbosch University. The SLADe quadrotor has a vehicle mass of 9.00 kg and is designed to carry a rigidly-attached payload with a mass of 5.00 kg [72]. A picture of the SLADe quadrotor is shown in Figure 3.8. The various plant parameters used to model the vehicle are presented in Appendix C.

Figure 3.8: SLADe quadrotor

The aerodynamic drag force coefficients for the quadrotor were characterised through testing during previous research done in the Electronic Systems Laboratory. The quadrotor was flown in no-wind conditions at various steady-state

velocities and the resulting tilt angle was recorded. The actual drag force was calculated by simple force balances. For example, consider Figure 3.9, where the quadrotor is shown to be flying at a constant velocity $\dot{y}$. In order to sustain the velocity, the quadrotor is rolled at an angle ϕ. The corresponding drag force in the inertial frame in the direction of flight, D_y, is calculated by

$$D_y = M_c g \tan \phi \tag{3.1.35}$$

With the drag force calculated, and by setting $C_D = 1$, the drag force reference area in the direction of flight in the inertial frame (A_y in this case) was solved. This method was used to determine the drag force reference areas for the quadrotor in the three inertial frame directions, A_x, A_y, and A_z.

The reference area for the payload, A_L, is chosen by setting it to be 1/4 of the reference area of the quadrotor; the exact value of the payload's drag reference area is not critical for this study. The drag force coefficients for the quadrotor and suspended payload are presented in Appendix C.

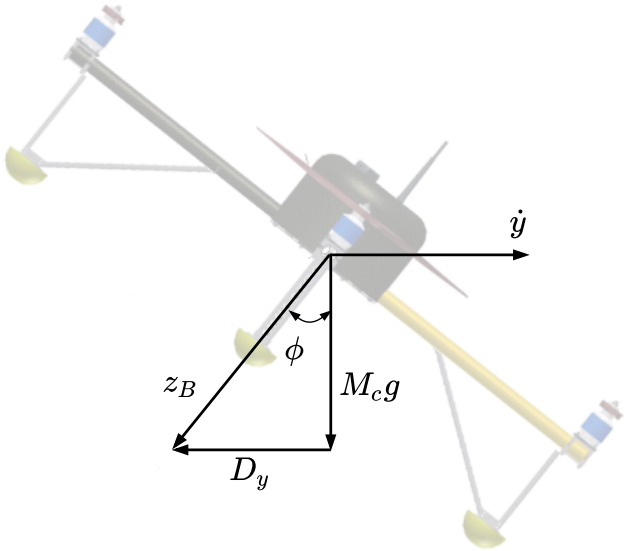

Figure 3.9: Quadrotor drag force calculation

A suspended payload with a nominal mass of 3.5 kg is assumed. The suspended payload is attached to the quadrotor using a cable with a nominal length of 1.5 m. As mentioned in the previous section, both the payload mass and the cable length are treated as uncertain parameters. The specific values of those uncertainties are given by Equations 3.1.36 to 3.1.40:

$$\Delta T_t \in \{-0.2, 0.2\} \tag{3.1.36}$$
$$M_{L_{min}} = 1\text{kg} \tag{3.1.37}$$
$$M_{L_{max}} = 6\text{kg} \tag{3.1.38}$$
$$L_{min} = 1.125\text{m} \tag{3.1.39}$$
$$L_{max} = 1.875\text{m} \tag{3.1.40}$$

These values are the equivalent of ±20% thrust magnitude uncertainty, ±25% cable length uncertainty, and ±72% payload mass uncertainty, all around the nominal values. The high value of payload mass uncertainty means that variations in payload mass of up to 500% can be expected (payload masses between 1kg and 6kg).

The simulation model of the quadrotor-payload system that is used for this research is based on the SLADe quadrotor vehicle simulation developed by the ESL during previous research. The SLADe quadrotor vehicle was characterised by Möller [72] through laboratory system identification tests and practical flight tests, and a high-fidelity simulation model was created. The simulation model includes sensor models, actuator models, and external wind disturbance models. The simulation model was used for hardware-in-the-loop simulation testing of the flight control system, and was validated with practical flight tests. The results obtained by Möller showed good agreement between the simulated behaviour and actual flight behaviour of the SLADe quadrotor vehicle.

Some example data from an actual flight test (conducted by Möller [72]) with the SLADe quadrotor without a payload is shown in Figure 3.10. This figure presents actual measurements of quadrotor velocity and pitch angle. This data is from the Extended Kalman Filter (EKF) on-board the SLADe quadrotor's flight computer. The EKF uses data from a Novatel Differential Global Position System (DGPS), as well as data from an Inertial Measurement Unit (IMU) made by Analog Devices, to estimate the vehicle states. It is clear from the figure that the quadrotor velocity measurement has a high signal-to-noise ratio (SNR) - this is due to the use of the Novatel DPGS, which has a predicted velocity error of 0.03 (m/s), and the use of the EKF, which further reduces the amount of noise on the velocity measurements.

The noise from the IMU was characterised during previous research by the ESL. The noise on the measurement of quadrotor velocity from the DGPS was characterised in lab tests by Möller. These noise sources are incorporated into the high-fidelity simulation by using Simulink's Band-Limited White Noise (BLWN) blocks. Data for sensor noise approximations is provided in Appendix C.

Wind disturbances are modelled using a simple combination of constant wind and wind gusts. The configuration used to incorporate wind disturbances into

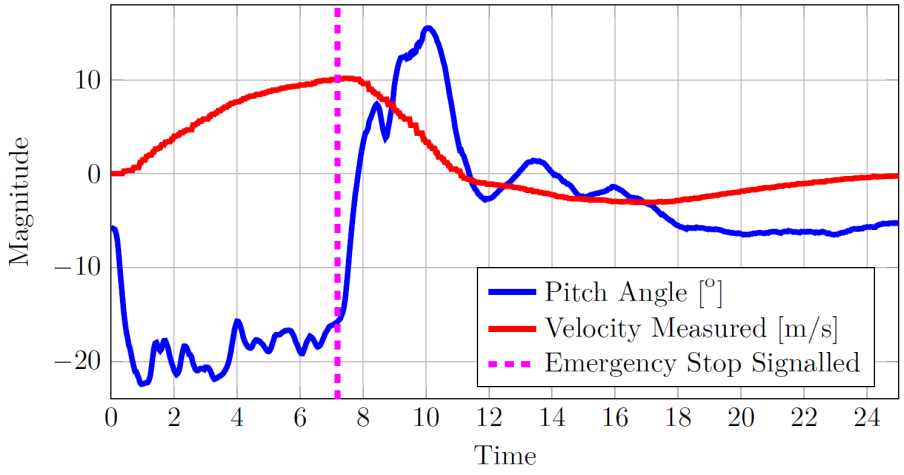

Figure 3.10: Data from flight tests using the SLADe quadrotor

the simulation is given in Appendix C. Wind disturbances are transformed into force disturbances on the translational dynamics of the quadrotor and suspended payload. This is implemented by adding the wind disturbances to the quadrotor and payload velocity terms, x, y, z, x_L, y_L, and z_L. These velocities are then transformed into non-conservative forces acting on the system, by the matrix $\mathbf{D}$.

The simulation model for the quadrotor with suspended payload was obtained by augmenting the established SLADe quadrotor vehicle simulation with the translational dynamics of the quadrotor and suspended payload that were derived in Section 3.1.1. A high-level view of the simulation model is shown in Figure 3.11.

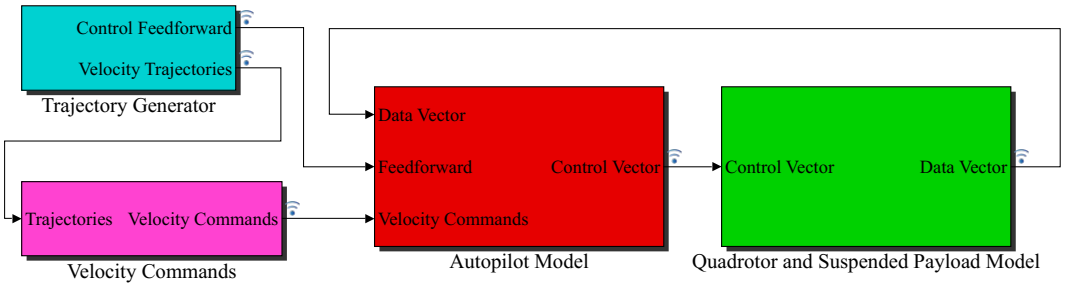

Figure 3.11: SLADe quadrotor vehicle with suspended payload simulation

3.1.4.1 Quadrotor and Suspended Payload Simulations

In this section, the simulated behaviour of the translational dynamics of the quadrotor and suspended payload without feedback control are presented.

First, a simulation is run where the input force reference $\boldsymbol{\tau}_{I_R}$ is set to maintain hover flight. In other words, $\boldsymbol{\tau}_{I_R} = [0, 0, -g(M_c+M_l)$, which is the force needed to keep the system at hover conditions. Also, the simulation is initialised with payload angles $\phi_L = 30$ degrees and $\theta_L = 7.5$ degrees. The simulated time histories of the resulting payload angles are shown in Figure 3.12, and the simulated time histories of the quadrotor North and East velocities are shown in Figure 3.13.

s

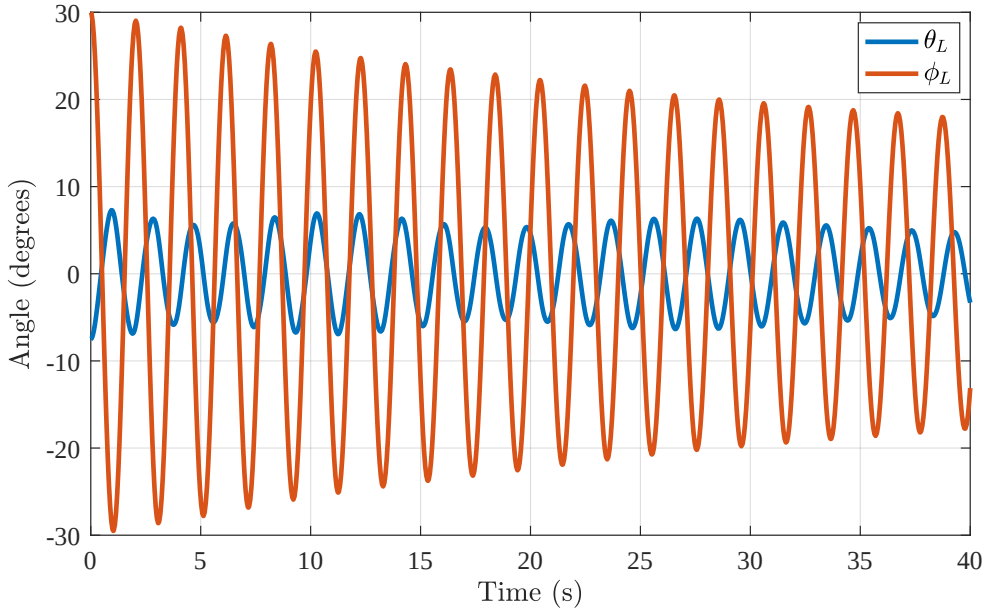

Figure 3.12: Simulated time history of payload angles when initialised to starting values of $\phi_L = 30$ degrees and $\theta_L = 7.5$ degrees.

The payload displays a very lightly damped swinging motion. Also, the effect of the payload swinging is evident on the quadrotor velocity - as the payload swings, it generates disturbance forces through the cable onto the quadrotor, pulling the quadrotor back and forth. Also present but not shown are oscillations in the vertical velocity $\dot{z}$ of the quadrotor; these are much smaller in magnitude than the oscillations in the velocities in the horizontal directions. From these figures, it is clear that in order for effective control of the quadrotor to be maintained, large residual swinging motion of the payload must be minimized. Large payload angles are necessary for aggressive manoeuvres, but residual swinging after a manoeuvre is not desired.

A second simulation scenario is shown in Figure 3.14 and Figure 3.15. In this scenario, the payload angles are initialized to $\phi_L = 7$ degrees and $\theta_L = 20$ degrees. Again, the system starts in a hover condition, yet in this simula-

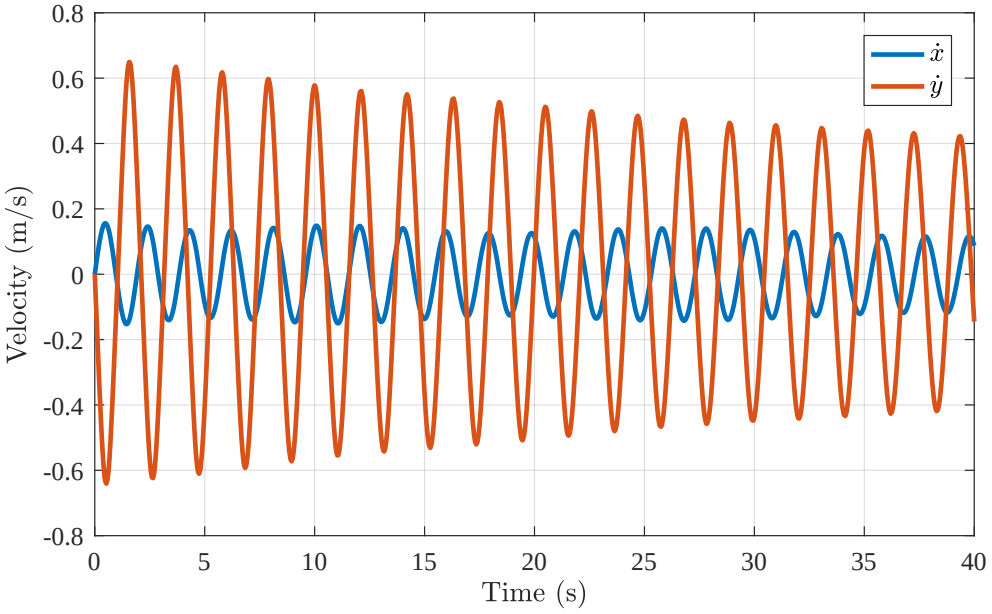

Figure 3.13: Horizontal quadrotor velocity time history when suspended payload is initialised with payload angles of $\phi_L = 30$ degrees and $\theta_L = 7.5$ degrees.

tion a nonzero force component in the North direction is applied. In other words, $\boldsymbol{\tau}_{I_R} = [18, 0, -g(M_c + M_l)$. This causes rapid acceleration in the North direction, shown by the increase in quadrotor velocity $\dot{x}$.

A steady-state $\dot{x}$ velocity of 7.228 m/s is achieved. Also, the payload angle θ_L responds accordingly: Initially, the angle increases to almost 25 degrees, due to the forward motion of the quadrotor. Eventually, the payload angle θ_L settles to a non-zero steady-state value. We can calculate this steady-state payload angle value for θ_L, denoted $\theta_L^{\bar{v}}$, using Equation 3.1.15, which is repeated here, but with $\theta_L^{\bar{v}}$ instead of $\phi_L^{\bar{v}}$, as

$$\theta_L^{\bar{v}} = \arctan\left[\left(\frac{\frac{1}{2}\rho C_D A_L}{M_L g}\right)\bar{v}^2\right] \tag{3.1.41}$$

Evaluating this equation with the steady-state velocity from Figure 3.15, which is $\dot{x} = \bar{v} = 7.228(\text{m/s})$, and a payload mass of $M_L = 3.5\text{kg}$, gives a payload angle of $\theta_L^{\bar{v}} = 0.0582$ rad, or 3.333 degrees. This correlates with the steady-state value of θ_L in Figure 3.14. This confirms that the aerodynamic drag forces are being modelled correctly and gives confidence that the simulation is displaying the correct behaviour of the suspended payload.

Notice how at moderate forward flight speeds, the damping of the swinging motion of the payload is drastically increased. This is expected as the aerodynamic drag forces acting on the quadrotor and payload increase quadratically

with forward flight speed - the drag forces push the payload into a non-zero swing angle position and also damp the oscillations around the steady-state payload angle.

Furthermore, only minor cross-coupling between the two swing angles is observed. We see that forward flight in the North direction has a strong effect on the payload angle motion in the θ_L coordinate, but it does not have a very pronounced effect on the payload angle motion in the ϕ_L coordinate.

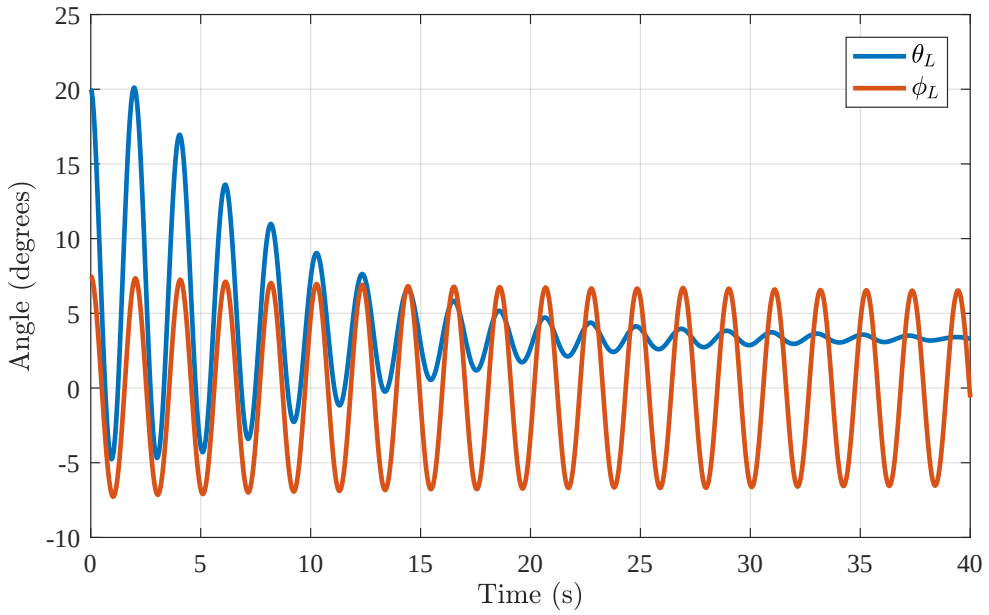

Figure 3.14: Simulated time history of payload angles when initialised to starting values of $\phi_L = 7.5$ degrees and $\theta_L = 20$ degrees, with an input force applied to the quadrotor in the North direction

3.1.4.2 Controller Requirements

Section 3.1.4.1 showed that the swinging motion of the suspended payload can display lightly damped oscillations. When the quadrotor moves at moderate forward flight speeds, the aerodynamic drag on the payload introduces additional damping into the swinging motion, and oscillations are reduced and effectively eliminated with 20 seconds of starting a manoeuvre. However, when the quadrotor is at near-hover conditions, the damping on the payload swinging motion is effectively negligible. Therefore, a potential flight control system must add damping to the swinging motion and ensure that satisfactory behaviour is observed. To this end, satisfactory payload swinging behaviour must be defined.

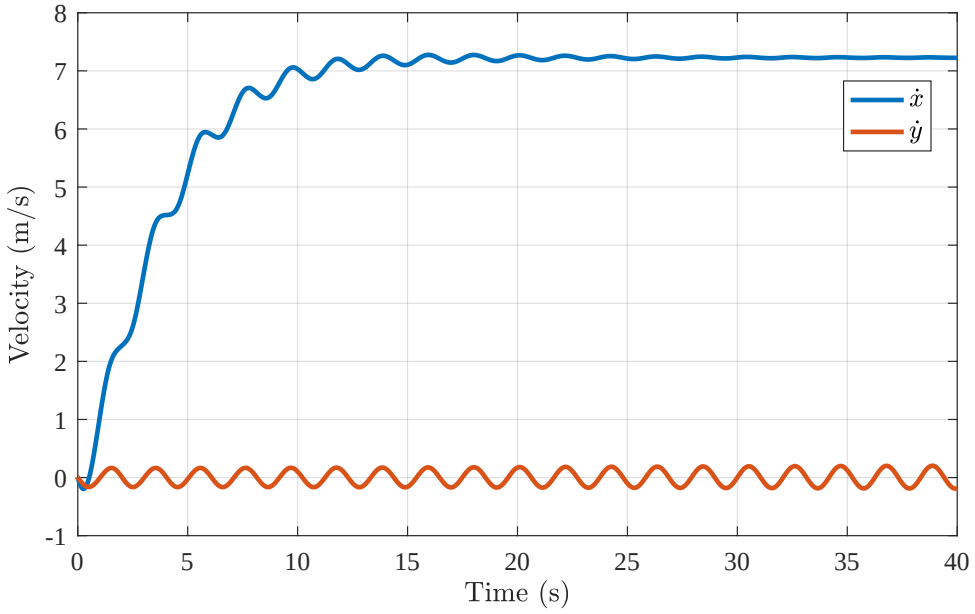

Figure 3.15: Horizontal quadrotor velocity time history when suspended payload is initialised with payload angles of $\phi_L = 7.5$ degrees and $\theta_L = 20$ degrees, with an input force applied to the quadrotor in the North direction

We define a control system to be successful with regards to payload oscillations if the following conditions are met:

- The controller allows dynamic manoeuvres to be performed
- The controller ensures that residual oscillations of the payload do not grow with unbounded exponential behaviour.
- The controller ensures that residual oscillations of the payload are less than 25% of the maximum payload angles exhibited during a manoeuvre.
- The controller meets the above conditions when considering the full range of uncertain parameters in the system.

3.2 Linearised Models

This section describes how linearised models of the quadrotor with suspended payload dynamics are derived to serve as the basis for the control design and analysis. A linearised model of the quadrotor and payload translational dynamics is derived, followed by a linearised model of the quadrotor attitude dynamics.

3.2.1 Linearised Quadrotor and Suspended Payload Dynamics

3.2.1.1 Derivation

We now linearise the quadrotor and payload point mass dynamics about a nominal operating point. We first represent the floating pendelum model in Equation 3.1.16 more concisely in the following nonlinear state space form

$$\mathbf{T}_I = \mathbf{F}(\mathbf{n}, \mathbf{v}, \dot{\mathbf{v}})$$

We now expand both sides of the nonlinear state space model into a Taylor series around the nominal operating point, as follows

$$\begin{aligned} \mathbf{T}_o + \Delta\mathbf{T} &= \mathbf{F}(\mathbf{n}_0 + \Delta\mathbf{n}, \mathbf{v}_0 + \Delta\mathbf{v}, \dot{\mathbf{v}}_0 + \Delta\dot{\mathbf{v}}) \\ &= \mathbf{F}(\mathbf{n}_0, \mathbf{v}_0, \dot{\mathbf{v}}_0) + \frac{\partial \mathbf{F}}{\partial \dot{\mathbf{v}}}|_{(\mathbf{n}_o, \mathbf{v}_o, \dot{\mathbf{v}}_o)} \Delta\dot{\mathbf{v}} \\ &\quad + \frac{\partial \mathbf{F}}{\partial \mathbf{v}}|_{(\mathbf{n}_o, \mathbf{v}_o, \dot{\mathbf{v}}_o)} \Delta\mathbf{v} + \frac{\partial \mathbf{F}}{\partial \mathbf{n}}|_{(\mathbf{n}_o, \mathbf{v}_o, \dot{\mathbf{v}}_o)} \Delta\mathbf{n} \\ &\quad + \text{higher order terms} \end{aligned} \tag{3.2.1}$$

where $\mathbf{n}_0$, $\mathbf{v}_0$, $\dot{\mathbf{v}}_0$, and $\mathbf{T}_0$ are the nominal states and inputs, $\Delta\mathbf{n}$, $\Delta\mathbf{v}$, $\Delta\dot{\mathbf{v}}$, and $\Delta\mathbf{T}$ are the state and input perturbations, and $\frac{\partial \mathbf{F}}{\partial \mathbf{n}}$, $\frac{\partial \mathbf{F}}{\partial \mathbf{v}}$, and $\frac{\partial \mathbf{F}}{\partial \dot{\mathbf{v}}}$ are the Jacobian matrices of $\mathbf{F}$ with respect to $\mathbf{n}$, $\mathbf{v}$, and $\dot{\mathbf{v}}$ respectively.

Assuming that the perturbations from the nominal operating point are small, the higher-order terms may be neglected. Also, at the nominal operating point $\mathbf{T}_0 = \mathbf{F}(\mathbf{n}_0, \mathbf{v}_0, \dot{\mathbf{v}}_0)$, which means that $\mathbf{T}_o$ and $\mathbf{F}(\mathbf{n}_0, \mathbf{v}_0, \dot{\mathbf{v}}_0)$ may be removed from both sides of the equation. The Taylor series expansion therefore reduces to

$$\Delta\mathbf{T} \approx \mathbf{F}_{\dot{v}} \Delta\dot{\mathbf{v}} + \mathbf{F}_v \Delta\mathbf{v} + \mathbf{F}_n \Delta\mathbf{n} \tag{3.2.2}$$

where we have defined $\mathbf{F}_{\dot{v}} = \frac{\partial \mathbf{F}}{\partial \dot{v}}$, $\mathbf{F}_v = \frac{\partial \boldsymbol{F}}{\partial v}$, and $\mathbf{F}_n = \frac{\partial \boldsymbol{F}}{\partial n}$ to simplify the notation.

We now wish to write the linearised model in linear state space form. Since the matrix $\mathbf{F}_{\dot{v}}$ is invertible, we may rearrange Equation 3.2.2 as follows

$$\Delta\dot{\mathbf{v}} = -(\mathbf{F}_{\dot{v}}^{-1})\mathbf{F}_v \Delta\mathbf{v} - (\mathbf{F}_{\dot{v}}^{-1})\mathbf{F}_n \Delta\mathbf{n} + (\mathbf{F}_{\dot{v}}^{-1})\Delta\mathbf{T} \tag{3.2.3}$$

We then change the notation to

$$\Delta\dot{\mathbf{v}} = \mathbf{A}_v\Delta\mathbf{v} + \mathbf{A}_n\Delta\mathbf{n} + \mathbf{B}_\tau\Delta\boldsymbol{\tau} \tag{3.2.4}$$

where we have defined $\mathbf{A}_v = (\mathbf{F}_{\dot{v}}^{-1})\mathbf{F}_v$, $\mathbf{A}_n = (\mathbf{F}_{\dot{v}}^{-1})\mathbf{F}_n$, $\mathbf{B}_\tau = (\mathbf{F}_{\dot{v}}^{-1})$, and $\Delta\boldsymbol{\tau} = [T_N, T_E, \Delta T_D]^T$. The matrices are

$$\mathbf{A}_v = \begin{bmatrix} -\frac{d_v}{M_c} & 0 & 0 & 0 & \frac{d_p}{LM_c} \\ 0 & -\frac{d_v}{M_c} & 0 & -\frac{d_p}{LM_c} & 0 \\ 0 & 0 & -\frac{d_v}{M_c+M_L} & 0 & 0 \\ 0 & -\frac{d_v}{LM_c} & 0 & -\frac{d_p(M_c+M_L}{L^2M_cM_L}) & 0 \\ -\frac{d_v}{LM_c} & 0 & 0 & 0 & -\frac{d_p(M_c+M_L}{L^2M_cM_L}) \end{bmatrix},$$

$$\mathbf{A}_n = \begin{bmatrix} 0 & 0 & 0 & 0 & g\frac{M_L}{M_c} \\ 0 & 0 & 0 & -g\frac{M_L}{M_c} & 0 \\ 0 & 0 & 0 & 0 & 0 \\ 0 & 0 & 0 & -g\frac{M_c+M_L}{LM_c} & 0 \\ 0 & 0 & 0 & 0 & -g\frac{M_c+M_L}{LM_c} \end{bmatrix},$$

$$\mathbf{B}_\tau = \begin{bmatrix} \frac{1}{M_c} & 0 & 0 \\ 0 & \frac{1}{M_c} & 0 \\ 0 & 0 & \frac{1}{M_c+M_L} \\ 0 & \frac{1}{LM_c} & 0 \\ -\frac{1}{LM_c} & 0 & 0 \end{bmatrix},$$

and d_p and d_v are small damping terms that are added to approximate the aerodynamic drag forces on the quadrotor and suspended payload, respectively. Note, for wind disturbance forces to be introduced into the linear model, the wind components would need to be transformed into associated drag force components and introduced through the force input Δ
$bm\tau$. However, we only introduce wind in the full nonlinear simulation, as described in the previous section.

Finally, we define our state vector as $\mathbf{x} = [\Delta\mathbf{n}, \Delta\mathbf{v}]^T$, our state vector derivative as $\dot{\mathbf{x}} = [\Delta\mathbf{v}, \Delta\dot{\mathbf{v}}]$, and our input vector as $\Delta\boldsymbol{\tau}$. We then obtain the following linear state space representation for our linearised quadrotor and payload point mass translational dynamics

$$\begin{aligned} \dot{\mathbf{x}} &= \mathbf{A}_{fp}\mathbf{x} + \mathbf{B}_{fp}\Delta\boldsymbol{\tau} \\ \mathbf{y} &= \mathbf{C}_{fp}\mathbf{x} \end{aligned} \tag{3.2.5}$$

with,

$$\mathbf{A}_{fp} = \begin{bmatrix} \mathbf{0} & \mathbf{I} \\ \mathbf{A}_n & \mathbf{A}_v \end{bmatrix}$$
$$\mathbf{B}_{fp} = \begin{bmatrix} \mathbf{0} \\ \mathbf{B}_{\boldsymbol{\tau}} \end{bmatrix}$$

The linear time-invariant model of the quadrotor and payload dynamics is represented by

$$\mathbf{P}_{fp}(s) \stackrel{s}{=} \left[\begin{array}{c|c} \mathbf{A}_{fp} & \mathbf{B}_{fp} \\ \hline \mathbf{C}_{fp} & \mathbf{D}_{fp} \end{array}\right], \tag{3.2.6}$$

where $\mathbf{P}_{fp}(s)$ is the multi-input, multi-output transfer function representation, and $\mathbf{A}_{fp}$, $\mathbf{B}_{fp}$, $\mathbf{C}_{fp}$, $\mathbf{D}_{fp}$ are the matrices of the state space representation. $\mathbf{C}_{fp}$ is the output matrix and $\mathbf{D}_{fp}$ is the feedthrough matrix (which is zero). The state space representation is translated into the transfer function representation using the following formula

$$\mathbf{P}_{fp} = \mathbf{C}_{fp}(s\mathbf{I} - \mathbf{A}_{fp})^{-1}\mathbf{B}_{fp} + \mathbf{D}_{fp}$$

3.2.1.2 Analysis

If we compare the linear model of the floating pendulum to the nonlinear model of the floating pendulum, we see (by examining the matrices $\mathbf{A}_v$, $\mathbf{A}_n$, and $\mathbf{B}_\tau$) that while there is coupling between the horizontal dynamics in the North and East directions in the *nonlinear* model, the horizontal dynamics in the North direction is decoupled from the horizontal dynamics in the East direction in the *linear* model. This is due to the linear model being evaluated at hover conditions, with $\phi_L = \theta_L = 0$, which means that all terms that pertain to cross coupling between $\ddot{x}$ and $\ddot{y}$, and between $\ddot{\phi}_L$ and $\ddot{\theta}_L$ evaluate to zero. That being said, even in the full nonlinear model, these cross coupling terms are not significant for small payload swing angles.

The linear time-invariant model of the quadrotor and payload horizontal dynamics in the North direction is given by

$$P_{fpx}(s) \stackrel{s}{=} \left[\begin{array}{c|c} \mathbf{A}_{fpx} & \mathbf{B}_{fpx} \\ \hline \mathbf{C}_{fpx} & \mathbf{D}_{fpx} \end{array}\right], \tag{3.2.7}$$

where $P_{fpx}(s)$ is the transfer function, and $\mathbf{A}_{fpx}$, $\mathbf{B}_{fpx}$, $\mathbf{C}_{fpx}$, and $\mathbf{D}_{fpx}$ are the state space matrices of the decoupled horizontal dynamics in the North direction. The state vector for the North dynamics is defined as as $\mathbf{x} = [\theta_L, \dot{x}, \dot{\theta}_L]$, and therefore includes the quadrotor North velocity $\dot{x}$, and the payload angle θ_L and angular rate $\dot{\theta}_L$ in the North direction. The input vector for the North dynamics is the North component of the quadrotor thrust force τ_x. The system matrix $\mathbf{A}_{fpx}$ and the input matrix $\mathbf{B}_{fpx}$ are submatrices of $\mathbf{A}_{fp}$ and $\mathbf{B}_{fp}$. The output matrix $\mathbf{C}_{fpx}$ is chosen to select the quadrotor North velocity as the output. The feedthrough matrix $\mathbf{D}_{fpx}$ is zero. $P_{fpx}(s)$ is a single-input single-output transfer function with the North component of the thrust force as input, the quadrotor velocity as output, and the payload angle and angular rate as internal states. Plotting the poles and zeroes of the system P_{fpx}, we obtain the pole-zero map shown in Figure 7.36.

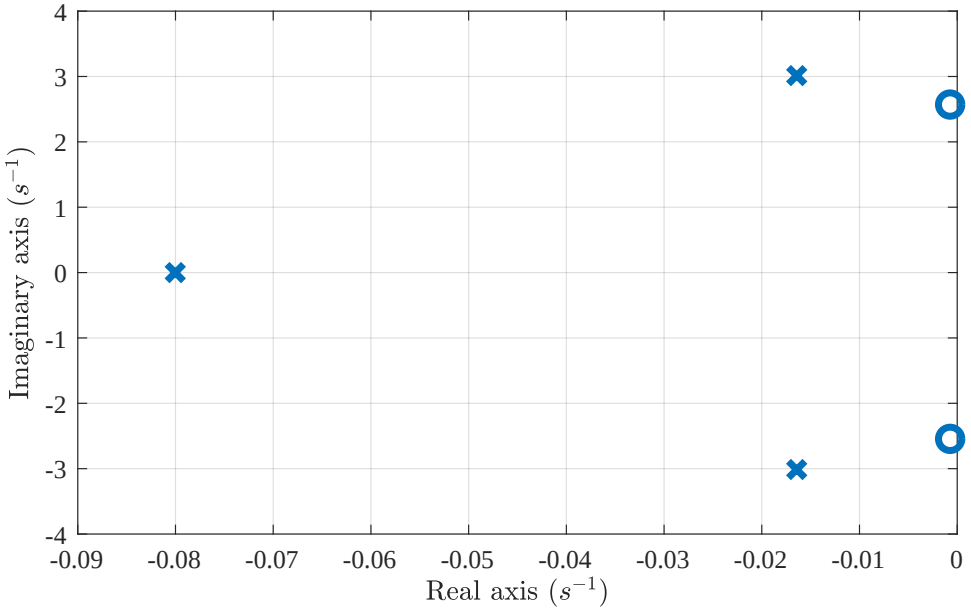

Figure 3.16: Pole-zero plot of P_{fpx}

The pole-zero map shows a stable, dominant complex pole pair at $s = -0.016 \pm 3.01j$, a complex zero pair at $s = -0.001 \pm 2.56j$, and a stable, non-dominant real pole at $s = -0.08$. The complex pole pair is lightly damped (damping ratio $\zeta = 0.05$) with a natural frequency of $w_n = 3.01$ rad/s, which represents the resonant frequency of the quadrotor and payload system. When an oscillating input force is applied at the resonant frequency, the quadrotor velocity will oscillate with a higher amplitude. At this frequency, the payload would swing out of phase with the quadrotor velocity, so both the quadrotor and the payload would oscillate severely when viewed in an inertial frame. The com-

plex zero pair has a natural frequency $w_z = 2.56$ rad/s, slightly lower than the natural frequency of the complex pole pair. At this frequency, an interesting phenomenon occurs. The complex zero pair represents a transmission zero, which means that an oscillating input force at that frequency is not transmitted to the quadrotor velocity output. The physical interpretation is that this is the frequency where the payload is swinging just enough to fully absorb the input energy applied to the system. This causes the quadrotor velocity to almost completely stop oscillating, as input energy is dissipated by swinging the payload back and forth.

Lastly, we see a real pole at $s = -0.08$. This is the first order lag that is due to the translational inertia of the system and the drag force of non-hover flight. This pole is the same as would be seen in the dynamics of a simple object in a fluid with an input force applied: it is like a standard spring-damper system, but with no spring.

Figure 3.17 shows the Bode plot of the North dynamics P_{fpx}. Shown in blue is when the output matrix $\mathbf{C}_{fpx}$ is chosen to select the quadrotor velocity $\dot{x}$ as the system output. Clearly seen are the transmission zero and the lightly damped pole-pair (resonant peak). Shown in red is when the output matrix $\mathbf{C}_{fpx}$ is chosen to select the payload angle rate $\dot{\theta}_L$ as the system output. Clearly, at the frequency of the trough in the magnitude of quadrotor velocity (from the complex zero-pair), the payload angle rate magnitude is not in a peak or trough. At the frequency of the peak in quadrotor velocity magnitude, the payload angle rate magnitude is also at a peak. This supports the physical interpretation given above.

The linearised horizontal dynamics in the East direction follows exactly the same format as the linearised horizontal dynamics in the North direction. The only difference is that the state vector of the East dynamics is defined as $\mathbf{x} = [\phi_L, \dot{y}, \dot{\phi}_L]$ and therefore includes the quadrotor East velocity $\dot{y}$, the payload angle ϕ_L, and payload angular rate $\dot{\phi}_L$. The input vector for the East dynamics is the East component of the quadrotor thrust force τ_y.

We can also extract the linear model associated with vertical motion, in the Down direction. This model is obtained directly from the matrices $\mathbf{A}_{fp}$ and $\mathbf{B}_{fp}$, as

$$\ddot{z} = -\frac{d_v}{M_c + M_L}\dot{z} + \frac{1}{M_c + M_L}\Delta\tau_z \tag{3.2.8}$$

The linear time-invariant mode of the quadrotor and payload decoupled vertical dynamics is given by

$$P_{fpz}(s) \stackrel{s}{=} \left[\begin{array}{c|c} \left(-\frac{d_v}{M_c+M_L}\right) & \left(\frac{1}{M_c+M_L}\right) \\ \hline 1 & 0 \end{array}\right] := \left[\begin{array}{c|c} \mathbf{A}_{fpz} & \mathbf{B}_{fpz} \\ \hline \mathbf{C}_{fpz} & \mathbf{D}_{fpz} \end{array}\right], \tag{3.2.9}$$

where $P_{fpz}(s)$ is the transfer function, and $\mathbf{A}_{fpz}$, $\mathbf{B}_{fpz}$, $\mathbf{C}_{fpz}$, and $\mathbf{D}_{fpz}$ are the state space matrices of the decoupled vertical dynamics. The state vector for the vertical dynamics is defined simply as as $\mathbf{x} = [\dot{z}]$ and therefore only includes the quadrotor vertical velocity $\dot{z}$. The input vector for the vertical dynamics is the change in Down component of the quadrotor thrust force $\Delta\tau_z$. The output matrix $\mathbf{C}_{fpz}$ is chosen to select the quadrotor Down velocity as the output. The feedthrough matrix $\mathbf{D}_{fpz}$ is zero. $P_{fpz}(s)$ is a single-input single-output transfer function with the Down component of the thrust force as input and the quadrotor velocity as output. The payload angles and angular rates do not appear as internal states, because the system is linearised with the payload directly below the quadrotor. A thrust force applied directly upward or directly downward will therefore not excite the payload to start swinging.

The model exhibits a simple first-order transient response with a time constant that is determined by the ratio of the aerodynamic damping to the combined mass of the quadrotor and payload. The vertical dynamics does not contain a complex pole pair, nor does it exhibit a resonant frequency, due to the fact that the system is linearised with the payload directly below the quadrotor.

3.2.2 Quadrotor Attitude

In this section we presented linearised models of the quadrotor attitude dynamics.

3.2.2.1 Linearised Pitch Dynamics

From Equation 3.1.23, we have the pitch rate dynamics as

$$\dot{Q} = \frac{1}{I_{yy}}\left[M - PR(I_{xx} - I_{zz})\right] \tag{3.2.10}$$

$$\dot{Q} = f(Q, M) \tag{3.2.11}$$

$$\dot{Q} + \Delta\dot{Q} = f(Q + \Delta Q, M + \Delta M) \tag{3.2.12}$$

We wish to linearise these dynamics at an operating point where P and R are constants, so we use a Taylor expansion of $\dot{Q}$, which is

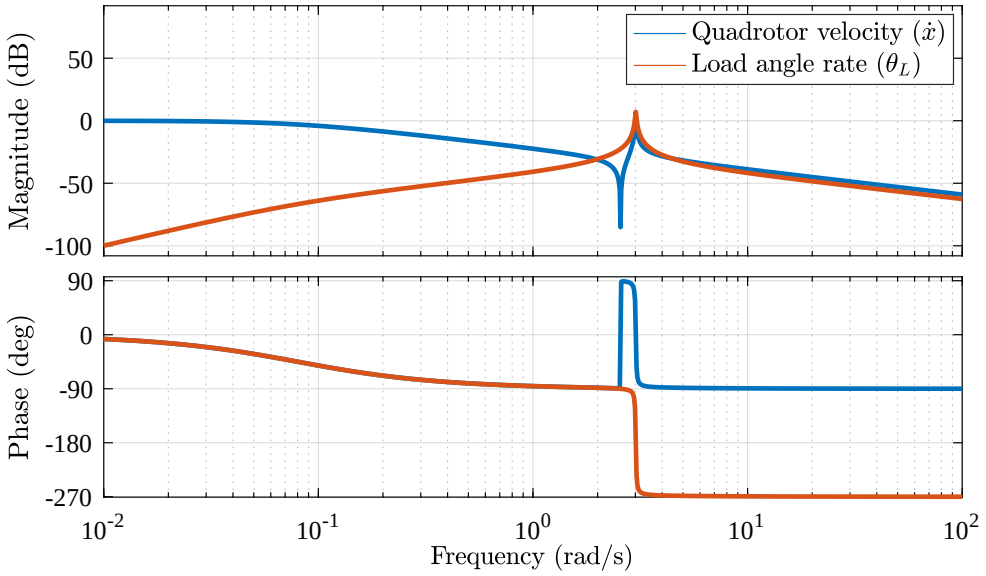

Figure 3.17: Bode plot of P_{fpx}. Shown in blue is when the output matrix $\mathbf{C}_{fpx}$ is chosen to select the quadrotor velocity $\dot{x}$ as the system output. Shown in red is when the output matrix $\mathbf{C}_{fpx}$ is chosen to select the payload angle rate $\dot{\theta}_L$ as the system output.

$$\dot{Q}_o + \Delta\dot{Q} = f(Q_o, M_o) + \frac{\partial f}{\partial Q}|_{(Q_o,M_o)}\Delta Q + \frac{\partial f}{\partial M}|_{(Q_o,M_o)}\Delta M + \text{higher order terms} \tag{3.2.13}$$

but $\dot{Q}_o = f(Q_o, M_o)$, and we neglect the higher order terms by setting them to zero, so

$$\Delta\dot{Q} = \frac{\partial f}{\partial Q}|_{(Q_o,M_o)}\Delta Q + \frac{\partial f}{\partial M}|_{(Q_o,M_o)}\Delta M \tag{3.2.14}$$

Evaluating the partial derivatives gives

$$\frac{\partial f}{\partial Q}|_{(Q_o,M_o)} = \frac{\partial}{\partial Q}\frac{1}{I_{yy}}\left[M - PR(I_{xx} - I_{zz})\right] = 0 \tag{3.2.15}$$

$$\frac{\partial f}{\partial M}|_{(Q_o,M_o)} = \frac{\partial}{\partial M}\frac{1}{I_{yy}}\left[M - PR(I_{xx} - I_{zz})\right] = \frac{1}{I_{yy}} \tag{3.2.16}$$

where the right-hand side of Equation 3.2.15 is zero because aerodynamic-induced moments are neglected. So

$$\Delta\dot{Q} = 0\Delta Q + \frac{1}{I_{yy}}\Delta M \tag{3.2.17}$$

$$\Delta\dot{Q} = \frac{1}{I_{yy}}\Delta M \tag{3.2.18}$$

Therefore, the linearised pitch dynamics are

$$M = I_{yy}\dot{Q} \tag{3.2.19}$$

Also, from Equation 3.1.25, we have that

$$M = d(T_1 - T_3) = d\delta_E \tag{3.2.20}$$

Combining Equation 3.1.27 and Equation 3.1.28, we get the virtual elevator model as

$$\dot{\delta}_E = -\frac{1}{\tau}\delta_E + \frac{1}{\tau}\delta_{E_R} \tag{3.2.21}$$

Therefore, the linear model of the quadrotor pitch attitude dynamics is given in state space form as follows

$$\begin{bmatrix} \dot{M} \\ \dot{Q} \end{bmatrix} = \begin{bmatrix} \frac{-1}{\tau} & 0 \\ \frac{1}{I_{yy}} & 0 \end{bmatrix} \begin{bmatrix} M \\ Q \end{bmatrix} + \begin{bmatrix} \frac{d}{\tau} \\ 0 \end{bmatrix} \delta_{E_R} \tag{3.2.22}$$

The state vector for the pitch rate dynamics is defined simply as $\mathbf{x} = [M, Q]$ and therefore only includes the quadrotor pitching moment and pitch rate. The input vector for the pitch rate dynamics is the virtual elevator deflection command δ_{E_R}. The output matrix $\mathbf{C}_Q$ is chosen to select the quadrotor pitch rate as the output. The feedthrough matrix $\mathbf{D}_Q$ is zero. The linear time-invariant model of the pitch rate dynamics is then given by

$$P_Q \overset{s}{=} \left[\begin{array}{c|c} \mathbf{A}_Q & \mathbf{B}_Q \\ \hline \mathbf{C}_Q & \mathbf{D}_Q \end{array}\right] \tag{3.2.23}$$

with

$$\mathbf{A}_Q = \begin{bmatrix} \frac{-1}{\tau} & 0 \\ \frac{1}{I_{yy}} & 0 \end{bmatrix}, \quad \mathbf{B}_Q = \begin{bmatrix} \frac{d}{\tau} \\ 0 \end{bmatrix} \tag{3.2.24}$$

where $P_Q(s)$ is the transfer function, and $\mathbf{A}_Q$, $\mathbf{B}_Q$, $\mathbf{C}_Q$, and $\mathbf{D}_Q$ are the state space matrices of the decoupled pitch rate dynamics. $P_Q(s)$ is a single-input single-output transfer function with the virtual elevator deflection command as input, the quadrotor pitch rate as output, and the quadrotor pitching moment as an internal state.

3.2.2.2 Linearised Roll Dynamics

Following the same linearisation process as in Section 3.2.2.1 with the roll attitude dynamics, the linear model of the quadrotor roll attitude dynamics is given in state space form as follows

$$\begin{bmatrix} \dot{L} \\ \dot{P} \end{bmatrix} = \begin{bmatrix} \frac{-1}{\tau} & 0 \\ \frac{1}{I_{xx}} & 0 \end{bmatrix} \begin{bmatrix} L \\ P \end{bmatrix} + \begin{bmatrix} \frac{d}{\tau} \\ 0 \end{bmatrix} \delta_{A_R} \tag{3.2.25}$$

The state vector for the roll rate dynamics is defined simply as $\mathbf{x} = [L, P]$ and therefore only includes the quadrotor rolling moment and roll rate. The input vector for the roll rate dynamics is the virtual aileron deflection command δ_{A_R}. The output matrix $\mathbf{C}_P$ is chosen to select the quadrotor roll rate as the output. The feedthrough matrix $\mathbf{D}_P$ is zero. The linear time-invariant model of the pitch rate dynamics is then given by

$$P_P(s) \stackrel{s}{=} \left[\begin{array}{c|c} \mathbf{A}_P & \mathbf{B}_P \\ \hline \mathbf{C}_P & \mathbf{D}_P \end{array}\right] \tag{3.2.26}$$

with

$$\mathbf{A}_P = \begin{bmatrix} \frac{-1}{\tau} & 0 \\ \frac{1}{I_{xx}} & 0 \end{bmatrix}, \quad \mathbf{B}_P = \begin{bmatrix} \frac{d}{\tau} \\ 0 \end{bmatrix} \tag{3.2.27}$$

where $P_P(s)$ is the transfer function, and $\mathbf{A}_P$, $\mathbf{B}_P$, $\mathbf{C}_P$, and $\mathbf{D}_P$ are the state space matrices of the decoupled roll rate dynamics. $P_P(s)$ is a single-input single-output transfer function with the virtual aileron deflection command as input, the quadrotor roll rate as output, and the quadrotor rolling moment as an internal state. Due to the symmetry of the quadrotor, the linearised pitch and roll rate dynamics will be equivalent.

3.2.2.3 Linear Yaw Dynamics

Following the same linearisation process as in Section 3.2.2.1 with the yaw attitude dynamics, the linear quadrotor yaw attitude dynamics are

$$N = I_{zz}\dot{R} \tag{3.2.28}$$

From Equation 3.1.25, the moment N can be represented as

$$N = r_D(-T_1 + T_2 - T_3 + T_4)/R_{LD} = r_D\delta_R/R_{LD} \tag{3.2.29}$$

Also, as with the virtual elevator dynamics, the rotor dynamics carry through to the virtual rudder dynamics by combining Equation 3.1.27 and Equation 3.1.28, resulting in

$$\dot{\delta}_R = -\frac{1}{\tau}\delta_R + \frac{1}{\tau}\delta_{R_R} \tag{3.2.30}$$

Therefore, the linear model of the quadrotor pitch attitude dynamics is given in state space form as follows

$$\begin{bmatrix} \dot{N} \\ \dot{R} \end{bmatrix} = \begin{bmatrix} \frac{-1}{\tau} & 0 \\ \frac{1}{I_{zz}} & 0 \end{bmatrix} \begin{bmatrix} N \\ R \end{bmatrix} + \begin{bmatrix} \frac{r_D}{R_{LD}\tau} \\ 0 \end{bmatrix} \delta_{R_R} \tag{3.2.31}$$

The state vector for the yaw rate dynamics is defined as $\mathbf{x} = [N, R]$ and therefore only includes the quadrotor yawing moment and yaw rate. The input vector for the yaw rate dynamics is the virtual rudder deflection command δ_{R_R}. The output matrix $\mathbf{C}_R$ is chosen to select the quadrotor yaw rate as the output. The feedthrough matrix $\mathbf{D}_R$ is zero. The linear time-invariant model of the yaw rate dynamics is then given by

$$P_R(s) \stackrel{s}{=} \left[\begin{array}{c|c} \mathbf{A}_R & \mathbf{B}_R \\ \hline \mathbf{C}_R & \mathbf{D}_R \end{array}\right] \tag{3.2.32}$$

with

$$\mathbf{A}_R = \begin{bmatrix} \frac{-1}{\tau} & 0 \\ \frac{1}{I_{zz}} & 0 \end{bmatrix}, \quad \mathbf{B}_R = \begin{bmatrix} \frac{d}{\tau} \\ 0 \end{bmatrix} \tag{3.2.33}$$

where $P_R(s)$ is the transfer function, and $\mathbf{A}_R$, $\mathbf{B}_R$, $\mathbf{C}_R$, and $\mathbf{D}_R$ are the state space matrices of the decoupled yaw rate dynamics. $P_R(s)$ is a single-input single-output transfer function with the virtual rudder deflection command as input, the quadrotor yaw rate as output, and the quadrotor yawing moment as an internal state.

3.3 Summary

This chapter presented the mathematical model of the quadrotor with suspended payload. The dynamics of the system was decomposed into the quadro-

tor-payload translational dynamics and the quadrotor rotational dynamics. The quadrotor-payload translational dynamics describes the motion of the vehicle and payload as point masses under the influence of a generalised force vector applied to the quadrotor point mass. The quadrotor attitude dynamics describes the rotational motion of the quadrotor under the influence of its rotor moments. The attitude of the quadrotor and the thrust produced by the rotors are translated into the force vector that is applied to the quadrotor-payload model. The major assumptions made in the model are that the payload cable is massless, rigid, and attached at the centre of gravity of the quadrotor, that the payload is spherical in shape, and that aerodynamic-induced moments on both the quadrotor and suspended payload are zero.

The equations of motion for the quadrotor and payload translational dynamics were derived by treating the system as a floating pendulum and applying the method of Lagrange. The potential uncertainties in the quadrotor and suspended payload system were identified and modelled.

An overview was given of the SLADe quadrotor simulation model that will be used for the simulation verification. Simulations were performed to verify that the quadrotor and suspended payload simulation model exhibits behaviour similar to what we intuitively expect from the physical system.

The nonlinear model of the quadrotor-payload system was linearised to obtain linear models of the horizontal dynamics and vertical dynamics, and the nonlinear model of the quadrotor rotational dynamics was decoupled and linearised to obtain linear models of the pitch, roll, and yaw dynamics.

Chapter 4

Cascade Control System Design

This chapter presents the design of an LQR-based flight control system for a quadrotor with suspended payload. The LQR-based control system uses a unique force-based inner-loop control system, where reference force commands are used to determine a desired quadrotor attitude. The control system architecture is discussed in Section 4.1. The design of the quadrotor attitude control system is presented next, in Section 4.2. The design of the quadrotor and payload translational control system is presented in Section 4.3. The LQR-based flight control system serves as the benchmark system against which the robust flight control system will be compared. The robust flight control system will be designed in subsequent chapters.

4.1 Control System Architecture

As mentioned in Chapter 3.1, the attitude dynamics of the quadrotor and the translational dynamics of the quadrotor and swinging payload are connected through the inertial force vector $\boldsymbol{\tau}_I$. Therefore, in order to control the translational motion of the quadrotor and suspended payload, the magnitude and direction of this inertial force resulting from the quadrotor's thrust must be controlled.

Therefore, an architecture that utilises this link is proposed. The architecture uses a unique force-based inner-loop control system, where reference force commands are used to determine a desired quadrotor attitude. The architecture in block diagram form is shown in Figure 4.1. Outer-loop controllers, or trajectory planners, determine a commanded inertial force $\boldsymbol{\tau}_{I_R}$ that must act on the quadrotor point mass in order to achieve some quadrotor velocity trajectory. The inner-loop controllers must control the orientation of the quadrotor, which, along with the thrust magnitude, generate a force $\boldsymbol{\tau}_I$ that acts on the quadrotor point mass model in the inertial frame.

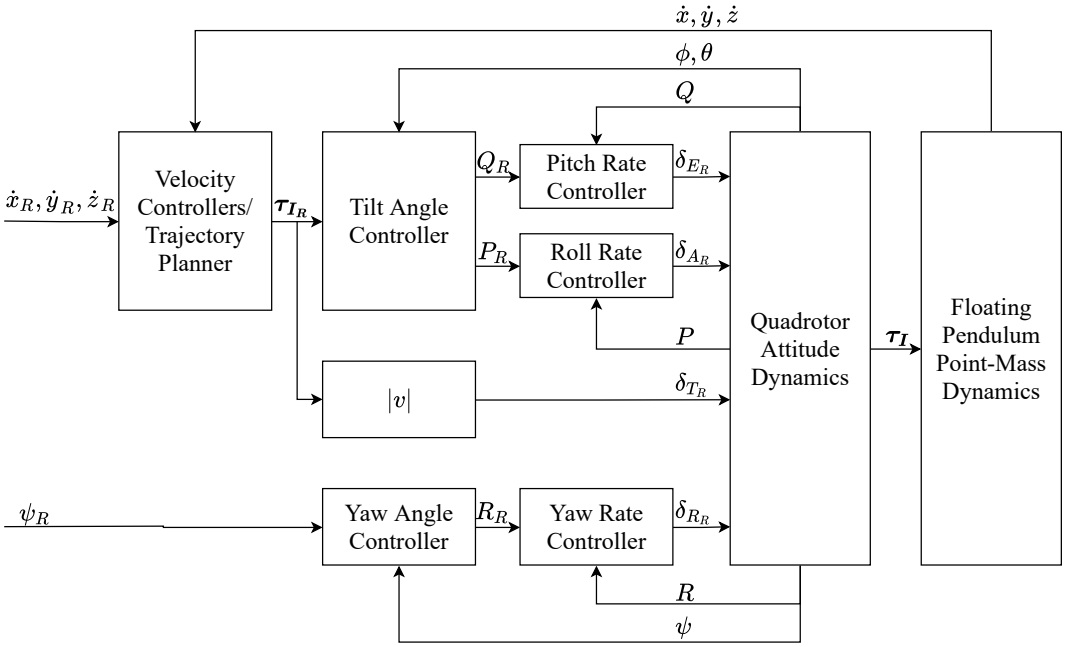

Figure 4.1: Quadrotor Control System Architecture

4.2 Quadrotor Attitude Control

This section describes the design and analysis of the quadrotor attitude control system. The linear models derived in the previous chapter are used to design the controllers, and the controllers are verified using the high-fidelity simulation model that includes models for sensor noise and wind disturbances.

4.2.1 Pitch Rate and Roll Rate Controller

The pitch and roll rates of the vehicle are controlled in order to improve damping in the pitch and roll dynamics. From Section 3.2.2.1, the linearised pitch rate dynamics are given as

$$P_Q(s) \overset{s}{=} \left[\begin{array}{c|c} \mathbf{A}_Q & \mathbf{B}_Q \\ \hline \mathbf{C}_Q & \mathbf{D}_Q \end{array}\right] \tag{4.2.1}$$

Figure 4.2 shows a block diagram of the controller architecture. This is based on the pre-existing pitch rate control system architecture that was used in previous research using the SLADe quadrotor. A combination of proportional gain, lead compensation, and low-pass filtering is used in order to achieve a controller with sufficient bandwidth, steady state tracking, efficient actuator usage, and high frequency roll-off. High-frequency roll-off is required to atten-

uate high-frequency angular rate measurement noise. The controller $K_Q(s)$ is therefore:

$$K_Q(s) = K_p \frac{s + z_1}{s + p_1} \frac{s}{s + p_2} \tag{4.2.2}$$

where K_p is proportional gain, z_1 and p_1 are the zero and pole of the lead compensator, and p_2 is the pole of the low-pass filter. We have that $|p_1| > |z_1|$, with the poles and zeros in the left half plane. The low-pass filter is used to reduce the amount of high-frequency gain added by the lead compensator. The controller output is a virtual elevator command δ_{E_R}, which is mapped using the mixing matrix in Equation 3.1.29 to individual rotor thrust commands.

As shown in Figure 4.2, actuator saturation is prevented by limiting the magnitude of the virtual elevator command δ_{E_R}. The value used for the saturation limit has been verified in flight tests by Möller [72]. This prevents the case of certain rotors producing zero thrust, which could occur if excessively large pitching moments are commanded.

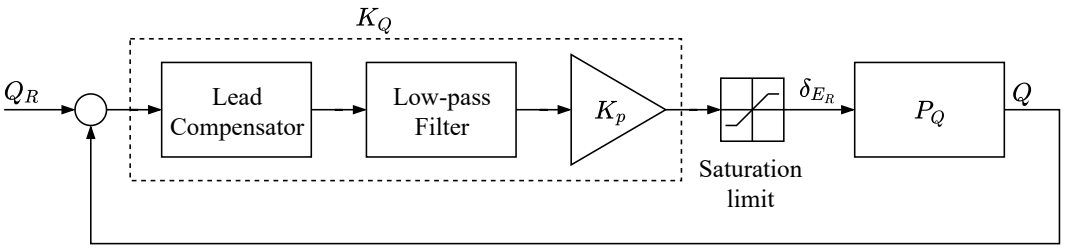

Figure 4.2: Closed-loop pitch rate control system

The frequency response of the open loop pitch rate dynamics is shown in Figure 4.3, with and without the controller $K_Q(s)$. The system is type 1, and has a slope of -20dB per decade in the low frequency region. This means the steady-state tracking response to step inputs will be zero, which is sufficient for the pitch rate system. The primary purpose of the pitch rate controller is to increase the bandwidth of the pitch rate system, without excessive actuator usage. Clearly seen from Figure 4.3 is the bandwidth increase due to the proportional gain (cross-over frequency $w_c = 16$ rad/s), the addition of phase lead from the lead compensator, and the increase in high frequency roll-off below the cut off frequency due to the low-pass filter. The phase margin is ≈ 60 degrees, and the gain margin is ≈ 20dB. The design was deemed acceptable because any further increase in bandwidth resulted in actuator saturation even when relatively small pitch rates were commanded. The design is such that actuator saturation only occurs when large pitch rate commands are received, and the effects of the actuator saturation are benign. This will be demonstrated in the next section when the tilt angle controller is presented.

The step response of the closed loop pitch rate system $T_Q = P_Q K_Q/(1 + P_Q K_Q)^{-1}$ to a command of 1 rad/s is shown in Figure 4.4. Almost no overshoot is observed, as a result of the large phase margin. The settling time of the system is $t_s = 0.15$ seconds. Also, as mentioned earlier, the slope of -20dB per decade in the low frequency region means the system has zero steady-state tracking error to the step command.

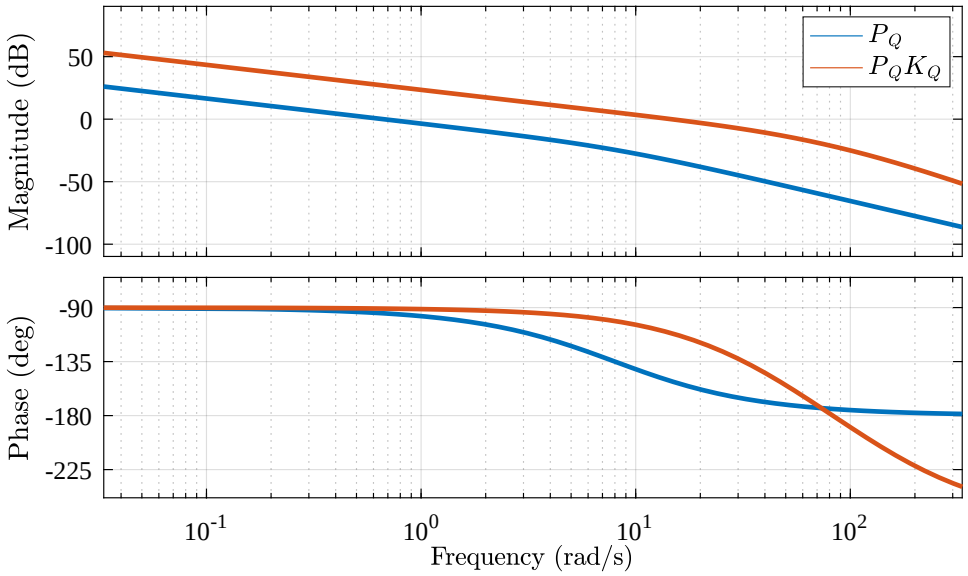

Figure 4.3: Bode plot of open loop pitch rate system

The roll rate controller has exactly the same architecture, and is designed in exactly the same way, except that it uses the virtual aileron command δ_{A_R} to command the roll rate P.

4.2.2 Tilt Angle Controller

We now discuss the architecture of the pitch angle and roll angle controllers, which are combined into a single controller termed the tilt angle controller. This architecture is based on the architecture used in previous projects using the SLADe quadrotor, such as the work presented by Möller [72]. A reference force vector in inertial coordinates $\boldsymbol{\tau}_{I_R}$ is generated by higher-level quadrotor velocity controllers or a trajectory planner. The magnitude of this reference force vector is used as the commanded thrust force, δ_{T_R}.

The reference force vector is normalized and multiplied by -1 to form a reference inertial unit vector $\hat{\boldsymbol{\tau}}_{I_R}$ in the opposite direction as the reference force

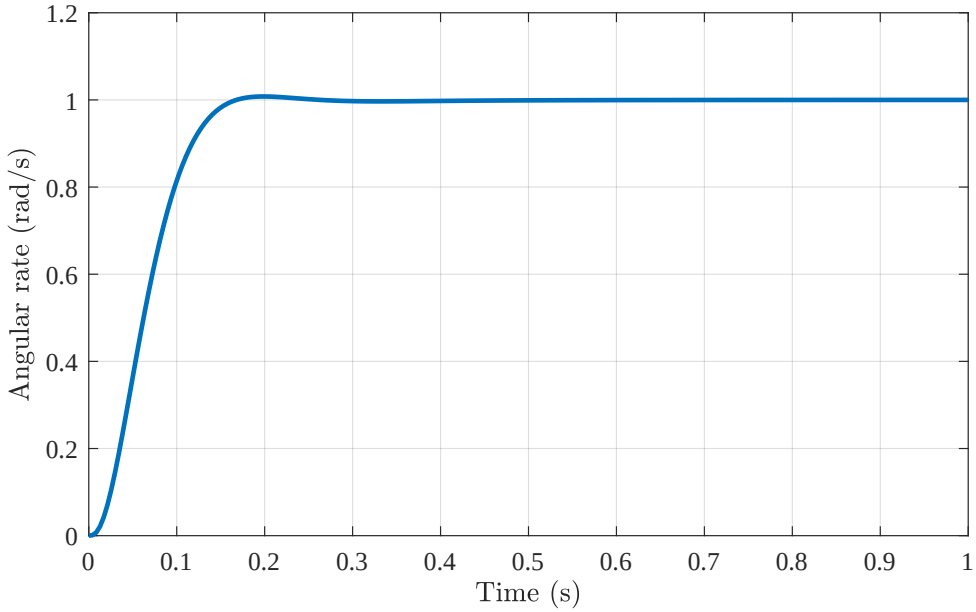

Figure 4.4: Step response of closed loop pitch rate system T_Q, from input Q_R to pitch rate Q

vector. The vector $\hat{\boldsymbol{\tau}}_{I_R}$ is then converted into a body axis unit vector $\boldsymbol{k}_{\tau_B}$ by rotating the vector using the inverse of the direction cosine matrix shown in Equation 3.1.31. By taking the arccosine of the dot product between the $\boldsymbol{k}_{\tau_B}$ vector and a unit vector in the body z-axis $\boldsymbol{k}_Z$, and multiplying the result by a proportional gain K_S, a total tilt rate S_R is calculated. By taking the cross product between the two vectors, the direction of S_R in body axes is calculated, resulting in pitch rate P_R and roll rate R_R reference commands. The objective of the tilt angle controller is to align the z-axis of the vehicle (in other words, the direction opposite to the actual thrust vector) with a unit vector in the opposite direction to the reference force vector in inertial coordinates. This architecture is shown diagrammatically in Figure 4.5, and can be expressed mathematically as:

$$\hat{\boldsymbol{\tau}}_{I_R} = -\frac{\boldsymbol{\tau}_{I_R}}{|\boldsymbol{\tau}_{I_R}|} \tag{4.2.3}$$

$$\boldsymbol{k}_{\tau_B} = \boldsymbol{R}^{-1}\hat{\boldsymbol{\tau}}_{I_R} \tag{4.2.4}$$

$$S_R = K_S \arccos\left(\boldsymbol{k}_{\tau_B} \cdot \boldsymbol{k}_z\right) \tag{4.2.5}$$

$$\begin{bmatrix} P_R \\ Q_R \\ 0 \end{bmatrix} = S_R \frac{\boldsymbol{k}_{\tau_B} \times \boldsymbol{k}_z}{|\boldsymbol{k}_{\tau_B} \times \boldsymbol{k}_z|} \tag{4.2.6}$$

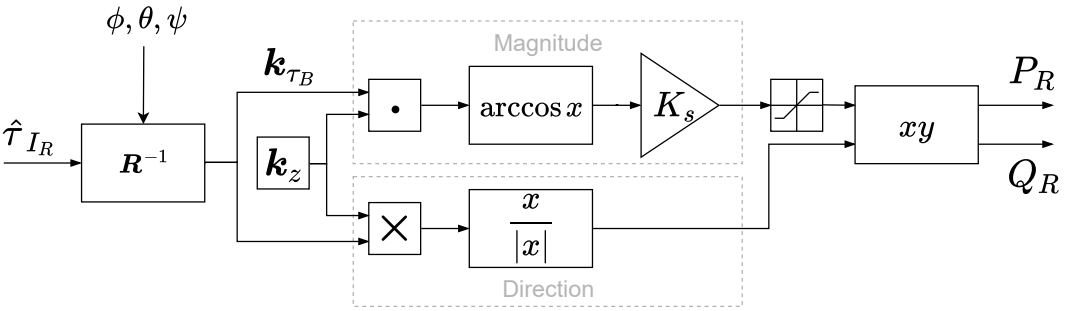

Figure 4.5: Tilt Angle Controller

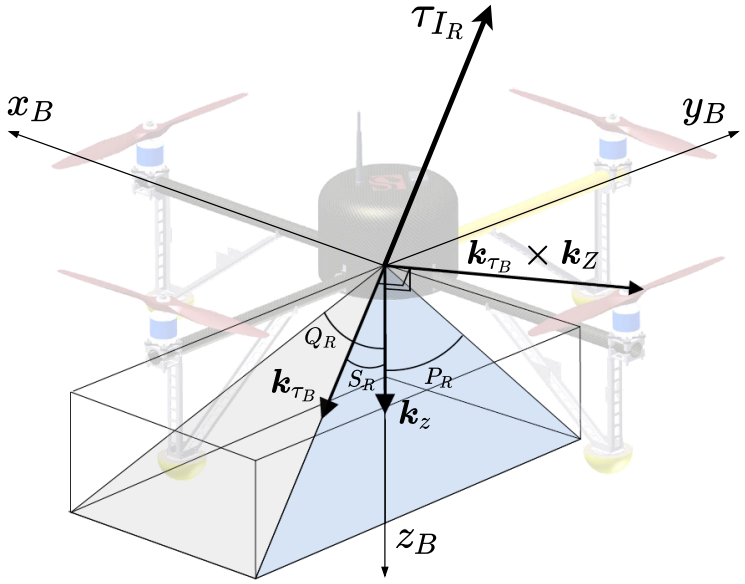

Figure 4.6: Tilt Angle Calculation

Note that the commanded pitch and roll rates are limited via a saturation block. Figure 4.6 displays this process more intuitively. The objective of the tilt angle controller is to align the vectors $\boldsymbol{k}_z$ and $\boldsymbol{k}_{\tau_B}$. The value S_R is a scalar quantity determining an error angle between the two vectors. For $\boldsymbol{k}_z = \boldsymbol{k}_{\tau_B}$, $S_R = \arccos 1 = 0$. The unit vector $\boldsymbol{k}_{\tau_B} \times \boldsymbol{k}_z$ is a vector in body-fixed axes that the quadrotor must rotate around in order to align these vectors. This rotation is achieved by rotating around the body-fixed axes x_B and y_B in appropriate proportions as determined by the coordinates of $\boldsymbol{k}_{\tau_B} \times \boldsymbol{k}_z$.

In order to analyse the linearised dynamics associated with the tilt angle control system, we use the simplified closed-loop system shown in Figure 4.7. Firstly, the roll rate P and yaw rate R are assumed to be zero during analysis of the tilt angle control system performing a pitching motion. The pitch rate output Q of the closed-loop pitch rate system $T_Q(s)$ is then naturally integrated to obtain the pitch angle (the tilt angle dynamics could also have been based on the roll dynamics, as they are equivalent). The result is the linearised open-loop pitch angle dynamics $P_T(s)$, which are therefore given as

$$P_T(s) = \frac{T_Q(s)}{s} \tag{4.2.7}$$

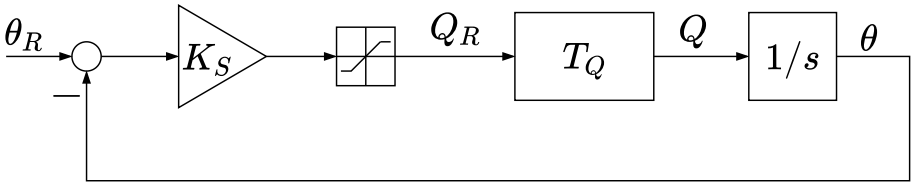

Figure 4.7: Tilt Angle Controller - simplified

The Bode plot of the open-loop pitch angle dynamics is given in Figure 4.8. A slope of −20dB per decade is seen in the low-frequency region, due to the natural integration of pitch rate to pitch angle. Therefore, the system is type 1 and will track step commands with zero steady-state error. This is deemed sufficient because if non-zero steady-state tilt angle errors occur due to disturbances, these can be compensated for by outer-loop quadrotor velocity controllers.

A simple proportional gain K_S is used as the controller and the Bode plot of $P_T(s)$ and $P_T K_S(s)$ is shown in Figure 4.8. The gain is designed to increase the bandwidth as much as possible while still maintaining adequate phase margin and without causing excessive actuator saturation. From Figure 4.8, the crossover frequency of the compensated system $P_T(s)K_S$ is 7.5 rad/s. The phase margin is approximately 60 degrees, and the gain margin is approximately 12 dB.

The step response of the closed-loop system $T_T(s) = P_T(s)K_S/(1+P_T(s)K_S)$ is shown in Figure 4.9. This closed-loop system represents the dynamics associated with commanding a reference force vector $\boldsymbol{\tau}_{I_R}$, and the tilt angle controller rotating the quadrotor to achieve the correct direction for the force. The step response has an overshoot of 6% and a settling time of 0.5 seconds. Furthermore, the steady-state tracking error to the step command is zero, because the system is type 1.

The step response shown in Figure 4.9 is of the linearised system $T_T(s)$, and does not include the effects of actuator saturation. The effects of actuator saturation will be shown in the next section, in which the tilt angle controller is verified by using the full nonlinear simulation.

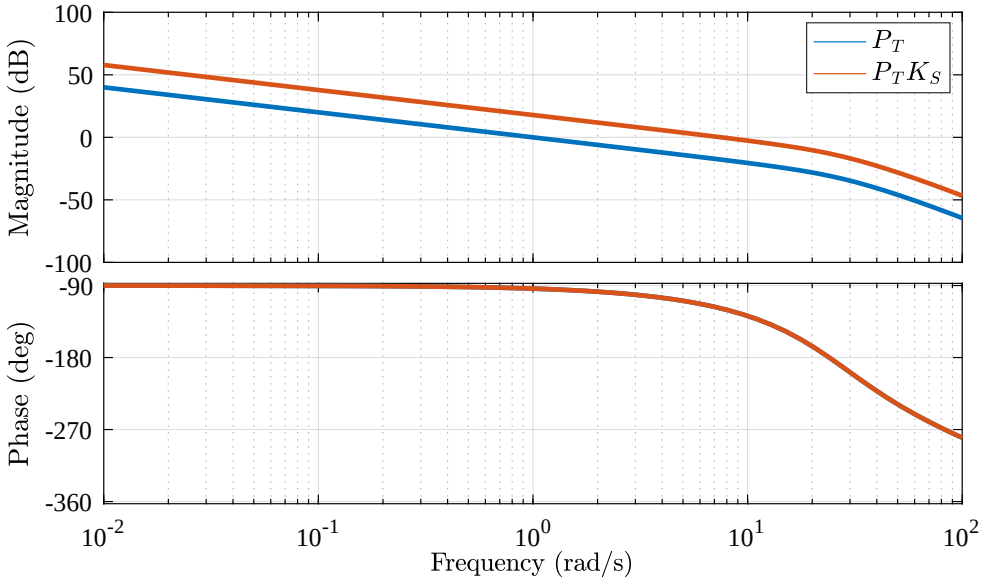

Figure 4.8: Bode plot of open-loop tilt angle system (both compensated and uncompensated)

4.2.3 Simulation with Nonlinear Attitude Dynamics

The angular rate controllers and the tilt angle control system are now implemented and verified in the full nonlinear simulation. Two simulation tests are performed: a small-signal step response and a large-signal step response. For the small signal step response, a small North force command $\tau_{x_R} = 15\text{N}$ is given, while the vertical force component is maintained at the level that balances the gravitational force. The quadrotor is initialised with zero yaw angle, meaning the North force component should be realized by tilting the pitch angle only.

Figure 4.10 presents the results of the simulation. The plot shows the commanded North force reference τ_{x_R} and the response of the actual North force τ_x. We can see that the commanded force value is achieved, indicating that the quadrotor is pitching in order to align the thrust vector with the commanded force $\boldsymbol{\tau}_{I_R} = [15, 0, g(M_c + M_L)]^T$. Also plotted is the response of the linear system $T_T(s)$. Clearly, there is very good agreement between the responses

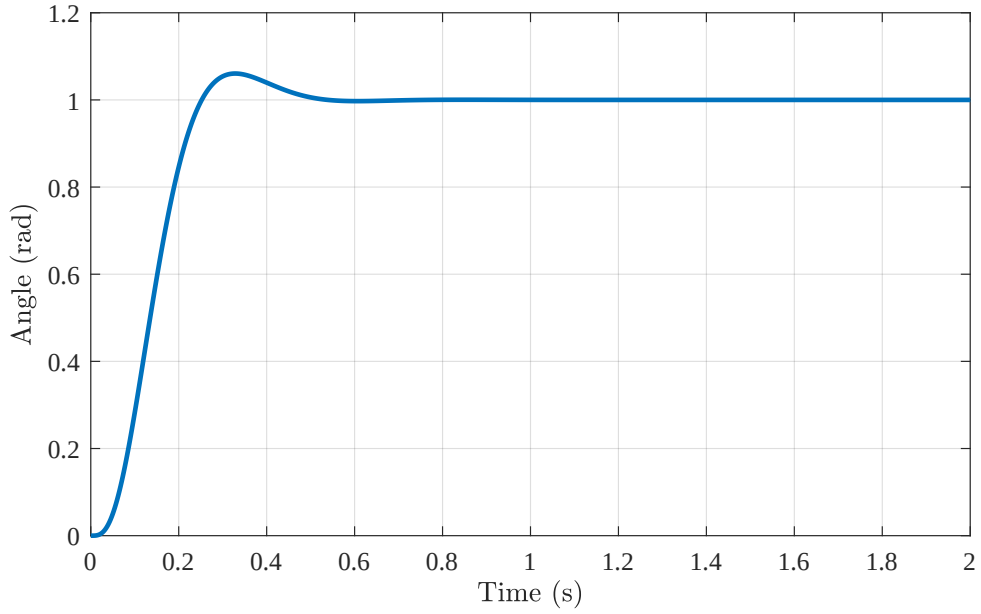

Figure 4.9: Step response of closed-loop tilt angle system $T_T(s)$, from tilt angle reference θ_R to tilt angle θ

of the linear model and the high-fidelity nonlinear simulation. The overshoot and settling time characteristics of the response of the linear model are seen in the response of the high-fidelity simulation.

For the large-signal step response, a larger North force command $\tau_{x_R} = 45\text{N}$ is given. The results of the simulation are shown in Figure 4.11. For the larger force command, there is a transient deviation between the nonlinear response and the linear model. This is due to actuator saturation, as a larger pitch angle is achieved in order to realize the commanded horizontal force.

Figure 4.12 shows the associated pitch angle, θ, along with the response of the linear closed loop pitch angle system T_T. This is plotted for the second scenario only, when $\tau_{x_R} = 45\text{N}$. Again, there is fairly significant deviation between the nonlinear simulation and the linear model. The linear model does not include the pitch rate (or roll rate) saturation blocks, which explains the deviation between the linear response and the nonlinear response of the tilt angle controller for large signals.

When large horizontal forces are commanded, larger roll and pitch angles will be commanded by the tilt angle controller. This can cause saturation in the pitch or roll rate commands, and in the actuator commands from the pitch and roll rate controllers. This leads to deviations away from the behaviour anticipated by the linear model. As expected, the small-signal behaviour of the nonlinear system agrees well with the behaviour of the linear model, while

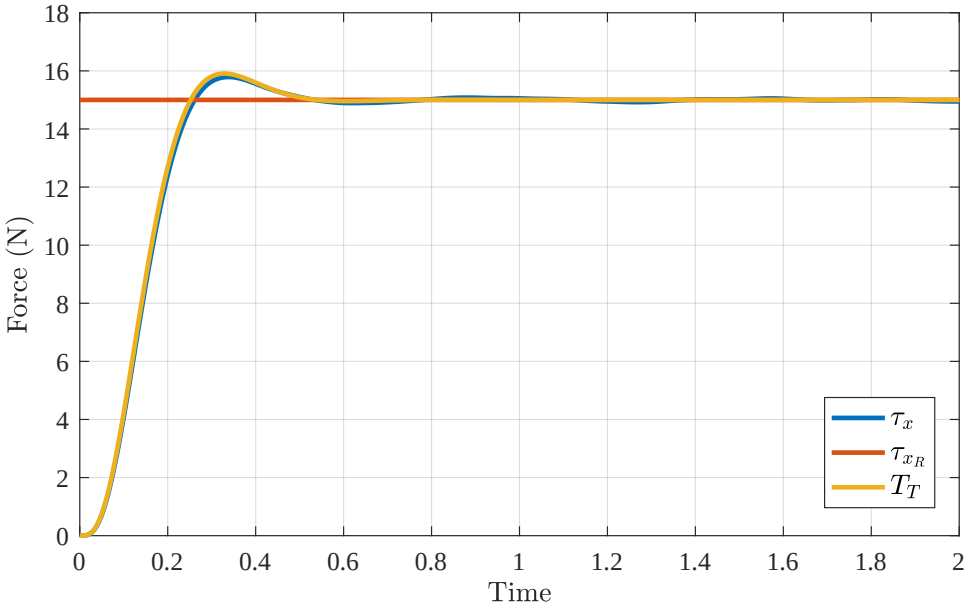

Figure 4.10: Step response of tilt angle controllers to reference step force command in high-fidelity simulation

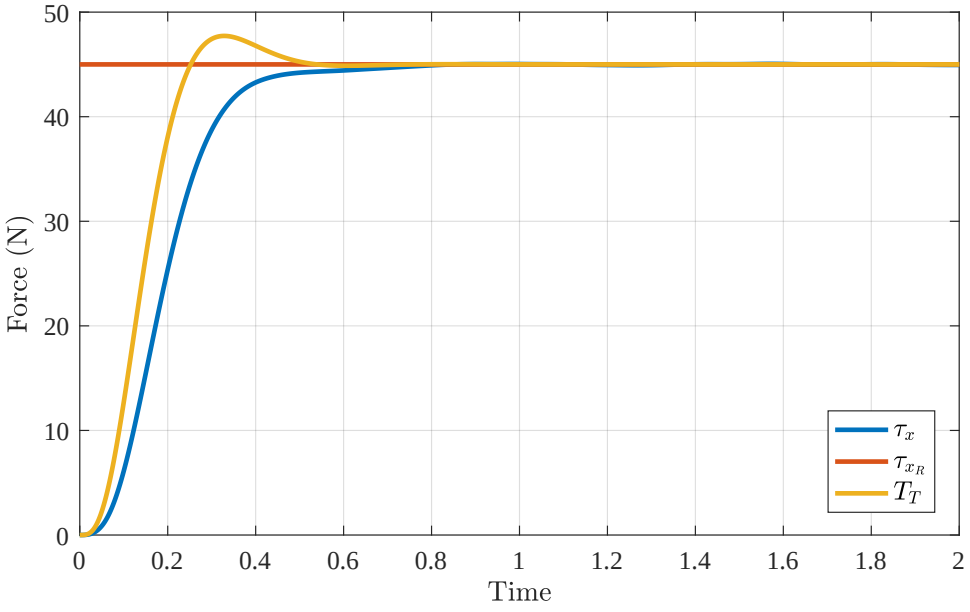

Figure 4.11: Step response of tilt angle controllers to reference step inertial force command in high-fidelity simulation

the large-signal behaviour differs somewhat due to the nonlinearities in the

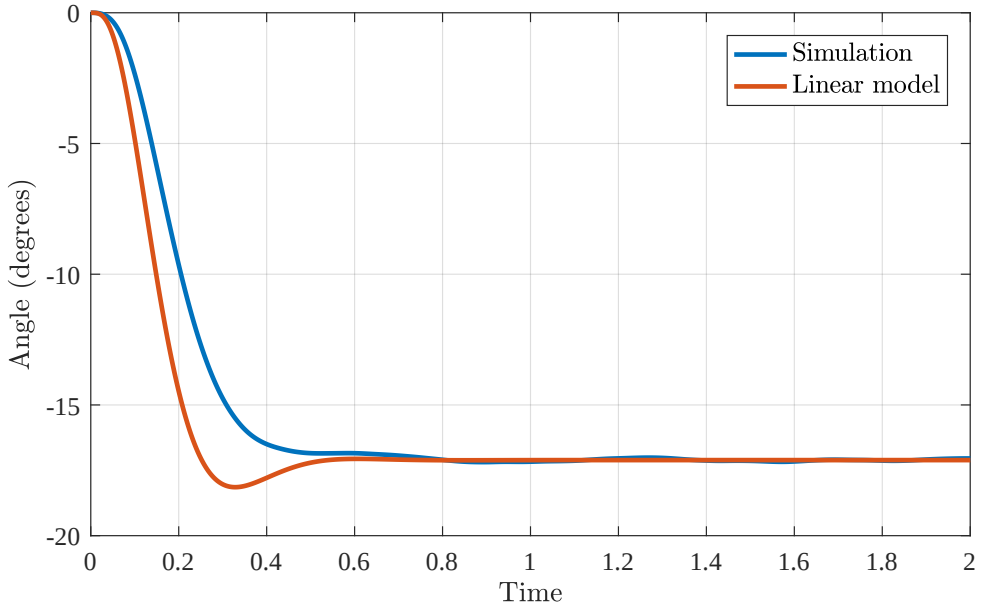

Figure 4.12: Step response of pitch angle in high-fidelity simulation

system. However, the large-signal behaviour has been tested extensively in both simulation and in practice, and this architecture and controller have proven to be successful in flight tests performed in previous projects.

The differences between the large-signal quadrotor attitude dynamics of the linear model and of the actual nonlinear system manifests as uncertainty in the thrust force direction. The uncertainty in the thrust force $\boldsymbol{\tau}_I$ modelled in Chapter 3 therefore represents both thrust magnitude uncertainty and thrust direction uncertainty.

4.2.4 Quadrotor Thrust Control

In our proposed flight control system architecture, there is no feedback control system for quadrotor thrust. Instead, thrust is controlled open-loop by commanding the rotor speeds through the virtual actuator command δ_{T_R}, which is then mapped to individual rotor commands. The virtual actuator command δ_{T_R} is simply the magnitude of the commanded force vector $\boldsymbol{\tau}_I$.

The behaviour of the rotors from commanded thrust values (or rotor speeds) to achieved thrust values is modelled by the rotor lag dynamics presented in Chapter 3. These have been determined by laboratory system identification tests. However, there will still be uncertainty in the achieved thrust relative to the commanded thrust, which is included in the gain uncertainty T_t. Therefore, this uncertainty represents both thrust magnitude uncertainty and thrust

direction uncertainty.

4.3 Quadrotor and Payload Translational Control

This section presents the design of the quadrotor velocity control system. This controller controls the quadrotor velocity in all three inertial coordinates, North, East, and Down. An overview of the controller is presented first, followed by the design of the velocity controllers for each inertial direction.

4.3.1 Overview

The controller uses quadrotor velocity as feedback and actuates the force vector command $\boldsymbol{\tau}_{I_R}$ in inertial coordinates. The controller does not receive sensor measurements of the payload angles or payload angular rates as feedback.

As mentioned in Chapter 3, the linearised model of the floating-pendulum point mass dynamics is decoupled in the three inertial directions. Therefore, three decoupled velocity controllers are used to control the quadrotor velocity; one for each inertial direction. The structure of the controller is presented in Figure 4.13.

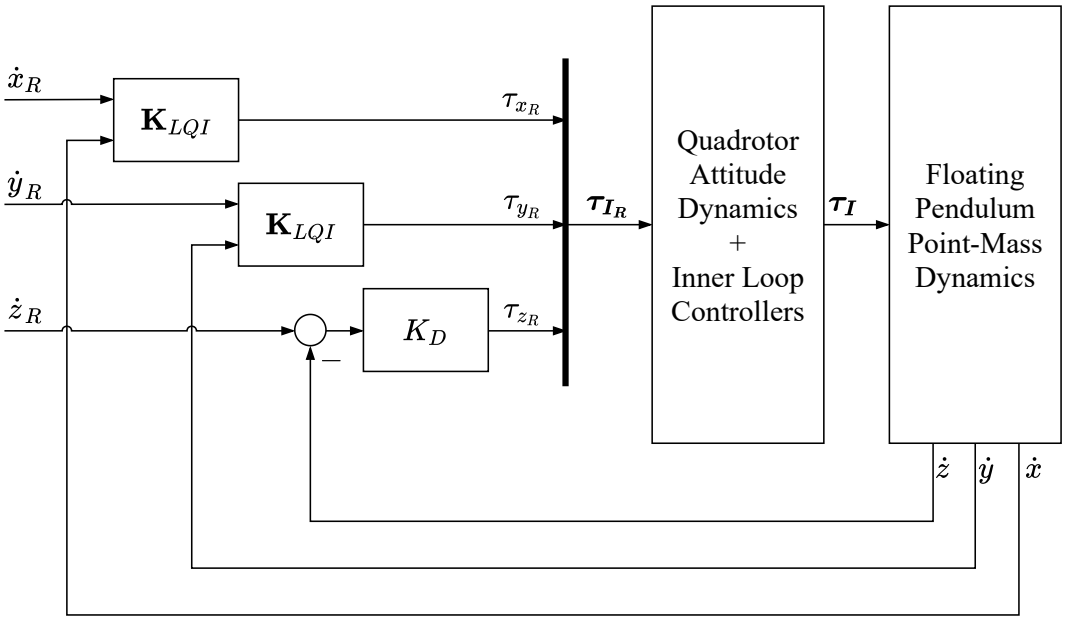

Figure 4.13: Benchmark controller implemented in high-fidelity simulation

The controller consists of three separate controllers: a North velocity controller, an East velocity controller, and a Down velocity controller. The North velocity controller and the East controller are identical controllers that are designed using the horizontal dynamics of the quadrotor and suspended payload system. The North and East velocity controllers are designed using LQR methods. The resulting controllers use state estimators to estimate the payload angles and payload angular rates, and then use full-state feedback to determine the required horizontal components of the commanded force $\boldsymbol{\tau}_{I_R}$.

The Down velocity controller is a proportional-integral controller that uses quadrotor velocity in the Down direction to actuate the vertical component of the commanded force $\boldsymbol{\tau}_{I_R}$.

4.3.2 Quadrotor Vertical Velocity Control

In this section, we present the design of the controller that controls the quadrotor velocity in the Down direction. The structure of the controller is shown in Figure 4.14. The controller, denoted K_D receives the error between the current vertical velocity command $\dot{z}_R$ and the measurement of vertical velocity, $\dot{z}$. The controller actuates the vertical component of the force vector command $\boldsymbol{\tau}_{I_R}$, which is τ_{z_R}.

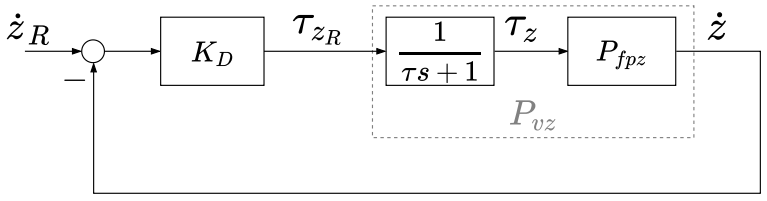

Figure 4.14: Linear quadrotor vertical velocity control system

4.3.2.1 Linearized Plant Model

The linearised model of the floating-pendulum in the Down direction is given by equation 3.2.9, repeated here:

$$P_{fpz}(s) \overset{s}{=} \left[\begin{array}{c|c} \left(-\frac{d_v}{M_c+M_L}\right) & \left(\frac{1}{M_c+M_L}\right) \\ \hline 1 & 0 \end{array}\right] := \left[\begin{array}{c|c} \mathbf{A}_{fpz} & \mathbf{B}_{fpz} \\ \hline \mathbf{C}_{fpz} & \mathbf{D}_{fpz} \end{array}\right], \tag{4.3.1}$$

The input to this linear model is the change in inertial force in the Down direction, $\Delta\tau_z$. However, this model excludes the rotor lag dynamics that

determine the response of the rotors to changing thrust command values. The rotor lag dynamics are presented in Equation 3.1.27, repeated here as

$$\dot{T}_i = (-T_i + T_{i_R})/\tau \tag{4.3.2}$$

The linear time-invariant transfer function that represents these dynamics is given as

$$P_r(s) = \frac{1}{\tau s + 1} \tag{4.3.3}$$

The model used to design a quadrotor velocity controller for the Down inertial direction is formed by combining the model $P_{fpz}(s)$, with the rotor lag dynamics $P_r(s)$. This gives a new system of the two first-order lags cascaded, denoted $P_{vz}(s)$. This now forms the plant model used to design the vertical velocity control system. The cascaded systems are shown graphically in Figure 4.14.

4.3.2.2 Controller Design and Analysis

The model P_{vz} does not contain the lightly damped mode associated with the swinging motion of the suspended payload, due to the fact that ideal vertical motion with the payload directly below the quadrotor does not induce payload swinging motions. A Bode plot of the nominal open-loop system $P_{vz}(s)$ is given in 4.15. From this figure we see that the system does not contain the lightly damped resonant peak that characterises the swinging motion of the suspended payload.

Further, we see that the system P_{vz} is type 0, with the slope in the low-frequency region being 0 dB per decade. This is because the dynamics are that of two cascade first-order lags. The cut-off frequency of approximately 10^{-1} (rad/s) is from the first-order lag representing the vertical dynamics of the floating pendulum system. This cut-off frequency is determined by the ratio of aerodynamic damping to the combined mass of the quadrotor and payload. In the higher-frequency region, we see the effects of the rotor lag dynamics, which have a time constant of 0.125 seconds and therefore a cut-off frequency of 5 rad/s.

The objectives of the vertical controller are two-fold. Firstly, the controller must track vertical velocity step commands with zero steady-state tracking error. The vertical velocity controller must therefore change the slope of the low-frequency asymptote of the open-loop system to -20 dB per decade in order to improve steady-state tracking, which motivates the use of integral action in the controller.

Secondly, the velocity controller must reject disturbances caused by the horizontal velocity controllers. If a horizontal velocity controller commands a non-zero horizontal component of the force vector command $\boldsymbol{\tau}_{I_R}$, the tilt angle controller will respond by tilting the quadrotor to achieve this force component. This causes a momentary decrease in the vertical component of the quadrotor's thrust force, which will act as a disturbance into the vertical velocity control system. Thus, the vertical velocity controller must have adequate bandwidth to reject these disturbances.

Therefore, the bandwidth of the horizontal velocity controllers presents a minimum required bandwidth for the vertical control system. This is because the crossover frequency of the horizontal velocity controllers represents the maximum frequencies of the disturbances that are likely to enter into the vertical velocity control system. From previous projects done at the ESL, the horizontal velocity controllers should have a bandwidth of ≈ 0.7 rad/s. Therefore, this is the bandwidth requirement of the vertical velocity control system.

With these requirements in mind, a proportional-integral controller was selected. The vertical velocity controller, denoted $K_D(s)$, is therefore given as

$$K_D(s) = K_{DP} + K_{DI}/s \tag{4.3.4}$$

where the proportional gain K_{DP} and the integrator gain K_{DI} are chosen to meet the requirements of the low-frequency gain of the system and the bandwidth of the system without excessive actuator usage. A Bode plot of the compensated open-loop system $P_{vz}K_D$ is given in Figure 4.15. Clearly seen are the -20dB per decade slope in the low frequency region, which meets the steady-state tracking requirement, and the crossover frequency of 1 rad/s, which meets the bandwidth requirement of 0.7 rad/s. Also, the phase margin is 70 degrees and the gain margin is infinite.

The closed-loop block diagram of the vertical velocity control system (with controller $K_D(s)$ and linearised plant) is shown in Figure 4.14. The closed-loop step response of the system is shown in Figure 4.16. The system displays 10% overshoot, which is a consequence of adding the integrator into the controller. However, this amount of overshoot is deemed acceptable because this overshoot can easily be accounted for by a higher-level altitude controller. The response shows a rise time of 2 seconds, and zero steady-state tracking error.

Also shown are the response of the system when the uncertainties in the system are considered. In the case of motion in only the vertical direction, only variations in the payload mass M_L and the thrust uncertainty ΔT_t have any effect on the system. Variations in the cable length parameter L have no effect on the vertical velocity control as it is eliminated from the linearised model. It is clear from Figure 4.16 that robustness to uncertainty is not of great concern for motion in the vertical direction only, at least not with the

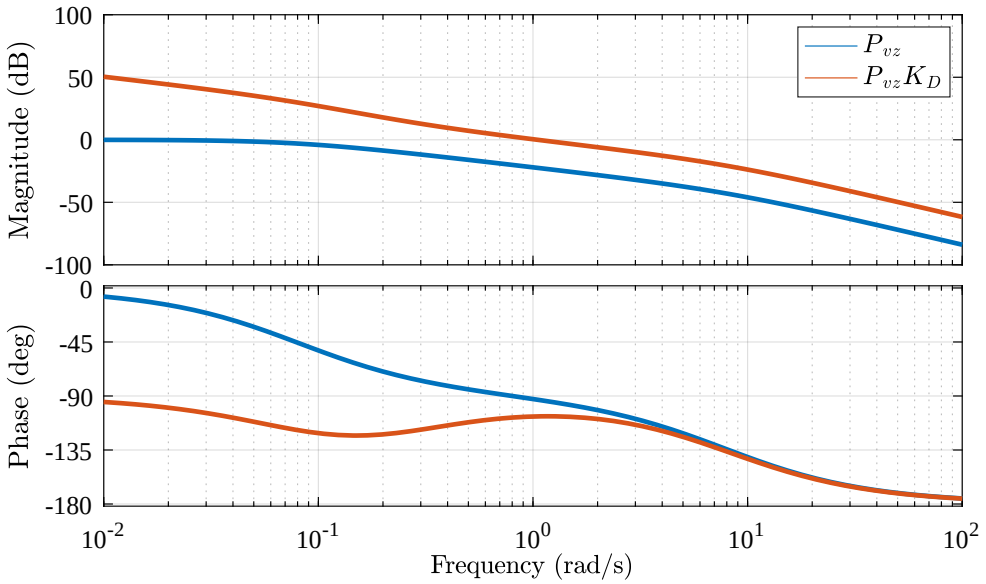

Figure 4.15: Bode plot of linear floating point model P_{vz} and linear model with controller, $P_{vz}K_D$.

velocity controller K_D presented here. The gain and phase margins of system with the PI controller are deemed adequate to ensure a robust design.

4.3.3 Horizontal Velocity Control

This section presents the design of the horizontal velocity controllers that control the horizontal velocities of the quadrotor in the North and East directions. Two identical, decoupled velocity controllers are used; one for control of the quadrotor velocity in the North direction, and one for control of the quadrotor velocity in the East direction. Because the two horizontal controllers are identical, we present the design of the North velocity controller only. The controller receives measurements of quadrotor velocity in the North direction as feedback, and actuates the North component of the force vector command $\boldsymbol{\tau}_{I_R}$. The structure of the North velocity controller, denoted K_{LQI}, is given in Figure 4.17.

The controller is a linear-quadratic regulator, with added integral action. Integral action is used to ensure that the commanded horizontal velocity reference is followed with zero steady-state tracking error for step references. The error between the current quadrotor velocity $\dot{x}$ and the commanded velocity $\dot{x}_R$ is integrated and then used to augment the full-state feedback provided by the linear-quadratic regulator.

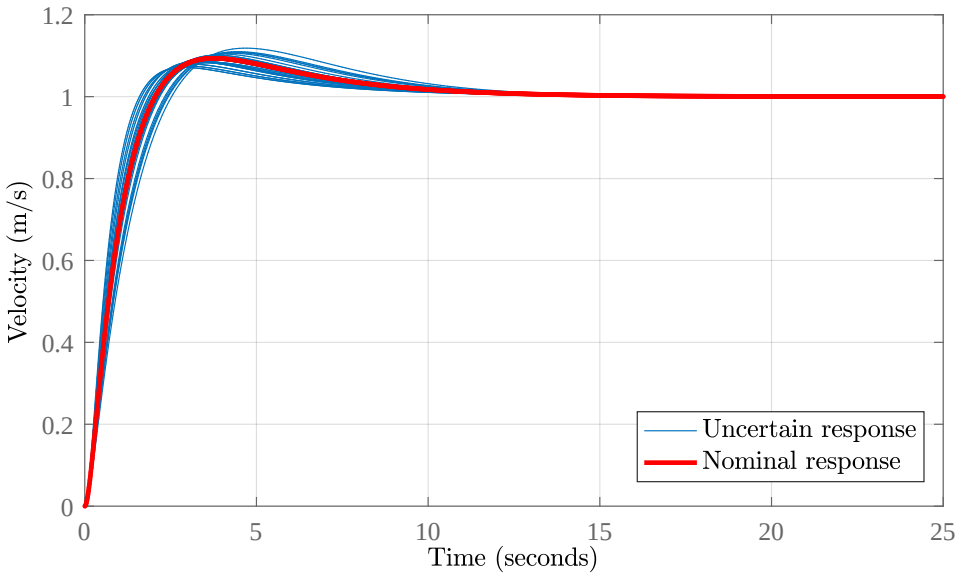

Figure 4.16: Step response of linear model P_{vz} with PI controller K_D. Also shown are the responses when the payload mass M_L and the thrust uncertainty T_t are varied.

The dynamics representing the relationship between a commanded force in the North direction, τ_{x_R}, and the actual force in the North direction, τ_x, are the tilt angle dynamics, $T_T(s)$. This function represents the dynamics associated with requesting a certain reference inertial force $\boldsymbol{\tau}_{I_R}$ and the tilt angle controller acting to rotate the quadrotor to achieve the desired force. Therefore, these are included in the design and analysis of the controller. The system $P_{fpx}(s)$ is the linearised dynamics of the floating pendulum model in the North direction. The input to the system $P_{fpx}(s)$ is the force in the North direction, τ_x.

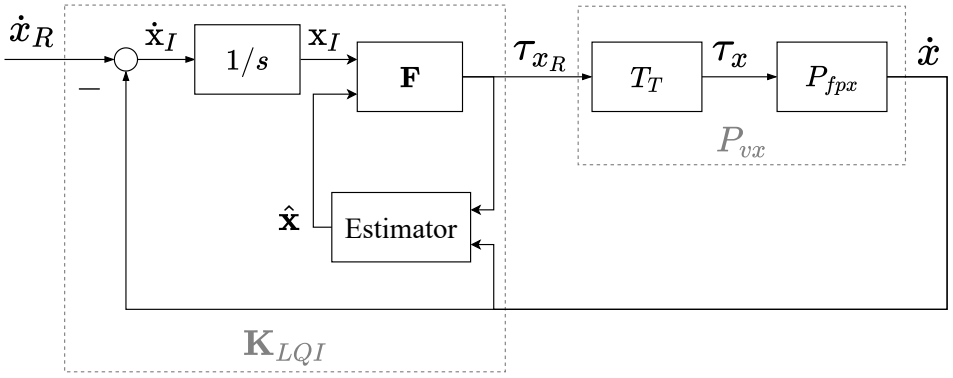

Figure 4.17: Horizontal velocity controller architecture

4.3.3.1 Linearized Plant Model

As discussed in Section 3.2.1.2, the linearised model of the floating pendulum is decoupled in the three inertial directions, so we consider each direction separately. Therefore, the model used to represent the quadrotor and suspended payload point mass dynamics is given by the linear time-invariant model P_{fpx}. The states of the model are $\mathbf{x} = [\theta_L, \dot{x}, \dot{\theta}_L]$. The input is an inertial force command in the North direction, τ_{x_R}. To accomplish trajectory tracking and disturbance rejection, the velocity of the quadrotor $\dot{x}$ will be controlled.

Figure 4.18 shows the frequency response of P_{fpx}. Clearly visible from the plot is the resonant zero pair and resonant pole pair, with the resonant pole pair being at the natural frequency of the floating pendulum. Also, the system is type 0, with a slope of 0 dB per decade in the low frequency region. This is due to the aerodynamic drag forces on the quadrotor and suspended payload. This motivates the use of integral action in the controller, in order to ensure that step commands are tracked with zero steady-state error.

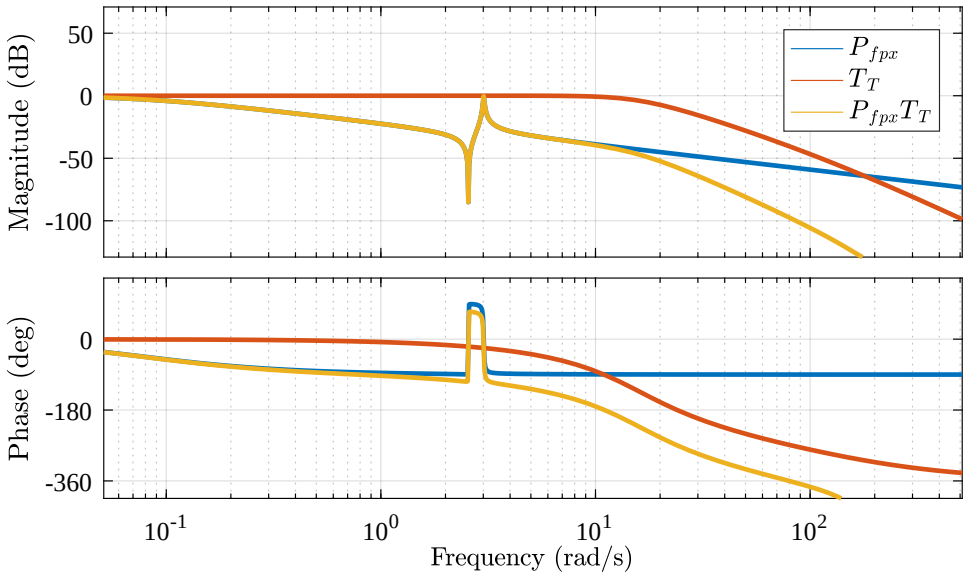

Figure 4.18: Bode plot of linear floating point model P_{fpx}, tilt angle dynamics T_T, and combined model $P_{vx} = P_{fpx}T_T$.

The dynamics of the tilt angle system are included when designing the controller. In Taylor et al. [5], the authors assume a time-scale separation between the dynamics of the inner-loop tilt angle system and an outer-loop velocity control system. Figure 4.18 also shows the frequency response of the linearised tilt angle system T_T. Clearly, the bandwidth of the tilt angle system is higher than

the bandwidth of the floating-pendulum system and the time-scale separation is a reasonable assumption. However, we will not make this assumption and therefore include the inner-loop dynamics because we may wish to increase the loop gain of the velocity system significantly in which case the inner-loop dynamics may become significant. Therefore, the plant for the design of a velocity control system for the quadrotor and suspended payload, that includes the quadrotor rotational dynamics, is given as

$$P_{vx}(s) = P_{fpx}(s)T_T(s) \tag{4.3.5}$$

such that $\dot{x} = P_{vx}\tau_{x_R}$. The frequency response of P_{vx} is also shown in Figure 4.18.

4.3.3.2 Controller Design and Analysis

As a benchmark control system, we present the design of an LQR-based controller. For this system, integral action is added to the LQG design to in order to ensure that step commands are tracked with zero steady-state error. The state we are controlling is the quadrotor velocity, and we assume that the quadrotor's velocity can be measured by a GPS or other on-board sensors through estimation. However, the payload angle states cannot be measured directly and need to be estimated in order to use full-state feedback. The control input is the reference force in the North direction τ_{x_R}, denoted u in the discussion to follow. Furthermore, denoting the desired velocity as r, and the current velocity as y, we can write the error as $e = \dot{\mathrm{x}}_I = r - y$. Adding the integral of this error to the plant dynamics P_{vx} gives us the augmented plant P_{vxi} as follows:

The additional state is

$$\dot{\mathrm{x}}_I = e = r - y = r - \mathbf{C}_{vx}\mathbf{x} - \mathbf{D}_{vx}u.$$

Writing the plant P_{vx} in state space format, we have

$$\begin{aligned}\dot{\mathbf{x}} &= \mathbf{A}_{vx}\mathbf{x} + \mathbf{B}_{vx}u\\ y &= \mathbf{C}_{vx}\mathbf{x} + \mathbf{D}_{vx}u.\end{aligned}$$

So combining the two gives the augmented plant P_{vxi} as

$$\begin{bmatrix}\dot{\mathbf{x}}\\ \dot{\mathrm{x}}_I\end{bmatrix} = \begin{bmatrix}\mathbf{A}_{vx} & \mathbf{0}\\ \mathbf{C}_{vx} & 0\end{bmatrix}\begin{bmatrix}\mathbf{x}\\ \mathrm{x}_I\end{bmatrix} + \begin{bmatrix}\mathbf{B}_{vx}\\ -\mathbf{D}_{vx}\end{bmatrix}u + \begin{bmatrix}\mathbf{0}\\ 1\end{bmatrix}r.$$

so,

$$P_{vxi} \overset{s}{=} \left[\begin{array}{cc|cc} \begin{bmatrix} \mathbf{A}_{vx} & \mathbf{0} \\ \mathbf{C}_{vx} & 0 \end{bmatrix} & & \begin{bmatrix} \mathbf{B}_{vx} \\ -\mathbf{D}_{vx} \end{bmatrix} & \begin{bmatrix} \mathbf{0} \\ 1 \end{bmatrix} \\ \hline \multicolumn{2}{c|}{\mathbf{C}_{vxi}} & \mathbf{D}_{vxi1} & \mathbf{D}_{vxi2} \end{array}\right] = \left[\begin{array}{c|c} \mathbf{A}_{vxi} & \mathbf{B}_{vxi} \\ \hline \mathbf{C}_{vxi} & \mathbf{D}_{vxi} \end{array}\right].$$

The general linear-quadratic-regulator problem minimizes the following cost function,

$$J = E\left\{\lim_{t\to\infty} \frac{1}{T}\int_0^T \left[\mathbf{x}^T(t)\mathbf{Q}\mathbf{x}(t) + \mathbf{u}^T(t)\mathbf{R}\mathbf{u}(t)\right] dt\right\}$$

where $\mathbf{Q}$ and $\mathbf{R}$ are chosen weighting matrices. The solution is a controller that exhibits a separation structure between a state observer and state feedback gains. Denote the estimator gain as $\mathbf{L}$ and the state feedback gain as $\mathbf{F}_x$ for the original plant states and F_I for the added integral state. The state feedback gains are determined as

$$\begin{bmatrix} \mathbf{F}_x & F_I \end{bmatrix} = R^{-1}\mathbf{B}_{vxi}^T\mathbf{X}, \tag{4.3.6}$$

where $\mathbf{X} = \mathbf{X}^T \geq 0$ is the unique positive semi-definite solution to the following algebraic Riccati equation:

$$\mathbf{A}_{vxi}^T\mathbf{X} + \mathbf{X}\mathbf{A}_{vxi} - \mathbf{X}\mathbf{B}_{vxi}R^{-1}\mathbf{B}_{vxi}^T\mathbf{X} + \mathbf{Q} = 0 \tag{4.3.7}$$

Note that we consider R as a scalar, because we are considering a single-input system. The estimator gain $\mathbf{L}$ (which is the steady-state Kalman gain) is given as

$$\mathbf{L} = \mathbf{Y}\mathbf{C}_{vxi}^T V^{-1}, \tag{4.3.8}$$

where $\mathbf{Y} = \mathbf{Y}^T \geq 0$ is the unique positive semi-definite solution to the following algebraic Riccati equation:

$$\mathbf{Y}\mathbf{A}_{vx}^T + \mathbf{A}_{vx}\mathbf{Y} - \mathbf{Y}\mathbf{C}_{vx}^T V^{-1}\mathbf{C}_{vx}\mathbf{Y} + \mathbf{W} = 0 \tag{4.3.9}$$

and V is the variance of the noise on the quadrotor velocity measurement. Note, the integral states are not included in the estimator - the estimator is calculated with the original plant matrices only. This is because we do not

want to estimate the integrated error, as we have access to the error directly by using the measurement. The final controller is constructed by writing the equations for the state estimate $\hat{\mathbf{x}}$ as

$$\dot{\hat{\mathbf{x}}} = (\mathbf{A}_{vx} - \mathbf{L}\mathbf{C}_{vx})\hat{\mathbf{x}} + \mathbf{B}_{vx}u + \mathbf{L}y \tag{4.3.10}$$

Now, noting that the controller output u is

$$u = -\begin{bmatrix} \mathbf{F}_x & F_I \end{bmatrix} \begin{bmatrix} \hat{\mathbf{x}} \\ \mathrm{x}_I \end{bmatrix}, \tag{4.3.11}$$

Equation 4.3.10 can be expanded into

$$\dot{\hat{\mathbf{x}}} = (\mathbf{A}_{vx} - \mathbf{L}\mathbf{C}_{vx} - \mathbf{B}_{vx}\mathbf{F}_x)\hat{\mathbf{x}} - \mathbf{B}_{vx}\mathbf{F}_I\mathrm{x}_I + \mathbf{L}y \tag{4.3.12}$$

Therefore, the final controller written in state space form is

$$\begin{bmatrix} \dot{\hat{\mathbf{x}}} \\ \dot{\mathrm{x}}_I \end{bmatrix} = \begin{bmatrix} \mathbf{A}_{vx} - \mathbf{B}_{vx}\mathbf{F}_x - \mathbf{L}\mathbf{C}_{vx} & -\mathbf{B}_{vx}\mathbf{F}_I \\ \mathbf{0} & 0 \end{bmatrix} \begin{bmatrix} \hat{\mathbf{x}} \\ \mathrm{x}_I \end{bmatrix} + \begin{bmatrix} \mathbf{0} & \mathbf{L} \\ 1 & -1 \end{bmatrix} \begin{bmatrix} r \\ y \end{bmatrix}$$

$$u = -\begin{bmatrix} \mathbf{F}_x & F_I \end{bmatrix} \begin{bmatrix} \hat{\mathbf{x}} \\ \mathrm{x}_I \end{bmatrix}$$

The controller can also be written in transfer function form, as

$$u = \mathbf{K}_{lqi}(s) \begin{bmatrix} r \\ y \end{bmatrix}$$

with

$$\mathbf{K}_{lqi}(s) \stackrel{s}{=} \left[\begin{array}{cc|c} \begin{bmatrix} \mathbf{A}_{vx} - \mathbf{B}_{vx}\mathbf{F}_x - \mathbf{L}\mathbf{C}_{vx} & -\mathbf{B}_{vx}F_I \\ \mathbf{0} & 0 \end{bmatrix} & & \begin{bmatrix} \mathbf{0} & \mathbf{L} \\ 1 & -1 \end{bmatrix} \\ \hline -\begin{bmatrix} \mathbf{F}_x & F_I \end{bmatrix} & & \mathbf{0} \end{array}\right]$$

The controller is implemented as shown in Figure 4.17. This is a two-degrees-of-freedom controller, because the controller receives two inputs: the measurement y and the reference r.

The design parameters that are chosen are the weighting matrices $\mathbf{Q}$ and R. The matrix $\mathbf{Q}$ is chosen to weight the effects of the states on the cost function, and the matrix R is chosen to weight the effects of the input on the cost function. Therefore, giving R a larger relative magnitude will result in control inputs affecting the cost function more strongly, and so control inputs will be kept small by the controller. This tends to reduce the gain of the controller, favouring small control signals and allowing larger deviations in the states. Similarly, setting large values in the elements of $\mathbf{Q}$ that correspond to a certain state will cause the controller to emphasise keeping that particular state small.

The objectives of the horizontal velocity controller are to ensure step commands are tracked with zero steady-state error, to add damping to the residual swinging of the suspended payload, and to ensure adequate trajectory tracking bandwidth. In previous projects where the SLADe quadrotor was used, velocity controllers that gave a closed-loop bandwidth of approximately 0.7 rad/s were successfully used in practical flights. However, the quadrotor was not carrying a suspended payload at that time. Therefore, we set a closed-loop bandwidth of 0.7 rad/s as a design goal.

With these design goals in mind, the following process was used to select the weighting matrices $\mathbf{Q} = [0.1, 0.11, 0.1, 0, 0, 0, 0, 0.8]^T$ and $R = 0.0625$:

- The diagonal element of $\mathbf{Q}$ corresponding to the error integral state, x_I, was given a relatively large magnitude to emphasize the steady-state tracking of step commands.
- The diagonal element of $\mathbf{Q}$ corresponding to the payload angle state, θ_L, was given a relatively small magnitude to allow large swing angles. Large swing angles are necessary for high bandwidth trajectory tracking of the quadrotor velocity
- The diagonal element of $\mathbf{Q}$ corresponding to quadrotor velocity state, $\dot{x}$, was given a relatively small magnitude to allow high quadrotor velocities.
- The diagonal element of $\mathbf{Q}$ corresponding to the payload angular rate state, $\dot{\theta}_L$, was given a relatively large magnitude in order to increase the damping of the swinging motion of the payload. In other words, the controller will act to prevent large payload angular rates, which increases the damping of the swinging motion.
- The scalar weight R was chosen to ensure efficient actuator usage.

A trial-and-error approach was used to converge on the values of $\mathbf{Q}$ and R given above. The frequency response of the resulting controller from a measurement $y = \dot{x}$ to a controller output $u = \tau_{x_R}$ is shown in Figure 4.19.

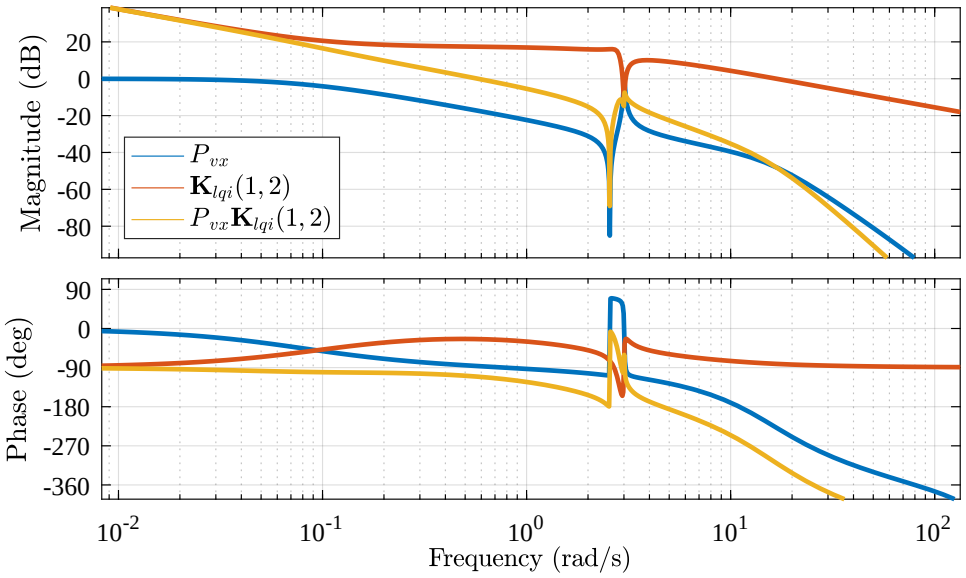

Figure 4.19: Bode plot of open-loop uncompensated plant P_{vx}, the transfer function from y to u of the linear quadratic controller, which is denoted $\mathbf{K}_{lqi}(1,2)$, and the compensated system $P_{vx}\mathbf{K}_{lqi}(1,2)$.

The controller contains a notch at the resonant frequency of the plant, due to the estimator. The severity of this notch is strongly governed by the ratio of expected plant disturbances to measurement noise. This is because the estimator gain $\mathbf{L}$ depends on this ratio. Also, the target bandwidth of 0.7 (rad/s) was achieved, and a slope of -20dB per decade in the low frequency region is achieved. Therefore, this design meets the design objectives.

The closed-loop step response of the horizontal velocity controller is shown in Figure 4.20. The same step response, but with variations in the uncertain parameters thrust scalar T_t, payload mass M_L, and cable length L included, is also shown in Figure 4.20. The uncertain parameters were varied over their entire ranges, so the set of resulting plots indicates the behaviour of the system with arbitrary combinations of these parameters. The plot shows that in the nominal case, the system responds with a rise time of about 3 seconds, which is similar to values achieved by the velocity control system used in previous projects with the SLADe [72]. This is a result of achieving the target bandwidth of 0.7 (rad/s).

Also, in the nominal response, the linear quadratic integral controller manages to add damping to the swinging motion of the payload, as is verified in the next subsection. Oscillations are seen on the quadrotor velocity, but these oscillations are removed after approximately 15 seconds.

When the system uncertainties are considered, the addition of damping to the payload swinging motion is severely compromised for cases where the exact quadrotor thrust, payload mass and cable length are not known. This is shown via the Monte Carlo simulation of the linear plant with varying values for these parameters. Clearly, the linear quadratic integral controller fails to produce a stable response for all the possible plants in the uncertainty set. This is to be expected from the pole-zero cancellation between the plant and controller. When the plant parameters are varied, the lightly damped plant open-loop poles are shifted, reducing the pole-zero cancellation effect of the LQI controller.

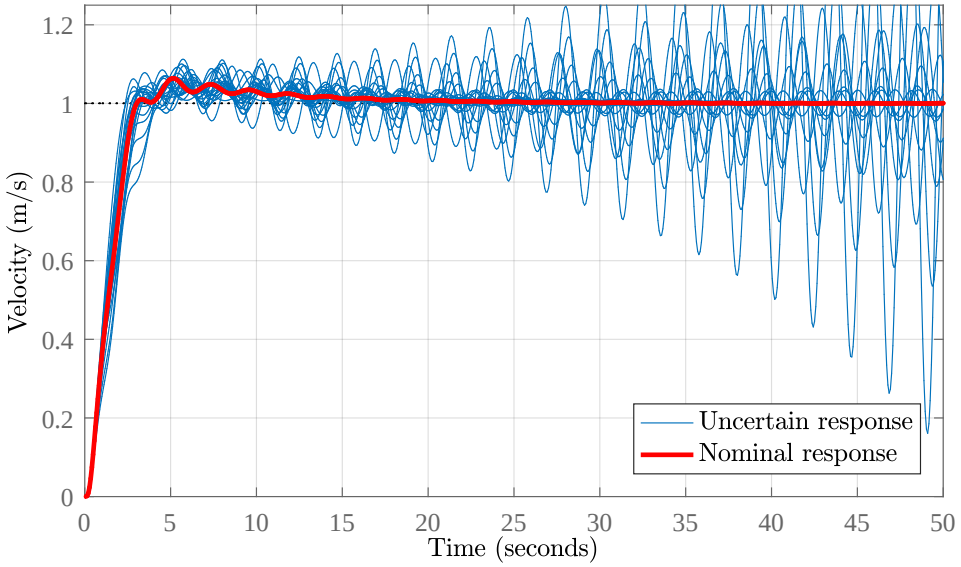

Figure 4.20: Step response of closed-loop system with LQI controller to a horizontal velocity command

A Monte Carlo style plot of the poles and zeros of the closed-loop system with the LQI controller is shown in Figure 4.21. This plot shows the poles and zeros of the closed-loop system when various plants in the uncertainty set are sampled. Also shown are the poles and zeros of the nominal, uncompensated, open-loop plant P_{vx}. Clearly, there are closed-loop systems in the closed-loop uncertainty set that have poles in the right-half plane of the complex plane, confirming that the system does not have robust stability.

Monte Carlo style Bode plots of the open- and closed-loop system with the LQI controller are given in Figure 4.22 and Figure 4.23, respectively. It is clear from these figures that when the uncertainty in the plant is considered, the

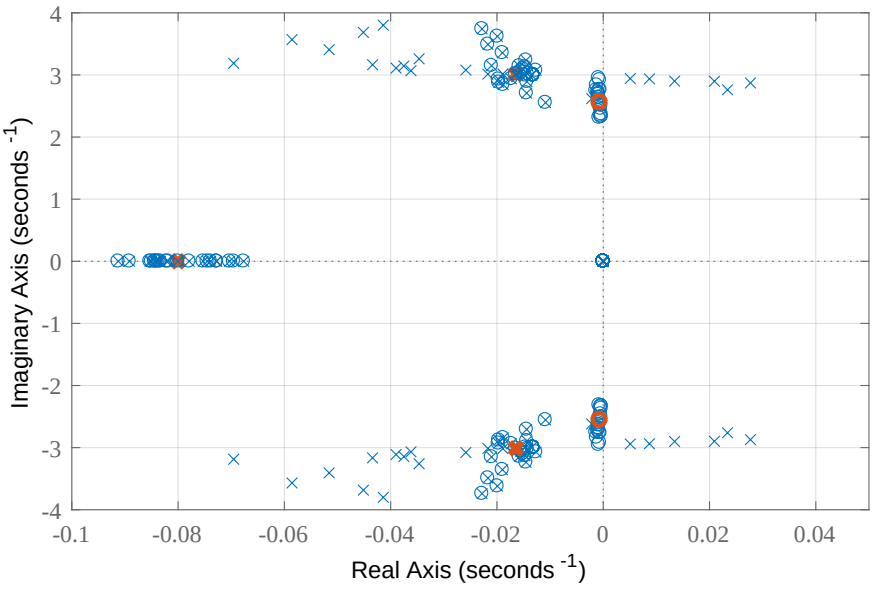

Figure 4.21: Poles and zeros of velocity control system with LQI controller. $\times$ is used to mark poles, and $\circ$ is used to mark zeros. Also shown are poles and zeros of the nominal open-loop system P_{vx}, shown in red.

frequency of the lightly-damped resonant mode of the system is shifted. The LQI controller fails to prevent the entire set of resonant peaks from reaching the 0 dB point, which is further evidence of instability.

4.3.4 Simulation Results with Benchmark Controller

The LQI-based quadrotor and payload translational control system was implemented and verified using the high-fidelity non-linear simulation, as shown in Figure 4.13. The closed-loop step response of the horizontal velocity controller is shown in Figure 4.24, along with the nominal response of the linear model P_{vx}. The horizontal velocity step response was performed in the North direction (but could also have been performed in the East direction with a similar result). The references for the East and vertical velocity controllers were set to zero, and these other two translational controllers therefore acted only to regulate the East and vertical velocities to zero, and to reject external disturbances. A velocity reference of $x_R = 3\ m/s$ was given at $t = 1$ second, followed by a velocity reference of $x_R = 0\ m/s$ given at $t = 10$ seconds.

This figure shows that there is good agreement between the response of the linearised model and the simulation. When the nominal values of the plant parameters thrust scalar T_t, payload mass M_L, and cable length L are consid-

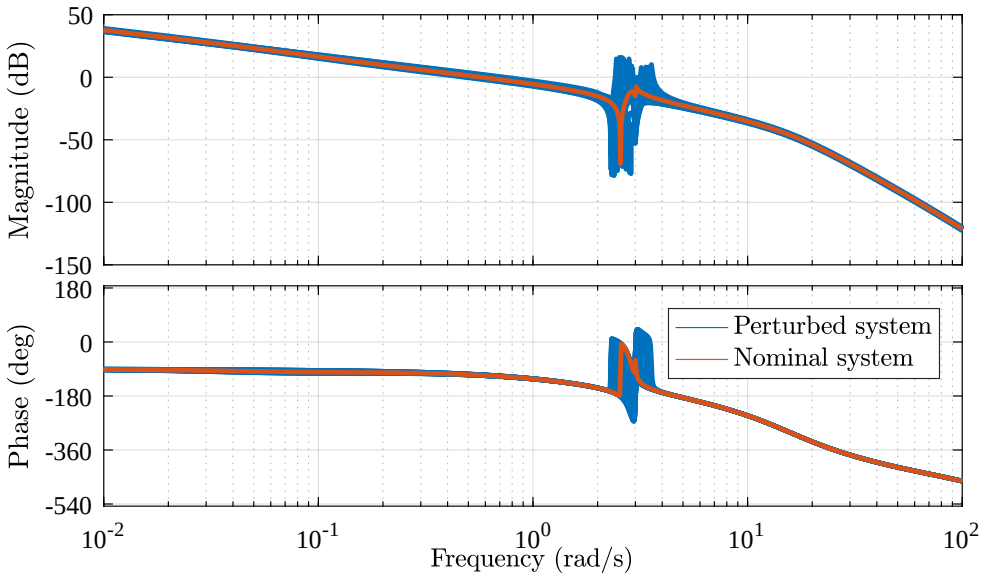

Figure 4.22: Bode plot of open-loop system with LQI controller. Also shown are the responses with perturbed plants from the uncertainty set.

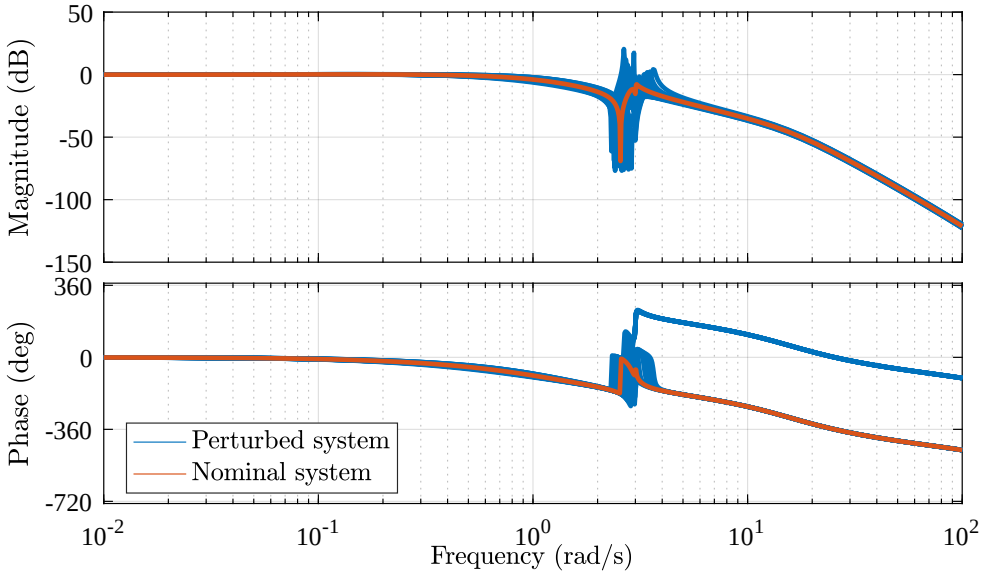

Figure 4.23: Bode plot of closed-loop system with LQI controller. Also shown are the responses with perturbed plants from the uncertainty set.

ered, the payload swinging motion is fairly damped when compared to the case

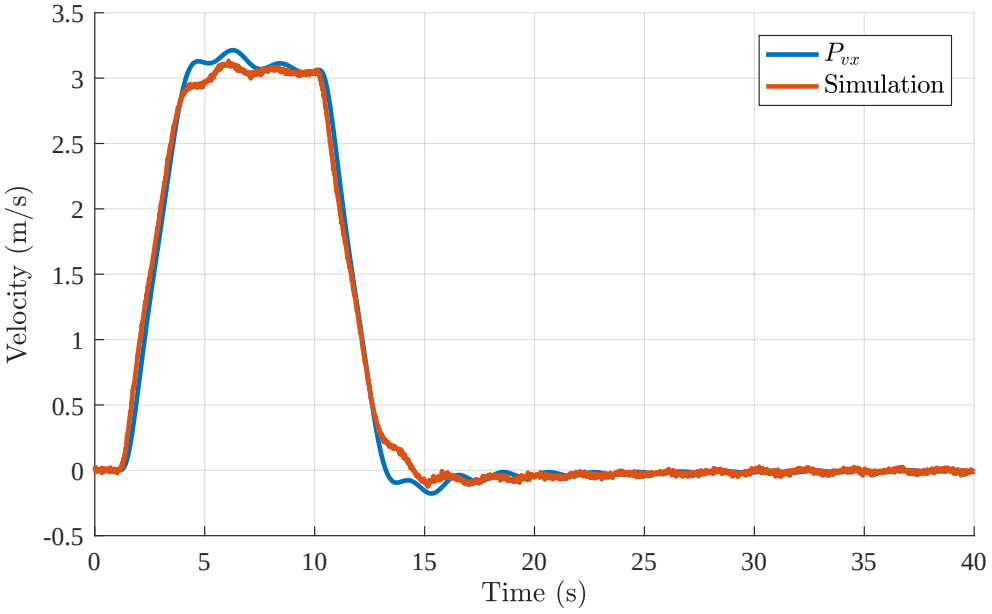

Figure 4.24: Response of quadrotor velocity $\dot{x}$ to a reference velocity command $\dot{x}_R$, with LQI controller. Also shown is the response of the linear model P_{vx} to the same reference input.

with no feedback controller, which is shown in Figure 3.12 and Figure 3.13.

The resulting payload swing angle θ_L from the simulation is shown in Figure 4.25 (with no motion in the East direction, $\phi_L \approx 0$). Clearly, there is some damping added to the payload swinging motion, which was a design objective.

A Monte Carlo simulation was performed using the high-fidelity simulation. The uncertain parameters in the plant were varied, and the same quadrotor velocity command was given to the controller. The results for the quadrotor velocity are given in Figure 4.26. The results for the payload angle θ_L are given in Figure 4.27. With the Monte Carlo simulation, we see that stability for all the plants in the uncertainty set is not guaranteed. This agrees with the results shown in Figure 4.20, and we identify that the system does not have robust stability.

A simulation with non-zero quadrotor velocity commands in North, East, and Down directions was performed. In this case, to maintain clarity of the figures, only a perturbed case with $M_L = 6$kg, $L = 1.7$m and $T = 1.2$ was simulated. The quadrotor velocity is plotted in Figure 4.28. The payload angles are plotted in Figure 4.29. We see very similar performance compared to the case when a non-zero velocity command in the North direction only was given. This confirms the assumption that the coupling between the three inertial directions (and associated payload angles) in the system is fairly weak and that

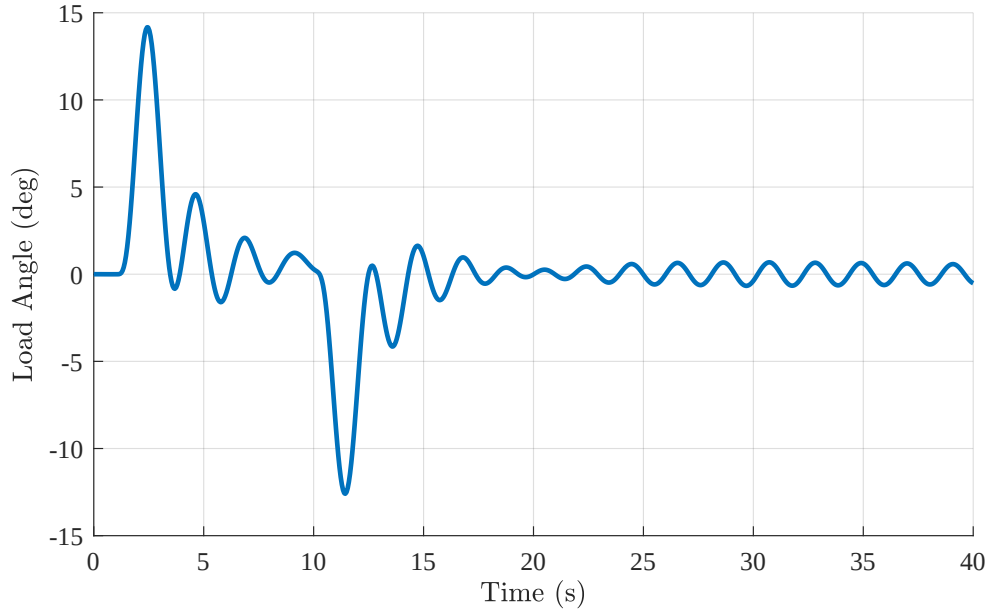

Figure 4.25: Response of payload angle θ_L to the same reference velocity command $\dot{x}_R$, with LQI controller.

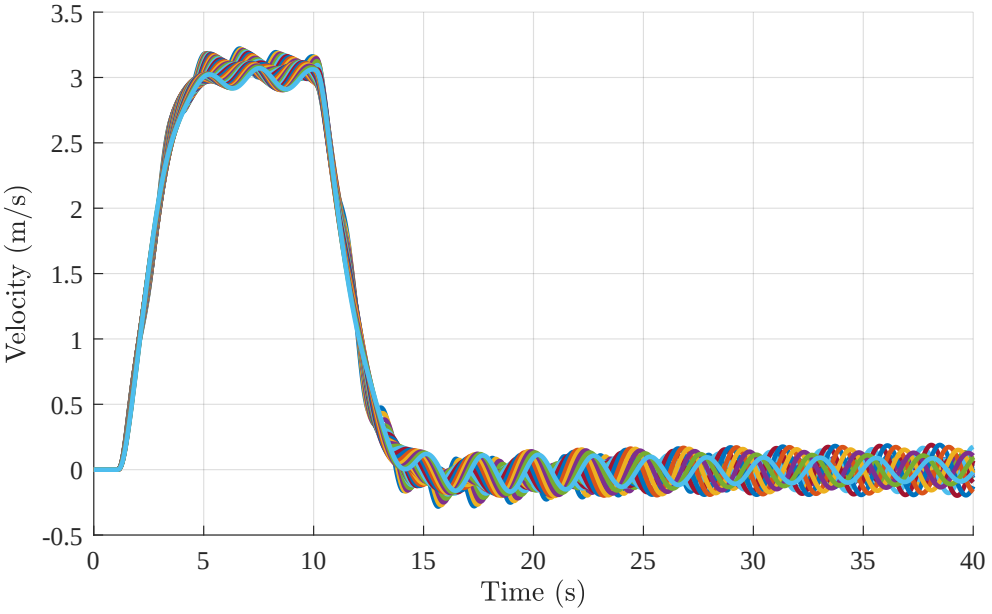

Figure 4.26: Monte Carlo simulation of quadrotor velocity $\dot{x}$, with LQI controller, using high-fidelity simulation

consequentially, the decoupled control design approach is valid. Also, we note

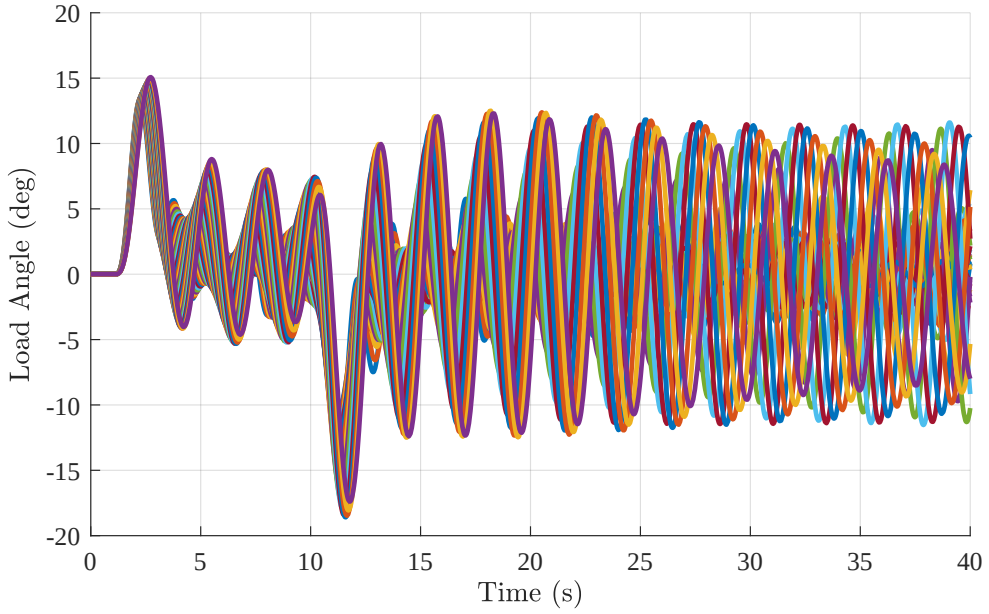

Figure 4.27: Monte Carlo simulation of payload angle θ_L, with LQI controller, using high-fidelity simulation

that the vertical velocity controller is successfully rejecting the disturbances introduced into the vertical dynamics by the tilt angle system.

4.4 Summary

In this chapter, the architecture and design of a benchmark LQR-based flight control system for a quadrotor with suspended payload was presented. The architecture is a cascaded control system, using successive loop closure to form inner and outer control loops. This methodology is very common in aerospace systems.

A unique force-based inner-loop control system was presented, where reference force commands are used to determine a desired quadrotor attitude. A tilt angle controller that allows tracking of reference inertial forces was presented. This is an adaptation of the acceleration-based control architecture presented in earlier research by the author [5].

Finally, an LQR-based outer-loop quadrotor and payload translational controller was presented. This controller achieved similar transient performance when compared to the velocity controllers used by Möller for the SLADe quadrotor to perform automated landing on a moving platform [72].

The benchmark LQI-based flight control system is able to control the quadrotor

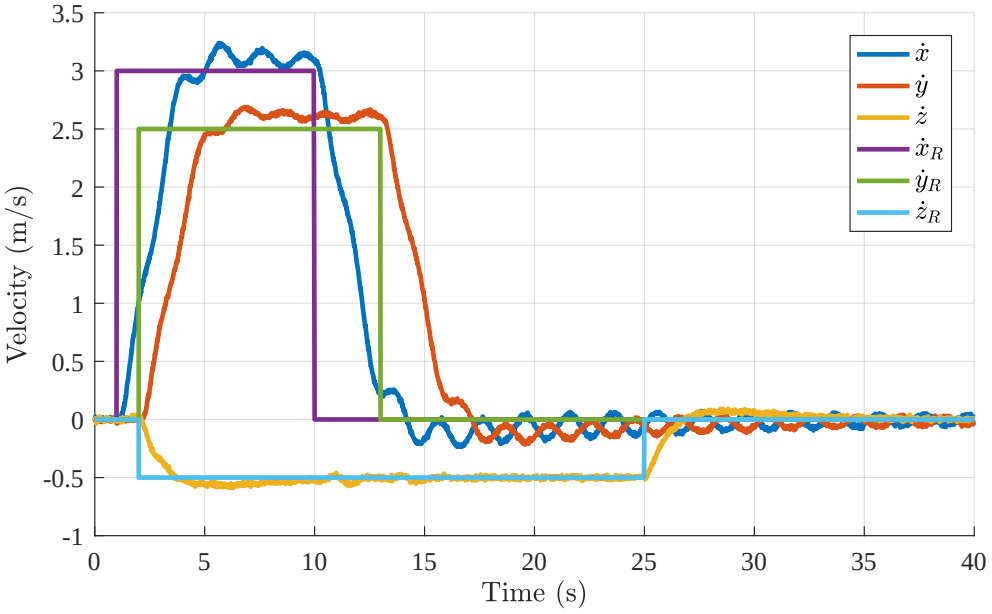

Figure 4.28: Response of quadrotor velocity $\dot{\mathbf{p}}$ to a reference velocity command $\dot{\mathbf{p}}_R$, with LQI controller. In this simulation, the uncertain plant parameters are set to $M_L = 6\text{kg}$, $L = 1.7\text{m}$ and $T_t = 1.2$.

with suspended payload to follow velocity reference commands, and provides satisfactory stability and dynamic response for the nominal plant. However, when uncertainty is introduced into the quadrotor thrust, payload mass, and cable length, the benchmark controller exhibits lightly damped behaviour and instability. This motivates the need for a robust control system that can achieve similar transient response as the benchmark control system in terms of rise time, while ensuring robust stability in the presence of the uncertainties.

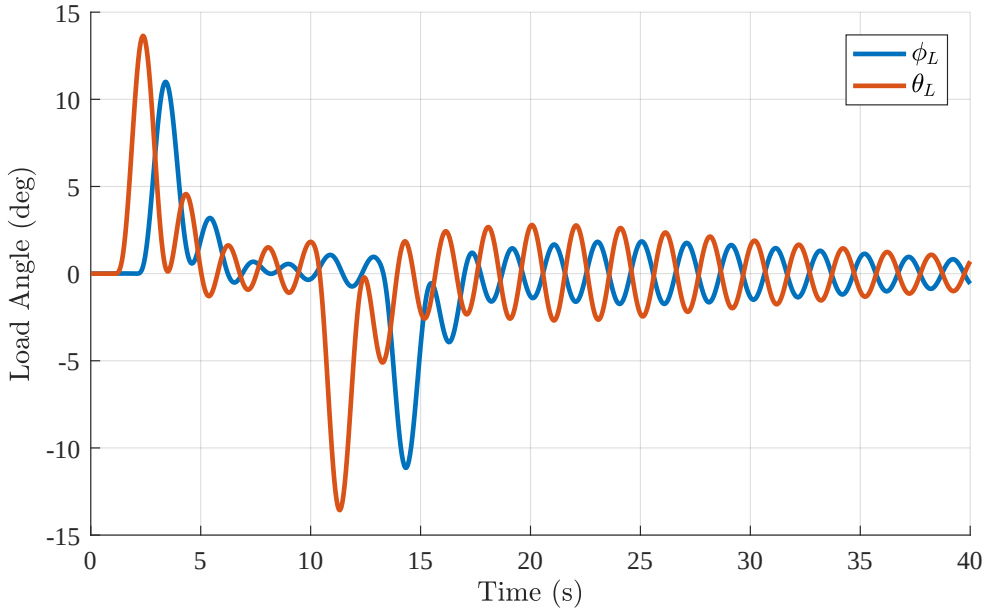

Figure 4.29: Response of payload angle ϕ_L and θ_L to a reference velocity command $\dot{\mathbf{p}}_R$, with LQI controller. In this simulation, the uncertain plant parameters are set to $M_L = 6\text{kg}$, $L = 1.7\text{m}$ and $T_t = 1.2$.

Chapter 5

H_∞ Robust Control Design

This chapter presents some of the main theoretical concepts regarding H_∞ control that are used to design a robust flight control system for the quadrotor and suspended payload. Some of these concepts are then used to design an H_∞ loop shaping controller for control of the quadrotor velocity. The relationship between H_∞ loop shaping and the ν-gap metric is presented, and a robust stability analysis is performed on the resulting system with the H_∞ loop shaping controller.

5.1 Overview of H_∞ Loop Shaping Approach

The H_∞ loop shaping technique is a robust control design technique that first shapes the open-loop transfer function $P_s(s)$ to achieve the performance specifications for the feedback control system, and then synthesises a feedback controller $K(s)$ that reduces the sensitivity of the closed-loop system towards uncertainties in the system.

The H_∞ loop shaping technique synthesises the controller $K(s)$ to robustify the closed-loop system without using explicit knowledge of the plant uncertainty. The synthesis of $K(s)$ is performed based only on the shaped nominal plant $P_s(s)$, with the objective of minimising the sensitivity of the closed-loop system to input and output disturbance signals. The premise is that the uncertainty in the plant may be parameterised as coprime factor uncertainty, which can be considered to be a sensible combination of multiplicative and inverse multiplicative uncertainty. Also, it can be shown that the controller that minimises the sensitivity of the closed-loop system to input and output disturbance signals is also the controller that adds robustness against comprime factor uncertainty. Therefore, the controller $K(s)$ minimises the gains of the closed-loop transfer functions from the disturbance signals to certain output signals, thereby minimizing the sensitivity of the closed-loop system to

these disturbance signals. This implicitly optimises the robust stability of the closed-loop system to the plant uncertainty parameterised as coprime factor uncertainty.

5.2 Robust Control Theory

In this section we highlight the theoretical tools that will be used to design a robust flight control system for the quadrotor and suspended payload. The majority of the presentation is based on the works of Zhou et al. [73], [74], and Vinnicombe [75].

5.2.1 H_∞ Control

We now describe a general H_∞ control problem and show how H_∞ optimization can be used to synthesize controllers.

5.2.1.1 General Problem Formulation

A general control system formulation is shown in Figure 5.1.

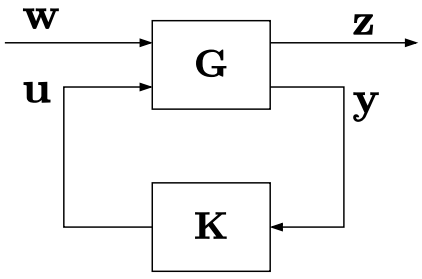

Figure 5.1: General Control Configuration

This is a control architecture into which many control problems can be cast. In this configuration $\mathbf{G}(s)$ is an open-loop plant that receives input signals $\mathbf{w}$ and $\mathbf{u}$, and has the signals $\mathbf{z}$ and $\mathbf{y}$ as outputs. In general:

- $\mathbf{u}$ is the set of input signals that can be actuated by the controller
- $\mathbf{w}$ is the set of exogenous input signals, including reference signals and disturbance signals
- $\mathbf{y}$ is the set of output signals that are measured and used for feedback control

– $\mathbf{z}$ is the set of regulated output signals, including error signals and control signals

Note that $\mathbf{u}$, $\mathbf{y}$, and $\mathbf{z}$ are not exclusive sets. For example, the control signal $\mathbf{u}$ may be a regulated output and therefore form part of the signal $\mathbf{z}$, or the plant output used for feedback, $\mathbf{y}$, may also be a regulated output and therefore also form part of $\mathbf{z}$.

The objective of H_∞ control design is to synthesise a controller $\mathbf{K}(s)$ for the plant $\mathbf{G}(s)$ so that the closed-loop transfer function from $\mathbf{w}$ to $\mathbf{z}$, denoted $\mathbf{T}_{zw}(s)$, satisfies some frequency-domain specifications. This is done by minimizing the following H_∞ norm:

$$\min_{\mathbf{K}} ||\mathbf{T}_{zw}||_\infty \tag{5.2.1}$$

where $||\mathbf{T}_{zw}||_\infty$ is the H_∞ norm of the stable and causal system $\mathbf{T}_{zw}$. A discussion of signal and system norms is presented in Appendix A. Some examples of closed-loop systems whose H_∞ norm one may wish to minimize are:

– The closed-loop transfer function from the reference signal $R(s) \in \mathbf{w}$ to the error signal $E(s) \in \mathbf{z}$ determines the ability of the feedback control system to track reference signals.

– The closed-loop transfer function from a disturbance signal $W(s) \in \mathbf{w}$ to the error signal $E(s) \in \mathbf{z}$ determines the ability of the feedback control system to reject disturbance signals.

– The closed-loop transfer function from the reference signal $R(s) \in \mathbf{w}$ or from a disturbance signal $W(s) \in \mathbf{w}$ to the control signal $U(s) \in \mathbf{z}$ determines the control effort used by the feedback control system.

A closed-loop system $\mathbf{T}_{zw}(s)$ is related to the plant $\mathbf{G}(s)$ and the controller $\mathbf{K}(s)$ through a lower linear fractional transformation (LFT). To define a lower LFT, partition the plant $\mathbf{G}$ as follows:

$$\left[\begin{array}{c} \mathbf{z} \\ \hdashline \mathbf{y} \end{array}\right] = \left[\begin{array}{cc} \mathbf{G}_{11} & \mathbf{G}_{12} \\ \mathbf{G}_{21} & \mathbf{G}_{22} \end{array}\right] \left[\begin{array}{c} \mathbf{w} \\ \hdashline \mathbf{u} \end{array}\right] \tag{5.2.2}$$

Then a lower LFT of $\mathbf{G}(s)$ and $\mathbf{K}(s)$ is

$$F_l(\mathbf{G}, \mathbf{K}) := \mathbf{G}_{11} + \mathbf{G}_{12}\mathbf{K}(\mathbf{I} - \mathbf{G}_{22}\mathbf{K})^{-1}\mathbf{G}_{21} = \mathbf{T}_{zw}(s) \tag{5.2.3}$$

For a given plant $\mathbf{G}$, state space formula to solve the problem in Equation 5.2.1 are given in Appendix A.

The H_∞ control design method attempts to achieve the frequency-domain specifications for the closed-loop transfer functions by minimising the H_∞ norm of the closed-loop transfer functions multiplied by frequency-domain performance weights. To see the usefulness of solving such a problem, consider a closed-loop system $\mathbf{S}$ and a performance weight $\mathbf{W}_p$. Ensuring that the H_∞-norm of $\mathbf{W}_p\mathbf{S}$ is less than a real parameter $\gamma > 0$ results in

$$||\mathbf{W}_p\mathbf{S}||_\infty < \gamma, \tag{5.2.4}$$

$$\Leftrightarrow \quad \bar{\sigma}(\mathbf{W}_p\mathbf{S}) < \gamma, \forall w \quad \Leftrightarrow \quad \bar{\sigma}(\mathbf{S}(jw)) < \gamma/\bar{\sigma}(\mathbf{W}_p(jw)), \forall w. \tag{5.2.5}$$

Therefore, setting $\gamma = 1$, $1/\bar{\sigma}(\mathbf{W}_p(jw))$ becomes an upper bound on the maximum singular value of $\mathbf{S}(jw))$. $1/\bar{\sigma}(\mathbf{W}_p(jw))$ can therefore be selected to "shape" $\bar{\sigma}(\mathbf{S}(jw))$, allowing frequency-domain specifications for $\mathbf{S}$ to be met. In this case, we have that $\mathbf{T}_{zw} = \mathbf{W}_p\mathbf{S}$. A practical example of such an objective is discussed next.

5.2.1.2 Mixed-Sensitivity H_∞ Control

Consider the case where a plant $\mathbf{P}(s)$ is to be controlled by a feedback controller. A method to do so would be to impose frequency-domain specifications on the resulting closed-loop system using the H_∞ norm as described in the previous section. Using the same general control configuration from Figure 5.1, the system shown in Figure 5.2 can be obtained.

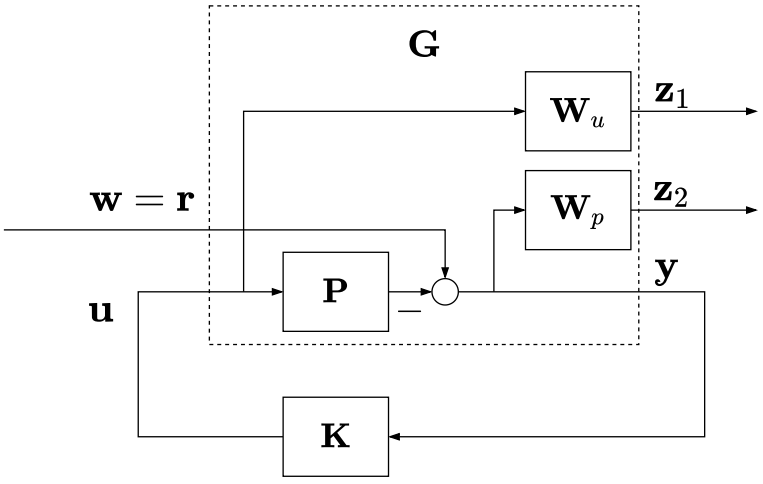

Figure 5.2: General control configuration with performance bounds

In this configuration, we have the performance weight $\mathbf{W}_u(s)$, which is the frequency-domain performance weight on the control effort, and the performance weight $\mathbf{W}_p(s)$, which is the frequency-domain performance weight on the transient response. The general system $\mathbf{G}$, which is the transfer function from $[\mathbf{w};\mathbf{u}]^T$ to $[\mathbf{z};\mathbf{y}]^T$, is found to be

$$\mathbf{G} = \begin{bmatrix} \begin{bmatrix} \mathbf{0} \\ \mathbf{W}_p\mathbf{I} \end{bmatrix} & \begin{bmatrix} \mathbf{W}_u\mathbf{I} \\ \mathbf{W}_p\mathbf{P} \end{bmatrix} \\ -\mathbf{I} & -\mathbf{P} \end{bmatrix} = \begin{bmatrix} \mathbf{G}_{11} & \mathbf{G}_{12} \\ \mathbf{G}_{21} & \mathbf{G}_{22} \end{bmatrix} \tag{5.2.6}$$

Applying a lower linear fractional transformation to $\mathbf{G}$ and $\mathbf{K}$ results in the transfer function $\mathbf{T}_{zw}$, as;

$$\mathbf{T}_{zw} = F_l(\mathbf{G},\mathbf{K}) := \mathbf{G}_{11} + \mathbf{G}_{12}\mathbf{K}(\mathbf{I} - \mathbf{G}_{22}\mathbf{K})^{-1}\mathbf{G}_{21} \tag{5.2.7}$$

Therefore, we have

$$\mathbf{T}_{zw} = \begin{bmatrix} \mathbf{0} \\ \mathbf{W}_p\mathbf{I} \end{bmatrix} + \begin{bmatrix} \mathbf{W}_u\mathbf{I} \\ \mathbf{W}_p\mathbf{P} \end{bmatrix} \mathbf{K}(\mathbf{I} + \mathbf{P}\mathbf{K})^{-1}(-\mathbf{I}) = \begin{bmatrix} -\mathbf{W}_u\mathbf{K}\mathbf{S} \\ \mathbf{W}_p\mathbf{S} \end{bmatrix} \tag{5.2.8}$$

where $(\mathbf{I} - \mathbf{G}_{22}\mathbf{K})^{-1} = (\mathbf{I} + \mathbf{P}\mathbf{K})^{-1} = \mathbf{S}_o(s) = \mathbf{S}(s)$ is the output sensitivity function. Then, the objective of the algorithm to synthesise an H_∞ optimal controller would be

$$\min_K ||\mathbf{T}_{zw}(\mathbf{K})||_\infty \tag{5.2.9}$$

.

The controller $\mathbf{K}(s)$ that minimises the H_∞ norm implicitly optimises the closed-loop transfer functions $\mathbf{S}(s)$ and $\mathbf{K}(s)\mathbf{S}(s)$ to achieve the design specifications represented by the performance weights. This form of controller synthesis is termed mixed-sensitivity H_∞ control, because it focuses on shaping the H_∞-norm of closed-loop sensitivity functions, such as $\mathbf{S}(s)$.

5.2.2 Uncertainty Descriptions

The uncertainty in the plant may be parameterised as right coprime factor uncertainty, as shown in Figure 5.3, where

- $\mathbf{P}_1(s) = \mathbf{N}(s)\mathbf{M}(s)^{-1}$ is the nominal plant
- $\mathbf{P}(s) = (\mathbf{N}(s) + \mathbf{\Delta}_N(s))(\mathbf{M}(s) + \mathbf{\Delta}_M(s))^{-1}$ is the perturbed plant

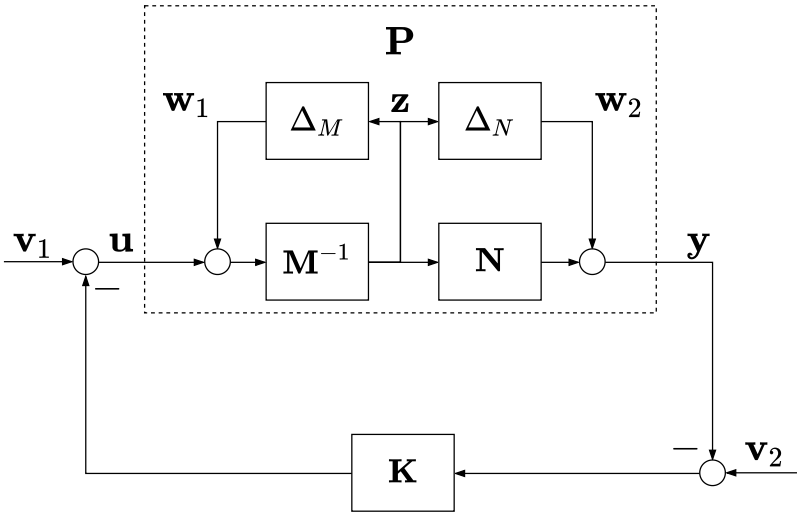

Figure 5.3: Coprime factor Uncertainty.

- $\mathbf{\Delta}_N(s)$ and $\mathbf{\Delta}_M(s)$ represent the uncertainties

Coprime factor uncertainty can be thought of as a sensible combination of multiplicative and inverse multiplicative uncertainty. It is a representation of uncertainty that overcomes the limitations of using only one of those types of uncertainty alone.

5.2.2.1 Coprime Factor Representations

Any real-rational transfer function $\mathbf{P}$ can be represented as the quotient of two real-rational functions in H_∞, such as

$$\mathbf{P}(s) = \mathbf{N}(s)\mathbf{M}(s)^{-1}, \mathbf{M}, \mathbf{N} \in H_\infty$$

which is a right factorisation of $\mathbf{P}$. There are many of these factorisation, but the set is reduced when we only consider coprime factorisations:

Definition 5.1: *Given* $\mathbf{M}, \mathbf{N} \in H_\infty$, $\mathbf{M}$ *and* $\mathbf{N}$ *are right-coprime if there exists* $\mathbf{X}, \mathbf{Y} \in H_\infty$ *such that*

$$\mathbf{XM} + \mathbf{YN} = \mathbf{I}$$

Definition 5.2: *The pair* $\mathbf{M}, \mathbf{N} \in H_\infty$ *is a right-coprime factorisation (rcf) of real-rational function* $\mathbf{P}$ *if*

i $\mathbf{M}$ *is invertible;*

ii $\mathbf{P} = \mathbf{N}\mathbf{M}^{-1}$:

iii $\mathbf{N}$ *and* $\mathbf{M}$ *are right-coprime.*

Definition 5.3: *Given the pair* $\mathbf{M}, \mathbf{N} \in H_\infty$ *is a normalised rcf of* $\mathbf{P}$ *if the pair is an rcf of* $\mathbf{P}$ *and*

$$\mathbf{M}^*\mathbf{M} + \mathbf{N}^*\mathbf{N} = \mathbf{I}$$

We can summarise the three definitions as: An ordered pair $\mathbf{N}, \mathbf{M}$ is a normalised rcf of $\mathbf{P}$ if $\mathbf{P} = \mathbf{N}\mathbf{M}^{-1}$ and there exists real-rational $\mathbf{X}, \mathbf{Y} \in H_\infty$ such that

$$\mathbf{X}\mathbf{M} + \mathbf{Y}\mathbf{N} = \mathbf{I}$$

$$\mathbf{M}^*\mathbf{M} + \mathbf{N}^*\mathbf{N} = \mathbf{I}.$$

Similarly, an ordered pair $\bar{\mathbf{N}}, \bar{\mathbf{M}}$ is a normalised left-coprime factorisation (lcf) of $\mathbf{P} = \bar{\mathbf{M}}^{-1}\bar{\mathbf{N}}$ and there exists real-rational transfer function $\bar{\mathbf{X}}, \bar{\mathbf{Y}} \in H_\infty$ such that

$$\bar{\mathbf{M}}\bar{\mathbf{X}} + \bar{\mathbf{N}}\bar{\mathbf{Y}} = \mathbf{I}$$

$$\bar{\mathbf{N}}\bar{\mathbf{N}}^* + \bar{\mathbf{M}}\bar{\mathbf{M}}^* = \mathbf{I},$$

and in this case $\bar{\mathbf{N}}, \bar{\mathbf{M}}$ are said to be left-coprime. Lastly, if a realisation of $\mathbf{P}$ is given as

$$\mathbf{P} \stackrel{s}{=} \left[\begin{array}{c|c} \mathbf{A} & \mathbf{B} \\ \hline \mathbf{C} & \mathbf{D} \end{array}\right]$$

then it is well known that

$$\begin{bmatrix} \bar{\mathbf{N}} & \bar{\mathbf{M}} \end{bmatrix} \stackrel{s}{=} \left[\begin{array}{c|cc} \mathbf{A}+\mathbf{L}\mathbf{C} & \mathbf{B}+\mathbf{L}\mathbf{D} & \mathbf{L} \\ \hline \mathbf{R}^{-1/2}\mathbf{C} & \mathbf{R}^{-1/2}\mathbf{D} & \mathbf{R}^{-1/2} \end{array}\right] \tag{5.2.10}$$

is a normalised left coprime factorisation of $\mathbf{P}$, where $\mathbf{L} := -(\mathbf{B}\mathbf{D}^T + \mathbf{Z}\mathbf{C}^T)\mathbf{R}^{-1}$ and $\mathbf{R} := \mathbf{I} + \mathbf{D}\mathbf{D}^T$. The matrix $\mathbf{Z} \geq 0$ is the unique stabilisation solution to the algebraic Riccati equation

$$(\mathbf{A} - \mathbf{B}\mathbf{S}^{-1}\mathbf{D}^T\mathbf{C})\mathbf{Z} + \mathbf{Z}(\mathbf{A} - \mathbf{B}\mathbf{S}^{-1}\mathbf{D}^T\mathbf{C})^T - \mathbf{Z}\mathbf{C}^T\mathbf{R}^{-1}\mathbf{C}\mathbf{Z} + \mathbf{B}\mathbf{S}^{-1}\mathbf{B}^T = \mathbf{0} \tag{5.2.11}$$

where $\mathbf{S} := \mathbf{I} + \mathbf{D}^T\mathbf{D}$. This algebraic Riccati is known as the generalised filter algebraic Riccati equation, and is an important component in robust stabilisation, which is discussed in a subsequent section.

5.2.2.2 Uncertainty Descriptions

This section will discuss the primary uncertainty description tools that will be used in this study.

Principle of the argument

Denote the number of open right half plane (RHP) poles of a function $g(s)$ as $\eta(g(s))$. Denote the number of open RHP zeros of $g(s)$ as $\zeta(g(s))$. Further, denote the winding number of $g(s)$, which is the number of counterclockwise encirclements around the origin as $g(s)$ is evaluated on a Nyquist contour, as $\text{wno}(g)$. The principle of the argument is

$$\text{wno}(g(s)) = \zeta(g(s)) - \eta(g(s)) \tag{5.2.12}$$

If we consider a square, non-singular, real rational transfer function matrix $\mathbf{G}(s)$, then the principle of the argument can be stated as

$$\text{wno}\det(\mathbf{G}(s)) = \zeta(\mathbf{G}(s)) - \eta(\mathbf{G}(s)) \tag{5.2.13}$$

where the poles and zeros of $\mathbf{G}(s)$ are evaluated in the usual multi-variable sense. As will be seen in the next section, certain restrictions on uncertainty descriptions can be replaced by allowing greater sets of uncertainty and relying on winding number contraints to ensure stability. These are considered homotopy arguments for robust control, and will be used in the next section.

Robust stability tools

The small gain theorem is commonly used to ensure robust stability in a feedback system. The small gain theorem can be stated as:

Small-gain theorem *Given real-rational* $\mathbf{M} \in H_\infty$, *the following are equivalent:*

i *The feedback system shown in Figure 5.4 is stable for all* $\mathbf{\Delta} \in H_\infty$ *for which the system is well-posed and* $||\mathbf{\Delta}||_\infty < 1$.

ii *The feedback system shown in Figure 5.4 is stable for all* $\mathbf{\Delta} \in H_\infty$ *that satisfy* $||\mathbf{\Delta}||_\infty < 1$.

iii $||\mathbf{M}||_\infty < 1$.

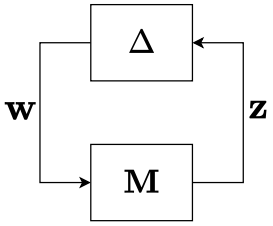

Figure 5.4: $\mathbf{M\Delta}$ used for robust stability analysis

The proof of the theorem, as well as some variations of, can be found in any text on robust control. In all cases, the principle behind the theorem is preventing the condition $\det(\mathbf{I} - \mathbf{M\Delta}) = 0$ as a Nyquist contour is traced around the right-half plane. Intuitively, the small gain theorem can be understood simply by stating that if both $\mathbf{M}$ and $\mathbf{\Delta}$ are stable, then one way to ensure that the feedback loop of $\mathbf{M}$ and $\mathbf{\Delta}$ is stable is to ensure that the loop gain at all frequencies and in all directions is less than one, which the theorem implies.

A key point from this theorem is that the small-gain theorem relies on considering the bounds of stable perturbations, i.e. perturbations of the form $\mathbf{\Delta} \in H_\infty$. Alternatively, homotopy arguments allow perturbations that are only bounded on the imaginary axis, i.e. perturbations of the form $\mathbf{\Delta} \in L_\infty$. To account for the fact that the perturbations are not stable and can introduce poles in the right-half plane, additional winding number conditions (from the principle of the argument) are used to ensure stability of the feedback structure shown in Figure 5.4. We will see such winding number restrictions in the next section, which discusses the chosen form of uncertainty representation.

Coprime factor uncertainty

Coprime factor uncertainty takes the form

$$\mathbf{P} = (\mathbf{N} + \mathbf{\Delta}_N)(\mathbf{M} + \mathbf{\Delta}_\mathbf{M})^{-1} : \left|\left| \begin{bmatrix} \mathbf{\Delta}_N \\ \mathbf{\Delta}_\mathbf{M} \end{bmatrix} \right|\right|_\infty < \frac{1}{\gamma}$$

where $\mathbf{P}_1 = \mathbf{N}\mathbf{M}^{-1}$ is a normalised rcf of $\mathbf{P}_1$ and $\gamma > 1$. Here, $\mathbf{P}_1$ is the nominal plant. In a feedback configuration, right coprime factor uncertainty can be shown as in Figure 5.5.

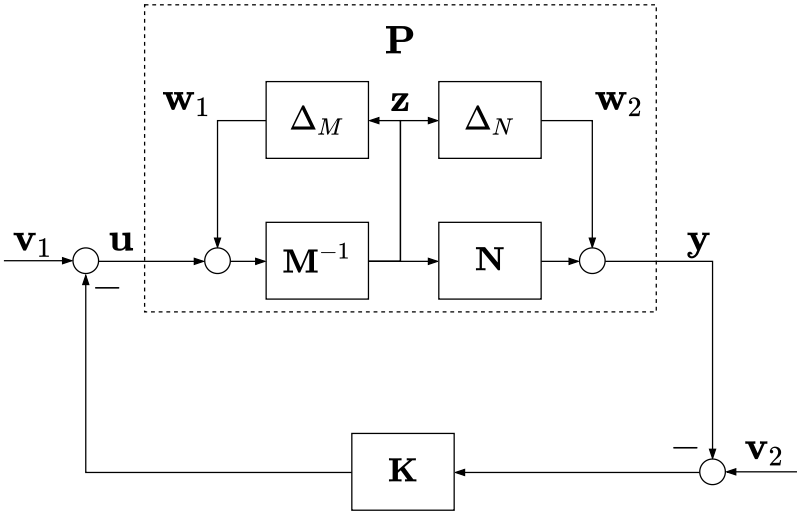

Figure 5.5: Coprime factor uncertainty.

Coprime factor uncertainty is seen as a sensible combination of multiplicative and inverse multiplicative uncertainty. In fact, Vinnicombe [75] provides a thorough argument as to why coprime factor uncertainty is in fact the least restrictive uncertainty representation, when compared to the other standard uncertainty configurations such as additive, multiplicative, and inverse multiplicative representations. For example, for a system to have robust stability, a representation using additive uncertainty does not allow for the number of RHP poles between the nominal plant and perturbed plant to change, and this is a fundamental issue with that form of representation. Multiplicative and inverse multiplicative uncertainty representations also have their own limitations. Therefore, based on the arguments in favour of coprime factor uncertainty presented by Vinnicombe [75], it is the chosen form of uncertainty representation in this study.

In order to put the system into the configuration shown in Figure 5.4, the transfer function from $\mathbf{w}$ to $\mathbf{z}$ is

$$\mathbf{z} = \mathbf{M}^{-1}(\mathbf{I} - \mathbf{K}\mathbf{P})^{-1} \begin{bmatrix} \mathbf{K} & \mathbf{I} \end{bmatrix} \begin{bmatrix} \mathbf{w}_2 \\ \mathbf{w}_1 \end{bmatrix}, \tag{5.2.14}$$

Application of the small-gain theorem gives:

Robust stability for feedback system with coprime factor uncertainty - small gain theorem: *Given real-rational plant* $\mathbf{P}_1$ *and controller* $\mathbf{K}$, *the following are equivalent:*

i *The feedback configuration shown in Figure 5.3 is stable for all* $\mathbf{P}$ *of the form*

$$\mathbf{P} = (\mathbf{N} + \mathbf{\Delta}_N)(\mathbf{M} + \mathbf{\Delta}_M)^{-1} : \begin{bmatrix} \mathbf{\Delta}_N \\ \mathbf{\Delta}_M \end{bmatrix} \in H_\infty, \left\| \begin{bmatrix} \mathbf{\Delta}_N \\ \mathbf{\Delta}_M \end{bmatrix} \right\|_\infty \leq \frac{1}{\gamma}, \\ \det(\mathbf{M} + \mathbf{\Delta}_M) \neq 0$$

ii *The nominal feedback system* ($\mathbf{\Delta} = 0$) *is stable and*

$$||\mathbf{M}^{-1}(\mathbf{I} - \mathbf{K}\mathbf{P}_1)^{-1} \begin{bmatrix} \mathbf{K} & \mathbf{I} \end{bmatrix}||_\infty < \gamma.$$

Application of homotopy arguments, as shown by Vinnicombe [75], gives

Robust stability for feedback system with coprime factor uncertainty - homotopy arguments: *Given real-rational plant* $\mathbf{P}_1$ *and controller* $\mathbf{K}$, *the following are equivalent:*

i *The feedback configuration shown in Figure 5.3 is stable for all* $\mathbf{P}$ *of the form*

$$\mathbf{P} = (\mathbf{N} + \mathbf{\Delta}_N)(\mathbf{M} + \mathbf{\Delta}_M)^{-1} : \begin{bmatrix} \mathbf{\Delta}_N \\ \mathbf{\Delta}_M \end{bmatrix} \in L_\infty, \left\| \begin{bmatrix} \mathbf{\Delta}_N \\ \mathbf{\Delta}_M \end{bmatrix} \right\|_\infty \leq \frac{1}{\gamma}, \\ \det(\mathbf{M} + \mathbf{\Delta}_M) \neq 0, \\ \eta(\mathbf{P}) = \text{wno}\det(\mathbf{M} + \mathbf{\Delta}_M)$$

ii *The nominal feedback system* ($\mathbf{\Delta} = 0$) *is stable and*

$$||\mathbf{M}^{-1}(\mathbf{I} - \mathbf{K}\mathbf{P}_1)^{-1} \begin{bmatrix} \mathbf{K} & \mathbf{I} \end{bmatrix}||_\infty < \gamma.$$

where wno($\mathbf{X}$) is used to denote the winding number of $\mathbf{X}$, as mentioned earlier.

In the first result (based on the small-gain theorem), we see perturbations in H_∞ only are allowed. In the second result (based on homotopy arguments), we see perturbations in L_∞ are allowed, and an additional winding number constraint $\eta(\mathbf{P}) = \text{wno}\det(\mathbf{M} + \mathbf{\Delta}_M)$ is added. The difference between the two sets is subtle, yet Vinnicombe [75] shows that any $\mathbf{P}$ in the set described in the second result will also be in the set of the form described in the first result, but for a smaller γ. This leads to two definitions, the latter of which will be used extensively in this project.

Definition 1: *Let* $\mathbf{P}_1 = \mathbf{N}\mathbf{M}^{-1}$ *be a normalised rcf. We define the directed gap-metric between* $\mathbf{P}_1$ and $\mathbf{P}_2$ *as*

$$\vec{\delta}_g(\mathbf{P}_1, \mathbf{P}_2) := \inf_{\begin{bmatrix} \mathbf{\Delta}_N \\ \mathbf{\Delta}_M \end{bmatrix} \in H_\infty} \left\{ \left\| \begin{bmatrix} \mathbf{\Delta}_N \\ \mathbf{\Delta}_M \end{bmatrix} \right\|_\infty : \mathbf{P}_2 = (\mathbf{N} + \mathbf{\Delta}_N)(\mathbf{M} + \mathbf{\Delta}_M)^{-1} \right\},$$

and the ν-gap metric as

$$\delta_v(\mathbf{P}_1, \mathbf{P}_2) := \inf_{\substack{\begin{bmatrix} \mathbf{\Delta}_N \\ \mathbf{\Delta}_M \end{bmatrix} \in L_\infty : \\ \eta(\mathbf{P}_2) = \text{wno}\det(\mathbf{M} + \mathbf{\Delta}_M).}} \left\{ \left\| \begin{bmatrix} \mathbf{\Delta}_N \\ \mathbf{\Delta}_M \end{bmatrix} \right\|_\infty : \mathbf{P}_2 = (\mathbf{N} + \mathbf{\Delta}_N)(\mathbf{M} + \mathbf{\Delta}_M)^{-1} \right\}$$

The ν-gap metric will always be smaller than the directed gap metric between two plants. Furthermore, the condition $\begin{bmatrix} \mathbf{\Delta}_N \\ \mathbf{\Delta}_M \end{bmatrix} \in H_\infty$ in the case of the directed gap guarantees the satisfaction of $\eta(\mathbf{P}_2) = \text{wno}\det(\mathbf{M}+\mathbf{\Delta}_M)$, because

$$\begin{aligned} \eta(\mathbf{P}_2) &= \eta((\mathbf{N} + \mathbf{\Delta}_N)(\mathbf{M} + \mathbf{\Delta}_M)^{-1}) \\ &= \eta(\mathbf{N} + \mathbf{\Delta}_N) + \eta((\mathbf{M} + \mathbf{\Delta}_M)^{-1}) \\ &= \text{wno}\det(\mathbf{M} + \mathbf{\Delta}_M) \end{aligned}$$

with $\eta(\mathbf{N} + \mathbf{\Delta}_N) = 0$ due to $(\mathbf{N} + \mathbf{\Delta}_N) \in H_\infty$, and $\eta((\mathbf{M} + \mathbf{\Delta}_M)^{-1}) = \zeta(\mathbf{M}+\mathbf{\Delta}_M) = \text{wno}\det(\mathbf{M}+\mathbf{\Delta}_M)$ due to $(\mathbf{M}+\mathbf{\Delta}_M) \in H_\infty$, so $\eta(\mathbf{M}+\mathbf{\Delta}_M) = 0$. The condition $\begin{bmatrix} \mathbf{\Delta}_N \\ \mathbf{\Delta}_M \end{bmatrix} \in H_\infty$ is sufficient, but it is not necessary for $\eta(\mathbf{P}_2) = \text{wno}\det(\mathbf{M} + \mathbf{\Delta}_M)$. This shows that the ν-gap metric is similar to the gap metric, but it has less restrictions on the perturbations. This allows for perturbations of a smaller norm (in the L_∞ sense) to represent the difference between two plants with the ν-gap metric than with the gap metric, which is why the ν-gap metric between two plants is always smaller than or equal to the gap metric. This motivates the use of the ν-gap metric, because it gives the tightest possible bounds for representing coprime factor uncertainty in a system.

By using either the small-gain theorem or by homotopy arguments, we have that in the face of coprime factor uncertainty $\left\| \begin{bmatrix} \mathbf{\Delta}_N \\ \mathbf{\Delta}_M \end{bmatrix} \right\|_\infty \leq \frac{1}{\gamma}$, we wish to ensure that

$$||\mathbf{M}^{-1}(\mathbf{I} - \mathbf{K}\mathbf{P}_1)^{-1} \begin{bmatrix} \mathbf{K} & \mathbf{I} \end{bmatrix}||_\infty < \gamma \tag{5.2.15}$$

in order to ensure robust stability. Importantly, this norm has to be taken in the H_∞ sense, as this transfer function needs to be in the function space H_∞ because it must be stable. Of course, the L_∞ norm and H_∞ norm of a function in H_∞ are equal due to the maximum modulus principle of complex analysis. The minimization of this norm will be elaborated on in the next section.

Lastly, another definition for the ν-gap metric is

ν-gap metric The ν-gap metric between two functions $\mathbf{P}_1$ and $\mathbf{P}_2$ is

$$\delta_\nu(\mathbf{P}_1, \mathbf{P}_2) = \left\{ \begin{array}{cc} ||\Phi(\mathbf{P}_1, \mathbf{P}_2)||_\infty & \text{if } \det(\mathbf{I} + \mathbf{P}_2^T\mathbf{P}_1) \neq 0 \text{ and} \\ & \text{wno } \det(\mathbf{I} + \mathbf{P}_2^T\mathbf{P}_1) + \eta(\mathbf{P}_1) \\ & -\eta(\mathbf{P}_2) - \eta_0(\mathbf{P}_2) = 0, \\ 1, & \text{otherwise} \end{array} \right\}$$

with

$$\Phi(\mathbf{P}_1, \mathbf{P}_2)(jw) = (\mathbf{I} + \mathbf{P}_2\mathbf{P}_2^T)^{-1/2}(\mathbf{P}_1 - \mathbf{P}_2)(\mathbf{I} + \mathbf{P}_1^T\mathbf{P}_1)^{-1/2}(jw)$$

Clearly,

$$\delta_\nu(\mathbf{P}_1, \mathbf{P}_2) = \sup_w \bar{\sigma}(\Phi(\mathbf{P}_1, \mathbf{P}_2))(jw)$$

provided the winding number condition is met. This definition of the ν-gap metric shows that it can be calculated from frequency response measurements between two plants.

In the next section, we will show that the ν-gap metric provides the basis for a unified treatment of robustness and performance. In particular, we will show that minimizing the H_∞ norm of certain closed-loop transfer functions improves nominal plant performance *and* provides robustness to uncertainties as measured by the ν-gap metric. This will form part of the H_∞ loop shaping framework, which will be discussed in the next section.

5.2.3 H_∞ Loop Shaping Design Theory

The H_∞ loop shaping technique is a robust control design technique that first shapes the open-loop transfer function $\mathbf{P}_s(s)$ to achieve the performance specifications for the feedback control system, and then synthesises a feedback controller $\mathbf{K}(s)$ to robustify the closed-loop system against coprime factor uncertainty.

First, pre- and post-compensating weights $\mathbf{W}_1(s)$ and $\mathbf{W}_2(s)$ are added to the plant $\mathbf{P}(s)$ to obtain the shaped plant

$$\mathbf{P}_s = \mathbf{W}_2\mathbf{P}\mathbf{W}_1 \tag{5.2.16}$$

The open-loop transfer function of the shaped plant is shaped to achieve frequency-domain design goals, such as high low-frequency gain (for steady-state error specifications), a high crossover frequency (to achieve closed-loop bandwidth specifications), a low resonant peak (to achieve damping specifications), and low high-frequency gain (to attenuate noise and unmodelled high-frequency dynamics).

The feedback control system is then "robustified" by synthesising the feedback controller $\mathbf{K}(s)$ that minimises the H_∞ norm of the following closed-loop transfer function:

$$\min_K \left\| \begin{bmatrix} \mathbf{I} \\ \mathbf{K} \end{bmatrix} (\mathbf{I} - \mathbf{P}_s\mathbf{K})^{-1} \begin{bmatrix} \mathbf{I} & \mathbf{P}_s \end{bmatrix} \right\|_\infty \tag{5.2.17}$$

The controller $\mathbf{K}$ is a controller that adds robustness to general coprime factor uncertainty. Therefore, the performance benefits of the shaping weights are combined with a controller $\mathbf{K}$ that is designed to increase the robustness of the system. The H_∞ loop shaping method is popular due to the fact that classical control principles are the foundation of the method. The fact that the open-loop plant is shaped in the frequency-domain presents an intuitive design procedure for most control engineers.

5.2.3.1 Generalised Stability Margin

In the last section, we defined the ν-gap metric and how it is linked to coprime factor uncertainty. We also presented the fact that in order to provide robustness against coprime factor uncertainty, we have the following objective

$$\min_K \left\| \mathbf{M}^{-1}(\mathbf{I} - \mathbf{K}\mathbf{P})^{-1} \begin{bmatrix} \mathbf{K} & \mathbf{I} \end{bmatrix} \right\|_\infty . \tag{5.2.18}$$

If we have a system $\mathbf{P}$ with normalised $\mathbf{P} = \bar{\mathbf{M}}^{-1}\bar{\mathbf{N}} = \mathbf{N}\mathbf{M}^{-1}$, Zhou et al. [74] show how the closed-loop system above is related to other closed-loop systems of a standard feedback configuration. We summarise these results as

$$\begin{aligned}\left|\left|\mathbf{M}^{-1}(\mathbf{I}-\mathbf{KP})^{-1}\begin{bmatrix}\mathbf{K} & \mathbf{I}\end{bmatrix}\right|\right|_\infty &= \left|\left|\begin{bmatrix}\mathbf{I}\\ \mathbf{P}\end{bmatrix}(\mathbf{I}-\mathbf{KP})^{-1}\begin{bmatrix}\mathbf{K} & \mathbf{I}\end{bmatrix}\right|\right|_\infty \\ &= \left|\left|\begin{bmatrix}\mathbf{I}\\ \mathbf{K}\end{bmatrix}(\mathbf{I}-\mathbf{PK})^{-1}\begin{bmatrix}\mathbf{I} & \mathbf{P}\end{bmatrix}\right|\right|_\infty \\ &= \left|\left|\begin{bmatrix}\mathbf{I}\\ \mathbf{K}\end{bmatrix}(\mathbf{I}-\mathbf{PK})^{-1}\bar{\mathbf{M}}^{-1}\right|\right|_\infty \qquad (5.2.19)\end{aligned}$$

The last of these equalities is important because it shows that a controller that minimises the sensitivity to rcf uncertainty is also the controller that minimises the sensitivity to lcf uncertainty. To see this, consider Figure 5.6, which shows a feedback system with left coprime factor uncertainty. The transfer function from $\mathbf{w}$ to $\mathbf{z}$ is derived directly from the figure as

$$\begin{bmatrix}\mathbf{z}_1\\ \mathbf{z}_2\end{bmatrix} = \begin{bmatrix}\mathbf{K}\\ \mathbf{I}\end{bmatrix}(\mathbf{I}-\mathbf{PK})^{-1}\bar{\mathbf{M}}\mathbf{w} \qquad (5.2.20)$$

The robust stability theorems in the previous section can also be written in terms of left coprime factor uncertainty. In the lcf uncertainty case, the transfer function to bound is given by Equation 5.2.20. And again, the last equality in Equation 5.2.19 means that a controller guaranteeing robust stability to rcf uncertainty will also do so to lcf uncertainty.

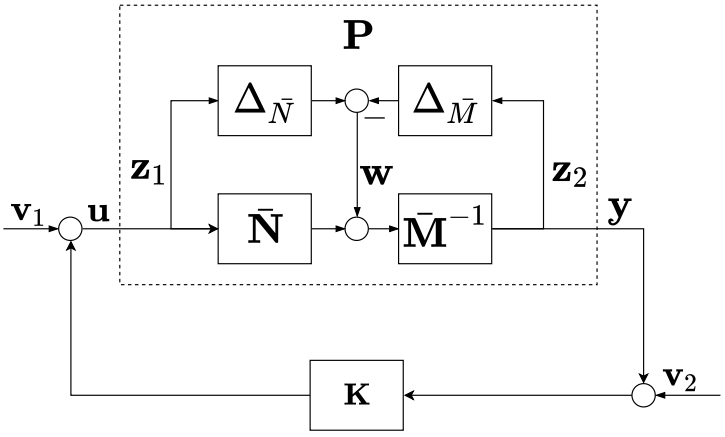

Figure 5.6: Feedback system with left coprime factor uncertainty

The first and second equality in Equation 5.2.19 are important because they show that a controller that minimises sensitivity to coprime factor uncertainty is also a controller that minimises the H_∞ norm of all eight transfer functions associated with Figure 5.7. It is well known that for a feedback system to be stable, all eight of these transfer functions need to be stable. These transfer

functions represent the effects of the inputs $\mathbf{v}$ and $\mathbf{w}$ on the outputs $\mathbf{y}$ and $\mathbf{u}$. They can be derived from the figure as

$$\begin{bmatrix} \mathbf{y} \\ \mathbf{u} \end{bmatrix} = \begin{bmatrix} \mathbf{P} \\ \mathbf{I} \end{bmatrix} (\mathbf{I} - \mathbf{KP})^{-1} \begin{bmatrix} \mathbf{K} & \mathbf{I} \end{bmatrix} \begin{bmatrix} \mathbf{v}_2 \\ \mathbf{v}_1 \end{bmatrix} + \begin{bmatrix} \mathbf{I} \\ \mathbf{K} \end{bmatrix} (\mathbf{I} - \mathbf{PK})^{-1} \begin{bmatrix} \mathbf{I} & \mathbf{P} \end{bmatrix} \begin{bmatrix} \mathbf{w}_2 \\ \mathbf{w}_1 \end{bmatrix}$$

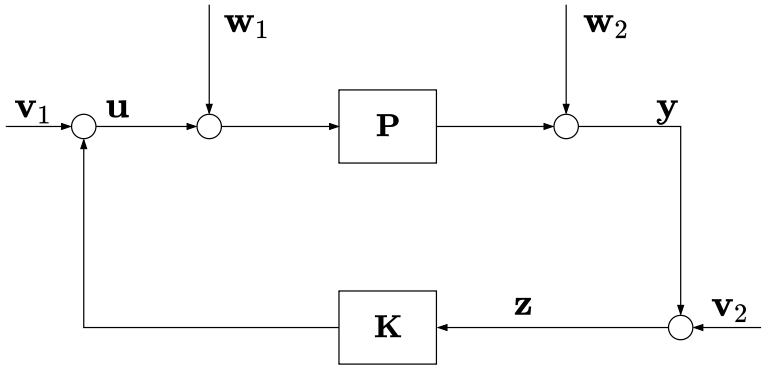

Figure 5.7: Standard feedback configuration.

Of particular interest is the quantity $b_{P,K}$, which is defined as

$$b_{P,K} = \left(\left\| \begin{bmatrix} \mathbf{I} \\ \mathbf{K} \end{bmatrix} (\mathbf{I} - \mathbf{PK})^{-1} \begin{bmatrix} \mathbf{I} & \mathbf{P} \end{bmatrix} \right\|_\infty \right)^{-1}$$

if the feedback system is stable, or 0 otherwise. Clearly, a large $b_{P,K}$ (low H_∞ norm of closed-loop system) is desirable because it reduces sensitivity to coprime factor uncertainty, and for this reason it is termed a *generalised stability margin*.

Adding further motivation to $b_{P,K}$ being used as a generalised stability margin is the fact that it is implicitly related to the standard gain and phase margins used to describe system stability. In fact, in the SISO case, the following is shown by Vinnicombe [71]: If given a SISO plant P and a stabilising controller K, then

$$M_G \geq \frac{1 + b_{P,K}}{1 - b_{P,K}}$$

and

$$M_P \geq 2 \arcsin\left(b_{P,K}\right)$$

where M_G and M_P are used here to denote gain and phase margin, respectively.

$b_{P,K}$ also has performance implications associated with it. In particular, if a large $b_{P,K}$ is achieved during synthesis, we are guaranteed to have minimal open- and closed-loop shape degradation. For instance, a large $b_{P,K}$ guarantees that at frequencies where $\bar{\sigma}(\mathbf{P}) >> 1$ is large, then $\bar{\sigma}(\mathbf{PK}) >> 1$ will also be large and have a theoretically bounded *minimum*. Conversely, at frequencies where $\bar{\sigma}(\mathbf{P}) << 1$ is small, then $\bar{\sigma}(\mathbf{PK}) << 1$ will also be small and have a theoretically bounded *maximum*. Macfarlane et al. [54] present the theoretical proof of this claim and we present a summary of this as

$$\underline{\sigma}(\mathbf{P}) \to \infty \Rightarrow \underline{\sigma}(\mathbf{K}) \gtrsim \frac{1}{\sqrt{\gamma^2 - 1}} \tag{5.2.21}$$

and

$$\bar{\sigma}(\mathbf{P}) \to 0 \Rightarrow \bar{\sigma}(\mathbf{K}) \lesssim \sqrt{\gamma^2 - 1}, \tag{5.2.22}$$

which says that if $\mathbf{P}$ has desirable loop shape in the form of high loop gain in a certain frequency range and low loop gain in another frequency range, then $b_{P,K}$ gives a bound on how much the introduction of a controller $\mathbf{K}$ will degrade that loop shape. In other words, if the plant $\mathbf{P}$ has a region of high gain (such as in the low frequency region), then the controller $\mathbf{K}$ has a lower bound on its magnitude, which means the gain of $\mathbf{PK}$ in that region can only be decreased by a certain amount. If the plant $\mathbf{P}$ has a region of low gain (such as in the high frequency region), then the controller $\mathbf{K}$ has an upper bound on it's magnitude, which means the gain of $\mathbf{PK}$ in that region can only be increased by a certain amount. This ensures that the loop shape of the plant $\mathbf{P}$, which is assumed to be desirable, can only be degraded by a certain amount that is related to the magnitude of $b_{P,K}$.

Furthermore, bounds on the sensitivity function $\mathbf{S} = (\mathbf{I} + \mathbf{PK})^{-1}$ and complimentary sensitivity function $\mathbf{T} = \mathbf{PK}(\mathbf{I} + \mathbf{PK})^{-1}$ also exist. The following bounds are derived by Vinnicombe [71] and present bounds on the closed-loop transfer functions for the scalar case:

$$\max_{K:b_{P,K}\geq 1/\gamma} \frac{1}{|1 - PK|} = \frac{\sqrt{\gamma^2 - 1}|P| + 1}{|P|^2 + 1}, \tag{5.2.23}$$

$$\min_{K:b_{P,K}\leq 1/\gamma} \frac{1}{|1 - PK|} = \left\{ \begin{array}{cc} \frac{\sqrt{\gamma^2-1}|P|+1}{|P|^2+1} & \text{if} \quad |P| > 1/\sqrt{\gamma^2 - 1}, \\ 0 & otherwise \end{array} \right\} \tag{5.2.24}$$

and

$$\max_{K:b_{P,K}\geq 1/\gamma} \frac{PK}{|1-PK|} = \frac{\sqrt{\gamma^2-1}/|P|+1}{|1/P|^2+1}, \tag{5.2.25}$$

$$\min_{K:b_{P,K}\leq 1/\gamma} \frac{PK}{|1-PK|} = \left\{ \begin{array}{cc} \frac{\sqrt{\gamma^2-1}/|P|+1}{|1/P|^2+1} & \text{if} \quad |P| > \sqrt{\gamma^2-1}, \\ 0 & \text{otherwise} \end{array} \right\}. \tag{5.2.26}$$

Therefore, a high $b_{P,K}$ is desirable from both a performance and robust stability perspective. From the performance perspective, a high $b_{P,K}$ guarantees minimal loop shape degradation provided $\mathbf{P}$ has a desirable loop shape (high or low gain in certain frequency ranges). From a robust stability perspective, a high $b_{P,K}$ provides robustness against coprime factor uncertainty (as quantified by the ν-gap metric), which will be elaborated on later.

5.2.3.2 H_∞ Robust Stabilisation

As mentioned in the previous subsection, the inverse of the H_∞ norm of the following closed-loop transfer function can be considered a generalised stability margin, which we denote as

$$b_{P_s,K} = \left(\left|\left| \begin{bmatrix} \mathbf{I} \\ \mathbf{K} \end{bmatrix} (\mathbf{I}-\mathbf{PK})^{-1} \begin{bmatrix} \mathbf{I} & \mathbf{P} \end{bmatrix} \right|\right|_\infty \right)^{-1} \tag{5.2.27}$$

The minimization of the H_∞ norm (maximisation of $b_{P,K}$) is well known, and detailed in Zhou et al. [73]. The theoretical maximum of $b_{P,K}$, $b_{opt}(\mathbf{P})$, can be calculated explicitly by

$$b_{opt}^{-1} = \sqrt{1 - || \begin{bmatrix} \mathbf{NM} \end{bmatrix} ||_H^2} = (1+\rho(\mathbf{XZ}))^{1/2} \tag{5.2.28}$$

where $||\mathbf{Q}||_H$ is the Hankel norm of $\mathbf{Q}$, $\rho(\mathbf{Q})$ is the maximum spectral radius of $\mathbf{Q}$, and $\mathbf{X}$ and $\mathbf{Z}$ are the unique, semi-definite solutions to the generalised filter and generalised control algebraic Riccati equations, which are given as

$$\begin{aligned} (\mathbf{A}-\mathbf{BS}^{-1}\mathbf{D}^T\mathbf{C})\mathbf{Z} + \mathbf{Z}(\mathbf{A}-\mathbf{BS}^{-1}\mathbf{D}^T\mathbf{C})^T \\ -\mathbf{ZC}^T\mathbf{R}^{-1}\mathbf{CZ} + \mathbf{BS}^{-1}\mathbf{B}^T = \mathbf{0} \\ (\mathbf{A}-\mathbf{BS}^{-1}\mathbf{D}^T\mathbf{C})^T\mathbf{X} + \mathbf{X}(\mathbf{A}-\mathbf{BS}^{-1}\mathbf{D}^T\mathbf{C}) \\ -\mathbf{XBS}^{-1}\mathbf{B}^T\mathbf{X} + \mathbf{C}^T\mathbf{R}^{-1}\mathbf{C} = \mathbf{0}, \end{aligned} \tag{5.2.29}$$

where $\mathbf{S} = \mathbf{I} + \mathbf{D}^T\mathbf{D}$ and $\mathbf{R} = \mathbf{I} + \mathbf{D}\mathbf{D}^T$. For a given $b_{P,K} < b_{opt}$, a controller is given by

$$\mathbf{K}(s) \stackrel{s}{=} \left[\begin{array}{c|c} \mathbf{A} + \mathbf{BF} + \gamma^2(\mathbf{L}^T)^{-1}\mathbf{Z}\mathbf{C}^T(\mathbf{C} + \mathbf{DF}) & \gamma^2(\mathbf{L}^T)^{-1}\mathbf{Z}\mathbf{C}^T \\ \hline \mathbf{B}^T\mathbf{X} & -\mathbf{D}^T \end{array}\right] \tag{5.2.30}$$

where $\mathbf{F} = -\mathbf{S}^-1(\mathbf{D}^T\mathbf{C} + \mathbf{B}^T\mathbf{X})$ and $\mathbf{L} = (1 - \gamma^2)\mathbf{I} + \mathbf{XZ}$.

We can also consider a frequency-by-frequency version of $b_{P,K}$ by denoting

$$\rho(\mathbf{P}, \mathbf{K})(jw) = \left(\bar{\sigma}\left(\begin{bmatrix} \mathbf{I} \\ \mathbf{K} \end{bmatrix}(\mathbf{I} - \mathbf{PK})^{-1}\begin{bmatrix} \mathbf{I} & \mathbf{P} \end{bmatrix}\right)(jw)\right)^{-1}$$

where $\bar{\sigma}(\mathbf{X})$ is the maximum singular value of $\mathbf{X}$. This will be utilized in a later section.

5.2.3.3 H_∞ Loop Shaping Design Procedure

When performing an H_∞ loop shaping design, the designer selects dynamic weights to improve the nominal plant loop shape, to form the shaped plant:

$$\mathbf{P}_s = \mathbf{W}_2\mathbf{P}\mathbf{W}_1 \tag{5.2.31}$$

This shaped plant $\mathbf{P}_s$ should now have a desirable open-loop shape. The designer then synthesizes a controller that minimises the H_∞ norm of the closed-loop transfer function:

$$\min_K \left\| \begin{bmatrix} \mathbf{I} \\ \mathbf{K} \end{bmatrix}(\mathbf{I} - \mathbf{P}_s\mathbf{K})^{-1}\begin{bmatrix} \mathbf{I} & \mathbf{P}_s \end{bmatrix} \right\|_\infty \tag{5.2.32}$$

A lower value of the H_∞ norm (high value for $b_{P,K}$) guarantees that the controller $\mathbf{K}$ will not degrade the shape of $\mathbf{P}_s$ too severely, as discussed in the previous subsection. Also, a high value for $b_{P,K}$ also provides robustness towards coprime factor uncertainty. This generally lends to very effective designs, whereby time-domain performance is achieved through the pre- and post-compensating shaping weights. A feedback controller $\mathbf{K}$ is then synthesised and if the resulting value of $b_{P,K}$ is high, then the system should have good robustness to coprime factor uncertainty and the system should not lose too much performance in the time-domain due to the loop shape not degrading too much in the high and low frequency ranges.

5.3 Quadrotor and Suspended Payload Translational Control: H_∞ Loop Shaping Design

This section presents the design of a quadrotor velocity control system using the H_∞ loop shaping design procure. The controller controls the quadrotor velocity in all three inertial coordinates, North, East, and Down. The control system aims to be robust to the uncertainties in the system, which are the variations in payload mass, the cable length, and the magnitude and direction of the quadrotor thrust force. First, an overview of the controller is presented, followed by the detailed design of the horizontal velocity controllers. Thereafter, the controller is verified using the high-fidelity simulation model.

5.3.1 Overview

For this quadrotor velocity control system, an H_∞ loop shaping controller, denoted K_{LS}, will replace the LQI-based controllers in the unique reference force-based flight control architecture presented in Chapter 4. Therefore, the structure of the flight control system with H_∞ loop shaping controllers to control the horizontal quadrotor velocity is shown in Figure 5.8.

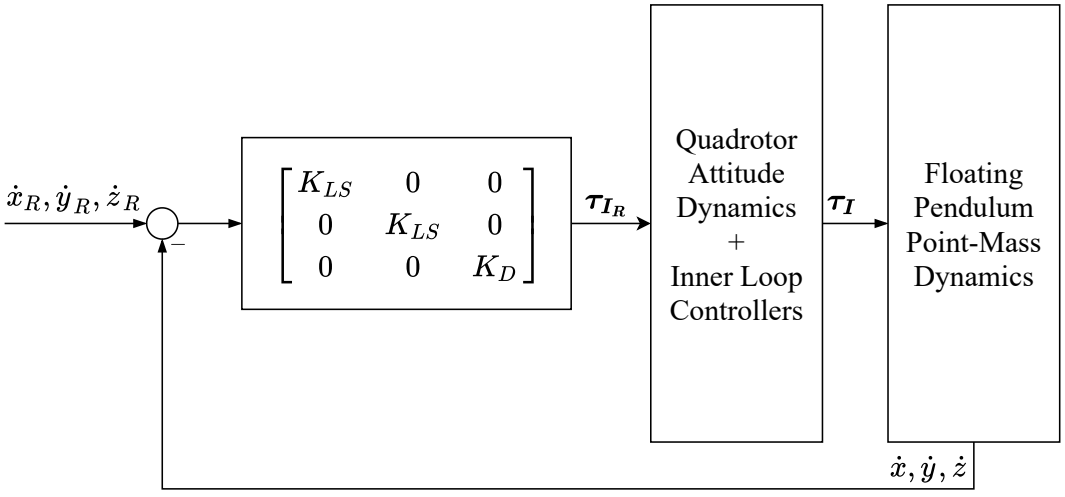

Figure 5.8: H_∞ loop shaping controller

In this configuration, the same PI controller from Chapter 4 is used to control the vertical velocity. For horizontal velocity control, the H_∞ loop shaping controller will be designed with the same objectives that were used to design the LQI controller in Chapter 4. Specifically, the controller objectives are zero steady-state tracking error to step commands, a bandwidth of 0.7 rad/s

to meet similar closed-loop velocity reference tracking performance as in previous projects, and the addition of damping to the swinging motion of the suspended payload. Another key objective of this controller is robust stability, which means the resulting control system must be robust to the uncertainty in the horizontal translational dynamics that stem from the thrust magnitude and direction uncertainty (due to the quadrotor attitude dynamics), the cable length uncertainty, and the payload mass uncertainty. This will be analysed later in the chapter.

5.3.2 Quadrotor Horizontal Velocity Control

Two identical controllers are used to control the quadrotor velocity, one for control of velocity in the North direction, and one for control of velocity in the East direction. Therefore, we consider the design of only one of these controllers. In block diagram form, the structure of the horizontal velocity controller is shown as in Figure 5.9.

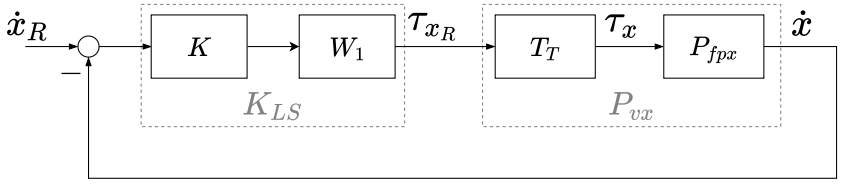

Figure 5.9: H_∞ loop shaping controller used to control quadrotor velocity

The controller consists of a pre-compensating weight W_1 that is designed to improve the open-loop frequency response of the plant, and a robustifying controller K. The pre-compensating weight is chosen to meet the design objectives in terms of transient performance and steady-state tracking. The controller K is responsible for added robustness to general coprime factor uncertainty, as discussed earlier in the chapter.

The controller receives the error between measurements of the current quadrotor velocity, $\dot{x}$ ($\dot{y}$ for the East velocity controller), and velocity commands $\dot{x}_R$ ($\dot{y}_R$ for the East velocity controller). The controller actuates the horizontal components of the reference force $\boldsymbol{\tau}_{I_R}$.

The plant used to design the controller is the linear model derived in Section 4.3.3.1, $P_{vx}(s)$, which represents the dynamic response from a reference horizontal force input to a horizontal quadrotor velocity. It includes the closed-loop quadrotor tilt angle dynamics, $T_T(s)$.

5.3.2.1 Loop Shaping Weight Selection

The nominal frequency response of the plant P_{vx} is undesirable. The gain of the plant in the low-frequency region is low, the cut-off frequency is at a low frequency, and the resonant peak of the lightly damped mode reaches the 0dB point. This is shown again in Figure 5.10.

The benchmark LQI controller attempted to remedy the poor loop shape of P_{vx} by adding overall gain to lift the crossover frequency of the plant, by adding low frequency gain through the addition of an integral state, and by reducing the resonant peak through placing a notch at that frequency. It does this by estimating the payload swing states and then using state feedback to try reduce the swinging motion. However, the LQI controller performed poorly when the exact location of the resonant peak is not known due to system uncertainties.

In this section, we present the design of a new pre-compensating weight W_1 that will be used when developing a robust flight controller. The aim of the weight is to improve the open-loop shape of the plant P_{vx}. Also, we set the post-compensating weight W_2 to 1.

A pre-compensating scalar shaping weight W_1 was designed using the following method:

- A wide notch is placed around the frequencies of the resonant peak. The notch is made wide in order to try to compensate for the exact location of the resonant peak not being precisely known and moving as plant parameters change.
- A proportional-integral-derivative (PID) controller is designed using the plant P_{vx} augmented with the wide notch to achieve a higher crossover frequency, higher low-frequency gain from the integral term in the controller, phase lead from the derivative term in the controller, and high-frequency attenuation. A low-pass filter is used on the derivative term to assist the high-frequency attenuation, as is common in practice when using PID controllers.

The shaping weight W_1 was then formed by combining the notch filter and the PID controller. The favourable loop shaping properties of a PID controller are combined with the notch to prevent the resonant peaks reaching 0dB. The frequency response of W_1 is given in Figure 5.10. Also shown is the response of the shaped plant $P_{vx}W_1$. When comparing P_{vx} and $P_{vx}W_1 = P_s$, we see a significantly more desirable response for P_s. The crossover frequency is higher and the resonant peak is attenuated. The crossover frequency of the shaped plant is 1 rad/s. Also, the slope is -20 dB in the low-frequency region, which ensures zero steady-state error when tracking step commands.

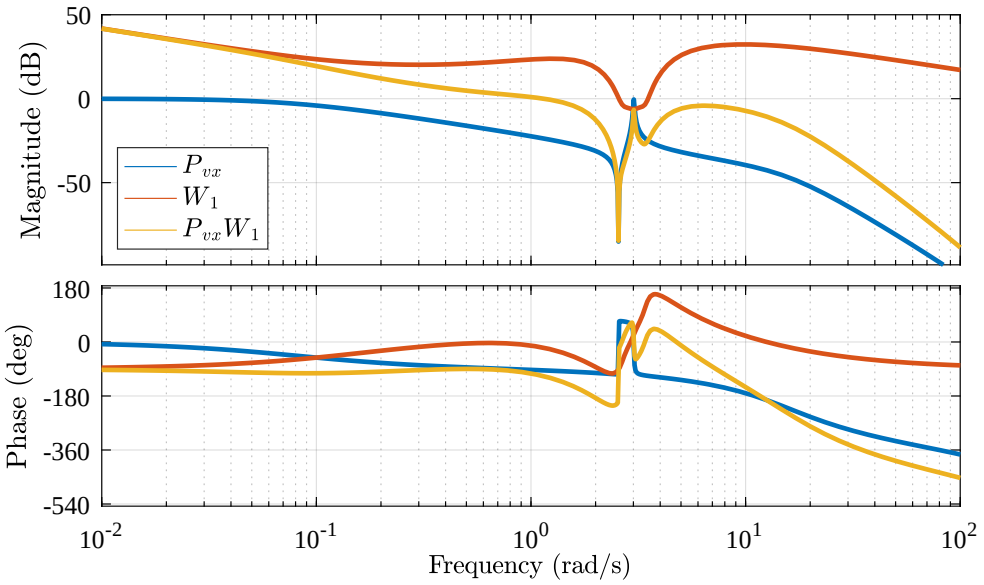

Figure 5.10: Bode plot of plant P_{vs}, shaped plant $P_s = P_{vs}W_1$, and shaping weight W_1.

5.3.2.2 Robust Stabilisation

Solving the Ricatti equations in Equation 5.2.29, and then calculating the maximum $b_{P_s,K}$ using Equation 5.2.28 above yields $b_{P_s,K} = 0.62$ (values above 0.3 are generally considered sufficient for most designs), and a plot of $\rho(P_s, K)(jw)$ is shown in Figure 5.11. Clearly, $b_{P_s,K} = \min_w \rho(P_s, K)(jw)$, as per the definition of $b_{P_s,K}$ and $\rho(P_s, K)$.

Generally, these values for $b_{P_s,K}$ and $\rho(P_s, K)$ would be considered very good, with any general uncertainty in the plant unlikely to have a significant effect on stability and performance. Also, high values of $b_{P_s,K}$ and $\rho(P_s, K)$ also guarantee that the synthesized H_∞ controller will cause minimal degradation of the loop shape P_s.

Forming the controller K with Equation 5.2.30, and then forming the final controller $K_{LS} = W_1K$, the frequency response of the plant and final controller, $P_{vx}W_1K = P_{vx}K_{LS}$, is given in Figure 5.12. It is clear from this figure that the loop shape of the shaped plant in the low-frequency and high-frequency regions, where there is high and low loop gain, respectively, is not altered by any significant amount. The controller K mostly tries to effect the crossover region and the resonant peak. The bandwidth of the open-loop system with the shaping weight W_1 and the controller K is 0.7 rad/s, which is the target bandwidth (as per Chapter 4). Therefore, the robustifying controller K

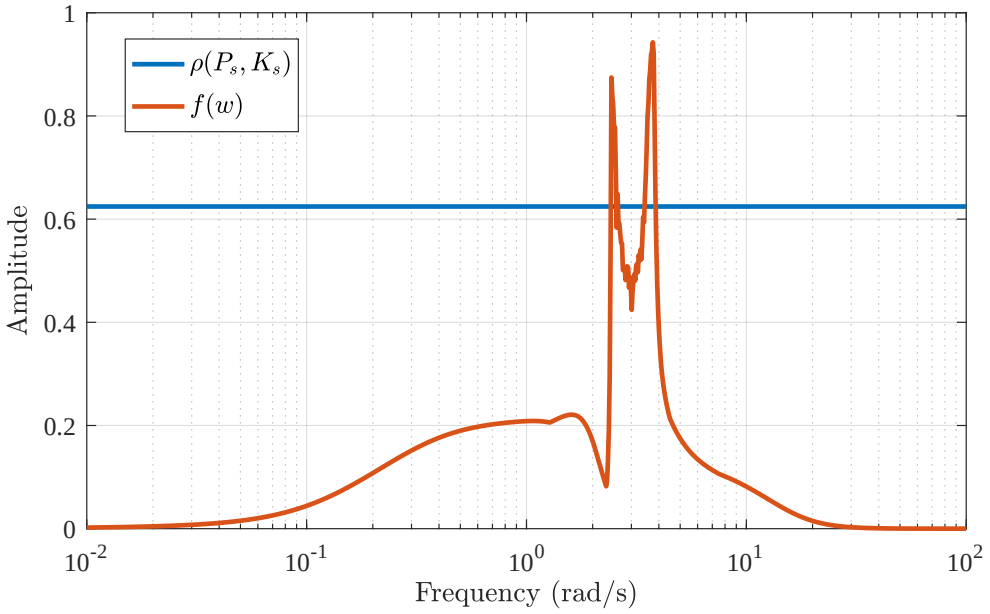

Figure 5.11: Magnitude of $\rho(P_s, K)$ and $f(w) = \max_{P_{s-unc}} \Phi(P_s, P_{s-unc})(jw)$

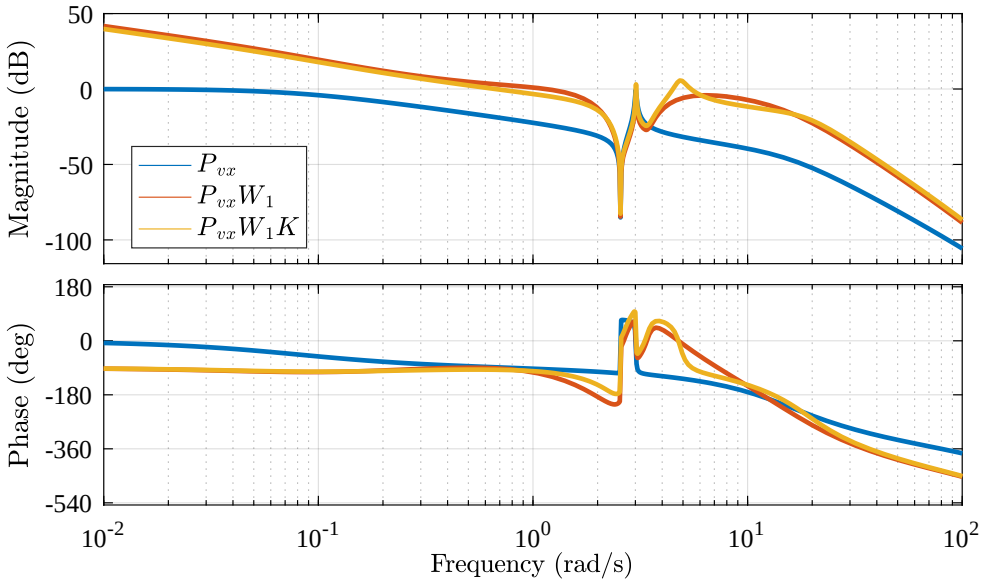

Figure 5.12: Bode plot of plant P_{vs}, shaped plant $P_s = P_{vs}W_1$, and shaped plant with H_∞ controller $P_sK = P_{vx}K_{LS}$.

reduces the bandwidth of the compensated system from 1 rad/s (with the shaping weight only), to 0.7 rad/s, with the shaping weight and robustifying

controller K. The controller is implemented with the linear model as shown by Figure 5.9.

The step response from a reference $\dot{x}_R$ to output $\dot{x}$ is shown in Figure 5.13. The settling time of the system is approximately 4.5 seconds, and the step command is tracked with zero steady-state error. The same step response, but with variations in the uncertain parameters thrust T_t, cable length C_L, and payload mass M_L included, is also shown in Figure 5.13. The plot shows that the even in the nominal case, the response is not desirable. In order to cancel the swinging motion of the payload, the controller performs a slight reversal just after forward motion begins. This appears to provide some damping to the swinging motion in the nominal case, but when uncertainties are considered, the system is unstable. Clearly, the level of robustness provided by the controller K is not sufficient for this application. This will be elaborated on in the next chapter, when the ν-gap metric is applied to analyses the robust stability of the resulting closed-loop system

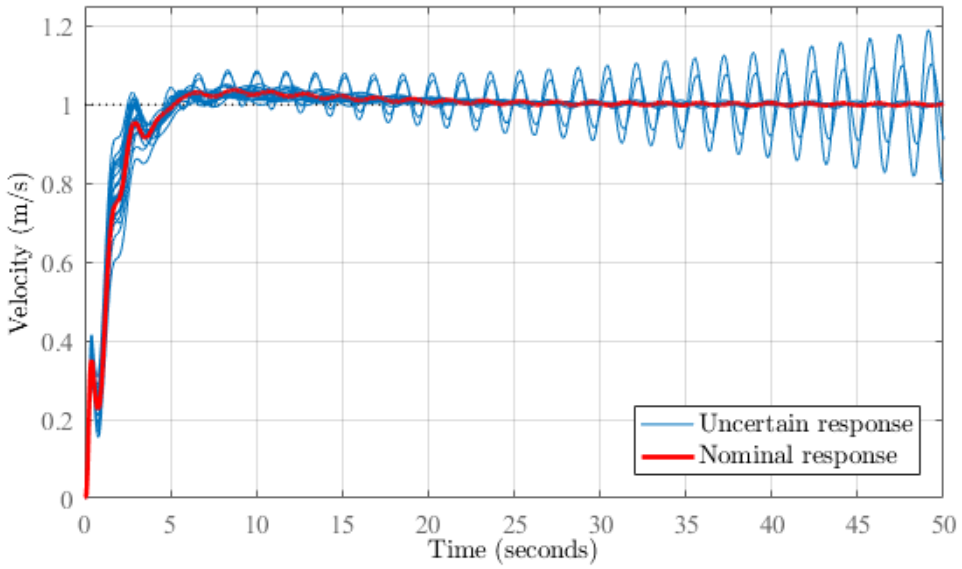

Figure 5.13: Step response of closed-loop system with H_∞ loop shaping controller to a reference velocity command.

A Monte Carlo style plot of the poles and zeros of the closed-loop system with the H_∞ loop shaping controller is shown in Figure 5.14. This plot shows the poles and zeros of a the closed-loop system when various plants in the uncertainty set are sampled. Also shown are the poles and zeros of the nominal, uncompensated, open-loop plant P_{vx}. Clearly, there are closed-loop systems

in the closed-loop uncertainty set that have poles in the right-half plane of the complex plane, confirming that the system does not have robust stability.

Monte Carlo style Bode plots of the open- and closed-loop systems with the H_∞ loop shaping controller are given in Figure 5.15 and Figure 5.16, respectively. It is clear from these figures that when the uncertainty in the plant is considered, the frequency of the lightly-damped resonant mode of the system is shifted. The H_∞ loop shaping controller fails to prevent the entire set of resonant peaks from reaching the 0 dB point, which is further evidence of instability.

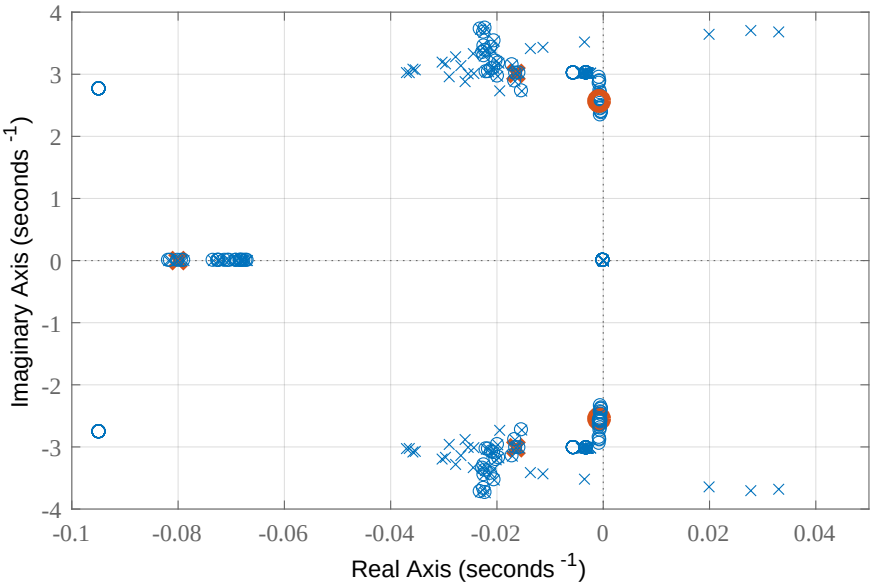

Figure 5.14: Poles and zeros of velocity control system with H_∞ loop shaping controller. $\times$ is used to mark poles, and $\circ$ is used to mark zeros. Also shown are poles and zeros of the nominal open-loop system P_{vx}, shown in red.

5.3.3 Simulation Results with H_∞ Loop Shaping Controller

The H_∞ loop shaping quadrotor and payload translational control system was implemented and verified using the full nonlinear simulation, as shown in Figure 5.8. The closed-loop step response of the horizontal velocity controller is shown in Figure 5.17, along with the nominal response of the linear model P_{vx}. The horizontal velocity step response was performed in the North direction. The references for the East and vertical velocity controllers were set to zero,

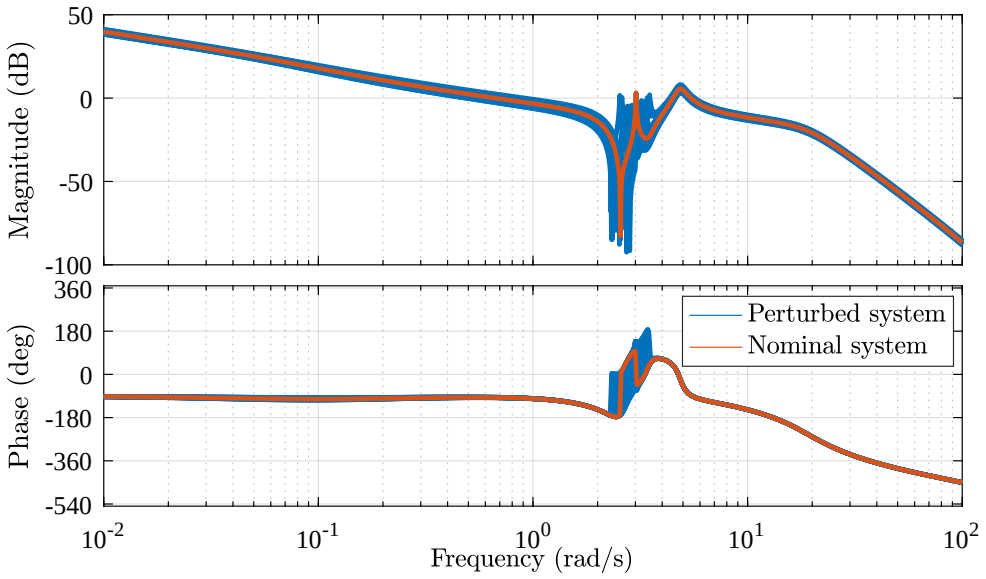

Figure 5.15: Bode plot of open-loop system with H_∞ loop shaping controller. Also shown are the responses with perturbed plants from the uncertainty set.

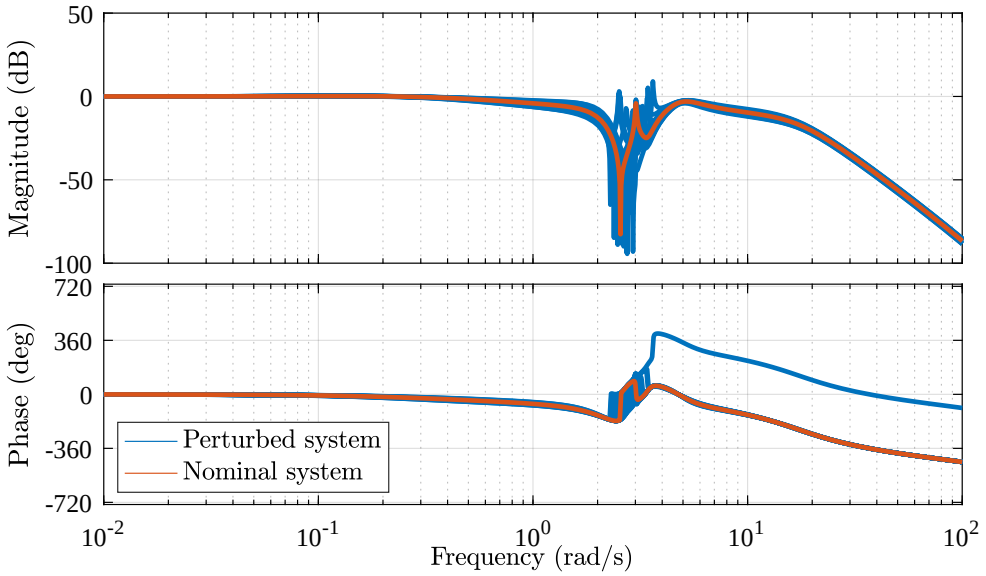

Figure 5.16: Bode plot of closed-loop system with H_∞ loop shaping controller. Also shown are the responses with perturbed plants from the uncertainty set

and these other two translational controllers therefore acted only to regulate

the East and vertical velocities to zero, and to reject external disturbances.

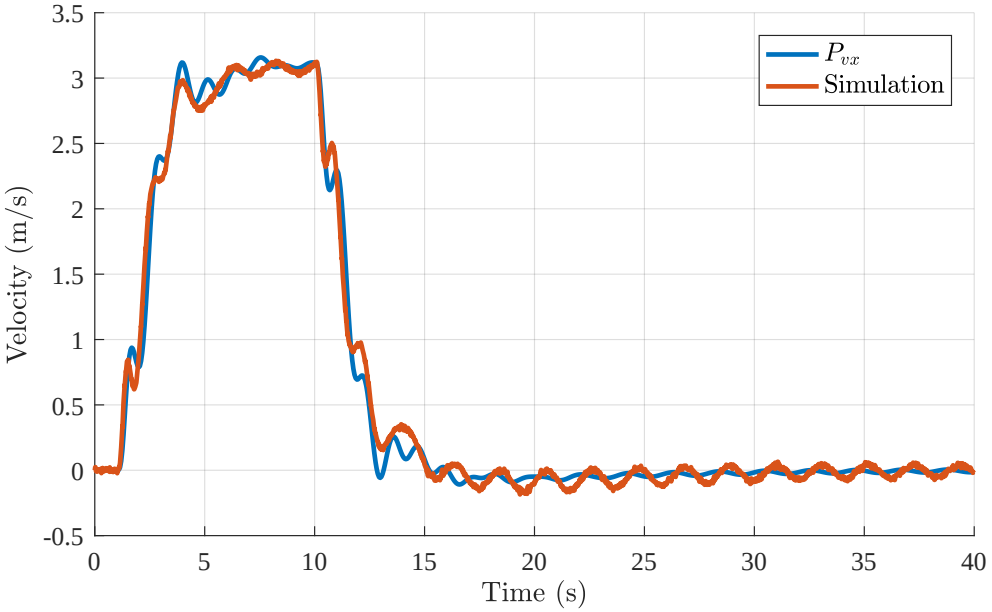

Figure 5.17: Response of quadrotor velocity $\dot{x}$ to a reference velocity command $\dot{x}_R$, with H_∞ loop shaping controller.

This figure shows that there is fairly good agreement between the response of the linearised model and the simulation. In both cases, even when the nominal values of the thrust scalar T_t, payload mass M_L, and cable length L are considered, the payload swinging motion is poorly damped, as is evident by the oscillations in the quadrotor velocity. The oscillations appear much worse in the results from the high-fidelity simulation.

The resulting payload swing angle θ_L from the simulation is shown in Figure 5.18 (with no motion in the East direction, $\phi_L \approx 0$). Clearly, there is little damping added to the payload swinging motion, which was a design objective.

A Monte Carlo simulation was performed using the high-fidelity simulation. The uncertain parameters in the plant were varied, and the same quadrotor velocity command was given to the controller. The results for the quadrotor velocity are given in Figure 5.19. The results for the payload angle θ_L are given in Figure 5.20. With the Monte Carlo simulation, we see that stability for all the plants in the uncertainty set is not guaranteed. This agrees with the results shown in Figure 5.13, and we identify that the system does not have robust stability.

Lastly, a simulation with non-zero quadrotor velocity commands in North, East, and Down directions was performed. In this case, to maintain clarity of

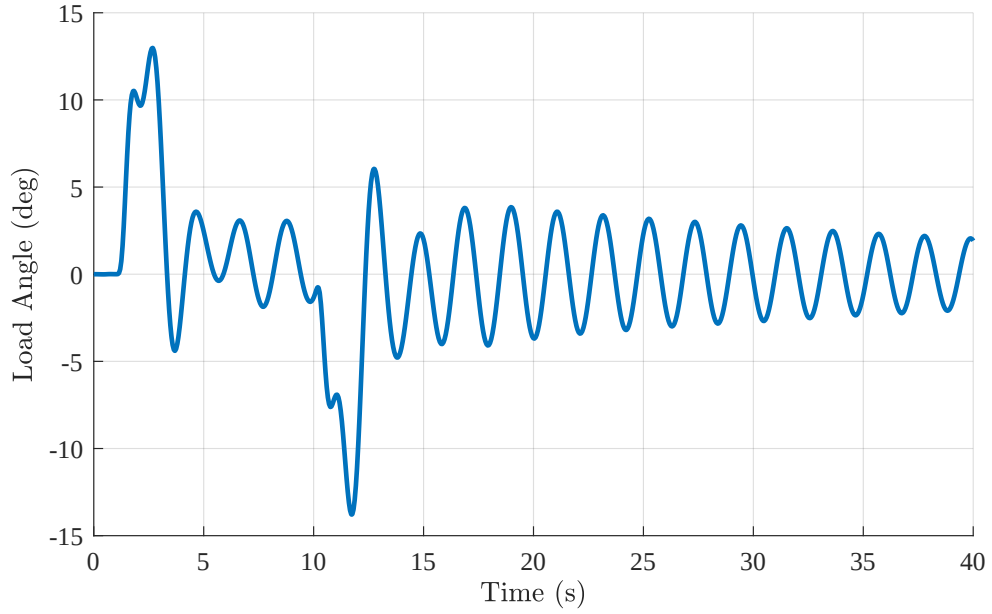

Figure 5.18: Response of payload angle θ_L to a reference velocity command $\dot{x}_R$, with H_∞ loop shaping controller.

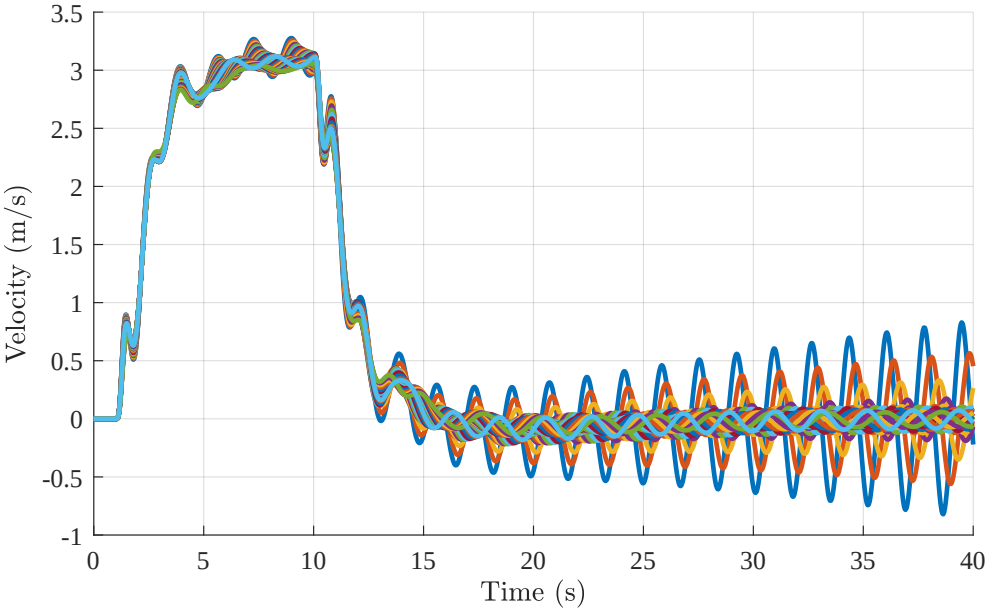

Figure 5.19: Monte Carlo simulation of quadrotor velocity $\dot{x}$, with H_∞ loop shaping controller, using high-fidelity simulation

the figures, only the perturbed case with $M_L = 6$kg, $L = 1.7$m and $T_t = 1.2$

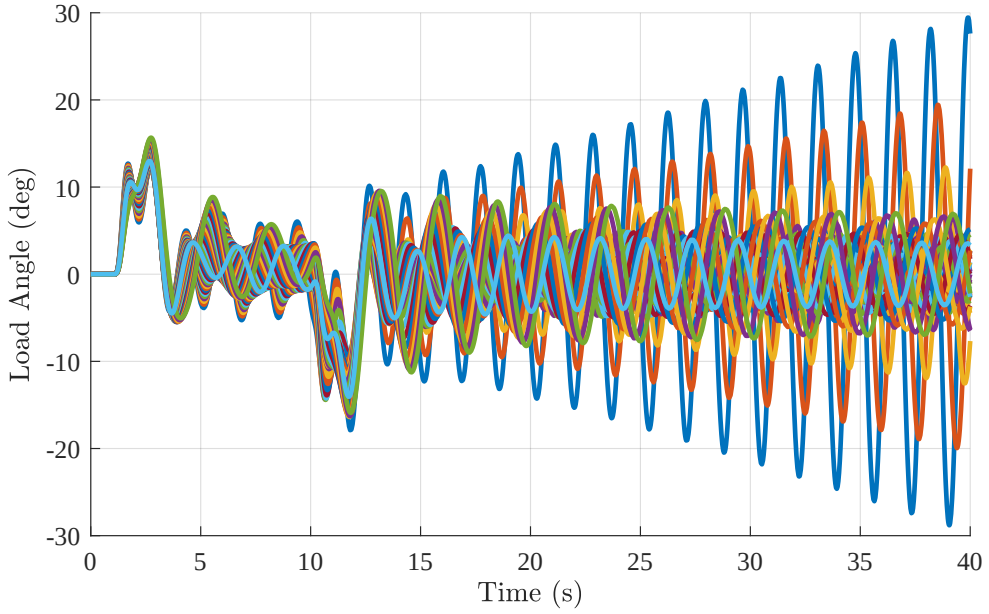

Figure 5.20: Monte Carlo simulation of payload angle θ_L, with H_∞ loop shaping controller, using high-fidelity simulation.

was simulated. The quadrotor velocity is plotted in Figure 5.21. The angles are plotted in Figure 5.22. As in the case with the controller K_{LQI}, we see very similar performance compared to the case when a non-zero velocity command in the North direction only was given, further motivating the decoupled velocity controller design approach.

5.4 Summary

In this chapter, the concepts of H_∞ control, H_∞ loop shaping, and the ν-gap metric were introduced. The link between the ν-gap metric and H_∞ loop shaping was shown. Together, these form a unified treatment of feedback controller synthesis, controller performance, and robust stability analysis.

An H_∞ loop shaping controller was designed. This included the design of a pre-compensating weight that is used to change the open-loop shape of the plant. A high value of $b_{P_s,K}$ was achieved, and this was reflected in the fact that the synthesised controller did not degrade the desirable properties of the shaped plant's open-loop response.

Although a high value of $b_{P_s,K}$ is achieved, the system does not exhibit robust stability. As mentioned in previous sections, the quantity $b_{P_s,K}$ is a measure of how robust the system is towards coprime factor uncertainty. However,

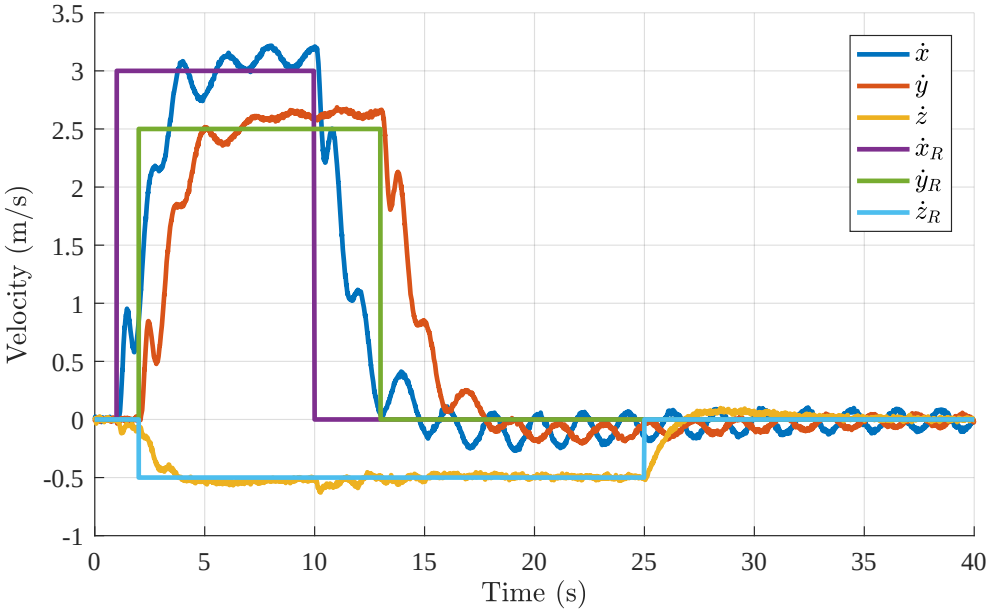

Figure 5.21: Response of quadrotor velocity $\dot{\mathbf{p}}$ to a reference velocity command $\dot{\mathbf{p}}_R$, with H_∞ loop shaping controller. In this simulation, the uncertain plant parameters are set to $M_L = 6$kg, $L = 1.7$m and $T = 1.2$.

the H_∞ loop shaping procedure, and in particular the robust stabilisation step to generate the controller K, does not factor in any knowledge of the actual uncertainty that is present in the system. It simply aims to achieve a high value of $b_{P_s,K}$, providing robustness towards general coprime factor uncertainty that may be present. Practical applications have shown that this robustness is usually enough for most designs, but clearly it is not enough for this application. This motivates the use of the ν-gap metric in the design - the metric can be used to determine the variation between the plants in the uncertainty set. A design using the ν-gap metric is presented in the following chapter.

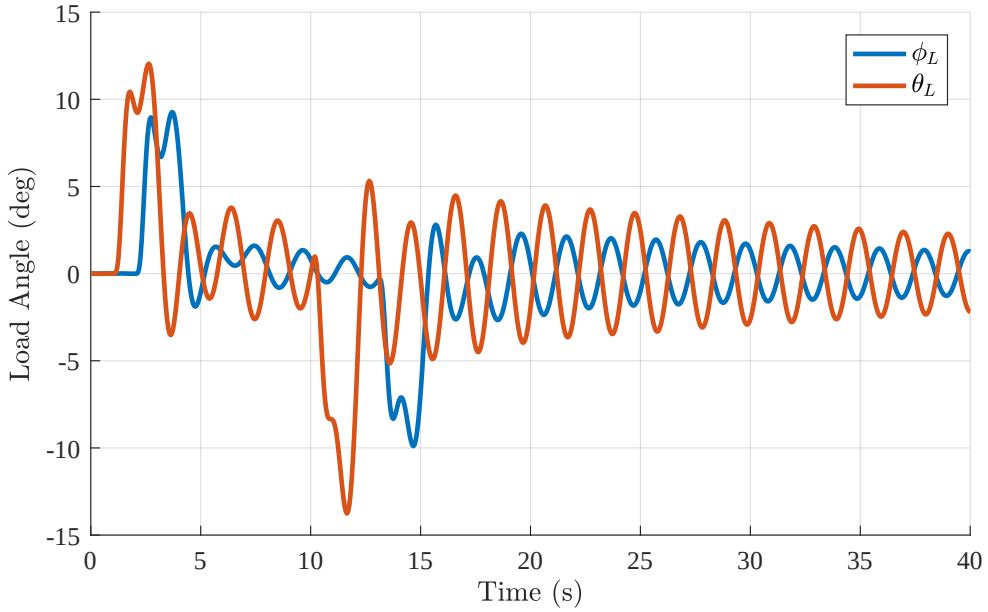

Figure 5.22: Response of payload angle ϕ_L and θ_L to a reference velocity command $\dot{\mathbf{p}}_R$, with H_∞ loop shaping controller. In this simulation, the uncertain plant parameters are set to $M_L = 6$kg, $L = 1.7$m and $T = 1.2$.

Chapter 6

Extended H_∞ Loop Shaping Design

In previous chapters, an LQI controller and an H_∞ loop shaping controller were presented. These were designed to control the velocity of the quadrotor. However, neither of these designs used explicit knowledge of the uncertainty present in the system; the uncertainty in the payload mass, the cable length, and the amount of thrust from the quadrotor. In this chapter we present the design of a controller that is robust to these uncertainties, using the tools established in Chapter 5. This chapter will present a novel H_∞ optimisation based algorithm that will consider the uncertainty in the system and synthesise a controller that ensures robust stability. The algorithm can be considered a modified version of the algorithms proposed by Vinnicombe [6], and Zhou [74].

6.1 Overview of the Extended H_∞ Loop Shaping Approach

The extended loop shaping design synthesises the controller $K_\infty(s)$ using explicit knowledge of the plant uncertainty as represented by the supremum ν-gap metric between the nominal shaped plant and the perturbed shaped plants in the uncertainty set. (The standard H_∞ loop shaping design technique does not use explicit knowledge of the plant uncertainty, and that it simply provides general robustness to coprime factor uncertainty.) The synthesis of $K_\infty(s)$ is performed using the shaped nominal plant $P_s(s)$, and a weighting function $W_\delta(s)$ that represents a target generalised stability margin and a maximum variation of the perturbed shaped plant relative to the nominal shaped plant. The controller synthesis is performed iteratively by setting a target generalised stability margin, synthesising the controller, and checking whether the generalised stability margin is achieved for all shaped plants in the uncertainty set.

The target generalised stability margin is adjusted iteratively until the maximum possible generalised stability margin is achieved for all shaped plants in the uncertainty set. The controller $K_\infty(s)$ produced by the extended H_∞ loop shaping technique therefore provides guaranteed robust stability for all plants in the uncertainty set.

6.2 Robust Stability Using the ν-gap Metric

In this section, robust stability theorems using the ν-gap metric and the generalised stability margin are presented. These include a frequency-by-frequency robust stability theorem that takes advantage of the fact that the generalised stablity margin and the ν-gap metric can both be viewed on a frequency-by-frequency basis. Finally, the robust stability of the quadrotor and suspended payload with the H_∞ loop shaping controller is determined.

6.2.1 Robust Stability Theorems

Previously, we have discussed the link between the ν-gap metric and the generalised stability margin. Together, these quantities facilitate a unified treatment of performance and robustness. We now consider the robustness aspects in more detail. The following theorem, which is proven by Vinnicombe [75], is the basis for our robust stability analyses:

Robust stability using ν-gap metric:

i *Given* $\mathbf{P}_1$, $\mathbf{K}$, *and numbers* $\beta \leq \alpha < b_{opt}(\mathbf{P}_1)$ *then:*

$\arcsin b_{P_2,K} > \arcsin \alpha - \arcsin \beta$ *for all* $\mathbf{P}_2$ *satisfying* $\delta_\nu(\mathbf{P}_1, \mathbf{P}_2) \leq \beta$ *if, and only if,* $b_{P1,K} > \alpha$.

ii *Given* $\mathbf{P}_1$, $\mathbf{P}_2$ *and numbers* $\beta \leq \alpha < b_{opt}(\mathbf{P}_1)$ *then:*

$\arcsin b_{P_2,K} > \arcsin \alpha - \arcsin \beta$ *for all* $\mathbf{K}$ *satisfying* $b_{P_1,K} > \alpha$ *if, and only if,* $\delta_\nu(\mathbf{P}_1, \mathbf{P}_2) \leq \beta$.

Intuitively, this theorem states that if a given plant $\mathbf{P}_1$ and a controller $\mathbf{K}$ achieves a certain generalised stability margin $b_{P_1,K}$, then the generalised stability margin of another plant $\mathbf{P}_2$ with the same controller $\mathbf{K}$ can degenerate by at most the value of $\delta_\nu(\mathbf{P}_1, \mathbf{P}_2)$.

As we saw in earlier sections, the quantities $b_{P_1,K}$ and $\delta_\nu(\mathbf{P}_1, \mathbf{P}_2)$ can both be viewed in a frequency-by-frequency perspective by considering the quantities $\rho(\mathbf{P}, \mathbf{K})(jw)$ and $\Phi(\mathbf{P}_1, \mathbf{P}_2)(jw)$, where $b_{P_1,K} = \min_w \rho(\mathbf{P}_1, \mathbf{K})(jw)$ and $\delta_\nu(\mathbf{P}_1, \mathbf{P}_2) = ||\Phi(\mathbf{P}_1, \mathbf{P}_2)(jw)||_\infty = \max_w \bar{\sigma}(\Phi(\mathbf{P}_1, \mathbf{P}_2))(jw)$. This leads to a

frequency-by-frequency version of the previous robust stability theorem. We define the following set of plants

$$\Omega(\mathbf{P}_1; f) := \{\mathbf{P} : \delta_\nu(\mathbf{P}_1, \mathbf{P}) < 1, \bar{\sigma}(\Phi(\mathbf{P}_1, \mathbf{P}))(jw) \leq f(w) \forall w\}$$

That is, if a plant $\mathbf{P}$ is in Ω, then it satisfies the winding number conditions and has $\Phi(\mathbf{P}_1, \mathbf{P})(jw) \leq f(w) \forall w$, for some function $f(w)$. The main robust stability theorem that we will use is:

Frequency-by-frequency robust stability Let $f(w) = |g(jw)|$ for some $g(s)$, with $g(s)$ being a real-rational stable transfer function.

i Given a plant $\mathbf{P}_1$ and a controller $\mathbf{K}$, then: $b_{P,K} > \alpha$ for all $\mathbf{P} \in \Omega$ if, and only if, the nominal feedback configuration with $\mathbf{P}_1$ and $\mathbf{K}$ is stable and

$$\arcsin \rho(\mathbf{P}_1, \mathbf{K}) > \arcsin f(w) + \arcsin(\alpha) \forall w \tag{6.2.1}$$

ii Given plants $\mathbf{P}$ and $\mathbf{P}_1$, then, provided there exists a $\mathbf{K}$ such that the nominal feedback configuration with $\mathbf{P}_1$ and $\mathbf{K}$ is stable and which satisfies $\arcsin \rho(\mathbf{P}_1, \mathbf{K}) > \arcsin f(w) + \arcsin \alpha \ \forall \ w$, then $b_{P,K} > \alpha$ for all $\mathbf{K}$ such that the nominal feedback configuration with $\mathbf{P}_1$ and $\mathbf{K}$ is stable, and which satisfy

$$\arcsin \rho(\mathbf{P}_1, \mathbf{K}) > \arcsin f(w) + \arcsin \alpha \forall w$$

if, and only if, $\mathbf{P} \in \Omega$.

The proof of this theorem is given in Vinnicombe [71]. This theorem is essentially a frequency-by-frequency version of the usual ν-gap metric robust stability theorems. To see the usefulness of this theorem, consider the case where, given plants $\mathbf{P}_1$, $\mathbf{P}_2$, and controller $\mathbf{K}$, we have that $\delta_\nu(\mathbf{P}_1, \mathbf{P}_2) > b_{P_1,K}$. However, it may be the case that $\bar{\sigma}(\Phi(\mathbf{P}_1, \mathbf{P}_2))(jw) \leq \rho(\mathbf{P}_1, \mathbf{K})(jw) \ \forall w$.

To see this, consider Figure 6.1, which shows an example plot of $\bar{\sigma}(\Phi(\mathbf{P}_1, \mathbf{P}))(jw)$ and $\rho(\mathbf{P}_1, \mathbf{K})(jw)$. Clearly, in this case $\delta_\nu(\mathbf{P}_1, \mathbf{P}_2) > b_{P_1,K}$. However, robust stability by the last theorem still holds because $\bar{\sigma}(\Phi(\mathbf{P}_1, \mathbf{P}_2))(jw) \leq \rho(\mathbf{P}_1, \mathbf{K})(jw) \ \forall w$.

6.2.2 Robust Stability Analysis

We wish to analyze the ν-gap metric between the shaped nominal plant $P_s = P_{vx}W_1$ and various shaped perturbed plants P_uW_1. Here, P_u represents P_{vx},

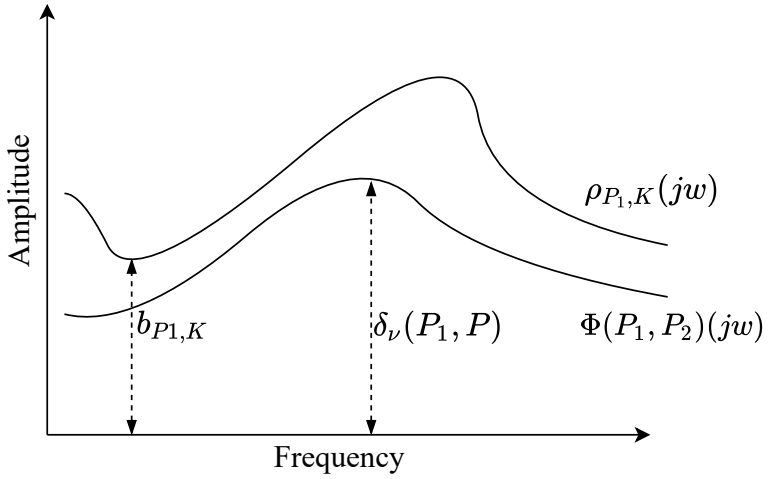

Figure 6.1: Example frequency-by-frequency plot of $\bar{\sigma}(\Phi(\mathbf{P}_1,\mathbf{P}))(jw)$ and $\rho(\mathbf{P},\mathbf{K})(jw)$.

but with variations in the system parameters. We perform the analysis by considering multiple perturbed plants (plants with different values of payload mass M_L, cable length L and thrust gain uncertainty ΔT_t) and then calculating the ν-gap metric between the nominal plant and the perturbed plant, while including the weights. The extreme values of M_L, L and ΔT_t are also used. We make the assumption that if the extreme values of the parametric uncertainty are used, as well as numerous samples of plants with the uncertain parameters not at the extreme values, then it is very likely that the entire range of uncertainty is covered.

The value $\bar{\sigma}(\Phi(P_{vx}W_1, P_uW_1))$ between all the various perturbed plants P_uW_1 and the nominal plant $P_{vx}W_1$ is plotted and displayed in Figure 6.2. This is denoted $f(w)$, and denotes the worst case ν-gap metric between the nominal plant and any plant in the uncertainty set, at each frequency. Also, plotted on the same figure is the value $\rho(P_s, K)$ for the nominal plant and H_∞ loop shaping controller from Chapter 5. Clearly, the value of $\bar{\sigma}(\Phi(P_{vx}W_1, P_uW_1))$ exceeds the value of $\rho(P_s, K)$ for some plants in our defined uncertainty set. Therefore, although a value of $b_{P_s,K} = 0.62$ would usually be assumed to be satisfactory, we have that with our uncertainty set some plant and controller combinations that have no guaranteed stability margin and no guaranteed robust stability.

6.3 Extended H_∞ Loop Shaping Design Theory

In this section we present the algorithm that will be used to generate a controller that achieves guaranteed stability margins for a set of shaped uncertain plants.

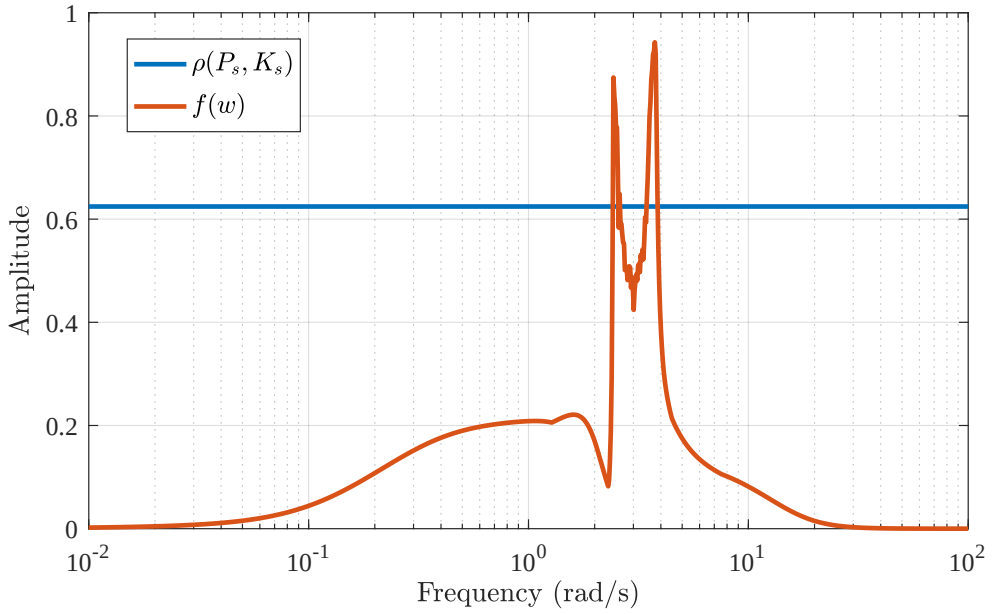

Figure 6.2: Magnitude of $\rho(P_s, K)$ and $f(w) = \max_{P_{s-unc}} \Phi(P_s, P_{s-unc})(jw)$

6.3.1 Theoretical Tools

Suppose we desire a minimum generalised stability margin $\inf_{P\in\Omega} b_{P,K} > \alpha$ for all plants in our uncertainty set $P \in \Omega$. In other words, the value of α is the worst-case stability margin that is required for all the plants in the set. Then, by the frequency-by-frequency robust stability theorem presented in Section 6.2, it is sufficient to have

$$\arcsin \rho(\mathbf{P}_1, \mathbf{K})(w) - \arcsin \bar{\sigma}(\Phi(\mathbf{P}_1, \mathbf{P})) > \arcsin \alpha, \forall w, \mathbf{P} \in \Omega,$$

which is equivalent to

$$\rho(\mathbf{P}_1, \mathbf{K})(w) > \sin(\arcsin \bar{\sigma}(\Phi(\mathbf{P}_1, \mathbf{P})) + \arcsin \alpha), \forall w, \mathbf{P} \in \Omega,$$

Now, if we set a real-rational stable transfer function $W_\delta(s)$ such that

$$|W_\delta(s)| > \sin(\arcsin \bar{\sigma}(\Phi(\mathbf{P}_1, \mathbf{P})) + \arcsin \alpha), \forall w, \mathbf{P} \in \Omega,$$

Then we need to guarantee that

$$\rho(\mathbf{P}_1, \mathbf{K})(w) > |W_\delta(s)| \tag{6.3.1}$$

Therefore we need that

$$\bar{\sigma}\left(\begin{bmatrix}\mathbf{I}\\ \mathbf{K}\end{bmatrix}(\mathbf{I}-\mathbf{P}_1\mathbf{K})^{-1}\begin{bmatrix}\mathbf{I} & \mathbf{P}_1\end{bmatrix}W_\delta\right)(jw) < 1 \quad \forall w$$

which is equivalent to

$$\left\|\begin{bmatrix}\mathbf{I}\\ \mathbf{K}\end{bmatrix}(\mathbf{I}-\mathbf{P}_1\mathbf{K})^{-1}\begin{bmatrix}\mathbf{I} & \mathbf{P}_1\end{bmatrix}W_\delta\right\|_\infty < 1$$

Now, given a normalized left coprime factorisation $\mathbf{P}_1 = \bar{\mathbf{M}}^{-1}\bar{\mathbf{N}}$, the following equality is given in Equation 5.2.19:

$$\left\|\begin{bmatrix}\mathbf{I}\\ \mathbf{K}\end{bmatrix}(\mathbf{I}-\mathbf{P}_1\mathbf{K})^{-1}\begin{bmatrix}\mathbf{I} & \mathbf{P}_1\end{bmatrix}\right\|_\infty = \left\|\begin{bmatrix}\mathbf{I}\\ \mathbf{K}\end{bmatrix}(\mathbf{I}-\mathbf{P}_1\mathbf{K})^{-1}\bar{\mathbf{M}}^{-1}\right\|_\infty$$

Therefore, in order to guarantee that the equality in Equation 6.3.1 holds, we need to guarantee that

$$\inf_K \left\|\begin{bmatrix}\mathbf{I}\\ \mathbf{K}\end{bmatrix}(\mathbf{I}-\mathbf{P}_1\mathbf{K})^{-1}\bar{\mathbf{M}}^{-1}W_\delta\right\|_\infty < 1 \tag{6.3.2}$$

The generalised plant for solving this H_∞ optimisation problems is shown in Figure 6.3, where the general objective is $\min_K ||\mathbf{T}_{zw}||_\infty$. $\mathbf{T}_{zw}$ is the closed-loop transfer function from input $\mathbf{w}$ to output $\mathbf{z}$, and measurement and control variables are denoted $\mathbf{y}$ and $\mathbf{u}$ respectively.

Formulating the general plant $\mathbf{G}$ for the optimisation in Equation 6.3.2 results in

$$\mathbf{G} = \begin{bmatrix}\begin{bmatrix}\mathbf{0}\\ \bar{\mathbf{M}}^{-1}W_\delta\end{bmatrix} & \begin{bmatrix}\mathbf{I}\\ \mathbf{P}_1\end{bmatrix}\\ \bar{\mathbf{M}}^{-1}W_\delta & \mathbf{P}_1\end{bmatrix}. \tag{6.3.3}$$

Therefore, the optimisation in Equation 6.3.2 is solved by applying the standard state-space solutions of the H_∞ optimisation problem, presented in Appendix A, using the generalised plant $\mathbf{G}$ as shown in Equation 6.3.3.

Proof: We now prove that the optimisation problem in Equation 6.3.2 is solved by using the generalised plant given in Equation 6.3.3. Firstly, consider a plant with left coprime factor uncertainty, shown in Figure 6.4. The transfer

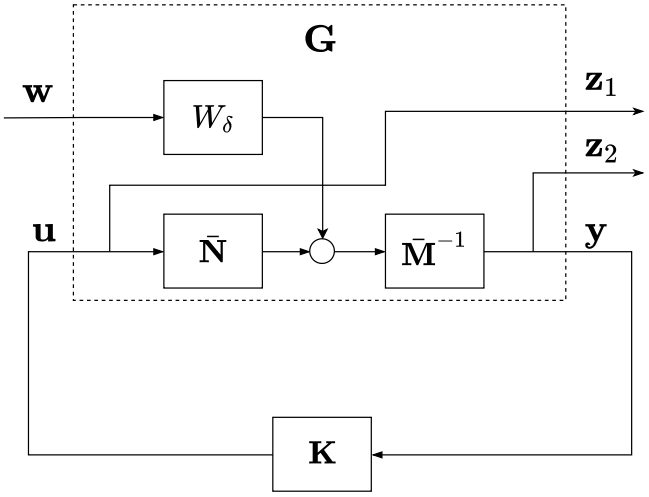

Figure 6.3: Generalised plant for solving extended robust stabilisation

function from $\mathbf{w}$ to $\mathbf{z}$ is derived directly from the figure as given in Equation 6.3.4.

$$\begin{bmatrix} \mathbf{z}_1 \\ \mathbf{z}_2 \end{bmatrix} = \begin{bmatrix} \mathbf{K} \\ \mathbf{I} \end{bmatrix} (\mathbf{I} - \mathbf{PK})^{-1} \bar{\mathbf{M}} \mathbf{w} \tag{6.3.4}$$

This system can be recast into the general configuration as shown in Figure 6.5. If it is desired to minimise the H_∞ norm of this transfer function, we can form the general plant $\mathbf{G}$ directly from the figure as

$$\mathbf{G} = \begin{bmatrix} \begin{bmatrix} \mathbf{0} \\ \bar{\mathbf{M}}^{-1} \end{bmatrix} & \begin{bmatrix} \mathbf{I} \\ \mathbf{P}_1 \end{bmatrix} \\ \bar{\mathbf{M}}^{-1} & \mathbf{P}_1 \end{bmatrix}. \tag{6.3.5}$$

The optimisation problem in Equation 6.3.2 is simply a weighted version of this - the weight W_δ is used as a shaping weight on the transfer function from $\mathbf{w}$ to $\mathbf{z}$ in a configuration that has left coprime factor uncertainty. Because of the equalities given in Equation 5.2.19, this is equivalent to shaping the frequency-by-frequency generalised stability margin $\rho(P_1, K)$. This completes the proof.

6.3.2 Algorithm

The optimisation problem in Equation 6.3.2 is for a general plant $\mathbf{P}_1$. The following can be considered an extended loop shaping design procedure similar to that presented in Vinnicombe [6]. The major difference between our algorithm to follow and the one from Vinnicombe is firstly, our algorithm includes

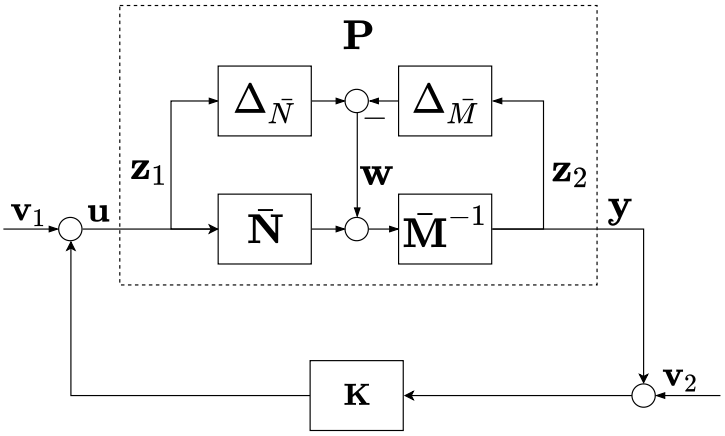

Figure 6.4: Feedback system with left coprime factor uncertainty

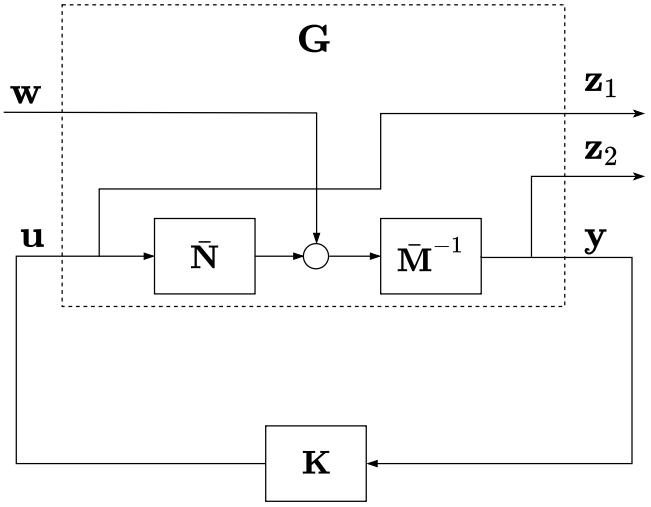

Figure 6.5: Feedback system with left coprime factor uncertainty cast into general configuration

the shaping weight W_1 in the algorithm. In other words, $\mathbf{P}_1 = \mathbf{P}_s$. Secondly, the algorithm by Vinnicombe uses Nevanlinna-Pick interpolation to solve the optimisation problem and therefore does not fit a real-rational transfer such as W_δ because the Nevanlinna-Pick interpolation solves the H_∞ optimisation directly in the frequency domain. Refer to Vinnicombe [6] for further details. The algorithm presented here is adapted from Zhou et al [74], but with a difference in how the performance weights are handled. The algorithm from Zhou et al. does not include the performance weight W_1 when the controller K_∞ is synthesised in step iii of the iteration. The new algorithm is presented in Algorithm 1.

Note that if $\beta > 1$ with $\alpha = 0$, it is necessary to terminate the algorithm and then repeat the algorithm after changing the shaping weights $\mathbf{W}_1$ and $\mathbf{W}_2$ to

Algorithm 1: Extended loop shaping design procedure

Initialisation:

i The nominal plant $\mathbf{P}_1$ is shaped with pre- and post-compensating weights to achieve a desirable loop shape that achieves satisfactory time-domain performance with the nominal plant. The shaped plant $\mathbf{P}_s = \mathbf{W}_2\mathbf{P}_1\mathbf{W}_1$ is formed.

ii Using the shaped plant $\mathbf{P}_s$ with state space matrices $(\mathbf{A}, \mathbf{B}, \mathbf{C}, \mathbf{D})$, solve the generalised filter algebraic Riccati equation given in Equation 5.2.11 to obtain the filter gain $\mathbf{L}$. Form the normalisd left coprime factors of $\mathbf{P}_s = \bar{\mathbf{M}}^{-1}\bar{\mathbf{N}}$, as:

$$\left[\begin{array}{cc} \bar{\mathbf{N}} & \bar{\mathbf{M}} \end{array}\right] \overset{s}{=} \left[\begin{array}{cc|cc} \mathbf{A}+\mathbf{LC} & \mathbf{B}+\mathbf{LD} & \mathbf{L} \\ \hline \mathbf{R}^{-1/2}\mathbf{C} & \mathbf{R}^{-1/2}\mathbf{D} & \mathbf{R}^{-1/2} \end{array}\right] \tag{6.3.6}$$

iii Compute

$$f(w) = \sup_{P\in\Omega} \bar{\sigma}(\Phi(\mathbf{W}_2\mathbf{P}_1\mathbf{W}_1, \mathbf{W}_2\mathbf{P}\mathbf{W}_1))$$

Iteration:

i Set $\alpha = 0$.

ii Fit a stable real-rational and minimum phase $W_\delta(s)$ so that

$$|W_\delta(jw)| > \sin(\arcsin f(w) + \arcsin \alpha), \forall w$$

iii Solve

$$\beta = \inf_{K_\infty} \left\| \left[\begin{array}{c} \mathbf{I} \\ \mathbf{K}_\infty \end{array}\right] (\mathbf{I} - \mathbf{P}_s\mathbf{K}_\infty)^{-1}\bar{\mathbf{M}}^{-1} W_\delta \right\|_\infty$$

by using the generalised plant $\mathbf{G}$ given in Equation 6.3.3, with $\mathbf{P}_1 = \mathbf{P}_s$.

iv If $\beta < 1$, increase α and reiterate. If $\beta > 1$, decrease α and reiterate. Lastly, if $\beta \approx 1$, terminate.

Termination:

i The final controller is $\mathbf{K}_{ELS} = \mathbf{W}_1\mathbf{K}_\infty\mathbf{W}_2$

ii Compare $\rho(\mathbf{W}_2\mathbf{P}_1\mathbf{W}_1, \mathbf{K}_\infty)$ and $f(w)$. The final result should be that

$$\rho(\mathbf{W}_2\mathbf{P}_1\mathbf{W}_1, \mathbf{K}_\infty)(w) > \sin(\arcsin f(w) + \arcsin \alpha), \forall w$$

reduce the value of $f(w)$. Vinnicombe [71] provides some guidelines to achieve lower values of $f(w)$.

By the frequency-by-frequency robust stability theorem in Section 6.2, the final controller should be such that $b_{W_2PW_1,K_\infty} > \alpha \; \forall \; \mathbf{P} \in \Omega$, which means we have a guaranteed generalised stability margin for all the plants in our uncertain set. This is because we have that

$$\rho(\mathbf{W}_2\mathbf{P}_1\mathbf{W}_1, \mathbf{K}_\infty)(w) > \sin(\arcsin f(w) + \arcsin \alpha), \forall w \tag{6.3.7}$$

and the quantity $\rho(\mathbf{W}_2\mathbf{P}\mathbf{W}_1, \mathbf{K}_\infty)(w)$ can only be reduced by at most the value of $f(w)$.

As mentioned earlier, the key difference here is that the algorithm presented by Zhou et al. [74] uses the *unweighted* plant in step iii of the iteration. Essentially, their algorithm uses pre- and post-compensating weights to shape performance of the nominal plant, and then they use the worst-case ν-gap metric between the shaped nominal and shaped uncertain plants to determine a frequency-by-frequency target for the general stability margin of the *unshaped* plant. However, we discovered that this then formulates an H_∞ controller that gives the guaranteed stability margin for the unshaped plant, but when the compensating weights are reintroduced into the final controller $\mathbf{K}_{ELS} = \mathbf{W}_2\mathbf{K}_\infty\mathbf{W}_1$, that general stability margin can deteriorate. Therefore, the only way to guarantee that the general stability margin is achieved for the plant with the compensating weights present is to include the compensating weights in the optimisation in equation 6.3.2 (and therefore into step iii in the iteration, as denoted by $\mathbf{P}_1 = \mathbf{P}_s$).

6.4 Quadrotor and Payload Translational Control: Extended H_∞ Loop Shaping Design

In this section, we present a novel robust flight control system for a quadrotor with a suspended payload. A quadrotor velocity control system is designed using the extended H_∞ loop shaping algorithm presented earlier in the chapter. The control system aims to be robust to the uncertainties in the system, which are the variations in payload mass, the cable length, and the magnitude and direction of the quadrotor thrust force. First, an overview of the controller is presented, followed by the detailed design of the horizontal velocity controllers. Thereafter, the controller is verified using the high-fidelity simulation model.

6.4.1 Overview

The structure of the quadrotor and suspended payload translational control system with the extended H_∞ loop shaping controller, denoted K_{ELS}, is shown in Figure 6.6.

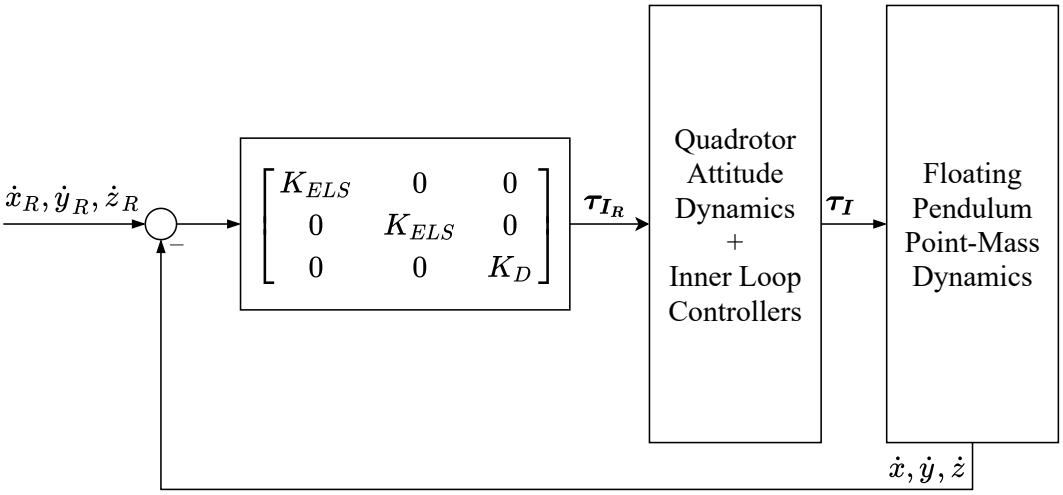

Figure 6.6: Extended H_∞ loop shaping controller

In this configuration, the extended H_∞ loop shaping controller replaces the standard H_∞ loop shaping controller, denoted K_{LS}, presented in Chapter 5. Two identical, decoupled controllers are used to control the quadrotor velocity in the North and East directions, with a PI controller controlling the vertical velocity of quadrotor. The PI controller is the same controller that was presented in Chapter 4. Therefore, this section will focus on the design of the horizontal velocity controllers.

6.4.2 Quadrotor Horizontal Velocity Control

We use the algorithm presented in the previous section to design a quadrotor horizontal velocity controller that has theoretically guaranteed robust stability to variations in the payload mass, cable length, and thrust value. The controller presented in this section replaces the standard H_∞ loop shaping controller designed in Chapter 5, and is responsible for controlling the horizontal velocity of the quadrotor. The controller can be shown in block diagram as in Figure 6.7, along with the linear model used to design the controller, which is $P_{vx}(s)$. As mentioned in earlier chapters, $P_{vx}(s)$ contains the dynamics of the floating pendulum in the horizontal direction, P_{fpx}, augmented with dynamics of the tilt angle control system, $T_T(s)$.

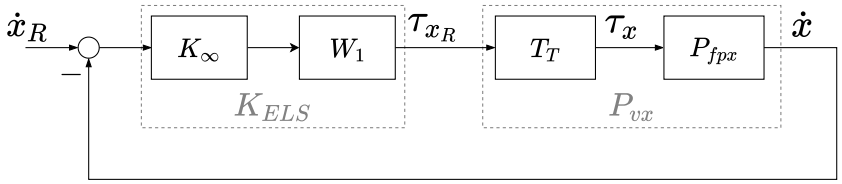

Figure 6.7: Extended H_∞ loop shaping controller used to control quadrotor horizontal velocity

The controller consists of a pre-compensating weight W_1 that is designed to improve the open-loop frequency response of the plant, and a controller K_∞. The pre-compensating weight is chosen to meet the design objectives in terms of transient performance and steady-state tracking. The controller K_∞ is responsible for providing guaranteed robust stability to the uncertainties in the system and is synthesised using the algorithm presented in the previous section.

The controller receives the error between measurements of the current quadrotor velocity, $\dot{x}$ ($\dot{y}$ for the East velocity controller), and velocity commands $\dot{x}_R$ ($\dot{y}_R$ for the East velocity controller). The controller actuates the horizontal components of the reference force $\boldsymbol{\tau}_R$, τ_{x_R} for the North controller (τ_{y_R} for the East controller).

6.4.2.1 Application of Extended H_∞ Loop Shaping Design Algorithm

The design objectives of the extended H_∞ loop shaping controller are the same as for the LQI controller presented in Chapter 4 and the standard H_∞ loop shaping controller presented in Chapter 5. Specifically, the requirements are a closed-loop bandwidth of 0.7 rad/s and zero steady-state tracking error to step commands.

With the objectives in mind for step i of the initialisation, the compensating weight W_1 that is used to shape the nominal plant is the shaping weight described in Section 5.3.2.1. Therefore, we have the compensated system $P_s = P_{vx}W_1$. This provides a compensated open-loop bandwidth of 1 rad/s, and a slope of -20 dB per decade in the low-frequency region, which satisfies the design objectives. With this shaped plant, the normalised left coprime factor is calculated in step ii of the initialisation.

For step iii of the initialisation, Figure 6.8 present a plot of the worst-case frequency-by-frequency ν-gap metric for all the plants in the uncertainty set, which is $f(w) = \sup_{P\in\Omega} \bar{\sigma}(\Phi(P_{vx}W_1, PW_1))$. P represents any plant in the uncertainty set, which is the quadrotor and suspended payload with variations in payload mass M_L, cable length L, and thrust uncertainty T_t.

For the iteration, Figure 6.8 presents the quantity $\sin(\arcsin f(w) + \arcsin \alpha)$, where α is our minimum desired stability margin for all the shaped uncertain plants. For $\alpha = 0.11$, the desired value of $\beta \approx 1$ was achieved.

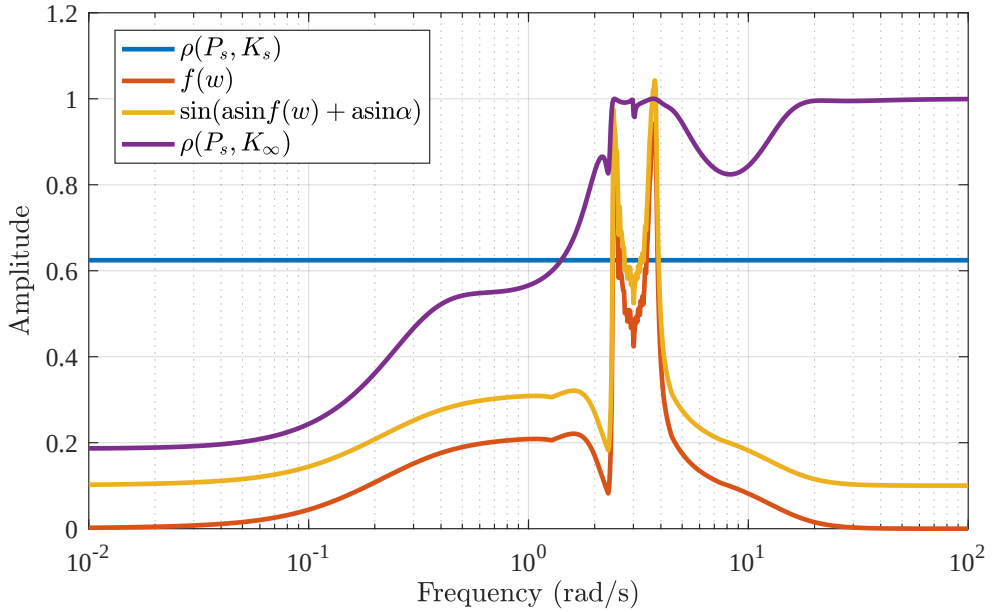

Figure 6.8: Magnitude of $\rho(P_s, K_\infty)$ and $\sin(\arcsin f(w) + \arcsin \alpha)$

Figure 6.8 also presents the frequency response of the quantity $\rho(P_s, K_\infty)$, where K_∞ is the synthesised controller. The objective of $\rho(Ps, K_\infty)(w) > \sin(\arcsin f(w) + \arcsin \alpha)\ \forall\ w$ was achieved, except for a small range near $w = 3$ rad/s where $\rho(Ps, K_\infty)(w) < \sin(\arcsin f(w) + \arcsin \alpha)$. This is purely due to the fact that the quantity $\sin(\arcsin f(w) + \arcsin \alpha)$ slightly exceeds 1 in this region. However, the value of $\rho(P_s, K_\infty)$ is still greater than the quantity of $f(w)$ at this region, so we still have guaranteed robust stability. This means that we are close to the objective of $\inf_{P\in\Omega} b_{PW_1,K_\infty} > \alpha$ (achieving the objective perfectly is not necessary, as α is a just a stability margin). So we state that the algorithm was successful in given a minimum stability margin $b_{PW_1,K_\infty} \approx \alpha$ for all the plants in our uncertainty set.

Also, from the figure, we can see that the value of $b_{P_s,K_\infty} = \min_w \rho(P_s, K_\infty)(w)$ achieves a value of $b_{P_s,K_\infty} \approx 0.2$. This is fairly low so we expect that the loop shape of the final loop system $P_{vx}K_{ELS} = P_{vx}W_1K_\infty$ could differ significantly from the desired loop shape $P_{vx}W_1$, meaning transient performance may be sacrificed.

Figure 6.9 presents the frequency response of the open loop system $P_{vs}W_1K_\infty = P_sK_\infty = P_{vx}K_{ELS}$. We observe that the frequencies at the resonant peak of the

plant P_{vx} are further attenuated by the controller K_∞. This is a natural consequence of the controller attempting to add significant general stability margin $\rho(Ps, K_\infty)(w)$ at that point. Also, as predicted by the low value of b_{P_s,K_∞}, the open-loop frequency response of the compensated system with controller, $P_{vx}W_1K_\infty$, is substantially different to the response of the compensated system without the controller, $P_{vx}W_1$. A slope of -20 dB per decade is maintained in the low-frequency region, but the overall gain of the system is lowered by the controller. This reduces the crossover frequency to 0.4 rad/s, from the original bandwidth of 0.7 rad/s.

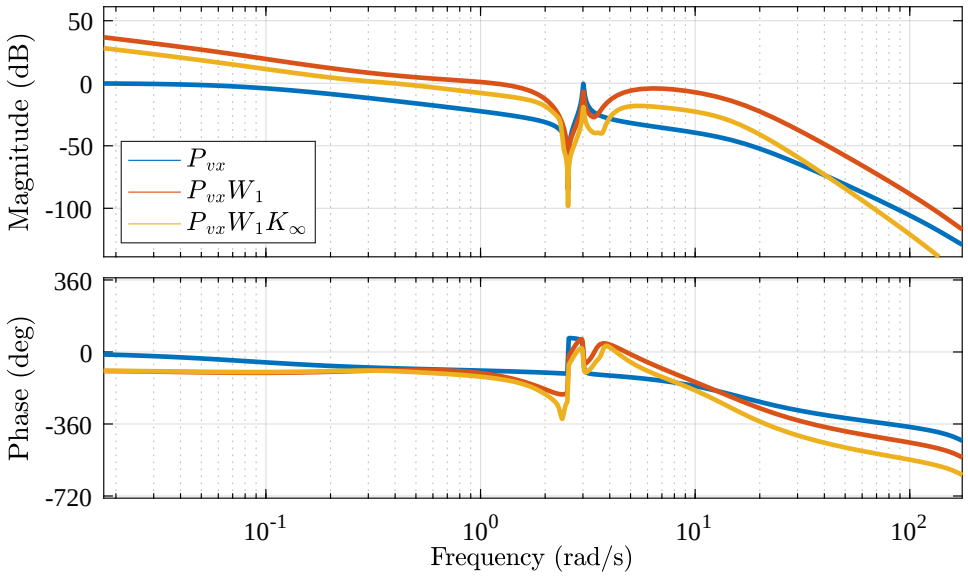

Figure 6.9: Bode plot of plant P_{vs}, shaped plant $P_s = P_{vs}W_1$, and shaped plant with extended H_∞ controller $P_sK_\infty = P_{vx}K_{ELS}$.

Figure 6.10 shows the frequency response of the controller K_∞, as well as the response of the controller $K_{ELS} = W_1K_\infty$. Note how the shaping weight W_1 and the synthesised controller K_∞ together form a relatively wide notch at the resonant frequencies. This is indicative of the behaviour of the controller: the controller acts to ensure robust stability by attenuating all the possible resonant frequencies. The width of the notch is governed by the change in natural frequency of the plant. Also, the change in loop shape is fairly significant - the controller K_∞ significantly reduces the gain in the system. This is because of the low value of b_{P_s,K_∞} that was achieved.

The controller is implemented with the linear model as shown in Figure 6.7. A step response to a velocity command is shown in Figure 6.11. Clearly, the algorithm gives a controller that adds significant damping to all of the plants

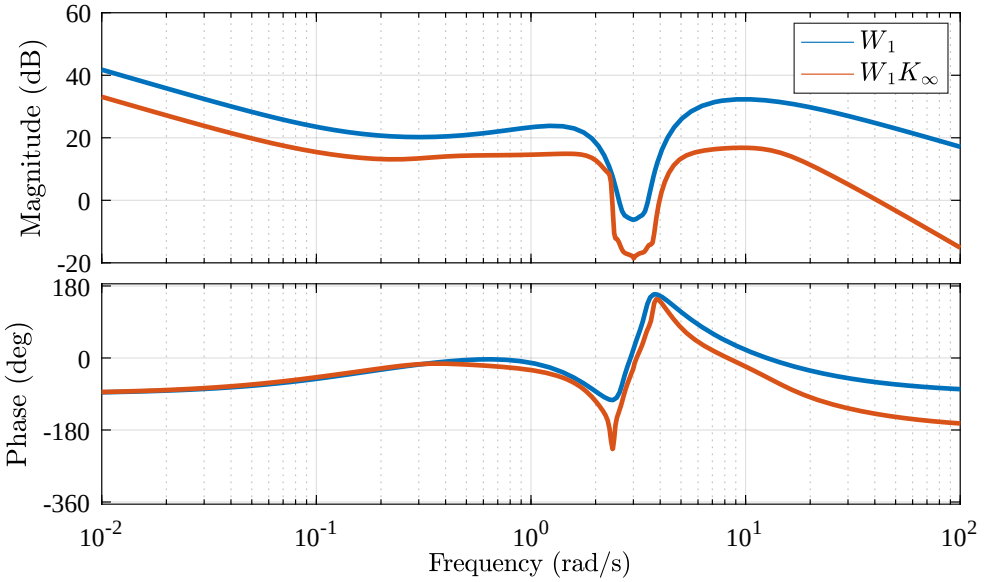

Figure 6.10: Bode plot of extended H_∞ controller $K_{ELS} = W_1 K_\infty$.

in the uncertainty set, due to the guaranteed minimum stability margin. Also clear is that the time-domain performance (in terms of rise time and overshoot) is slower than with the previous two controllers. The robust controller no longer reaches the time-domain performance requirement of having a rise time of about 3-5 seconds.

A Monte Carlo style plot of the poles and zeros of the closed-loop system with the extended H_∞ loop shaping controller is shown in Figure 6.12. This plot shows the poles and zeros of a the closed-loop system when various plants in the uncertainty set are sampled. Also shown are the poles and zeros of the nominal, uncompensated, open-loop plant P_{vx}. Clearly, there are no closed-loop systems in the closed-loop uncertainty set that have poles in the right-half plane of the complex plane, confirming that the system does have robust stability.

Monte Carlo style Bode plots of the open- and closed-loop systems with the extended H_∞ loop shaping controller are given in Figure 6.13 and Figure 6.14, respectively. It is clear from these figures that when the uncertainty in the plant is considered, the frequency of the lightly-damped resonant mode of the system is shifted, but the extended H_∞ loop shaping controller prevents the entire set of resonant peaks from reaching the 0 dB point, which is further evidence of stability.

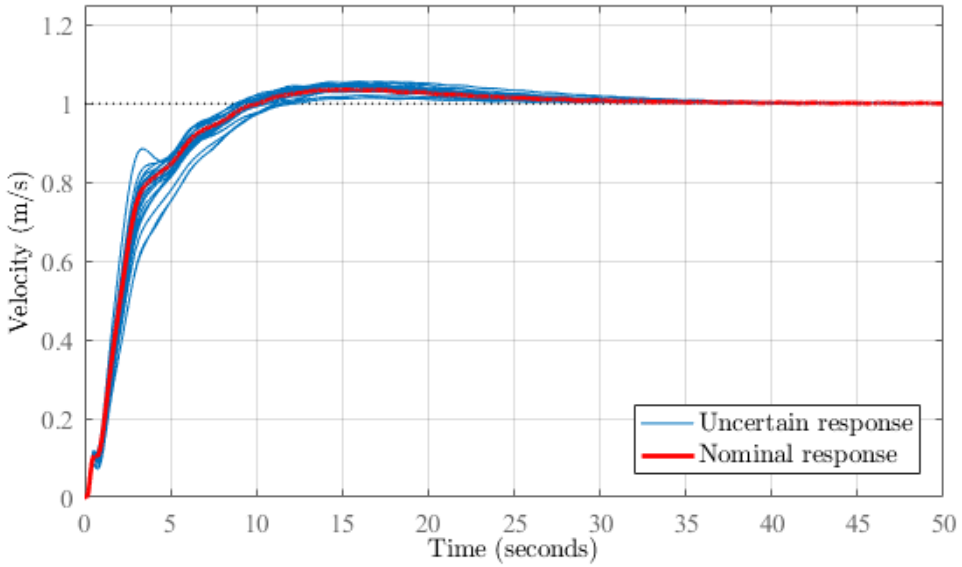

Figure 6.11: Step response of closed-loop system with extended H_∞ loop shaping controller to a reference velocity command

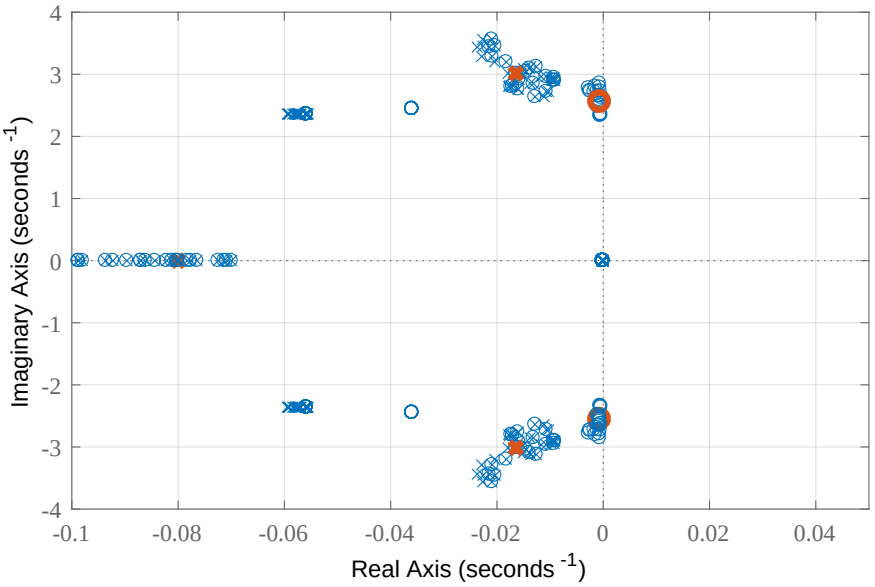

Figure 6.12: Poles and zeros of velocity control system with extended H_∞ loop shaping controller. $\times$ is used to mark poles, and $\circ$ is used to mark zeros. Also shown are poles and zeros of the nominal open-loop system P_{vx}, shown in red.

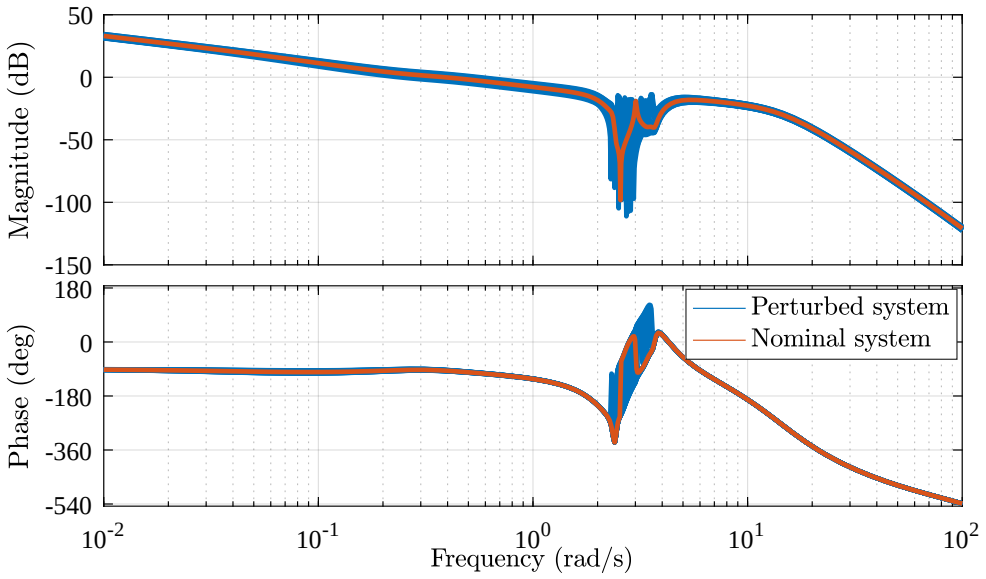

Figure 6.13: Bode plot of open-loop system with extended H_∞ loop shaping controller. Also shown are the responses with perturbed plants from the uncertainty set.

6.4.3 Controller Performance with Nonlinear Model

The extended H_∞ loop shaping quadrotor and payload translational control system was implemented and verified using the high-fidelity non-linear simulation, as shown in Figure 6.6. The closed-loop step response of the horizontal velocity controller is shown in Figure 6.15, along with the nominal response of the linear model P_{vx}. The horizontal velocity step response was performed in the North direction (but could also have been performed in the East direction with a similar result). The references for the East and vertical velocity controllers were set to zero, and these other two translational controllers therefore acted only to regulate the East and vertical velocities to zero, and to reject external disturbances.

This figure shows that there is good agreement between the response of the linearised model and the simulation. In both cases, when the nominal values of the thrust scalar T_t, payload mass M_L, and cable length L are considered, the payload swinging motion is damped, as is evident by lack of the oscillations in the quadrotor velocity.

The resulting payload swing angle θ_L from the simulation is shown in Figure 6.16 (with no motion in the East direction, $\phi_L \approx 0$). Clearly, there significant damping added to the payload swinging motion, which was a design objective.

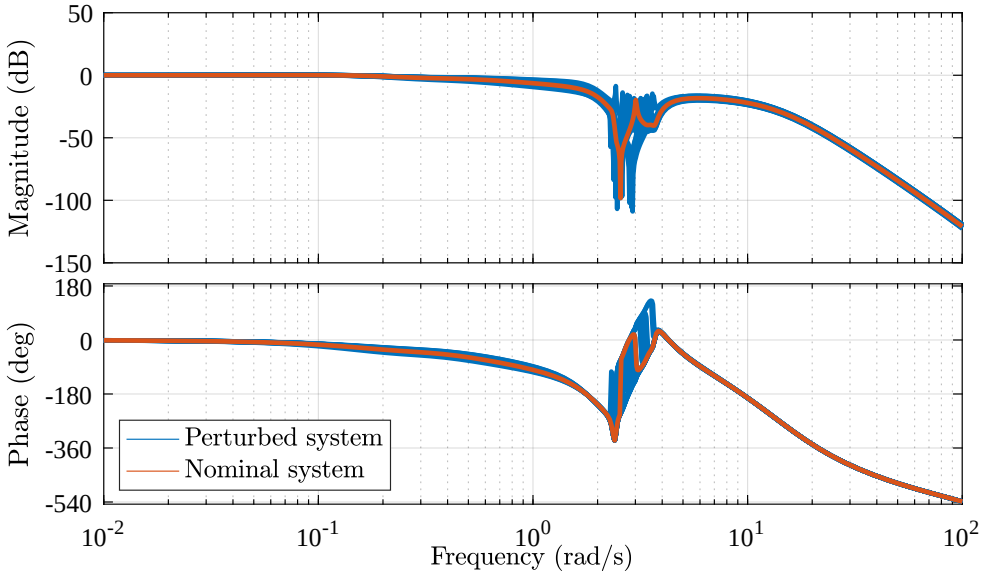

Figure 6.14: Bode plot of closed-loop system with extended H_∞ loop shaping controller. Also shown are the responses with perturbed plants from the uncertainty set.

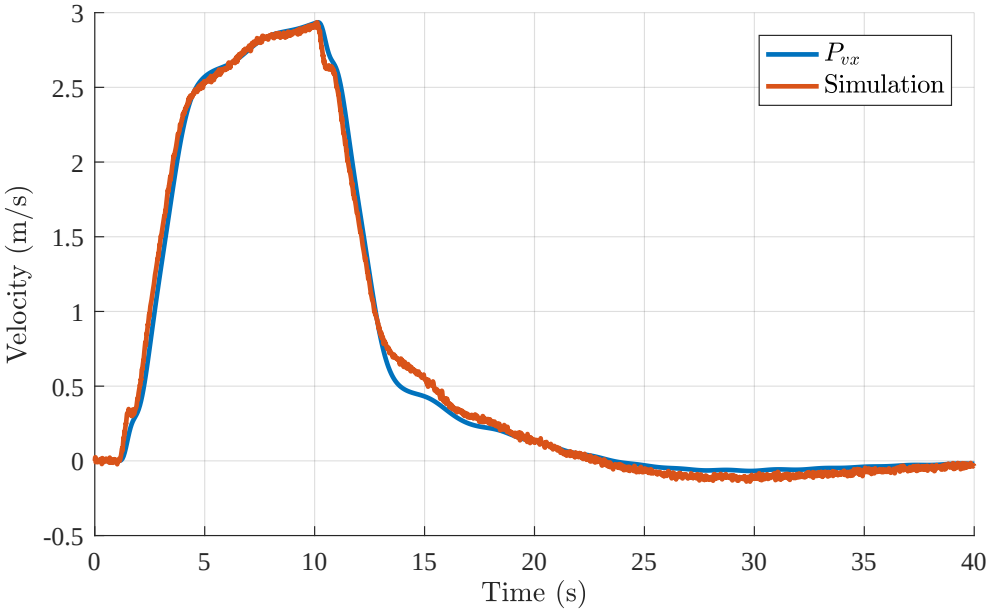

Figure 6.15: Response of quadrotor velocity $\dot{x}$ to a reference velocity command $\dot{x}_R$, with extended H_∞ loop shaping controller.

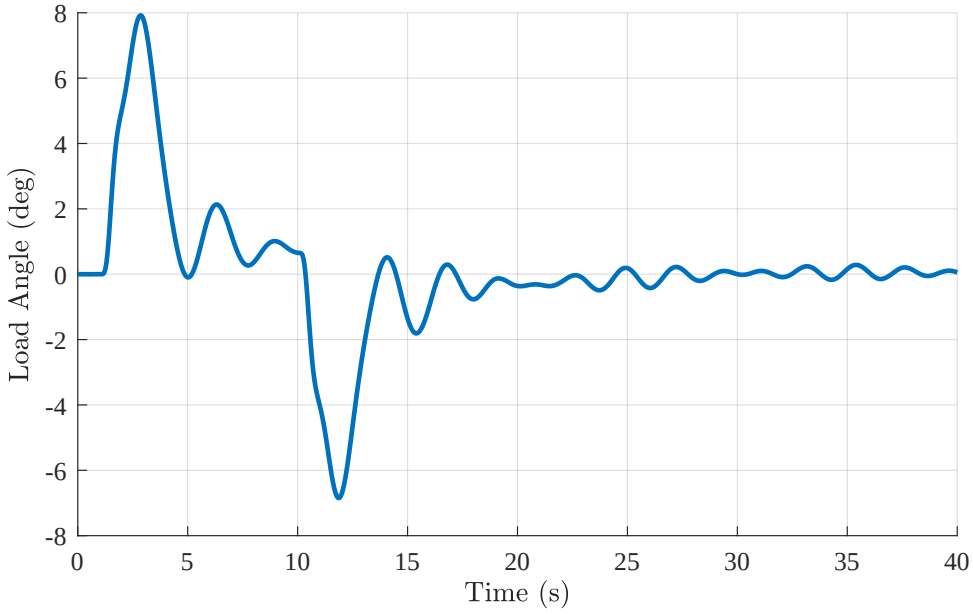

Figure 6.16: Response of payload angle θ_L to a reference velocity command $\dot{x}_R$, with extended H_∞ loop shaping controller.

A Monte Carlo simulation was performed using the high-fidelity simulation. The uncertain parameters in the plant were varied, and the same quadrotor velocity command was given to the controller. The results for the quadrotor velocity are given in Figure 6.17. The results for the payload angle θ_L are given in Figure 6.18. With the Monte Carlo simulation, we see that stability for all the plants in the uncertainty set is achieved. This agrees with the results shown in Figure 6.11, and the fact that the extended H_∞ loop shaping controller is theoretically guaranteed to provide robustness to all the plants in the uncertainty set.

The Monte Carlo simulation of the payload angle θ_L shows that in the worst case, a small payload angle oscillation can persist for some time. The reason for this is that the resulting payload angle oscillation is too small to have any significant effect on quadrotor velocity. This means the controller cannot actively add damping to the motion, because the feedback measurement, which is quadrotor velocity, does not contain the oscillation in any significant way. Thus, the controller effectively ignores that small oscillation and allows it to decay according to the natural damping of the plant, which is low at low quadrotor velocities. However, the system is still stable, as the controller will not excite unstable oscillations in the quadrotor velocity, like the other controllers presented in previous chapters would.

The controller K_{ELS} displays significantly better robustness to the uncertainties in the system, but this comes at the cost of less performance in terms

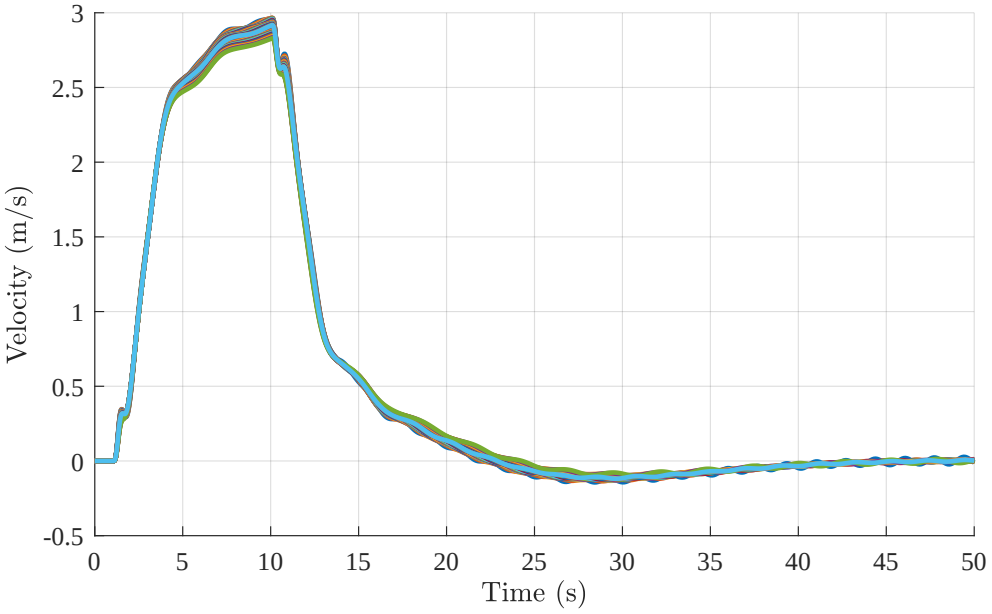

Figure 6.17: Monte Carlo simulation of quadrotor velocity $\dot{x}$, extended with H_∞ loop shaping controller, using high-fidelity simulation

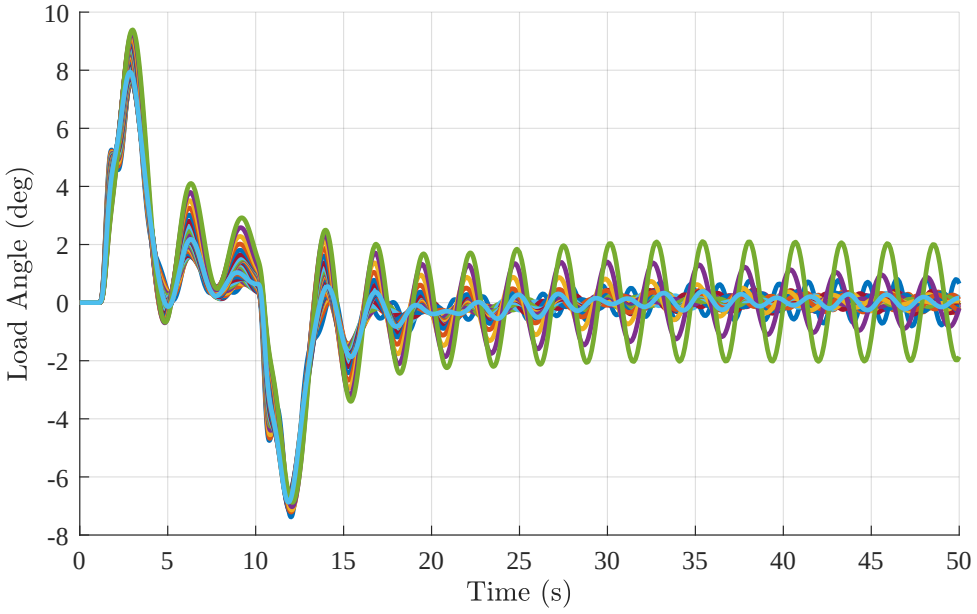

Figure 6.18: Monte Carlo simulation of payload angle θ_L, with extended H_∞ loop shaping controller, using high-fidelity simulation

of rise-time and bandwidth. In the next chapter, we present a two degrees-

of-freedom version of the extended H_∞ loop shaping controller that aims to achieve better transient performance while maintaining the robustness properties achieved with the controller K_{ELS}.

A simulation with non-zero quadrotor velocity commands in North, East, and Down directions was performed. In this case, to maintain clarity of the figures, only the perturbed case with $M_L = 6$kg, $L = 1.7$m and $T = 1.2$ was simulated. The quadrotor velocity is plotted in Figure 6.19. The payload angles are plotted in Figure 6.20. As in the case with the controllers K_{LQI} and K_{LS}, we see very similar performance compared to the case when a non-zero velocity command in the North direction only was given.

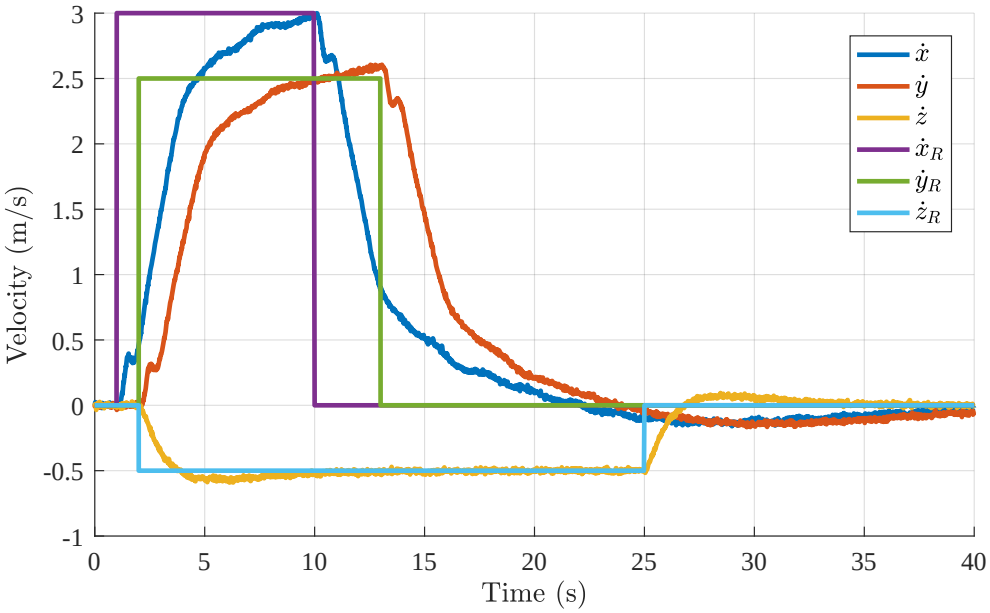

Figure 6.19: Response of quadrotor velocity $\dot{\mathbf{p}}$ to a reference velocity command $\dot{\mathbf{p}}_R$, with extended H_∞ loop shaping controller. In this simulation, the uncertain plant parameters are set to $M_L = 6$kg, $L = 1.7$m and $T = 1.2$.

6.5 Summary

In this chapter, an extended H_∞ loop shaping design algorithm was presented. The algorithm aims to maximize the residual stability margin given by the controller to all the plants in the uncertainty set. This algorithm was successfully used to design a robust flight control system that controls the velocity of the quadrotor. In contrast to the LQI controller and the H_∞ loop shaping controller designed in previous chapters, the extended H_∞ loop shaping controller

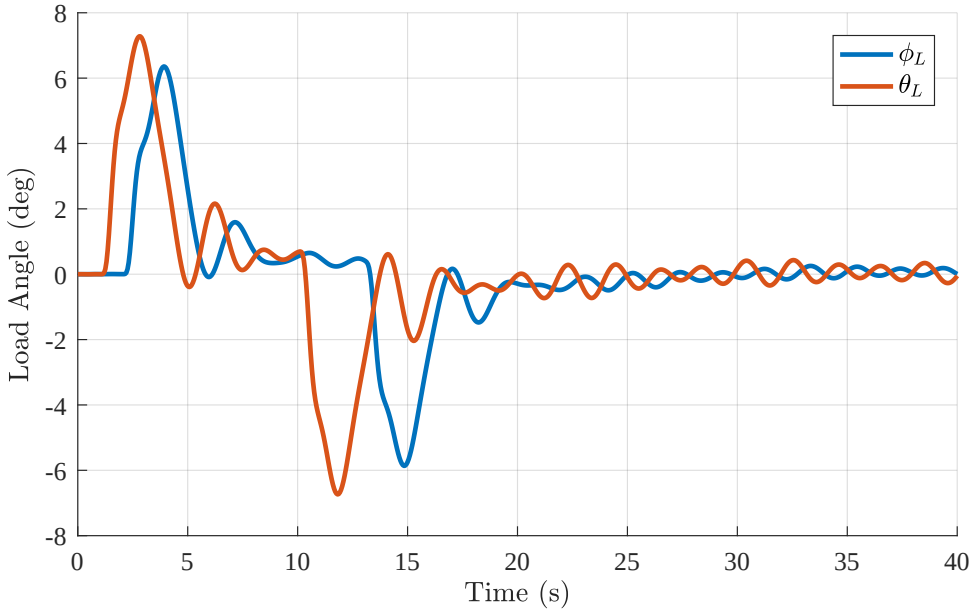

Figure 6.20: Response of payload angle ϕ_L and θ_L to a reference velocity command $\dot{\mathbf{p}}_R$, with extended H_∞ loop shaping controller. In this simulation, the uncertain plant parameters are set to $M_L = 6$kg, $L = 1.7$m and $T = 1.2$.

gives guaranteed robust stability. The system is robust to all the expected uncertainties in payload mass M_L, cable length L, and thrust uncertainty T_t. The controller also adds damping to the swinging motion of the suspended payload.

The maximum value the general stability margin b_{P_s,K_∞} that was achieved was fairly low (0.2). This means the loop shape of the final system differed from the loop shape that was designed using the shaping weight W_1. This resulted in a substantial decrease in the open-loop gain of the system, and consequently, slower transient performance in terms of rise time. In the next chapter, we present a robust two-degrees-of-freedom design that aims to achieve better transient performance.

Chapter 7

Robust Trajectory Tracking

In the last chapter, we presented an extended loop shaping algorithm that relies on H_∞ optimization to ensure that a feedback system with robust stability can be synthesised. In this chapter, we consider the problem of meeting more stringent time-domain performance requirements. To this end, this chapter first presents a quadrotor velocity control system based on a two-degrees-of-freedom version of the standard H_∞ loop shaping design procedure.

Thereafter, a novel two-degrees-of-freedom extended H_∞ loop shaping controller is presented. The extended H_∞ loop shaping controller from the last chapter is augmented with a pre-filter to create a two-degrees-of-freedom controller. The aim is to improve the time-domain performance of the velocity controller while still maintaining robust stability.

Finally, a different approach to aggressive manoeuvring is taken whereby input shaping is used to shape arbitrary inputs into the system in order to cancel residual vibrations of the suspended payload. This will be used in a feedforward configuration whereby shaped input force commands are used to drive the quadrotor velocity directly. The extended H_∞ loop shaping controller is also used to correct deviations from an expected nominal velocity trajectory, forming a robust flight control system capable of agile swing-free manoeuvres.

7.1 Two-Degrees-of-Freedom H_∞ Loop Shaping

In this section we present the design of a two-degrees-of-freedom version of a standard H_∞ loop shaping controller.

7.1.1 Overview

The H_∞ loop shaping controller designed in Section 5.2.3.3 was designed by forming a shaping weight W_1 to meet frequency domain performance criteria, and then performing robust stabilisation for coprime factor uncertainty. This resulted in a controller $\mathbf{K}_{LS} = \mathbf{W}_1\mathbf{K}$ that achieved a certain generalised stability margin $b_{\mathbf{P}_s,\mathbf{K}}$. As presented in Section 5.2.3.1, a high value of $b_{\mathbf{P}_s,\mathbf{K}}$ means frequency domain performance is not lost through the robust stabilisation step to synthesise $\mathbf{K}$. However, it may be the case that we wish to further improve the performance of the system. More specifically, we can improve the reference tracking ability of the controller by adding another degree of freedom to the controller.

The idea is that one degree of freedom is designed to meet robust stability requirements through feedback of measurement signals. The other degree of freedom is a pre-filter that is designed to make the closed-loop response from the reference inputs to the outputs behave in the same way as a reference system $\mathbf{T}_{ref}$.

The final structure of the controller is shown in Figure 7.1. The controller consists of a pre-compensating shaping weight $\mathbf{W}_1$, similar to the standard H_∞ loop shaping configuration. The post-compensating performance weight $\mathbf{W}_2$ is usually omitted in the two-degrees-of-freedom design. The controller also consists of a robustifying feedback controller $\mathbf{K}_2$, which is very similar to the robustifying controller $\mathbf{K}$ in the standard H_∞ loop shaping design. A pre-filter $\mathbf{K}_1$ is added to the controller configuration in order to improve the tracking performance of the system. Reference inputs are "shaped" by the pre-filter in order to achieve a more desirable transient response from the reference input to the plant output. Lastly, the controller contains a steady-state gain $\mathbf{W}_i$ that compensates for the case when the pre-filter does not have a steady-state gain of unity, which would cause a steady-state gain between the reference input and the plant output that is not unity.

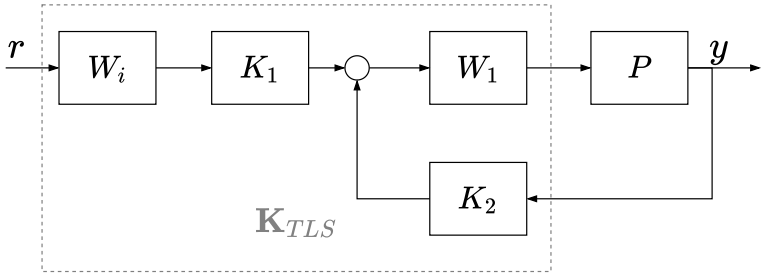

Figure 7.1: Two-degrees-of-freedom H_∞ loop shaping controller

7.1.2 Problem Formulation

The method used here is from Hoyle et al. [76] and can be considered a two-degrees-of-freedom version of the H_∞ loop shaping design procedure used in Chapter 5. The design problem can be shown as in Figure 7.2.

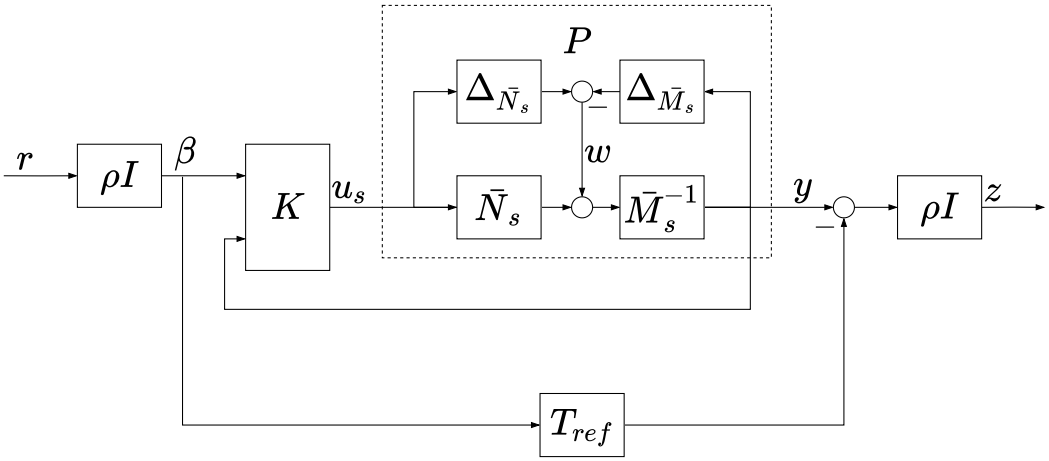

Figure 7.2: Two-degrees-of-freedom H_∞ loop shaping problem

Partitioning the controller as $\mathbf{K} = \begin{bmatrix} \mathbf{K}_1 & \mathbf{K}_2 \end{bmatrix}$, the control signal is given as

$$\mathbf{u} = \begin{bmatrix} \mathbf{K}_1 & \mathbf{K}_2 \end{bmatrix} \begin{bmatrix} \boldsymbol{\beta} \\ \mathbf{y} \end{bmatrix}$$

in which the $\mathbf{K}_1$ is a pre-filter and $\mathbf{K}_2$ is the feedback controller. A more intuitive view of the controller is shown in Figure 7.3, whereby the controller $\mathbf{K}$ is expanded into the pre-filter $\mathbf{K}_1$ and the feedback controller $\mathbf{K}_2$ graphically. Clearly, the inner feedback loop resembles the feedback loop shown in Figure 5.6, but with a left coprime factorisation of a shaped plant $\mathbf{P}_s = \mathbf{M}_s^{-1}\mathbf{N}_s$ instead of a left coprime factorisation of an unshaped plant $\mathbf{P} = \mathbf{N}\mathbf{M}^{-1}$.

The purpose of the pre-filter is to ensure that

$$||(\mathbf{I} - \mathbf{P}_s\mathbf{K}_2)^{-1}\mathbf{P}_s\mathbf{K}_1 - \mathbf{T}_{ref}||_\infty \leq \gamma\rho^{-2} \tag{7.1.1}$$

where $\mathbf{T}_{ref}$ is the desired closed loop transfer function which is chosen by the designer. This reference transfer function introduces additional time-domain specifications into the optimisation problem as the pre-filter $\mathbf{K}_1$ is synthesised to make the actual response as close to the reference response as possible. The constant ρ is chosen to emphasise model matching (higher values of ρ) or to emphasise the standard robust stabilisation (lower values of ρ). From Figure 7.3, we have that

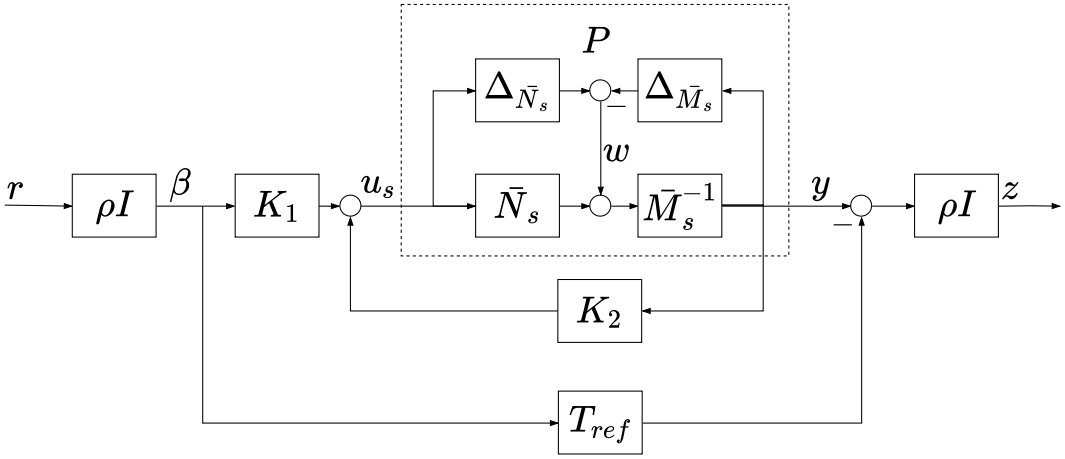

Figure 7.3: Two-degrees-of-freedom H_∞ loop shaping problem with controller $\mathbf{K}$ expanded

$$\begin{bmatrix} \mathbf{u}_s \\ \mathbf{y} \\ \mathbf{z} \end{bmatrix} = \begin{bmatrix} \rho(\mathbf{I}-\mathbf{K}_2\mathbf{P}_s)^{-1}\mathbf{K}_1 & \mathbf{K}_2(\mathbf{I}-\mathbf{P}_s\mathbf{K}_2)\bar{\mathbf{M}}_s^{-1} \\ \rho(\mathbf{I}-\mathbf{P}_s\mathbf{K}_2)\mathbf{P}_s\mathbf{K}_1 & (\mathbf{I}-\mathbf{P}_s\mathbf{K}_2)\bar{\mathbf{M}}_s^{-1} \\ \rho^2[(\mathbf{I}-\mathbf{P}_s\mathbf{K}_2)\mathbf{P}_s\mathbf{K}_1 - \mathbf{T}_{ref}] & \rho(\mathbf{I}-\mathbf{P}_s\mathbf{K}_2)\bar{\mathbf{M}}_s^{-1} \end{bmatrix} \begin{bmatrix} \mathbf{r} \\ \mathbf{w} \end{bmatrix} \tag{7.1.2}$$

Minimising the H_∞ norm of this transfer function will synthesise the desired controllers. Note that in Equation 7.1.2 the matrix elements at positions (1,2) and (2,2) come from the standard robust stabilisation for coprime uncertainty problem. The elements at positions (1,1) and (2,1) limit actuator usage. The element at (3,1) is the model-matching block, and the element at (3,3) is similar to the element at (2,2) and corresponds to the performance of the inner feedback loop. If ρ is chosen to be zero, we obtain the standard robust stabilisation problem from Section 5.3.2.2.

In order to solve the H_∞ optimisation, we can form the generalised plant $\mathbf{G}$ as

$$\begin{bmatrix} \mathbf{u}_s \\ \mathbf{y} \\ \mathbf{z} \\ \hdashline \boldsymbol{\beta} \\ \mathbf{y} \end{bmatrix} = \begin{bmatrix} \mathbf{G}_{11} & \mathbf{G}_{12} \\ \mathbf{G}_{21} & \mathbf{G}_{22} \end{bmatrix} \begin{bmatrix} \mathbf{r} \\ \mathbf{w} \\ \hdashline \mathbf{u}_s \end{bmatrix} \tag{7.1.3}$$

$$= \left[\begin{array}{ccc} \mathbf{0} & \mathbf{0} & \mathbf{I} \\ \mathbf{0} & \bar{\mathbf{M}}_s^{-1} & \mathbf{P}_s \\ -\rho^2\mathbf{T}_{ref} & \rho\bar{\mathbf{M}}_s^{-1} & \rho\mathbf{P}_s \\ \hdashline \rho\mathbf{I} & \mathbf{0} & \mathbf{0} \\ \mathbf{0} & \bar{\mathbf{M}}_s^{-1} & \mathbf{P}_s \end{array}\right] \begin{bmatrix} \mathbf{r} \\ \mathbf{w} \\ \hdashline \mathbf{u}_s \end{bmatrix} \tag{7.1.4}$$

Furthermore, if we have realizations for $\mathbf{P}_s$ and $\mathbf{T}_{ref}$ as

$$\mathbf{P}_s \stackrel{s}{=} \left[\begin{array}{c|c} \mathbf{A}_s & \mathbf{B}_s \\ \hline \mathbf{C}_s & \mathbf{D}_s \end{array}\right]$$

$$\mathbf{T}_{ref} \stackrel{s}{=} \left[\begin{array}{c|c} \mathbf{A}_o & \mathbf{B}_o \\ \hline \mathbf{C}_o & \mathbf{D}_o \end{array}\right]$$

then $\mathbf{G}$ can be realised as

$$\mathbf{G} := \left[\begin{array}{cc|cc:c} \mathbf{A}_s & \mathbf{0} & \mathbf{0} & (\mathbf{B}_s\mathbf{D}_s^T + \mathbf{Z}_s\mathbf{C}_s^T)\mathbf{R}_s^{-1/2} & \mathbf{B}_s \\ \mathbf{0} & \mathbf{A}_o & \mathbf{B}_o & \mathbf{0} & \mathbf{0} \\ \hline \mathbf{0} & \mathbf{0} & \mathbf{0} & \mathbf{0} & \mathbf{I} \\ \mathbf{C}_s & \mathbf{0} & \mathbf{0} & \mathbf{R}_s^{1/2} & \mathbf{D}_s \\ \rho\mathbf{C}_s & -\rho^2\mathbf{C}_o & -\rho^2\mathbf{D}_o & \rho\mathbf{R}_s^{1/2} & \rho\mathbf{D}_s \\ \hdashline \mathbf{0} & \mathbf{0} & \rho\mathbf{I} & \mathbf{0} & \mathbf{0} \\ \mathbf{C}_s & \mathbf{0} & \mathbf{0} & \mathbf{R}_s^{1/2} & \mathbf{D}_s \end{array}\right] \tag{7.1.5}$$

with $\mathbf{R}_s := \mathbf{I} + \mathbf{D}_s\mathbf{D}_s^T$. The matrix $\mathbf{Z}_s$ is the unique positive definite solution to the generalised filter Riccati equation, given in Equation 5.2.11. This matrix is the result of solving for the normalised coprime factor $\bar{\mathbf{M}}_s$, as presented in Equation 5.2.10. With the generalised plant $\mathbf{G}$ formed as above, the controller $\mathbf{K}$ is formed by applying the state space solutions to the H_∞ optimisation problem, as described in Appendix A. The resulting controller $\mathbf{K} = \begin{bmatrix} \mathbf{K}_1 & \mathbf{K}_2 \end{bmatrix}$ is then implemented as shown in Figure 7.1. The constant $\mathbf{W}_i$ is used to correct the steady-state gain (since the pre-filter may not have a steady state gain of unity), and can be calculated as:

$$\mathbf{W}_i = (\mathbf{I} - \mathbf{P}_s(0)\mathbf{K}_2(0))^{-1}\mathbf{P}_s(0)\mathbf{K}_1(0) \tag{7.1.6}$$

where $\mathbf{X}(0)$ is the value of $\mathbf{X}(s)$ at steady-state ($w = 0$ rad/s). Lastly, the transfer function from $\mathbf{r}$ to $\mathbf{y}$ in Figure 7.1, denoted $\mathbf{T}_{LS}$, can be calculated as:

$$\mathbf{T}_{LS} = \mathbf{P}_s(\mathbf{I} - \mathbf{P}_s\mathbf{K}_2)^{-1}\mathbf{K}_1\mathbf{W}_i \tag{7.1.7}$$

7.1.3 Quadrotor and Suspended Payload Translational Control: Two-degrees-of-freedom H_∞ Loop Shaping Design

We now present a design for the quadrotor and suspended payload translational control system, using the two-degrees-of-freedom H_∞ loop shaping design procedure.

7.1.3.1 Overview

The structure of the quadrotor and suspended payload translational control system with the two-degrees-of-freedom H_∞ loop shaping controllers, denoted $\mathbf{K}_{TLS}$, is shown in Figure 7.4.

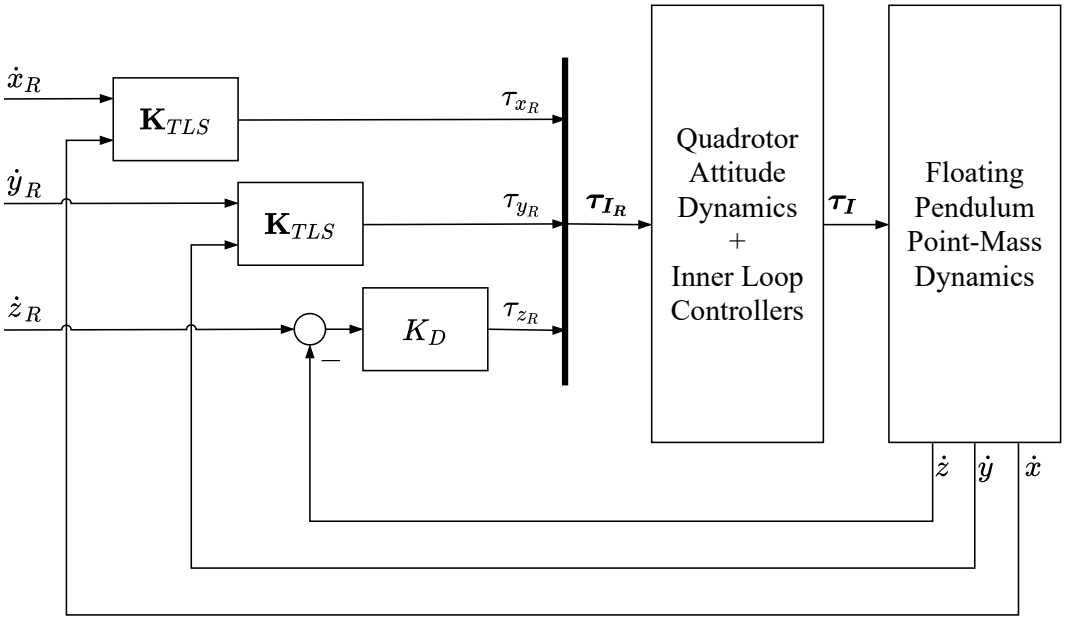

Figure 7.4: Quadrotor velocity control system with two-degrees-of-freedom H_∞ loop shaping controllers

In this configuration, the two-degrees-of-freedom H_∞ loop shaping controllers replace the LQI-based controllers presented in Chapter 4. Two identical, decoupled controllers are used to control the quadrotor velocity in the North

and East directions, with a PI controller controlling the vertical velocity of the quadrotor. The PI controller is the same controller that was presented in Chapter 4. Therefore, this section will focus on the design of the horizontal velocity controllers.

7.1.3.2 Quadrotor Horizontal Velocity Control

We use the two-degrees-of-freedom loop shaping technique described in the previous section to design a quadrotor horizontal velocity control system. The controller in block diagram form can be shown as in Figure 7.5. The linear model used in the design and analysis of the controller is the model $P_{vx}(s)$, which is the linearised dynamics of the floating pendulum system in the North direction, $P_{fpx}(s)$, augmented with the linearised dynamics of the tilt angle system, $T_T(s)$.

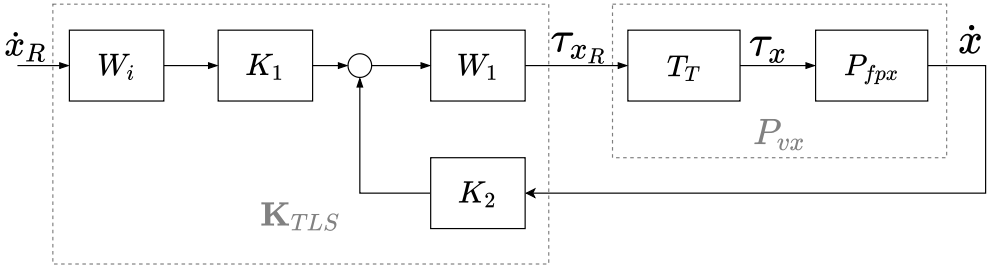

Figure 7.5: Two-degree-of-freedom H_∞ loop shaping controller used to control horizontal quadrotor velocity.

Controller Architecture The controller consists of a pre-compensating weight W_1 that is designed to improve the open-loop frequency response of the plant, and a robustifying controller K_2. The controller adds robustness to general coprime factor uncertainty, and is similar to the robustifying controller synthesised in the standard H_∞ loop shaping procedure. The controller also contains a dynamic pre-filter $K_1(s)$ that is designed to ensure the closed-loop response from reference commands to plant output matches the response of a reference system. The constant gain W_i ensure unity steady-state gain from the reference to the output.

The controller receives both the measurement of the current quadrotor velocity, $\dot{x}$ ($\dot{y}$ for the East velocity controller), and the velocity command $\dot{x}_R$ ($\dot{y}_R$ for the East velocity controller). The controller actuates the horizontal component of the reference force $\boldsymbol{\tau}_R$, namely τ_{x_R} (τ_{y_R} for the East controller).

Controller Design and Analysis The design objectives of the controller are the same as the objectives used to design the horizontal velocity controllers in previous chapters. Specifically, the objectives are to ensure zero steady-state tracking error with step commands, to achieve a closed-loop bandwidth of 0.7 rad/s, and to ensure adequate damping of the lightly damped swinging motion of the suspended payload.

The design parameters that need to be chosen are the performance weight W_1, the reference system T_{ref}, and the emphasis on model matching parameter ρ. For the performance weight, the same performance weight that was used in Chapter 5 and Chapter 6 is used here. This weight gives the compensated system $P_{vx}(s)W_1(s)$ a slope of -20 dB per decade in the low frequency region, and an open-loop bandwidth of 0.7 rad/s. The weight also attempts to filter out the resonant frequencies with a wide notch filter.

For this design, a pre-filter K_1 will be designed in conjunction with a robustifying controller K_2. The objective of the pre-filter is to ensure that the closed-loop system exhibits the same response as a reference system T_{ref}. Therefore, it is pertinent to ensure that the reference system is specified to have characteristics that meet the design objectives. For the reference system T_{ref}, a second order model was chosen as:

$$T_{ref} = \frac{w_n^2}{s^2 + 2\zeta w_n s + w_n^2} \tag{7.1.8}$$

where w_n is the natural frequency and ζ is the damping ratio. In order to satisfy the design requirements, the values chosen were $w_n = 0.9$ radians per second, and $\zeta = 0.8$. The response of the reference model to a step input is shown in Figure 7.6. With $\rho = 1$ (we chose to place equal emphasis on model-matching and robustness), the controller $\mathbf{K}$ is synthesised using the generalised plant in Equation 7.1.5, with the objective of minimising the H_∞-norm of Equation 7.1.2. Figure 7.7 shows the frequency response of the reference system T_{ref} and the resulting closed-loop system with two-degrees-of-freedom H_∞ loop shaping controller, T_{LS}. The closed-loop system $T_{LS}(s)$ is formed as

$$T_{LS} = P_{vx}W_1(1 - P_{vx}W_1K_2)^{-1}K_1W_i \tag{7.1.9}$$

The closed-loop system represents the linearised dynamics from a horizontal velocity command $\dot{x}_R$ to a horizontal quadrotor velocity $\dot{x}$. Finally, a value of $W_i = 1.7$ is calculated for the scalar constant W_i to obtain unity steady-state gain for the closed-loop transfer function.

The closed-loop step response of the two-degrees-of-freedom H_∞ loop shaping controller is shown in Figure 7.6 for the nominal plant.

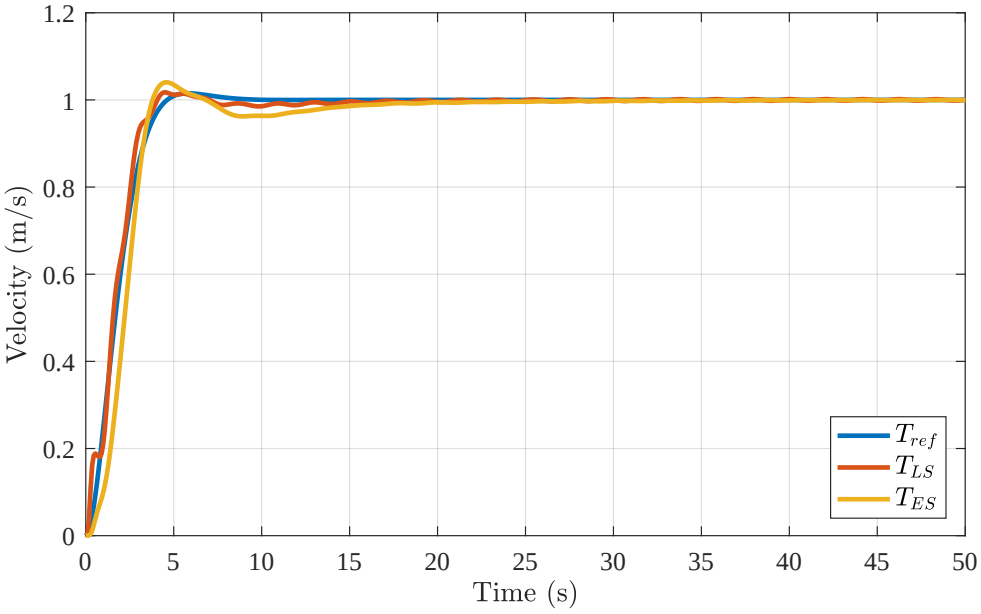

Figure 7.6: Step response of reference system T_{ref} and step response of nominal plant P_{vx} with two-degrees-of-freedom H_∞ loop shaping controller.

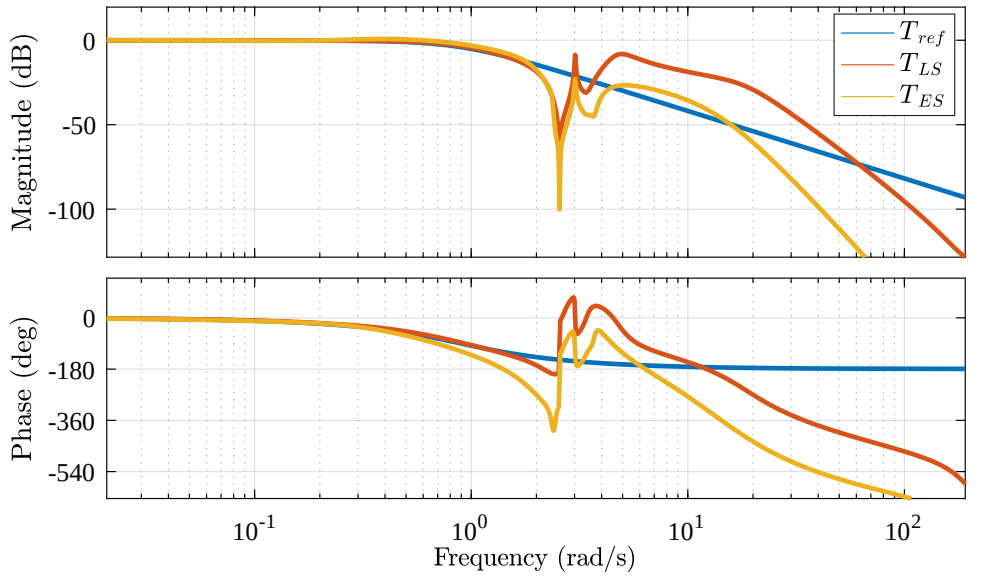

Figure 7.7: Bode plot of reference system T_{ref} and resulting closed-loop systems with two-degrees-of-freedom H_∞ loop shaping controller and two-degrees-of-freedom extended H_∞ loop shaping controller.

Clearly, we see fairly close matching of the reference system T_{ref} and the achieved closed-loop response with the two-degrees-of-freedom controller T_{LS}. However, this is the response with the nominal plant P_{vx}. In a similar fashion as in earlier chapters, the closed-loop step response of the horizontal velocity controller, with variations in the thrust uncertainty T, cable length L and payload mass M_L are shown in Figure 7.8. The step responses show that there are perturbed plants in the uncertainty set that cause the closed-loop system to be unstable, meaning the system does not exhibit robust stability.

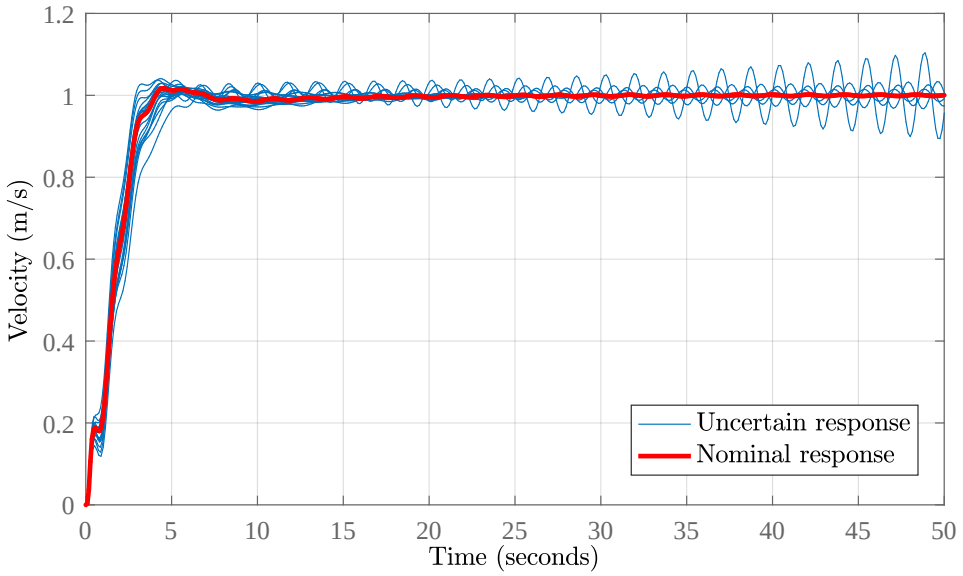

Figure 7.8: Step response of quadrotor velocity with two-degrees-of-freedom H_∞ loop shaping controller to a reference unit step, with perturbations present in the plant.

A Monte Carlo style plot of the poles and zeros of the closed-loop system with the two-degrees-of-freedom H_∞ loop shaping controller is shown in Figure 7.9. This plot shows the poles and zeros of the closed-loop system when various plants in the uncertainty set are sampled. Also shown are the poles and zeros of the nominal, uncompensated, open-loop plant P_{vx}. Clearly, there are closed-loop systems in the closed-loop uncertainty set that have poles in the right half of the complex plane, confirming that the system does not have robust stability.

A Monte Carlo style Bode plot of the closed-loop system with the two-degrees-of-freedom H_∞ loop shaping controller is given in Figure 7.10. It is clear from this figure that when the uncertainty in the plant is considered, the frequency

of the lightly-damped resonant mode of the system is shifted, and the two-degrees-of-freedom H_∞ loop shaping controller fails to prevent the entire set of resonant peaks from reaching the 0 dB point, which is further evidence of instability.

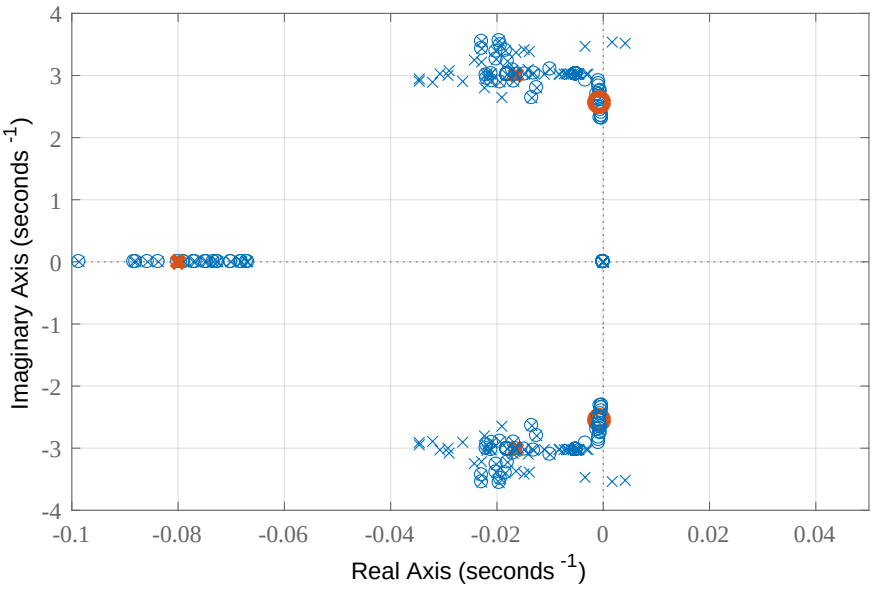

Figure 7.9: Poles and zeros of velocity control system with the two-degrees-of-freedom H_∞ loop shaping controller. $\times$ is used to mark poles, and $\circ$ is used to mark zeros. Also shown are poles and zeros of the nominal open-loop system P_{vx}, shown in red.

As was the case with the standard H_∞ loop shaping controller, the system is designed without any knowledge of the uncertainty. The resulting closed-loop system therefore does not exhibit stability for all plants in the uncertainty set.

7.1.3.3 Simulation Verification

The two-degrees-of-freedom H_∞ loop shaping quadrotor and payload velocity control system was implemented and verified using the full nonlinear nonlinear simulation, as shown in Figure 7.4. The closed-loop step response of the horizontal velocity controller is shown in Figure 7.11, along with the nominal response of the linear model P_{vx}. The horizontal velocity step response was performed in the North direction (but could also have been performed in the East direction with a similar result). The references for the East and vertical velocity controllers were set to zero, and these other two translational

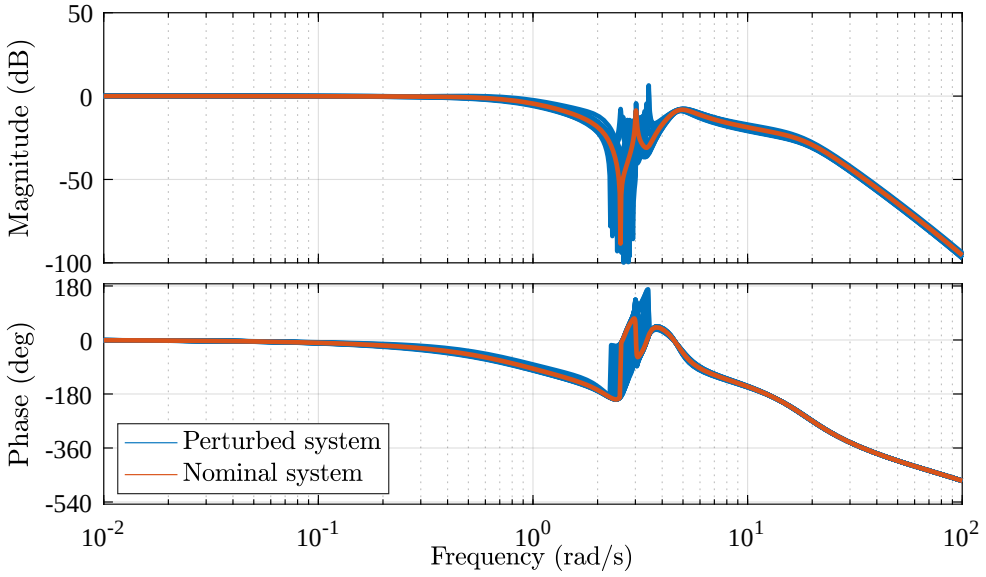

Figure 7.10: Bode plot of closed-loop system with the two-degrees-of-freedom H_∞ loop shaping controller. Also shown are the responses with perturbed plants from the uncertainty set.

controllers therefore acted only to regulate the East and vertical velocities to zero, and to reject external disturbances.

This figure shows that there is some discrepancy between the response of the linearised model and the simulation. Specifically, the simulated time history from the full nonlinear simulation displays a more damped response for the quadrotor velocity. The linear model predicts a less damped response. However, both responses show that the design requirement of bandwidth and steady-state tracking are achieved. More specifically, the settling time of the quadrotor velocity response to the step command is about 4 seconds, which is a satisfactory response time.

The resulting payload swing angle θ_L from the simulation is shown in Figure 7.12 (with no motion in the East direction, $\phi_L \approx 0$). Clearly, there is fairly significant damping added to the payload swinging motion, which was a design objective. However, this simulation was performed using the nominal values of payload mass, cable length, and quadrotor thrust uncertainty.

A Monte Carlo simulation was performed using the full nonlinear simulation. The uncertain parameters in the plant were varied, and the same quadrotor velocity command was given to the controller. The results for the quadrotor velocity are given in Figure 7.13. The results for the payload angle θ_L are given in Figure 7.14. With the Monte Carlo simulation, we see that stability

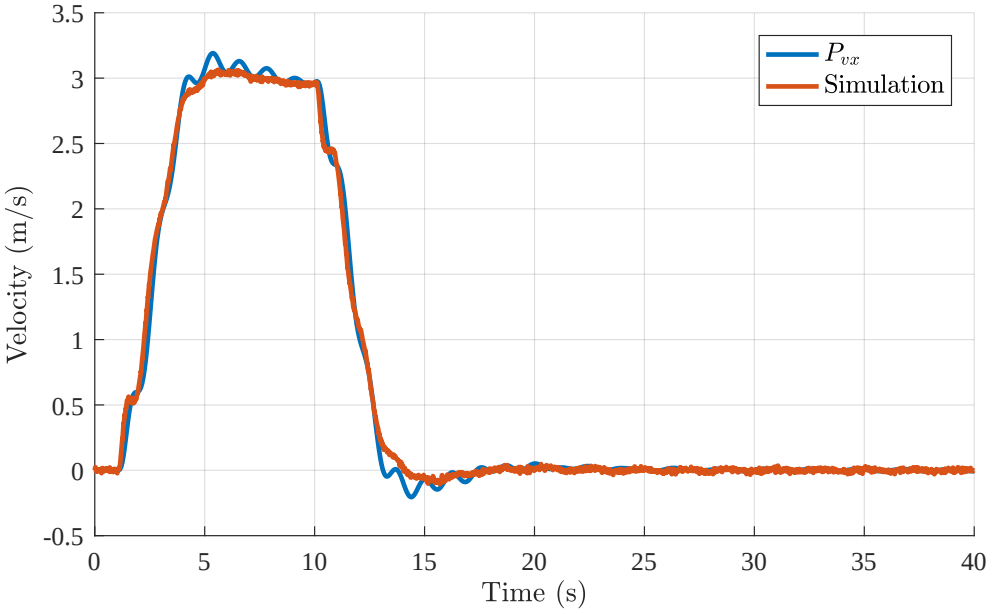

Figure 7.11: Response of quadrotor velocity $\dot{x}$ to a reference velocity command $\dot{x}_R$, with extended H_∞ loop shaping controller.

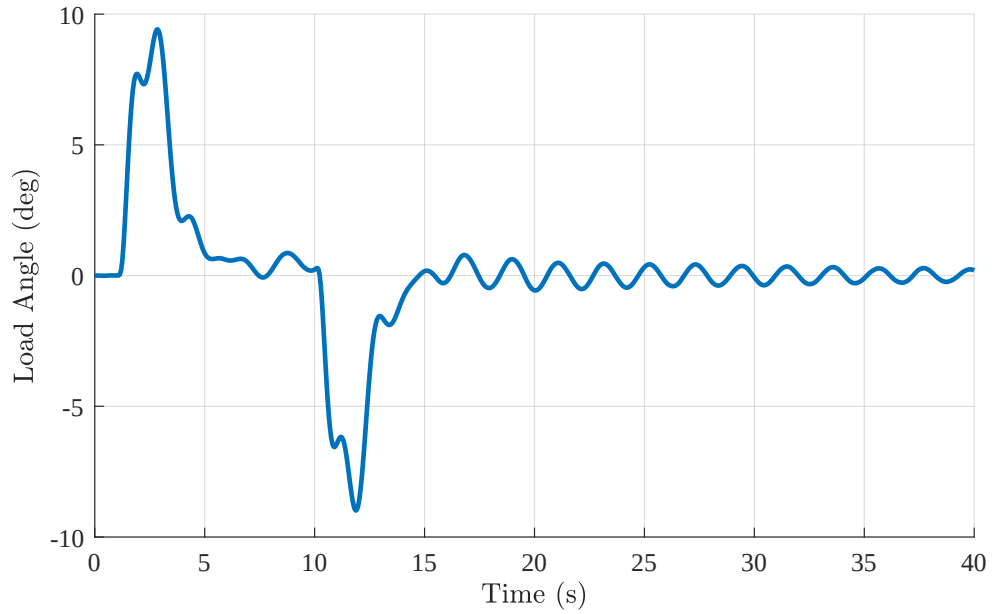

Figure 7.12: Response of payload angle θ_L to a reference velocity command $\dot{x}_R$, with extended H_∞ loop shaping controller.

for all the plants in the uncertainty set is not achieved. This agrees with

the results shown in Figure 7.8, and the fact that the two-degrees-of-freedom H_∞ loop shaping controller is not designed with any of the uncertainty in the system in mind. It must be noted that due to the (1,2) and (2,2) blocks in Equation 7.1.2, the resulting controller K_2 is essentially (to within numerical tolerances) the same controller as K from the standard H_∞ loop shaping design presented in Chapter 5. Therefore, $K_{LS} = W_1 K \approx W_1 K_2$. This means that the robust stability properties of the controller in Chapter 5 are applicable to this system. As shown in Section 6.2.2, the H_∞ loop shaping controller does not have robust stability, and therefore, neither does the two-degrees-of-freedom H_∞ loop shaping controller.

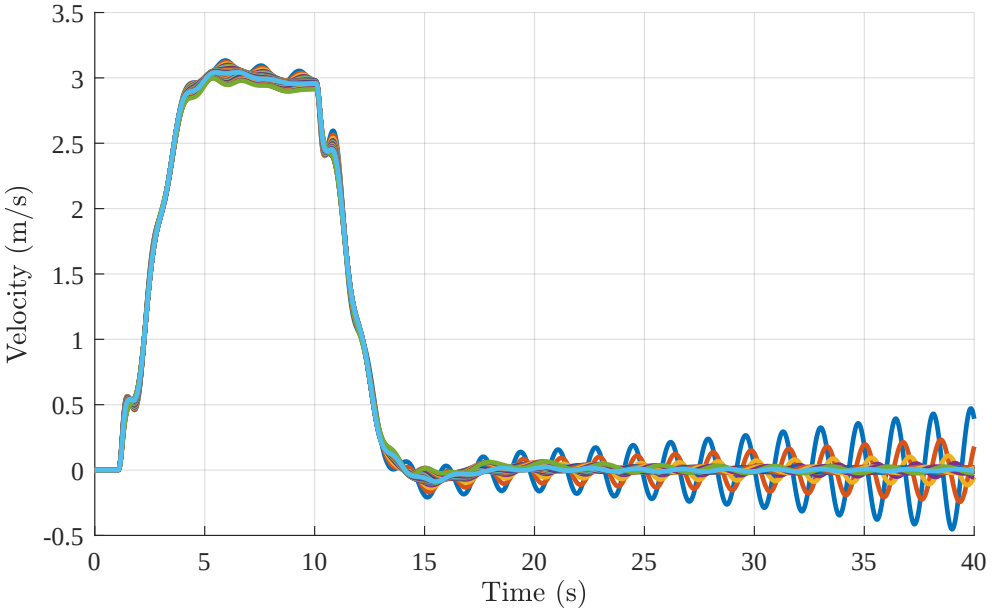

Figure 7.13: Monte Carlo simulation of quadrotor velocity $\dot{x}$, extended with H_∞ loop shaping controller, using full nonlinear simulation

A simulation with non-zero quadrotor velocity commands in North, East, and Down directions was performed. In this case, to maintain clarity of the figures, only the perturbed case with $M_L = 6$kg, $L = 1.7$m and $T = 1.2$ was simulated. The quadrotor velocity is plotted in Figure 7.15. The payload angles are plotted in Figure 7.16. As with the controllers presented in earlier chapters, the response shows very weak coupling between motion in each inertial direction.

Again, this controller is not designed with explicit knowledge of the plant uncertainty. In the next section, we present a novel control design solution that aims to rectify this. The extended H_∞ loop shaping controller developed in Chapter 6 is used in a similar model-matching problem to develop

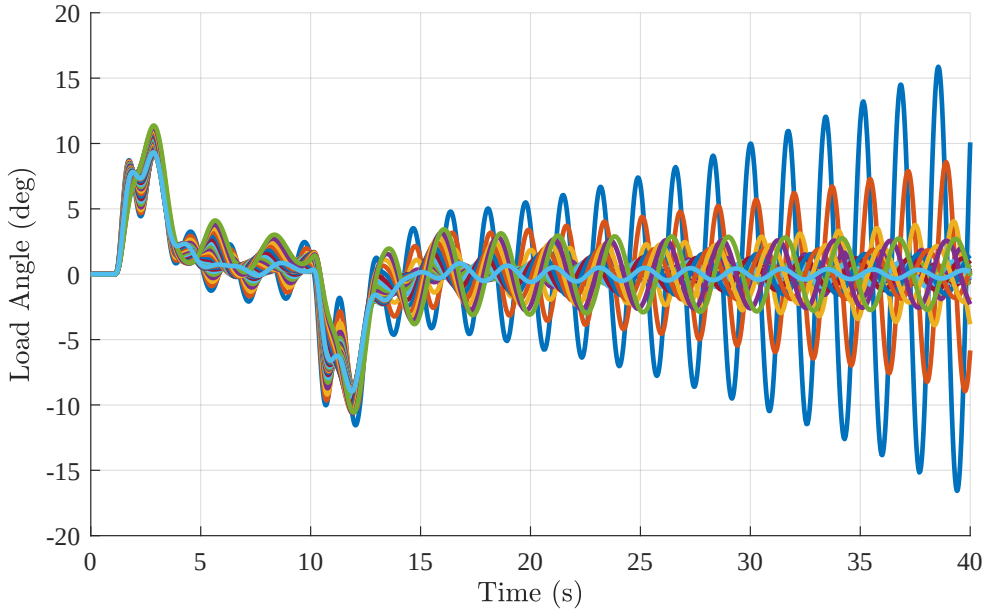

Figure 7.14: Monte Carlo simulation of payload angle θ_L, with extended H_∞ loop shaping controller, using full nonlinear simulation

a two-degrees-of-freedom extended H_∞ loop shaping controller that provides theoretically guaranteed robust stability.

7.2 Extended Two-Degrees-of-Freedom H_∞ Loop Shaping

In this section we present the design of a two-degrees-of-freedom version of the extended H_∞ loop shaping controller. The goal of the controller is to improve the transient performance of the extended H_∞ loop shaping controller, while maintaining the robust stability provided by it.

7.2.1 Overview

In the previous section, we presented a two-degrees-of-freedom H_∞ loop shaping design that aimed to improve the time-domain reference tracking performance of the system. However, this design did not use explicit knowledge of the uncertainty in the plant as measured by the ν-gap metric. The H_∞ optimisation problem that was solved was a two-degrees-of-freedom version of the standard robust stabilisation problem presented in Section 5.3.2.2.

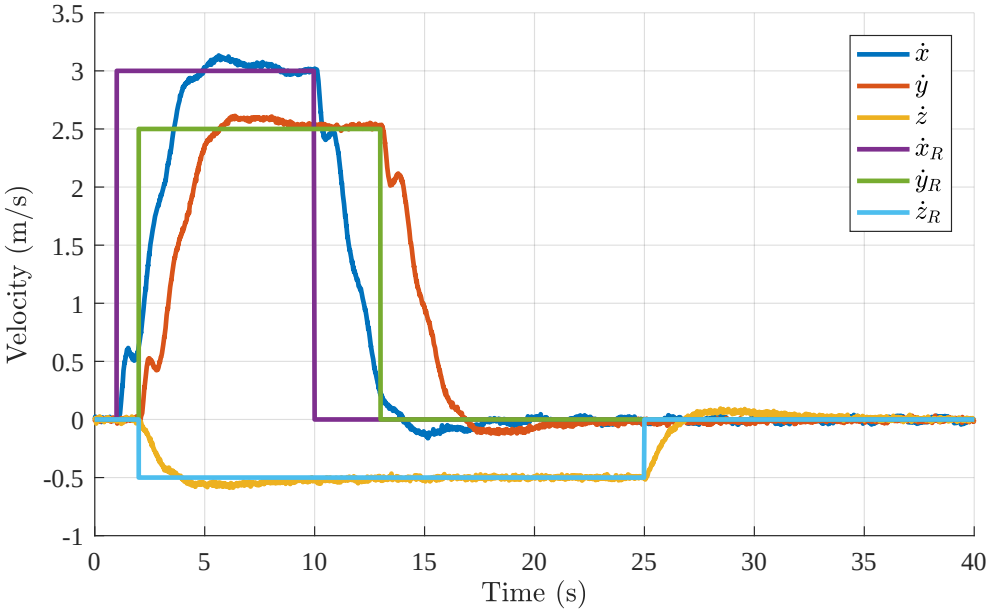

Figure 7.15: Response of quadrotor velocity $\dot{\mathbf{p}}$ to a reference velocity command $\dot{\mathbf{p}}_R$, with two-degrees-of-freedom H_∞ loop shaping controller. In this simulation, the uncertain plant parameters are set to $M_L = 6\text{kg}$, $L = 1.7\text{m}$ and $T = 1.2$.

This section presents the design of a novel two-degrees-of-freedom extended H_∞ loop shaping controller. The objective of the controller is to improve the transient response (improve time-domain performance) while maintaining the robust stability properties discussed in Chapter 6. The extended H_∞ loop shaping controller designed in Chapter 6 will be used as the feedback controller, thereby guaranteeing robust stability. A pre-filter will then be synthesised in a similar manner as in the previous section, whereby a model-matching problem is used to synthesise a pre-filter that aims to force the reference tracking response to be similar to that of a desired reference response.

The the architecture of the two-degree-of-freedom extended H_∞ loop shaping controller is shown in Figure 7.17. The controller consists of the pre-compensating shaping weight $\mathbf{W}_1$, and an extended H_∞ loop shaping controller, $\mathbf{K}_\infty$, that is designed using the algorithm in Chapter 6. The pre-compensating weight $\mathbf{W}_1$ is chosen to meet frequency domain performance requirements, and the feedback controller $\mathbf{K}_\infty$ is synthesised to provide robust stability, as per Chapter 6. Following this, the control system is augmented with a pre-filter K_1 that aims to force the transient response of the system to match that of a reference model $\mathbf{T}_{ref}$. Again, a constant gain $\mathbf{W}_i$ is used to correct steady-state gain errrors introduced by the pre-filter.

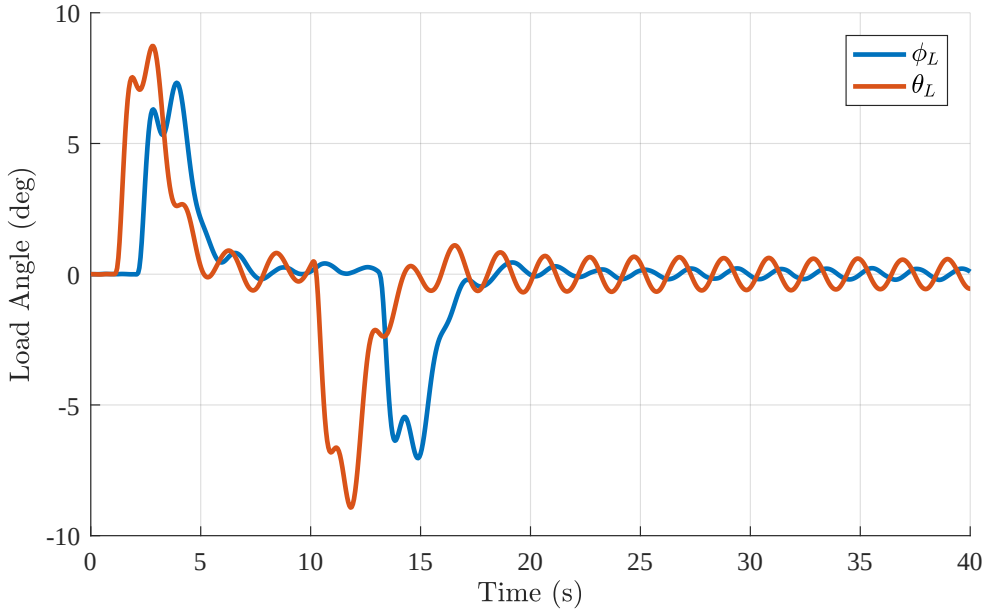

Figure 7.16: Response of payload angle ϕ_L and θ_L to a reference velocity command $\dot{\mathbf{p}}_R$, with two-degrees-of-freedom H_∞ loop shaping controller. In this simulation, the uncertain plant parameters are set to $M_L = 6\text{kg}$, $L = 1.7\text{m}$ and $T = 1.2$.

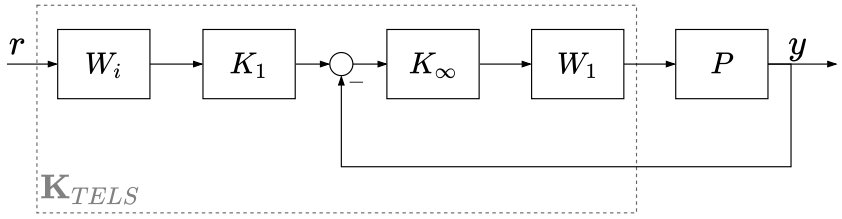

Figure 7.17: Two-degree-of-freedom extended H_∞ loop shaping controller

7.2.2 Problem Formulation

A key difference between the design in the last section and the design that will be presented now is that the design in the last section synthesised a full controller $\mathbf{K} = \begin{bmatrix} \mathbf{K}_1 & \mathbf{K}_2 \end{bmatrix}$, where $\mathbf{K}_1$ is the pre-filter and $\mathbf{K}_2$ is the feedback controller. In the design to follow, we will assume that a feedback controller is already given; in this case, an extended H_∞ loop shaping controller $\mathbf{K}_\infty$ that is synthesised using the algorithm presented in Chapter 6, and design a new pre-filter only. This allows the robustness properties of the $\mathbf{K}_\infty$ controller to be combined with the model-matching properties of a new pre-filter.

The problem can be cast into the formulation as shown in Figure 7.18. The system $\mathbf{T}_{els}$ is the closed-loop system formed with the extended loop shaping

controller, $\mathbf{K}_\infty$. This is similar to the configuration in Figure 7.3, but with the inner-loop controller $\mathbf{K}_2 = \mathbf{K}_\infty$ given. Also, the inner-loop controller is moved out of the feedback path (as in Figure 7.3) and into the forward path. This is to avoid the outputs of the pre-filter $\mathbf{K}_1$ from affecting the plant directly. The robust controller $\mathbf{K}_\infty$ acts to shape the inputs from the pre-filter which aids stability. Furthermore, the controller output $\mathbf{u}_l$ is moved to be outside of the inner-loop, because the controller output that we are now considering is the output of the pre-filter. Again we have the parameter ρ that will cause the model-matching properties of the pre-filter to be more or less aggressive depending on the value chosen for it.

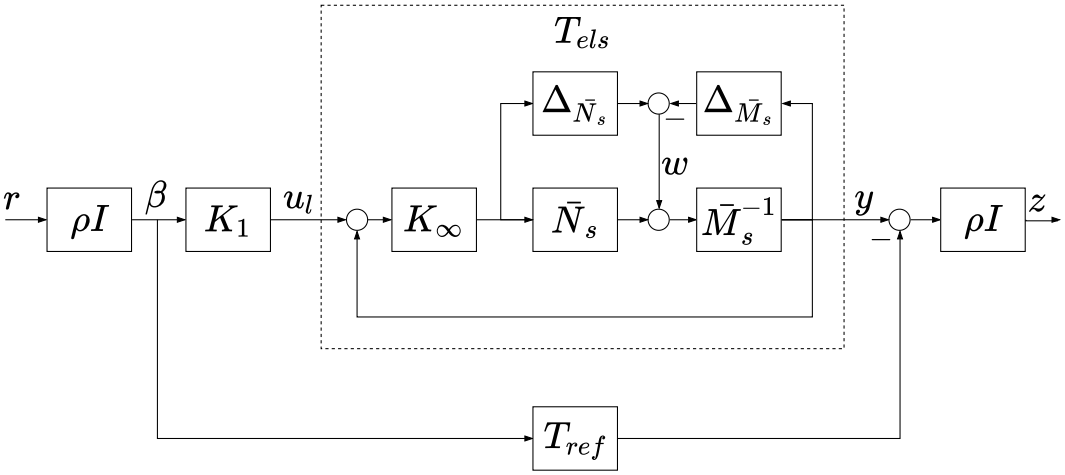

Figure 7.18: Two-degrees-of-freedom H_∞ extended loop shaping problem

In the configuration shown, we have that

$$\mathbf{T}_{els} = \mathbf{P}_s\mathbf{K}_\infty(\mathbf{I} - \mathbf{K}_\infty\mathbf{P}_s)^{-1}, \tag{7.2.1}$$

so the system can be simplified by replacing the inner-loop with $\mathbf{T}_{els}$, as shown in Figure 7.19.

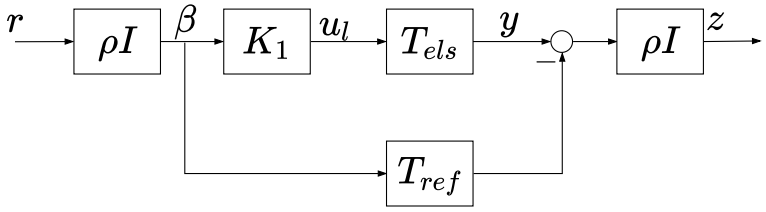

Figure 7.19: Simplified two-degrees-of-freedom H_∞ extended loop shaping problem

The objective is to choose the controller $\mathbf{K}_1$ that solves the following problem

$$||\mathbf{T}_{els}\mathbf{K}_1 - \mathbf{T}_{ref}||_\infty \leq \gamma\rho^{-2} \tag{7.2.2}$$

which means that the controller $\mathbf{K}_1$ will force the closed-loop response from the reference input $\mathbf{r}$ to the plant output $\mathbf{y}$ to match the response of the reference system. The controller $\mathbf{K}_1$ that does this will be the controller that minimises the transfer function from $\mathbf{r}$ to the regulated output $\mathbf{z}$ in Figure 7.19. This is because the output $\mathbf{z}$ is the difference between the output of the reference system $\mathbf{T}_{ref}$ and the output of the robust closed-loop system. Also, we add the output of the filter $\mathbf{u}_l$ to the set of regulated outputs in order to ensure that the magnitude of the control effort from the pre-filter is within reasonable values.

Therefore, we can formulate the generalised plant $\mathbf{G}$ to solve the H_∞ optimisation problem as shown in Figure 7.20. The output used for measurement feedback to the controller is $\boldsymbol{\beta}$, and the control input is $\mathbf{u}_l$. The regulated outputs to be minimised by the feedback controller are $[\mathbf{z}; \mathbf{u}_l]$.

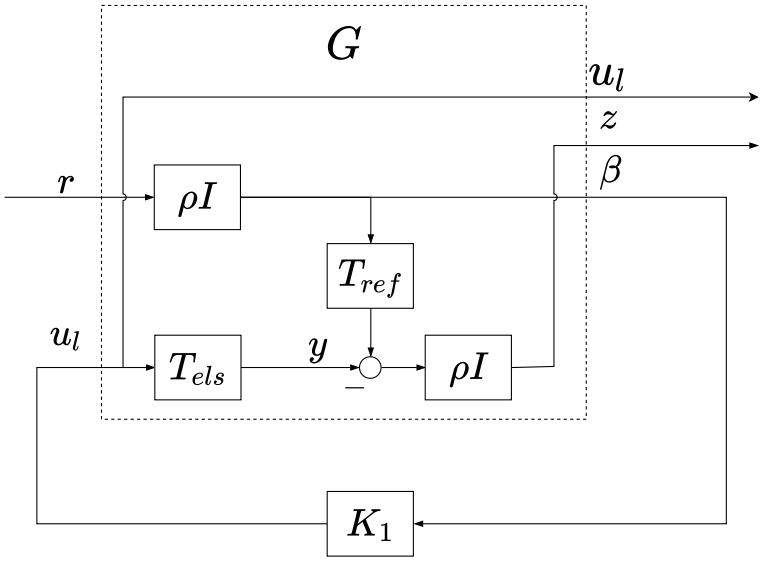

Figure 7.20: Generalised control configuration for two-degrees-of-freedom H_∞ extended loop shaping problem

From the figure, the generalised plant is

$$\begin{bmatrix} \mathbf{u}_l \\ \mathbf{z} \\ \hdashline \boldsymbol{\beta} \end{bmatrix} = \begin{bmatrix} \mathbf{G}_{11} & \mathbf{G}_{12} \\ \mathbf{G}_{21} & \mathbf{G}_{22} \end{bmatrix} \begin{bmatrix} \mathbf{r} \\ \hdashline \mathbf{u}_l \end{bmatrix} \tag{7.2.3}$$

$$= \left[\begin{array}{c:c} \mathbf{0} & \mathbf{I} \\ \hdashline -\rho^2 \mathbf{T}_{ref} & \rho \mathbf{T}_{els} \\ \hdashline \rho \mathbf{I} & \mathbf{0} \end{array}\right] \begin{bmatrix} \mathbf{r} \\ \hdashline \mathbf{u}_l \end{bmatrix}. \tag{7.2.4}$$

Using this plant, the standard H_∞ state space formulae in Appendix A are applied to solve for the controller $\mathbf{K}_1$ that minimises the H_∞ norm of the closed-loop system from exogenous input $\mathbf{r}$ to the regulated output $[\mathbf{z}; \mathbf{u}_l]$. From Figure 7.18, this closed-loop system is

$$\begin{bmatrix} \mathbf{u}_l \\ \mathbf{z} \end{bmatrix} = \begin{bmatrix} \mathbf{K}_1 \rho \mathbf{I} \\ \rho^2 \left[\mathbf{T}_{els} \mathbf{K}_1 - \mathbf{T}_{ref} \right] \end{bmatrix} \mathbf{r} \tag{7.2.5}$$

Once the controller that minimises the H_∞ norm of the transfer function in Equation 7.2.5 is synthesised (using the generalised plant in Equation 7.2.3), the system can be implemented as shown in Figure 7.17. Note that the extended H_∞ loop shaping controller $K_{ELS} = W_1 K_\infty$ is implemented in the forward path.

7.2.3 Quadrotor and Suspended Payload Translational Control: Two-degrees-of-freedom Extended H_∞ Loop Shaping Design

We now present a design for the quadrotor and suspended payload translational control system, using the two-degrees-of-freedom extended H_∞ loop shaping design procedure.

7.2.3.1 Overview

The structure of the quadrotor and suspended payload translational control system with the two-degrees-of-freedom extended H_∞ loop shaping controllers, denoted $\mathbf{K}_{TELS}$, is shown in Figure 7.21.

In this configuration, the two-degrees-of-freedom extended H_∞ loop shaping controllers replace the standard two-degrees-of-freedom H_∞ loop shaping controllers from the previous section. Again, two identical, decoupled controllers are used; one for control of the quadrotor velocity in the North direction, and one for control of the quadrotor velocity in the East direction. Also, the vertical velocity controller is the same PI controller as the one used in the

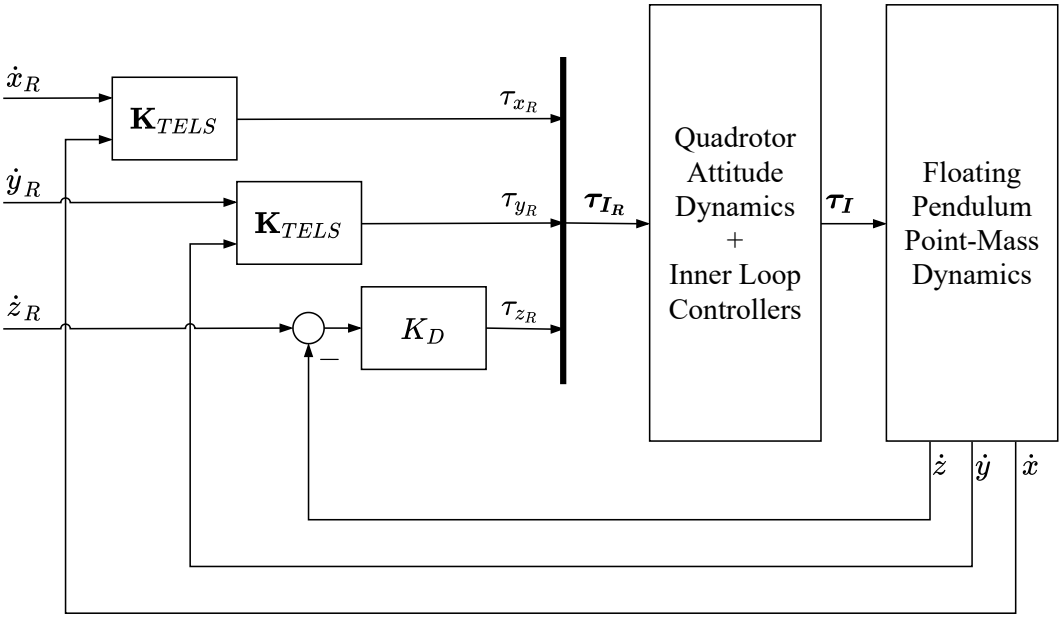

Figure 7.21: Quadrotor velocity control system with two-degrees-of-freedom extended H_∞ loop shaping controllers

configurations that were presented in earlier chapter. Therefore, we focus on the design of the horizontal velocity controllers only.

7.2.3.2 Quadrotor Horizontal Velocity Control

The two-degrees-of-freedom extended H_∞ loop shaping controller design procedure from the previous section is used to design a horizontal velocity controller for the quadrotor. The controller in block diagram form can be shown as in Figure 7.22.

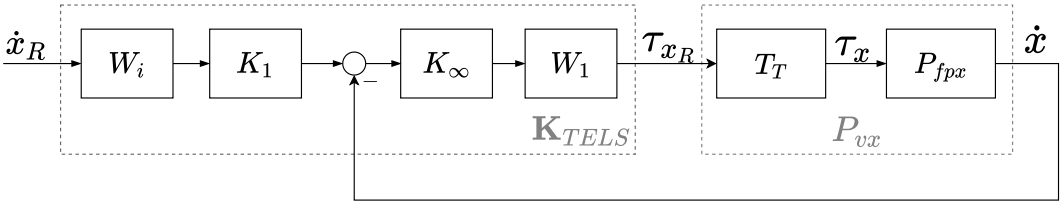

Figure 7.22: Two-degrees-of-freedom extended H_∞ loop shaping controller

Again, the linear model used to design the controller is the linear model $P_{vx}(s)$, which contains the linearised dynamics of the floating pendulum system in the North direction, $P_{fpx}(s)$, and the linearised dynamics of the tilt angle system $T_T(s)$.

Controller Architecture The controller contains a pre-compensating weight W_1 that is designed to improve the open-loop frequency response of the plant, which is the P_{vx}. The controller also contains the controller K_∞ that was formed in Chapter 6, providing theoretically guaranteed robust stability to the plants in the uncertainty set. Together, the pre-compensating weight and the robust controller form the extended H_∞ loop shaping controller from Chapter 6, K_{ELS}. A pre-filter K_1 is added to force the response of the closed-loop system to be similar to that of a reference system. The constant gain W_i ensure unity steady-state gain from the reference to the output.

The controller receives both the measurement of the current quadrotor velocity, $\dot{x}$ ($\dot{y}$ for the East velocity controller), and the velocity command $\dot{x}_R$ ($\dot{y}_R$ for the East velocity controller). The controller actuates the horizontal components of the reference force $\boldsymbol{\tau}_R$, τ_{x_R} for the North controller (τ_{y_R} for the East controller).

Controller Design and Analysis The design objectives of the controller are the same as the objectives used to design the horizontal velocity controllers in previous chapters. Specifically, the objectives are to ensure zero steady-state tracking error with step commands, to achieve a closed-loop bandwidth of 0.7 rad/s, and to ensure adequate damping of the lightly damped swinging motion of the suspended payload.

The design parameters to be chosen are ρ and T_{ref}. The value chosen for ρ was 1 in order to ensure the optimisation places sufficient emphasis on the model-matching problem. For T_{ref}, the same system was used as in the previous section, as this system aligns with the design objectives.

With the design parameters defined, the H_∞ optimisation state space formulae in Appendix A are applied with the generalised plant in Equation 7.2.3, in order to synthesise the pre-filter K_1. The resulting closed-loop system, denoted $T_{ES}(s)$, is determined to be

$$T_{ES} = P_{vx}W_1K_\infty(1 + P_{vx}W_1K_\infty)^{-1}K_1W_i \tag{7.2.6}$$

A Bode plot of the closed-loop system $T_{ES}(s)$ is given in Figure 7.7. Clearly, the response matches that of the reference system closely.

The step response of T_{ref} is shown in Figure 7.6. Also shown is the step response of T_{ES}. The response of the system T_{ES} matches that of the system T_{ref} closely. The rise time of the two systems are similar, but the system T_{ES} displays more overshoot. Figure 7.23 shows the step response of T_{ES} with variations in the thrust uncertainty T, cable length L, and payload mass M_L due to plant uncertainty.

It is evident from the figure that the objective of robust stability is achieved. This is to be expected because if two stable systems are cascaded, then the

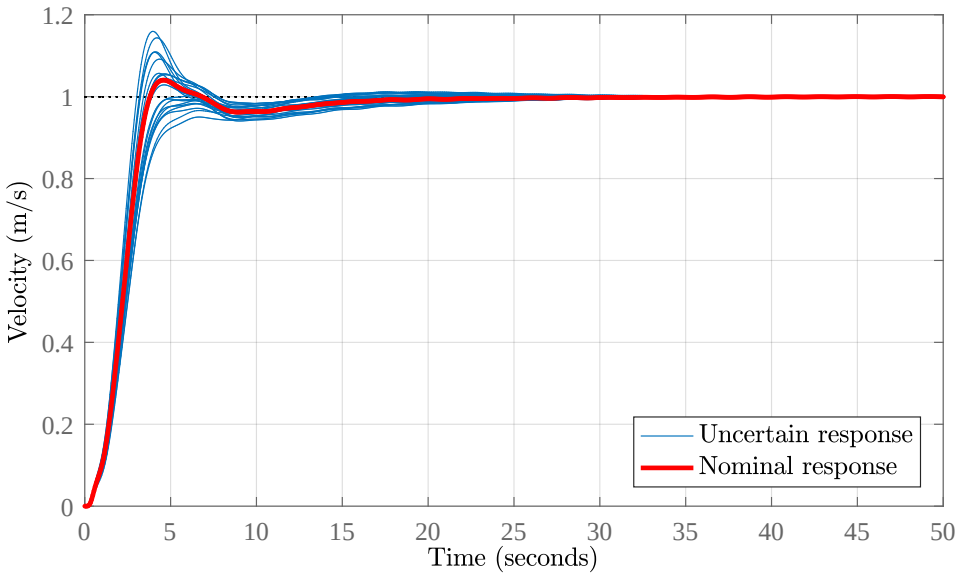

Figure 7.23: Step response of quadrotor velocity with two-degrees-of-freedom extended H_∞ loop shaping controller to a reference unit step, with perturbations present in the plant.

resulting system will be stable. In particular, if the pre-filter is stable, and the closed-loop system with the extended H_∞ loop shaping controller is stable, then the resulting system in Figure 7.22 must be stable.

A Monte Carlo style plot of the poles and zeros of the closed-loop system with the two-degrees-of-freedom extended H_∞ loop shaping controller is shown in Figure 7.24. This plot shows the poles and zeros of a the closed-loop system when various plants in the uncertainty set are sampled. Also shown are the poles and zeros of the nominal, uncompensated, open-loop plant P_{vx}. Clearly, there are no closed-loop systems in the closed-loop uncertainty set that have poles in the right-half plane of the complex plane, confirming that the system has robust stability.

A Monte Carlo style Bode plot of the closed-loop system with the two-degrees-of-freedom extended H_∞ loop shaping controller is given in Figure 7.25. It is clear from this figure that when the uncertainty in the plant is considered, the frequency of the lightly-damped resonant mode of the system is shifted, but the two-degrees-of-freedom H_∞ loop shaping controller prevents the entire set of resonant peaks from reaching the 0 dB point, which is further evidence of stability.

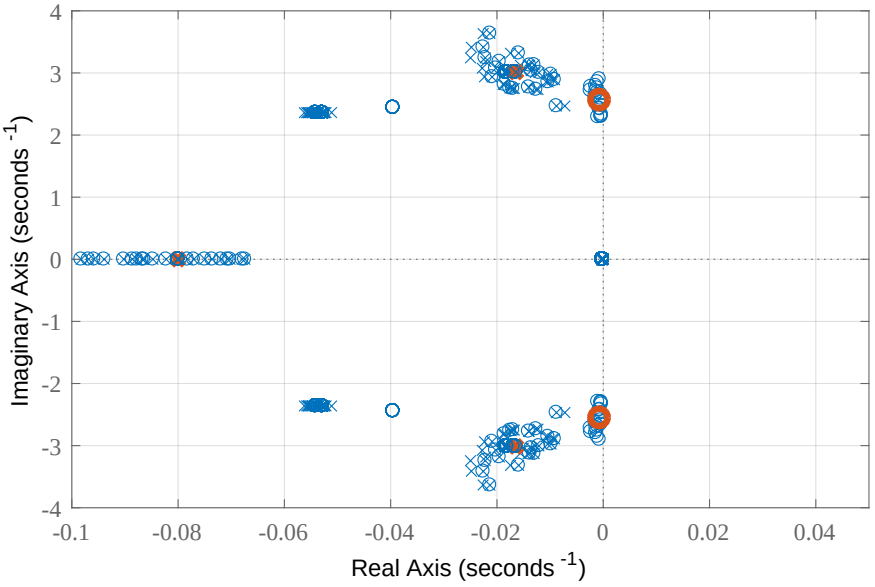

Figure 7.24: Poles and zeros of velocity control system with the two-degrees-of-freedom extended H_∞ loop shaping controller. $\times$ is used to mark poles, and $\circ$ is used to mark zeros. Also shown are poles and zeros of the nominal open-loop system P_{vx}, shown in red.

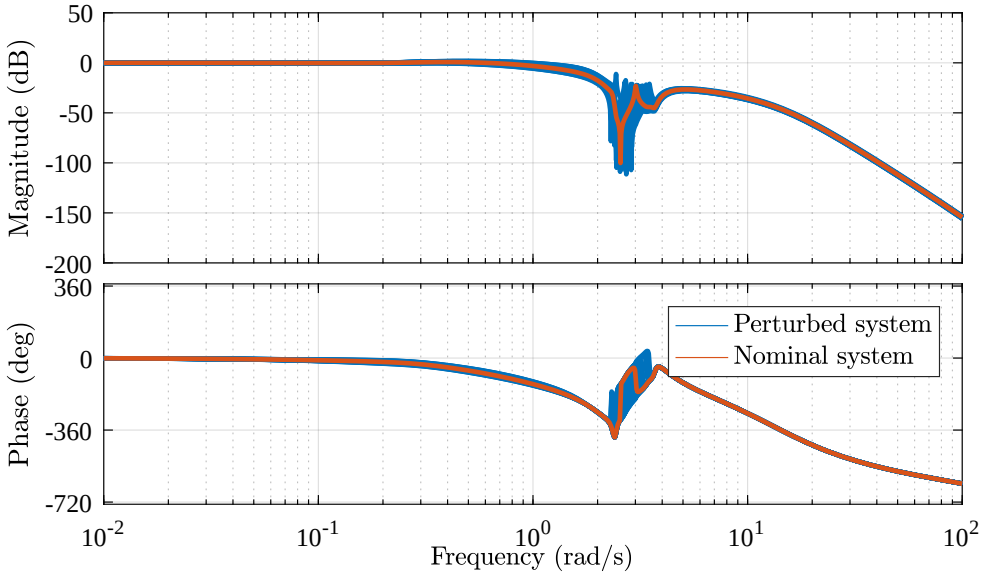

Figure 7.25: Bode plot of closed-loop system with the two-degrees-of-freedom extended H_∞ loop shaping controller. Also shown are the responses with perturbed plants from the uncertainty set.

7.2.3.3 Simulation Verification

The two-degrees-of-freedom extended H_∞ loop shaping quadrotor and payload velocity control system was implemented and verified using the full nonlinear simulation model. The closed-loop step response of the horizontal velocity controller is shown in Figure 7.26, along with the nominal response of the linear model P_{vx}. The horizontal velocity step response was performed in the North direction (but could also have been performed in the East direction with a similar result). The references for the East and vertical velocity controllers were set to zero, and these other two translational controllers therefore acted only to regulate the East and vertical velocities to zero, and to reject external disturbances.

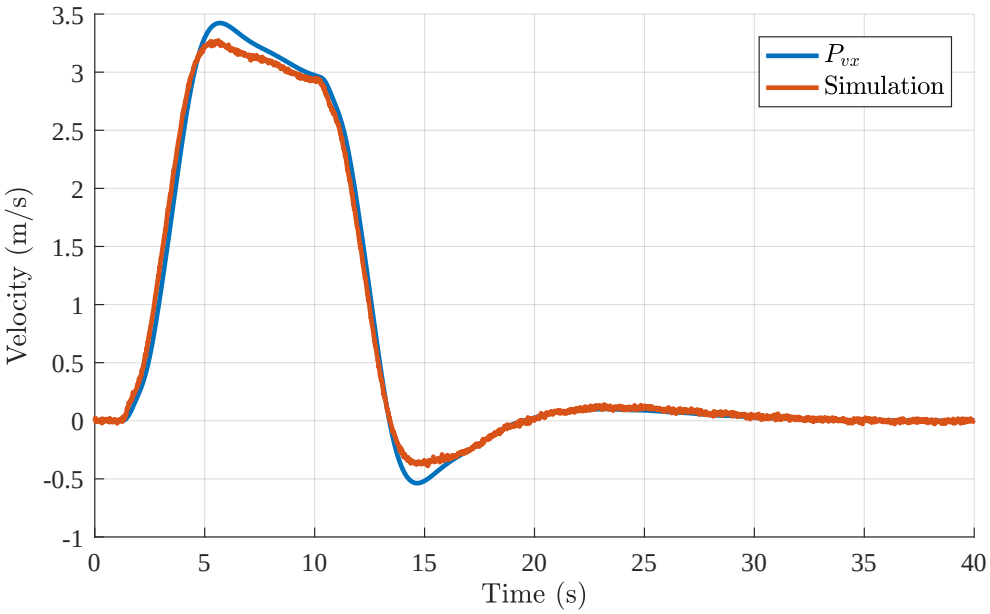

Figure 7.26: Response of quadrotor velocity $\dot{x}$ to a reference velocity command $\dot{x}_R$, with extended H_∞ loop shaping controller.

This figure shows that there is good agreement between the response of the linearised model and the simulation. In both cases, when the nominal values of the thrust scalar T_t, payload mass M_L, and cable length L are considered, the payload swinging motion is damped, as is evident by lack of the oscillations in the quadrotor velocity.

The resulting payload swing angle θ_L from the simulation is shown in Figure 7.27 (with no motion in the East direction, $\phi_L \approx 0$). Clearly, the controller adds significant damping to the payload swinging motion, which was a design objective.

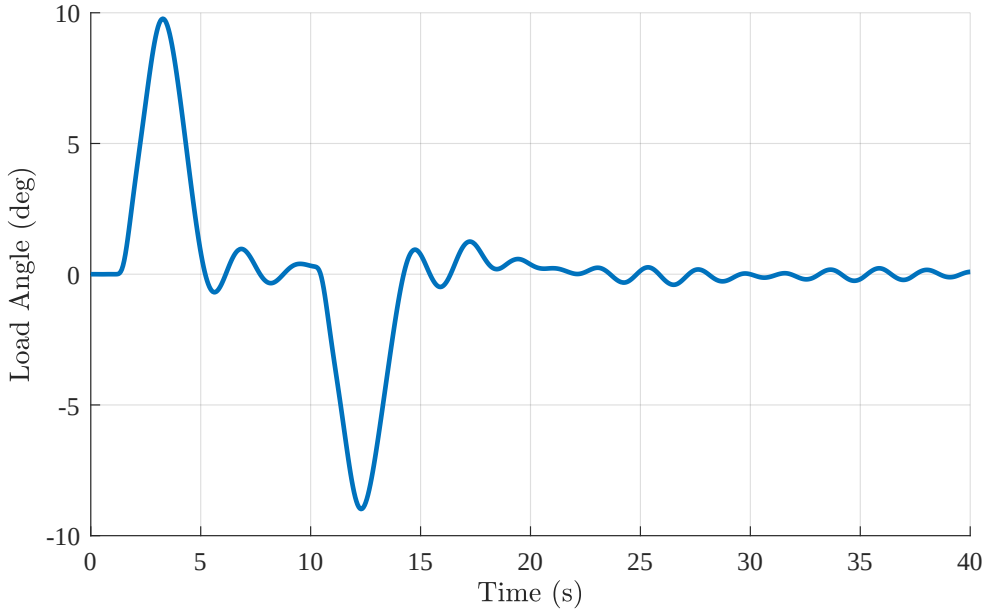

Figure 7.27: Response of payload angle θ_L to a reference velocity command $\dot{x}_R$, with extended H_∞ loop shaping controller.

Monte Carlo simulations were performed using the full nonlinear simulation model. The uncertain parameters in the plant were varied, and the same quadrotor velocity command was given to the controller. The simulated responses of the quadrotor horizontal velocity and the payload swing angle θ_L are shown in Figure 7.28 and 7.29 respectively. The Monte Carlo simulations show that stability is achieved for all of the plants in the uncertainty set. This agrees with the results shown in Figure 7.23, and the fact that the extended H_∞ loop shaping controller uses explicity knowledge of the plant uncertainty and is theoretically guaranteed to provide robustness to all the plants in the uncertainty set.

The Monte Carlo simulation of the payload angle θ_L shows that in the worst case, a small payload angle oscillation can persist for some time. The reason for this is that the resulting payload angle oscillation is too small to have any significant effect on quadrotor velocity. This means the controller cannot actively add damping to the motion, because the feedback measurement, which is quadrotor velocity, does not contain the oscillation in any significant way. Thus, the controller effectively ignores that small oscillation and allows it to decay according to the natural damping of the plant, which is low at low quadrotor velocities. However, the system is still stable, as the controller will not excite unstable oscillations in the quadrotor velocity, like the other controllers presented earlier would.

From these figures, we see that the two-degrees-of-freedom controller is suc-

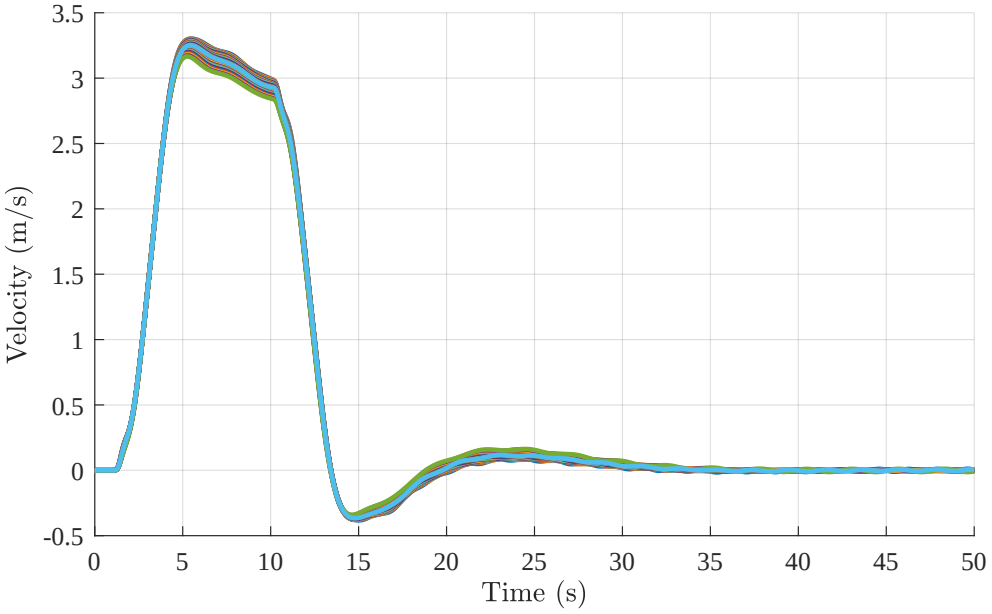

Figure 7.28: Monte Carlo simulation of quadrotor velocity $\dot{x}$, with two-degrees-of-freedom extended H_∞ loop shaping controller, using full nonlinear simulation

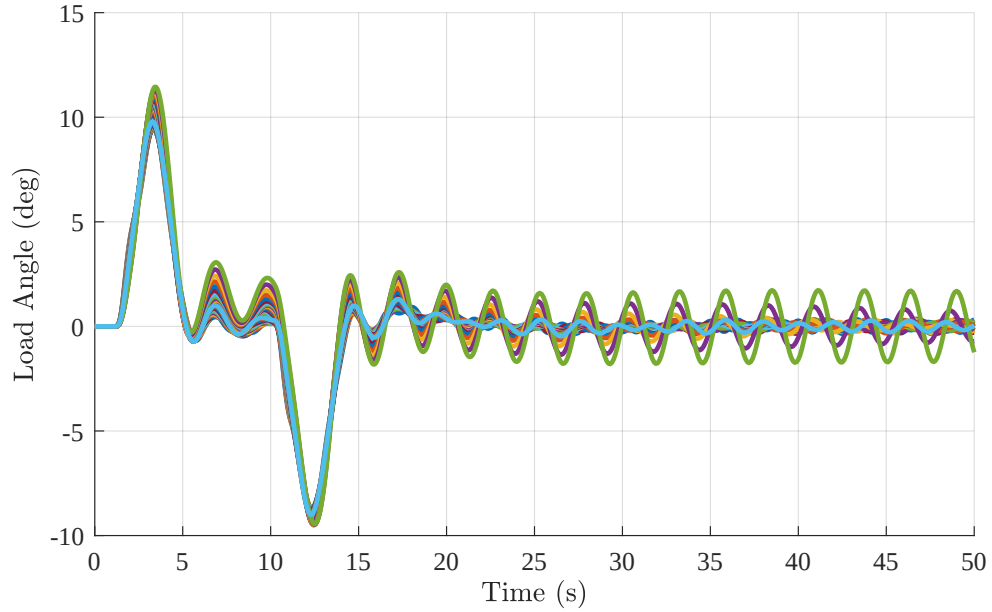

Figure 7.29: Monte Carlo simulation of payload angle θ_L, with two-degrees-of-freedom extended H_∞ loop shaping controller, using full nonlinear simulation

cessful in reducing the residual oscillations of the suspended payload. The time-domain performance in terms of rise time and trajectory tracking is improved, at the cost of some overshoot. The closed-loop step response shows a rise time of 3-5 seconds, and a zero steady-state tracking error for step references.

The performance of the two-degrees-of-freedom controller is similar to the LQI controller in terms of bandwidth and rise time, yet the two-degrees-of-freedom controller has guaranteed robust stability, as discussed in Chapter 6. The addition of the model-matching pre-filter drastically improves the transient response and the reference tracking ability of the extended H_∞ loop shaping controller.

A simulation with non-zero quadrotor velocity commands in North, East, and Down directions was performed. In this case, to maintain clarity of the figures, only the perturbed case with $M_L = 6\text{kg}$, $L = 1.7\text{m}$ and $T = 1.2$ was simulated. The quadrotor velocities and the payload swing angles are plotted in 7.30 and 7.31 respectively. As with all the previous controllers, the response shows very weak coupling between motion in each inertial direction.

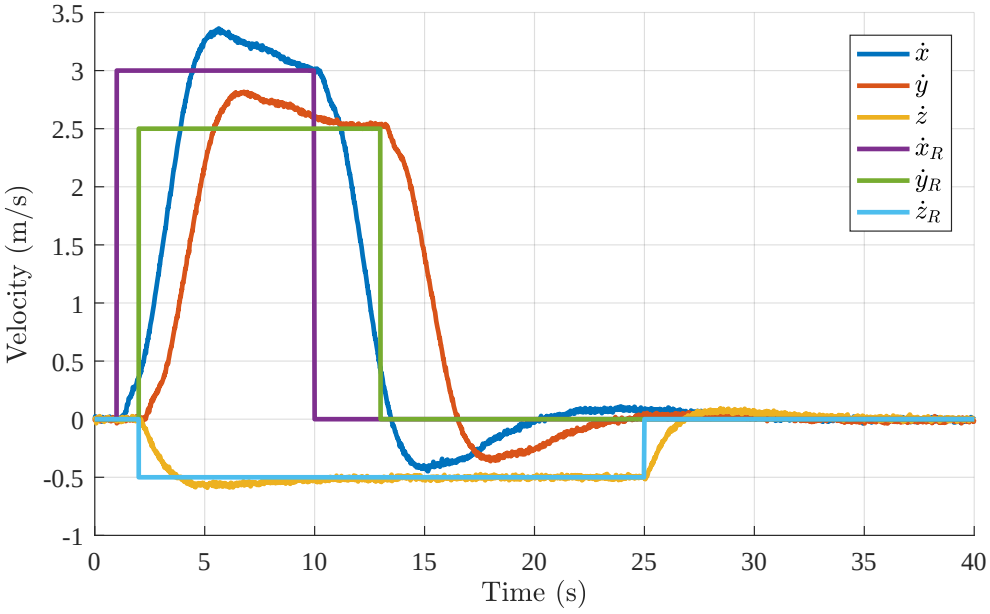

Figure 7.30: Response of quadrotor velocity $\dot{\mathbf{p}}$ to a reference velocity command $\dot{\mathbf{p}}_R$, with two-degrees-of-freedom extended H_∞ loop shaping controller. In this simulation, the uncertain plant parameters are set to $M_L = 6\text{kg}$, $L = 1.7\text{m}$ and $T = 1.2$.

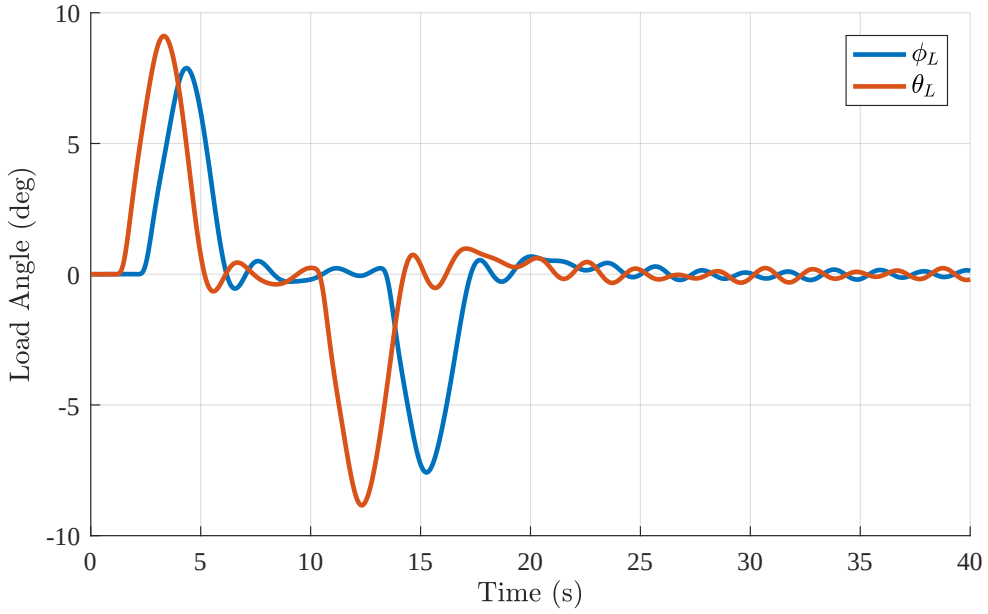

Figure 7.31: Response of payload angles ϕ_L and θ_L to a reference velocity command $\dot{\mathbf{p}}_R$, with the two-degrees-of-freedom extended H_∞ loop shaping controller. In this simulation, the uncertain plant parameters were set to $M_L = 6\text{kg}$, $L = 1.7\text{m}$ and $T = 1.2$.

In the next sections, we use input shaping as a means of generating inputs into the system. These inputs will be capable of more aggressive manoeuvres, but will aim to reduce residual swinging of the payload. Thereafter, the extended H_∞ loop shaping controller will be used to correct errors from a nominal trajectory, in a hybrid feedforward-feedback controller configuration.

7.3 Input Shaping

Input shaping is a technique that involves the use of specifically designed impulses to cancel out oscillations in a system with lightly damped modes. These impulses can be convolved with any desired input into the system, thereby "shaping" the input. The idea of shaping the input into a system in order to cancel resonances was first proposed in Smith [7], with later work being done by Starr et al. [9]. The method of using impulses to cancel out vibrations was developed by Singer [8]. In this section, we use this work of Singer to generate swing-free trajectories for the quadrotor and suspended payload.

7.3.1 Vibration Cancelling Impulses

A stable, linear, vibratory system of any order can be specified by a cascaded set of second-order poles with a decaying sinusoidal response. Denote A as the amplitude of an input impulse into the system, w as the undamped natural frequency, ζ is the damping ratio, and t_0 as the time that the impulse is applied. Then, the second-order decaying sinusoidal response is given as [77],

$$y(t) = \left[A \frac{w}{\sqrt{1-\zeta^2}} \exp\left(-\zeta w(t-t_0)\right) \right] \sin w\sqrt{1-\zeta^2}(t-t_0) \tag{7.3.1}$$

If two impulses are applied to the system, the response is the superposition of responses, each given by Equation 7.3.1. The superposition can be represented as

$$B_1 \sin(\alpha t + \phi_1) + B_2 \sin(\alpha t + \phi_2) = A_{amp} \sin(\alpha t + \psi) \tag{7.3.2}$$

where

$$\begin{aligned}
A_{amp} &= \sqrt{(B_1 \cos\phi_1 + B_2 \cos\phi_2)^2 + (B_1 \sin\phi_1 + B_2 \sin\phi_2)^2} \\
\psi &= \arctan\left(\frac{B_1 \cos\phi_1 + B_2 \cos\phi_2}{B_1 \sin\phi_1 + B_2 \sin\phi_2}\right) \\
B_j &= A_j \frac{w}{\sqrt{1-\zeta^2}} \exp\left(-\zeta w(t_j - t_{end})\right) \\
\phi_j &= w\sqrt{1-\zeta^2} t_j \\
\alpha &= w\sqrt{1-\zeta^2} t_{end}
\end{aligned}$$

where A_j is the magnitude of the j'th impulse, t_j is the time at which the j'th impulse is applied, and t_{end} is the point in time after which all the impulses have been applied and at which point zero residual vibration must be achieved. This can be generalised to N number of impulses as:

$$\begin{aligned}
A_{amp} &= \sqrt{\left(\sum_{j=1}^{N} B_j \cos\phi_j\right)^2 + \left(\sum_{j=1}^{N} B_j \sin\phi_j\right)^2} \\
&= w\sqrt{1-\zeta^2 t_j}
\end{aligned} \tag{7.3.3}$$

Elimination of all residual vibration after the sequence of inputs has ended requires that A_{amp} equals zero once the last input is applied, at time t_{end}. To achieve this, both of the squared terms in Equation 7.3.3 must be zero, so:

$$V_1 = \sum_{j=1}^{N} B_j \cos\phi_j = 0$$
$$V_2 = \sum_{j=1}^{N} B_j \sin\phi_j = 0 \tag{7.3.4}$$

These two constraint equations are used to generate an impulse sequence that achieves zero residual vibration. The unknowns are the number of impulses N, the amplitudes of the impulses A_j and the time of the impulses t_j. A revised simplex algorithm (IMSL Routine ZX3LP) was used by Singer to solve for the minimum number of impulses, the amplitude of those impulses, and the time of each impulse. Figure 7.32 (adapted from [8]) and Equation 7.3.5 are used to calculate the impulse sequence needed to ensure V_1 and V_2 are zero:

$$K = \exp\left(-\frac{\zeta\pi}{\sqrt{1-\zeta^2}}\right)$$
$$\Delta T = \frac{\pi}{w\sqrt{1-\zeta^2}} \tag{7.3.5}$$

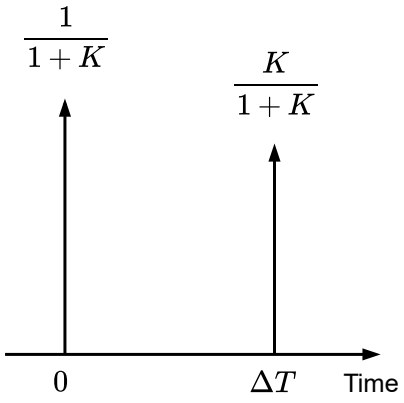

Figure 7.32: Two-impulse sequence (ZV shaper) designed to have zero vibration at the expected system natural frequency w with a certain damping ratio ζ.

A constraint placed on the solution is that the sum of all the amplitudes A_j must be one, which prevents the trivial solution of $A_j = 0 \ \forall \ j$.

This two-impulse sequence is commonly termed a Zero Vibration (ZV) shaper. The ZV shaper only cancels the vibration if the system natural frequency and damping ratio are known to within very small tolerance. Figure 7.33 displays

the residual vibration as a percentage of the original residual vibration with no vibration cancelling impulses applied. This is shown against changes in the natural frequency w of the system, which is represented as a normalized frequency w_{actual}/w, where w_{actual} is the actual natural frequency of the system and w is the frequency used in the design of the impulses.

In order to increase robustness for the vibration cancellation to variations in the system natural frequency, a new constraint is added. The residual vibrations are a function of the sizes of V_1 and V_2 in Equation 7.3.4. V_1 and V_2 must be zero at the systems natural frequency, which is the original contraint we have considered so far. However, the derivatives of Equation 7.3.4 can also be set to zero, which is the equivalent of ensuring that the magnitude of the residual vibrations (quantified by the size of V_1 and V_2) must change little for changes in the system natural frequency (because the derivative is zero at the system natural frequency).

Taking the derivatives of V_1 and V_2 results in the additional constraints:

$$\begin{aligned} \frac{dV_1}{dw} &= \sum_{j=1}^{N} B_j t_j \cos\phi_j = 0 \\ \frac{dV_2}{dw} &= \sum_{j=1}^{N} B_j t_j \sin\phi_j = 0 \end{aligned} \tag{7.3.6}$$

with proof given by Singer [8]. These two constraint equations are added to the optimisation routine and Figure 7.34 shows the results. This impulse sequence, designed to ensure that the residual vibrations and the derivative of the residual vibrations with respect to the system natural frequency are zero, is termed the Zero-Vibration-Derivative shaper, or ZVD shaper. Note, adding the additional contraints on the derivatives of V_1 and V_2 causes the resultant impulse sequences to be longer. For the ZV shaper, the last impulse occurs at time ΔT, whereas for the ZVD shaper, the last impulse occurs at time $2\Delta T$.

Figure 7.33 shows the residual vibrations as a function of normalised frequency w_{actual}/w. Clearly seen is that the derivative is zero at $w_{actual} = w$. The ZVD shaper is often termed a Robust Input Shaper, because it is less sensitive to changes in the system natural frequency. Also, taking higher-order derivatives of Equation 7.3.4 and adding additional constraints results in many different input shapers. The ZVD shaper will be applied to the quadrotor and suspended payload problem because of its reduced sensitivity to changes in the system's natural frequency.

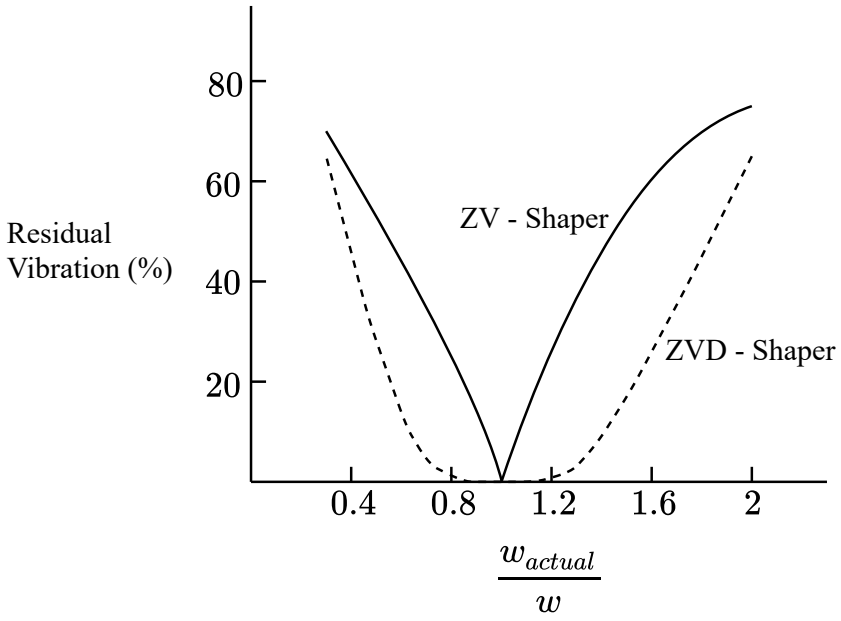

Figure 7.33: Residual vibrations as a function of normalised frequency w_{actual}/w. The ZV shaper is designed to have zero residual vibrations at $w_{actual} = w$. The ZVD shaper is designed to have zero residual vibration and zero residual vibration derivative at $w_{actual} = w$.

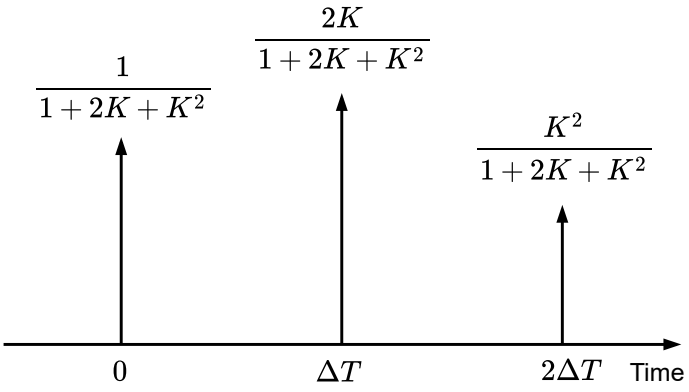

Figure 7.34: Three-impulse sequence (ZVD shaper) designed to have zero vibration at the expected system natural frequency w with a certain damping ratio ζ. The impulses are also designed to ensure the residual vibration is less sensitive to changes in natural frequency and damping.

7.3.2 Trajectory and Impulse Sequence Convolution

Any arbitrary input signal into a system can be written as a summation of scaled unit impulses. Therefore, we can use the convolution between an arbitrary input signal and the vibration cancelling impulse sequence from the previous section to generate arbitrary vibration-cancelling inputs into a sys-

tem. The process of convolving an arbitrary input with an impulse sequence from the previous section (such as the ZV shaper) produces the shortest actual system input that accomplishes the same motion without vibrations.

An example of such an input shaping convolution is shown Figure 7.35. Here we see that delay in the input is ΔT. If a higher-order shaper was used, such as a ZVD shaper, the time delay would be $(N-1)\Delta T$, where N is the number of impulses used. This is the trade-off between performance and robustness that must be considered when choosing a shaper.

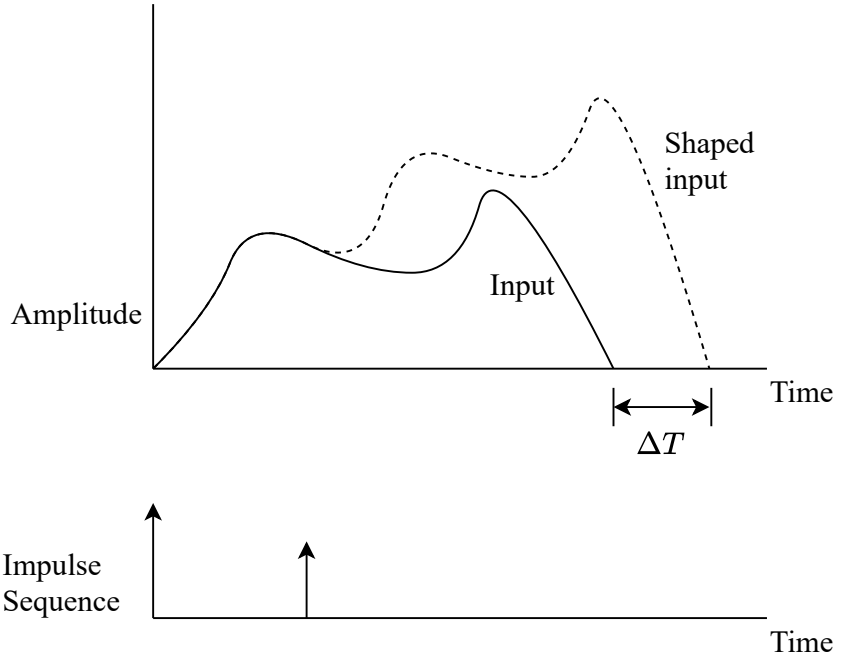

Figure 7.35: A arbitrary input being convolved with an impulse sequence to produce a shaped input

7.3.3 Input Shaper Design

The lightly damped mode of the quadrotor and suspended payload was discussed in Section 3.2.1.2. The pole-zero map of the floating pendulum horizontal dynamics is repeated here in Figure 7.36 for the convenience of the reader. The complex pole pair at $s = -0.016 \pm 3.01j$ represents the oscillatory payload angle dynamics.

From this, the parameters needed to calculate the values of K and ΔT using Equation 7.3.5 are obtained as $\zeta = 0.005$ and $w = 3.01$. The values of K and ΔT are calculated to be $K = 0.9830$ and $\Delta T = 1.0437$, from which the amplitudes of the ZVD shaper in Figure 7.34 are calculated.

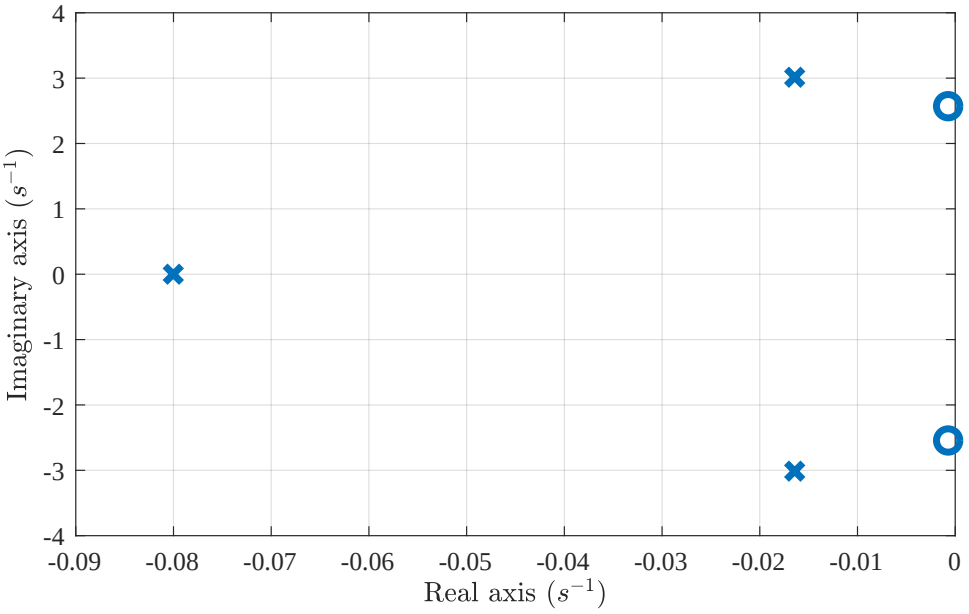

Figure 7.36: Pole-zero plot of P_{fpx}

Using the configuration shown in Figure 7.37, an arbitrary force command reference input $\boldsymbol{\tau}_{I_D}$ is applied. The input is shaped by the ZVD shaper through convolution of the input with the ZVD impulse sequence. This produces the shaped force command reference input $\boldsymbol{\tau}_{I_R}$. When no shaper is used, $\boldsymbol{\tau}_{I_R} = \boldsymbol{\tau}_{I_D}$.

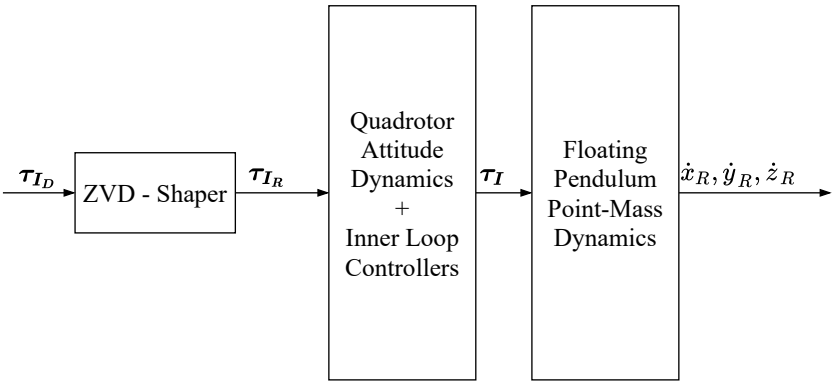

Figure 7.37: An arbitrary input in the form of a reference force command in the inertial frame, $\boldsymbol{\tau}_{I_D}$. The input is shaped by a ZVD shaper to form a shaped input $\boldsymbol{\tau}_{I_R}$.

An arbitrary horizontal force command reference τ_{x_D} and the corresponding shaped force command reference τ_{x_S} produced by the ZVD shaper is shown in Figure 7.38. The time delay caused by the convolution is evident in how

the shaped input is delayed by $2\Delta T$ after the original reference input. Also, observe how step inputs convolved with the three-impulse sequence result in three smaller steps making up the full step magnitude. Ramps also display a similar behaviour, where the gradient of the ramp is broken up into three distinct regions. These changes to the arbitrary reference signal are what causes residual vibrations to be cancelled.

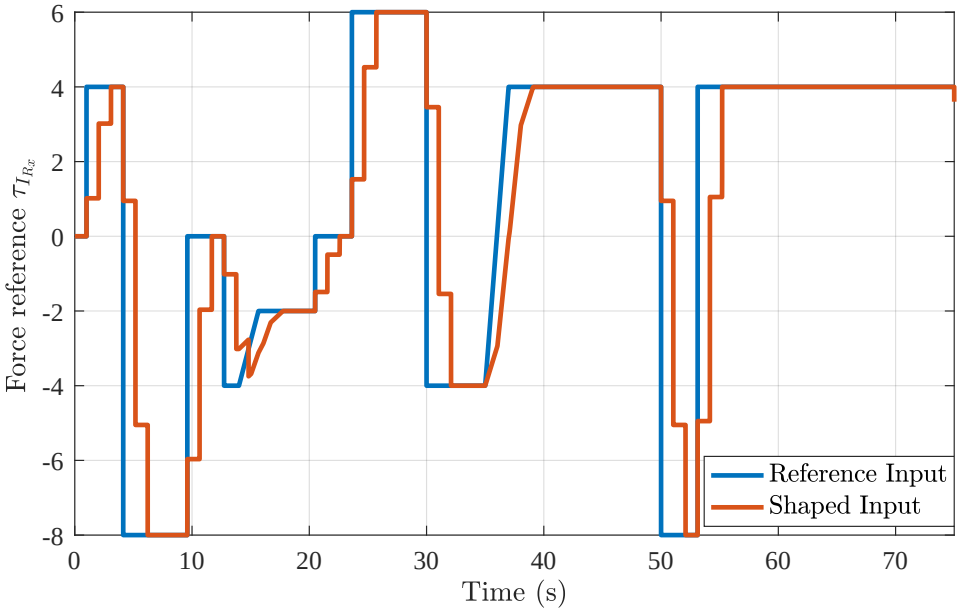

Figure 7.38: An arbitrary input in the form of a reference force command in the x direction, $\tau_{I_{R_x}}$. Also shown is the same input convolved with the ZVD shaper.

The quadrotor velocity responses for both the original and the input shaped reference signals are shown in Figure 7.39. The original force reference signal is aggressive and causes severe excitation of the lightly damped mode of the system, which is the swinging payload motion. This is evident from the oscillations in the quadrotor velocity, seen almost as a type of dither effect on the velocity. The resulting quadrotor velocity from the shaped input is completely smoothed of these vibrations. The velocity from the shaped input also displays a delay of $2\Delta T$ compared to the unshaped input; this is the time-domain penalty that is incurred by shaping the input. The velocity response from the shaped input is stored as a reference velocity for the quadrotor to track - this will be elaborated on in the next section.

The payload swing angle responses for both the original and the input shaped reference signals are shown in Figure 7.40. As was evident from the quadrotor velocity plot, the swinging motion of the payload is excited by the arbitrary

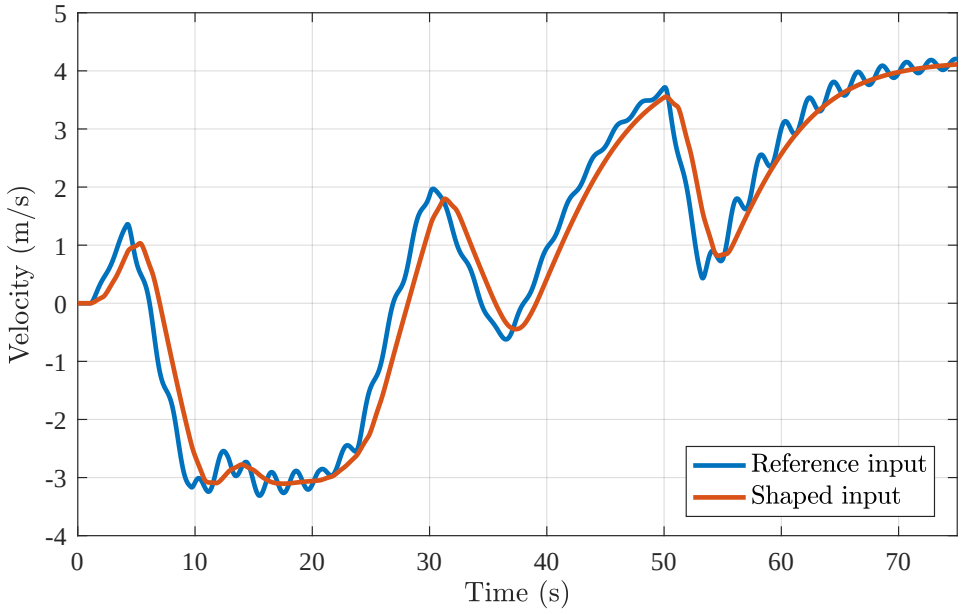

Figure 7.39: Quadrotor velocity response to arbitrary input, as well as to the shaped input.

reference input. Also clear is how the shaped input delivers remarkable cancellation of the residual vibrations of the swinging payload. In the shaped input case, we see the payload maintaining payload angles that are equivalent to the offset around which the oscillations occur in the non-shaped case.

These responses were simulated using the full nonlinear simulation model, for the nominal plant. In other words, only the nominal values of thrust uncertainty $T = 1$, cable length $L = 1.5$m, and payload mass $M_L = 3.5$kg, were used. In the next section, the response of the quadrotor and suspended payload with variations in thrust uncertainty ΔT_t, cable length Lm, and payload mass $M_L$kg will be considered. As mentioned earlier, the quadrotor velocity response from the shaped input is stored as a reference velocity for the quadrotor to track, denoted $\dot{x}_R$ (in the North direction). In the next section, the extended H_∞ loop shaping controller is added as a feedback controller to ensure that this velocity is tracked, even when there are variations in the plant parameters.

7.4 Extended Loop Shaping Controller with Feedforward

This section presents a novel feedforward-feedback control architecture that allows aggressive velocity trajectories to be tracked without exciting residual

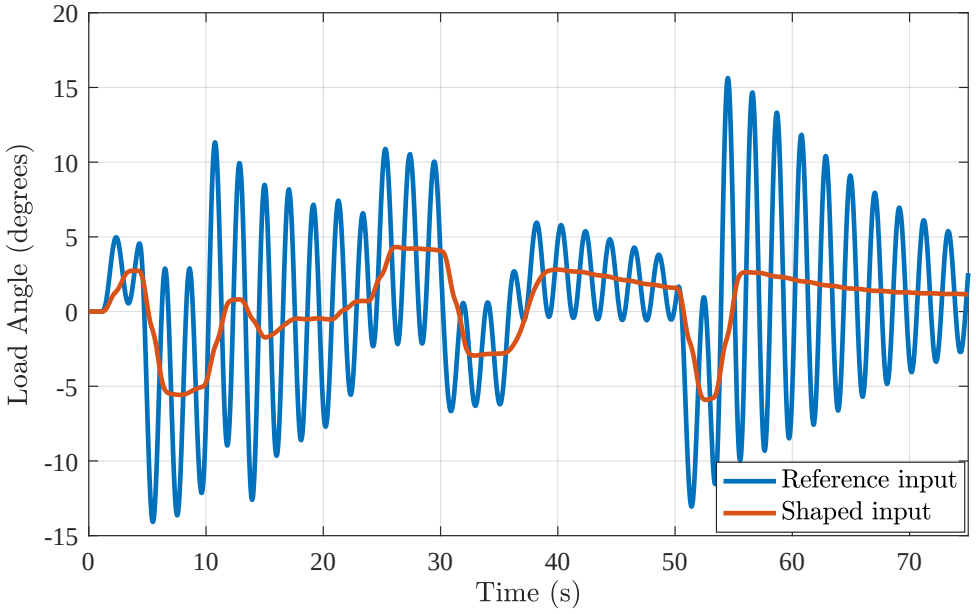

Figure 7.40: Load angle response to arbitrary input, as well as to the shaped input.

swinging of the suspended payload, while also providing guaranteed robust stability to plant uncertainty.

7.4.1 Proposed Controller Architecture

The proposed feedforward-feedback control architecture for quadrotor velocity trajectory tracking with swing damping for the suspended load and guaranteed robust stability is shown in Figure 7.41. The control architecture assumes that the quadrotor velocity reference trajectory $\dot{x}_R(t)$, $\dot{y}_R(t)$, and $\dot{z}_R(t)$ and the associated force command input signal τ_{I_D} has been generated with a trajectory planner and is supplied to the flight control system. The force command input signal is passed through the ZVD shaper, and the shaped force command is provided as a feedforward force command reference signal to the quadrotor's inner-loop attitude and thrust controllers. The velocity trajectory reference signal is provided to the quadrotor and payload outer-loop translational controllers. The force command reference signal supplied to the inner-loop controllers is therefore the superposition of the feedforward force command from the input shaper and the feedback force command from quadrotor velocity controllers, which include the extended H_∞ loop shaping horizontal velocity controllers. The feedforward input shaped force command allows the quadrotor to execute arbitrary quadrotor velocity reference trajectories without inducing oscillations in the suspended payload, while the velocity feedback control cor-

rects deviations from the planned trajectory and provides robust stability to plant uncertainty.

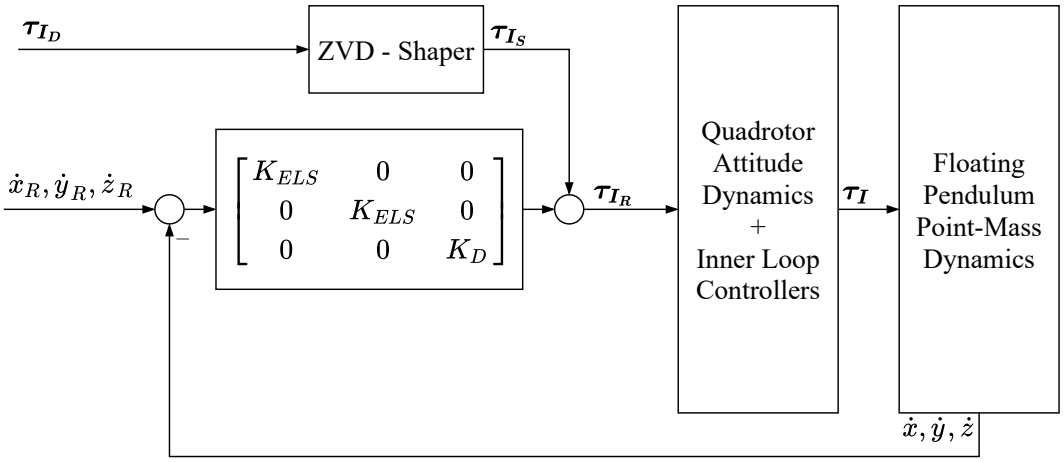

Figure 7.41: Flight control system using input shaping and extended H_∞ loop shaping controller

The reference commands $\dot{x}_R(t)$, $\dot{y}_R(t)$, and $\dot{z}_R(t)$ given to the outer loop quadrotor velocity controllers are generated by recording the response of the quadrotor velocity when the shaped input is applied to the nominal plant (with nominal values for thrust uncertainty T, cable length L, and payload mass M_L). These reference commands are used by the extended H_∞ loop shaping controller from Chapter 6, which acts to correct any deviations of the executed velocity trajectory from the planned reference velocity trajectory. Thus, in the nominal case when the shaped inputs cause the executed velocity trajectory to follow the planned reference trajectory, the error signal is zero and the feedback controller does not contribute to the force command. With the inevitable perturbations present in the plant, the executed velocity trajectory will deviate from the planned velocity reference trajectories $\dot{x}_R$, $\dot{y}_R$, and $\dot{z}_R$. In this case, the extended H_∞ loop shaping controller will superimpose corrective force commands on the feedforward force commands to return the executed trajectory to the reference trajectory.

7.4.2 Control System Performance with Nonlinear Model

Figure 7.39 and Figure 7.40 presented the response of the quadrotor velocity and the payload angle when a shaped input is applied to the nominal quadrotor-payload plant. Figures 7.42 and 7.43 show the simulated responses of the quadrotor velocity and the payload swing angle when the shaped input is applied to the nominal quadrotor-payload plant as well as multiple plants in

the uncertainty set for variations in the thrust uncertainty T_t, the cable length L, and the payload mass M_L.

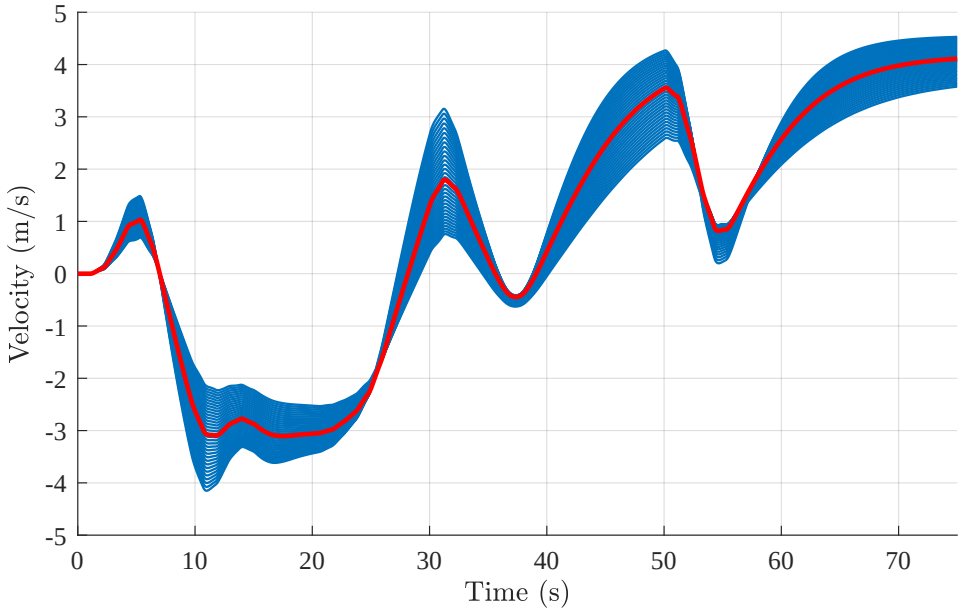

Figure 7.42: Quadrotor velocity responses of many plants in uncertainty set to shaped input alone.

As mentioned in the previous section, the three-impulse Zero-Vibration-Derivative shaper has additional constraints to it that enable it to be more robust to changes in the natural frequency of the system. Therefore, we see that although there are large changes in the quadrotor velocity response for different plant parameters, no oscillations are observed in the quadrotor velocity response for any of the plants in the uncertainty set. This verifies that the residual payload oscillations are suppressed for all the perturbed plants. This is supported by the payload swing angle responses shown in Figure 7.43, which show that the residual oscillations in the payload swing angle are also suppressed for all plants in the uncertainty set.

However, with input shaping alone, there can be large variations in the quadrotor velocity, as any disturbance causes deviations from the original expected velocity trajectories. This is expected behaviour when using open-loop control alone. To combat this, a feedback controller must be added.

For the feedback controller, the extended H_∞ loop shaping controller is used. The robust stability properties of this controller ensure stable tracking of velocity reference trajectories. However, the principle drawback of this controller, which is reduced time-domain performance, is overcome by using feedforward

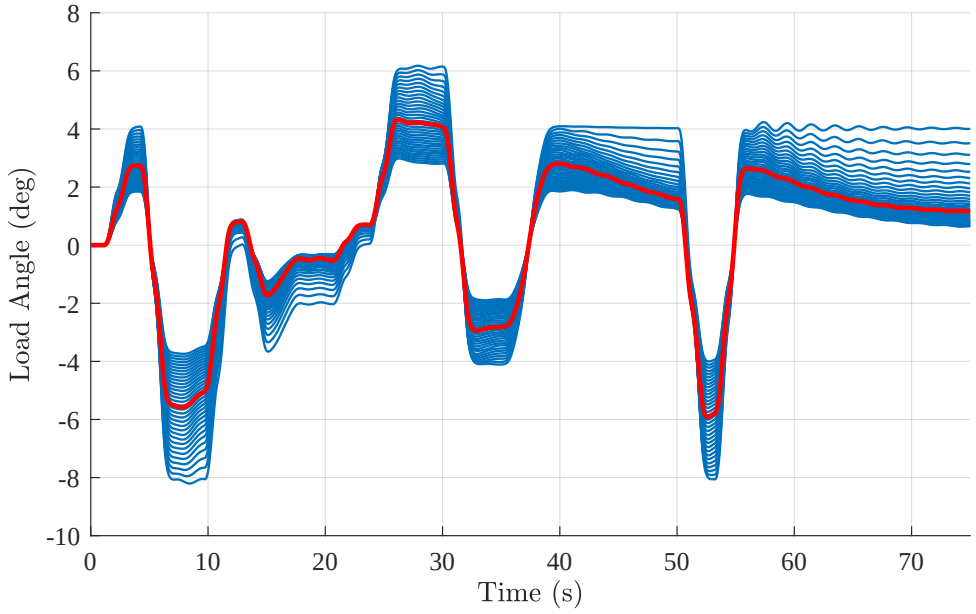

Figure 7.43: Load angle response of many plants in uncertainty set to shaped input alone.

control to drive the system. Figure 7.44 and 7.45 show the quadrotor velocity and payload swing angle responses when both the feedforward shaped input and the extended H_∞ loop shaping controller feedback was used. The responses are shown for the nominal plant as well as for multiple perturbed plants in the uncertainty set.

Figure 7.44 shows that the executed quadrotor velocity trajectories return to the reference velocity trajectory due to the corrective action provided by the feedback control. This is more prominent at steady-state velocities, when the feedback controller has enough time to correct the errors. Also, recall that the feedback controller is designed specifically to have robust stability and to reduce oscillations of the payload. This manifests in the fact that when the controller acts to correct deviations in the trajectory, these correcting actions are done in a manner such that oscillations are not excited and such that robust stability is ensured. Figure 7.45 shows that the feedback controller does not excite oscillations in the payload.

Figure 7.46 and 7.47 illustrates the response of the quadrotor velocity execution when a step disturbance is introduced into the quadrotor velocity measurement. The quadrotor velocity (and payload swing angle) responses are shown for the case where feedforward only is used, and for the case where both feedforward and feedback is used. The same arbitrary velocity reference trajectory and associated force commands are supplied to the flight control system as before, but the quadrotor velocity receives a step velocity measure-

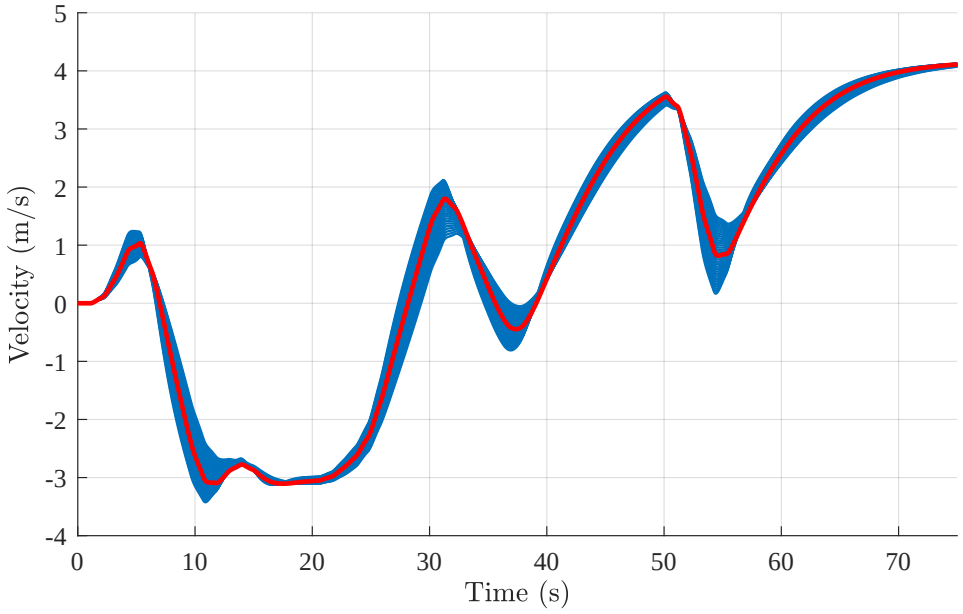

Figure 7.44: Quadrotor velocity responses of many plants in uncertainty set to shaped input in conjunction with extended H_∞ loop shaping controller.

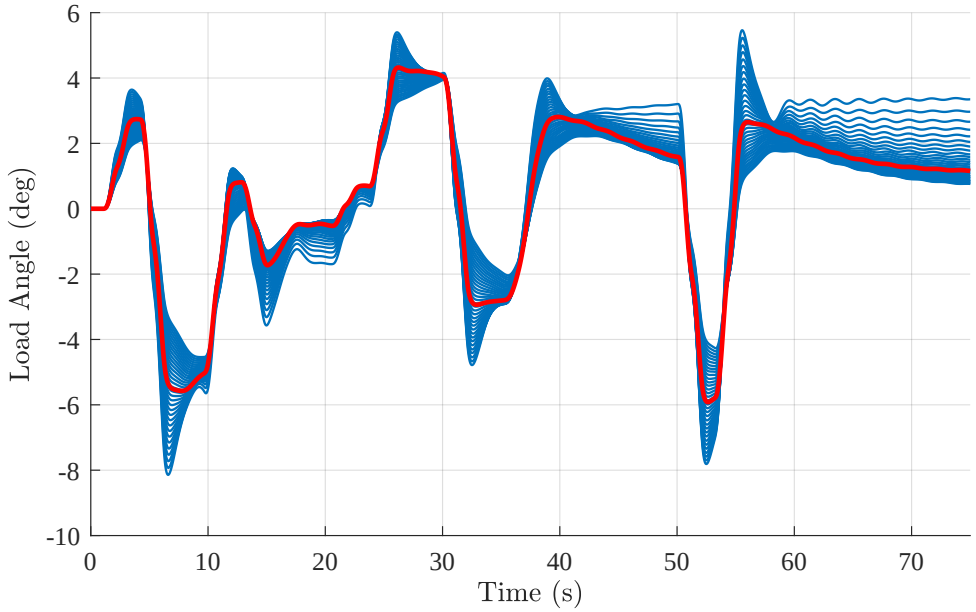

Figure 7.45: Load angle response of many plants in uncertainty set to shaped input in conjunction with extended H_∞ loop shaping controller

ment disturbance 20 seconds into the simulation. When feedforward only is used (ZVD shaper only, with no feedback controller K_{ELS}), the disturbance causes the quadrotor velocity trajectory to deviate from the reference velocity trajectory. The deviation is not corrected and persists until the end of the simulation. When both feedforward and feedback is used (ZVD shaper and feedback controller K_{ELS}), the disturbance still causes the quadrotor velocity trajectory to deviate from the reference velocity trajectory initially, but the feedback controller acts to reject the disturbance signal, and the quadrotor velocity trajectory returns to the reference trajectory.

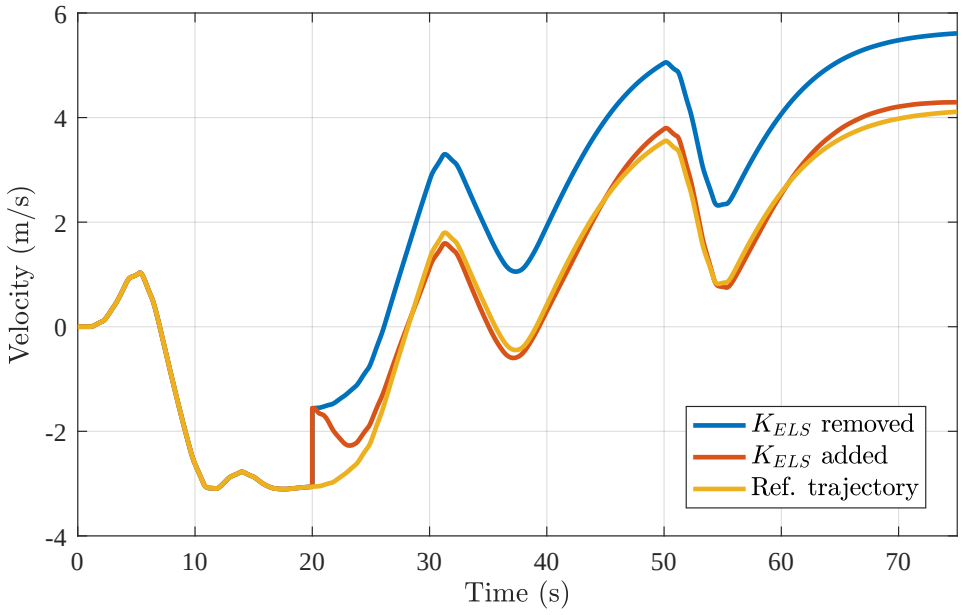

Figure 7.46: Quadrotor velocity response to shaped input with and without extended H_∞ loop shaping controller acting as a feedback controller. The quadrotor velocity receives a step disturbance 20 seconds into the simulation.

Furthermore, as shown by Figure 7.47, the controller performs the correction to velocity trajectory without causing excessive oscillations in the payload angle. Also, the robust stability of the controller, analysed in Chapter 6, ensures that for any perturbed plant, the controller will act to correct deviations from the nominal trajectory. This solution is therefore a robust flight controller that allows trajectory tracking in a robust manner. Trajectories can be generated to be aggressive or to accomplish specific tasks, if required. In this case, input shaping is used to ensure the trajectories do not cause residual swinging of the suspended payload.

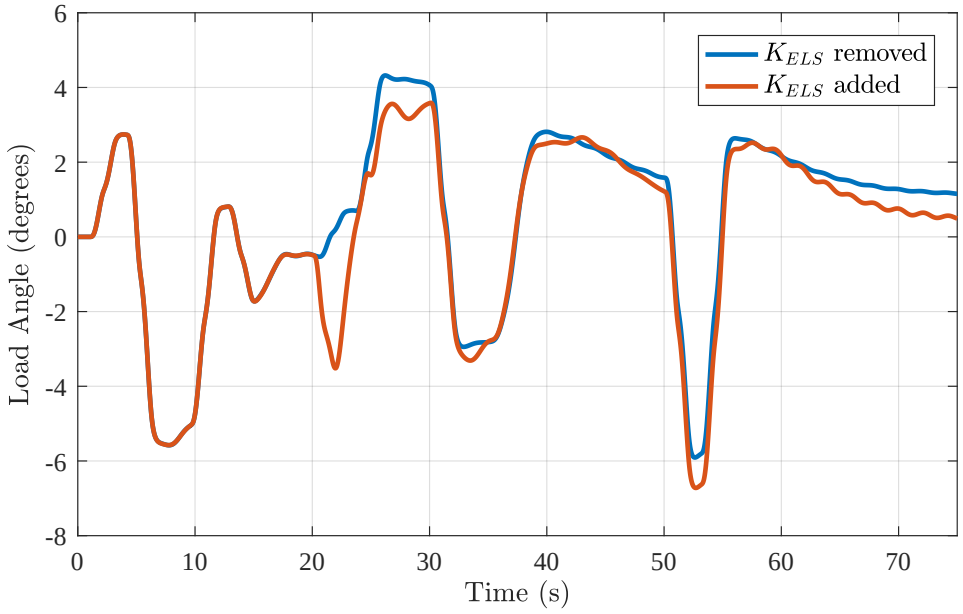

Figure 7.47: Load angle response to shaped input with and without extended H_∞ loop shaping controller acting as a feedback controller. The quadrotor velocity receives a step disturbance 20 seconds into the simulation.

7.5 Summary

This chapter presented two-degrees-of-freedom versions of the standard and extended H_∞ loop shaping designs presented in Chapters 5 and 6, respectively. In both cases, the controllers were expanded by adding a pre-filter that aimed to improve reference tracking performance. The pre-filters were designed through the solution of a model-matching H_∞ optimisation problem.

In the case of the standard two-degrees-of-freedom H_∞ loop shaping controller, the resulting system showed superior performance when compared to the original one-degree-of-freedom system, when simulated for two isolated cases in the nonlinear simulation. However, simulation with a variety of plant parameters using the linear models revealed that the system does not have robust stability.

The two-degrees-of-freedom extended H_∞ loop shaping controller performed significantly better than the one-degree-of-freedom version presented in Chapter 6. Also, because only a new pre-filter was designed in the model-matching problem, the robustness properties of the controller designed in Chapter 6 are carried over to the two-degrees-of-freedom design. The two-degrees-of-freedom extended H_∞ loop shaping controller meets the time-domain performance requirements, and provides robust stability. The controller also provides significant amounts of damping to the swinging motion of the suspended payload.

This chapter also presented a hybrid feedforward-feedback control configuration that allows for more aggressive trajectories to be tracked. The configuration uses a robust input shaper to ensure that inputs into the system do not excite residual swinging of the suspended payload. The extended H_∞ loop shaping controller from Chapter 6 is used as a feedback controller to reject disturbances and ensure trajectory tracking. Because the controller provides robust stability, trajectory errors will be corrected in a stable manner.

Chapter 8

Conclusions and Recommendations

8.1 Summary

In this dissertation, a flight control architecture for a quadrotor with a suspended payload was proposed. The flight control architecture placed an overall emphasis on robustness to large variations in systems parameters, as this was identified as an area of shortcoming in the current body of literature pertaining to quadrotors with suspended loads.

A mathematical model of a quadrotor with a suspended payload was derived, and a full nonlinear simulation model of the SLADe quadrotor augmented with a cable-suspended payload was created. The quadrotor model parameters were identified and validated in previous research done by the Electronic Systems Laboratory. Also, the uncertainties in the system were presented.

The existing acceleration-based control architecture used for the SLADe quadrotor in previous projects was adapted into a novel reference force-based control architecture for use with a cable-suspended payload. This architecture allows the rotational dynamics of a quadrotor and the translational dynamics of a quadrotor with a cable-suspended payload to be decoupled and controlled independently. The proposed architecture consists of outer-loop quadrotor velocity controllers that generate a reference force command vector in order to control the velocity of the quadrotor. The reference force command vector is used by the inner-loop quadrotor attitude controllers to determine a desired magnitude and direction for the quadrotor thrust vector. The inner-loop controllers then rotate the quadrotor in order to align the thrust vector with the reference force command vector.

Using the proposed architecture, a focus was placed on the development of a robust quadrotor velocity control system. Due to to fact that the linearised

vertical translational dynamics of the quadrotor and suspended payload do not contain the lightly damped resonant mode of the swinging motion of the payload, a proportional-integral controller is used to control the quadrotor velocity in the vertical direction. This feedback system exhibits good robustness towards the uncertainties in the system.

For the control of the quadrotor velocity in the horizontal direction, the first velocity control system presented is a linear quadratic integral (LQI) controller. For the nominal plant, the LQI controller provided good transient response and steady-state tracking without inducing oscillations in the payload swing angle. However, when the plant parameters were varied, the payload swing angle exhibited lightly damped behaviour and even instability.

Thereafter, an H_∞ loop shaping controller was presented. The H_∞ loop shaping controller replaced the LQI controller in the controller architecture, meaning it is used to control the horizontal velocity of the quadrotor. The objective of the design was to achieve the same transient performance and steady-state tracking performance achieved by the LQI controller, but with improved robustness to the uncertainty in the system. As part of the design procedure, a shaping weight was proposed to shape the open-loop frequency response of the plant in order to satisfy the design objectives. Furthermore, the H_∞ loop shaping design procedure produced a controller that theoretically has good robustness to general coprime factor uncertainty, but Monte Carlo simulations, as well as a subsequent robust stability analysis using the ν-gap metric, showed that the resulting closed-loop system does not have robust stability with the uncertainties present in the quadrotor-payload system. This was because the H_∞ loop shaping controller was designed without explicit knowledge of the uncertainty present in the system.

In order to incorporate explicit knowledge of the uncertainty in the system during the design of a controller, an extended H_∞ loop shaping algorithm was presented. This algorithm uses the ν-gap metric to quantify the uncertainty in a system, because of the intrinsic relationship between H_∞ loop shaping controllers and the ν-gap metric. The objective of the algorithm is to produce a controller that has theoretically guaranteed robust stability in the presence of the expected uncertainty, by ensuring that the resulting closed-loop system has sufficient generalised stability margins to handle the expected uncertainty.

This algorithm enabled the design of a quadrotor horizontal velocity controller that uses explicit knowledge of the uncertainty in the quadrotor-payload system, as measured by the ν-gap metric, and ensured that the resulting closed-loop velocity control system has robust stability. The resulting extended H_∞ loop shaping controller displayed significantly improved damping of the suspended payload swinging motion, and robust stability for all the plants in the uncertainty set, as verified using a Monte Carlo analysis. However, the resulting robust controller exhibited significantly decreased transient response

performance when compared to the H_∞ loop shaping controller and the LQI controller.

To recover these losses in transient performance, two-degrees-of-freedom versions of both the standard H_∞ loop shaping controller and the extended H_∞ loop shaping controller were presented. The first was a two-degrees-of-freedom configuration of the standard H_∞ loop shaping algorithm. This configuration produced slightly improved transient performance when compared to the standard H_∞ loop shaping controller, but again, the controller failed to display robust stability for all plants in the uncertainty set.

The second version was a novel two-degrees-of-freedom configuration of the extended H_∞ loop shaping controller. This procedure utilised the same extended H_∞ loop shaping controller designed earlier, but synthesised a pre-filter that aims to force the closed-loop response from the reference input to the plant output to match the response of a reference system. The two-degrees-of-freedom H_∞ loop shaping controller achieves transient performance that is comparable to the performance achieved with the LQI controller, yet the closed-loop system exhibits robust stability.

As an alternative to the two-degrees-of-freedom extended H_∞ loop shaping configuration, input shaping was investigated as a methodology to ensure that inputs into the system did not cause oscillations of the suspended payload. An input shaper that was specifically designed to be robust to variations in the natural frequency of the lightly damped modes of the system was presented. This shaper is known as the Zero-Vibration-Derivative shaper.

The ZVD shaper was then implemented in a hybrid feedforward-feedback architecture whereby shaped inputs from the ZVD shaper are used to drive the velocity of the quadrotor, without causing oscillations of the suspended payload. The extended H_∞ loop shaping controller is used as a feedback controller, in order to correct any deviations from the nominal expected velocity trajectory. Also, because the controller has theoretically guaranteed robust stability, these trajectory corrections are ensured to be stable and not cause oscillations of the suspended payload. The resulting hybrid feedforward-feedback architecture is therefore a robust flight control solution that allows aggressive, swing-free, and robust control of the velocity of a quadrotor with a suspended payload.

8.2 Future Work

We now highlight some points to consider for future work:

1. A requirement for the design of the quadrotor velocity controller was that it should suppress oscillations of the suspended payload. Therefore, damping of the payload swinging motion was a desirable trait of the controller.

However, a limitation of the proposed control architectures is that the payload angles are not measured by any external or on-board sensors. This means that the payload angles are estimated in the feedback controllers. However, estimating the payload angles can be a weak point in the robustness problem - deviations in plant parameters cause poor performance from state estimators, which in turn causes poor controller performance. The quadrotor velocity is not affected very strongly by the swinging motion of the suspended payload - these effects will also vary depending on the ratio of the quadrotor mass to the suspended payload mass. Therefore, a controller that has quadrotor velocity measurements only will be ineffective at controlling the suspended payload angles. Most examples of quadrotors with suspended loads currently in literature use external sensors to measure the payload angles. In this research, we opted not to, but future work could be to incorporate ways of actively measuring suspended payload angles.

2. The algorithm presented in Chapter 6 could be improved in the following ways:

   - Nevanlinna-Pick interpolation could be used to solve the H_∞ optimisation problem, instead of the method used in this dissertation. The algorithm presented in this research calculates the worst-case uncertainty in the plant (as measured by the ν-gap metric), and then fits a real-rational transfer function to cover this uncertainty. However, the accuracy of the algorithm can be compromised in this step due to poor fitting of the function. Using Nevanlinna-Pick interpolation allows the step of fitting a function to be omitted.
   - The algorithm currently produces a controller that gives a guaranteed generalised stability margin at all frequencies. However, the algorithm tends to give excessive stability margins at certain frequencies. These excessive margins can be reduce by further modifying the design weight that encapsulates the uncertainties present in the plant.

3. The design configuration in which the extended H_∞ loop shaping controller is incorporated into a two-degrees-of-freedom design can be further developed. Currently, the design configuration is a model-matching problem that uses an existing inner-loop feedback controller and then designs a pre-filter to improve time-domain performance. This idea can be extended to incorporate the robust stability requirements into the design of the inner-loop controller *and* the outer-loop pre-filter by reconfigurating the design problem. A new algorithm that develops a controller that has robust stability and simultaneously attempts to modify the closed-loop response to match the response of a reference system could be developed.

4. Currently, arbitrary inputs into the system are shaped by a ZVD shaper to ensure they do not cause oscillations of the suspended payload. However,

an optimal control formulation and trajectory planning approach could be used to generate specific trajectories to accomplish certain tasks. These specific trajectories can be incorporated into the hybrid feedforward-feedback configuration. The trajectories could be designed to accomplish tasks such as agile manoeuvres or obstacle avoidance, while having a robust feedback controller to correct deviations from the nominal trajectory.

Appendices

Appendix A

H_∞ Control Concepts

This Appendix highlights some of the main theoretical concepts used in this project, which are taken from Zhou et al. [73], [74] and Vinnicombe [75]. System and signal norms are dicussed, in order to place the discussions about H_∞ norms throughout the dissertation into context. Also, the state-space formulae for the standard H_∞ optimization problem are presented. These formulae are used to solve H_∞ optimization problems throughout the study.

A.1 Norms of Systems and Signals

This section will describe the norms on systems and signals that are used in this project.

A.1.1 Signal Spaces

$\mathcal{L}_{2(-\infty,\infty)}$ is the time domain space of all signals with bounded energy, with the associated norm for a signal $\mathbf{x}(t) \in \boldsymbol{R}^n$ being

$$||\mathbf{x}||_2 = \sqrt{\int_{-\infty}^{\infty} \mathbf{x}^T(t)\mathbf{x}(t)dt}. \tag{A.1.1}$$

This has the interpretation of being the RMS energy of the signal. $\mathcal{L}_{2(-\infty,\infty)}$ can also be defined as a frequency domain space with norm

$$||\hat{\mathbf{x}}||_2 = \sqrt{\frac{1}{2\pi}\int_{-\infty}^{\infty} \hat{\mathbf{x}}^T(jw)\hat{\mathbf{x}}(jw)dw}, \tag{A.1.2}$$

and if $\hat{\mathbf{x}}(jw) \in \mathcal{L}_{2(-\infty,\infty)}$ is the Fourier transform of $\mathbf{x}(t) \in \mathcal{L}_{2(-\infty,\infty)}$, then $||\hat{\mathbf{x}}||_2 = ||\mathbf{x}||_2$ by Parseval's theorem.

$\mathcal{L}_{2(-\infty,\infty)}$ can be decomposed into $\mathcal{L}_{2(0,\infty)}$, which is the set of signals in $\mathcal{L}_{2(-\infty,\infty)}$ that are zero for negative time, and $\mathcal{L}_{2(-\infty,0)}$, which is the set of signals in $\mathcal{L}_{2(-\infty,\infty)}$ that are zero for positive time. Lastly, the frequency domain space H_2 is the space of Fourier transforms of signals in $\mathcal{L}_{2(0,\infty)}$, and $H_2^\perp$ is the space of Fourier transforms of signals in $\mathcal{L}_{2(-\infty,0)}$.

A.1.2 Function Spaces

Systems can be considered to be operators on signal spaces. H_∞ is the space of transfer functions of stable, linear, time-invariant, continuous time systems. The fact that they are stable means that for any input signal in H_2, the output will also be in H_2. The associated norm for a system $\mathbf{P}$ in H_∞ is

$$||\mathbf{P}||_\infty = \sup_{u \in H_2, u \neq 0} \frac{||\mathbf{Pu}||_2}{||\mathbf{u}||_2}, \tag{A.1.3}$$

and the interpretation of this is the maximum possible RMS energy gain of the input signal. In the frequency domain, the norm can be defined as

$$||\mathbf{P}||_\infty = \sup_{s:\Re(s)>0} \bar{\sigma}(\mathbf{P}(s)). \tag{A.1.4}$$

If $\mathbf{P}$ is rational, a result from complex analysis called the maximum modulus principle gives that the maximum will be achieved on the boundary $s = jw$. Therefore, if $\mathbf{P}$ is rational and $\mathbf{P} \in H_\infty$, then

$$||\mathbf{P}||_\infty = \max_{w \in \boldsymbol{R}} \bar{\sigma}(\mathbf{P}(jw)), \tag{A.1.5}$$

and the interpretation of this is the maximum possible gain in the frequency domain between the input and output signals. Lastly, the superset containing H_∞ is the space L_∞, which is the space of all functions essentially bounded on the imaginary axis with norm

$$||\mathbf{P}||_\infty := \operatorname{ess\,sup}_w \bar{\sigma}(\mathbf{P}(jw)). \tag{A.1.6}$$

Any proper real rational transfer function with no poles on the imaginary axis is in L_∞, and any proper real rational transfer function with no poles on the imaginary axis or in the right-half plane are in H_∞.

A.2 H_∞ Norm Optimization

A.2.1 Solution to H_∞ Sub-Optimal Control Problem

Consider the system shown by the block diagram

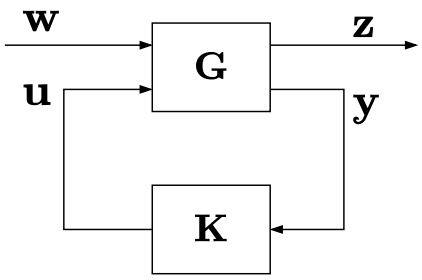

Figure A.1: General Control Configuration

where $\mathbf{G}$ has the following state space realization and is assumed to be real rational and proper.

$$\mathbf{G}(s) = \left[\begin{array}{c|cc} \mathbf{A} & \mathbf{B}_1 & \mathbf{B}_2 \\ \hline \mathbf{C}_1 & \mathbf{0} & \mathbf{D}_{12} \\ \mathbf{C}_2 & \mathbf{D}_{21} & \mathbf{0} \end{array}\right] \tag{A.2.1}$$

The following assumptions are made:

i $(\mathbf{A}, \mathbf{B}_1)$ is controllable and $(\mathbf{C}_1, \mathbf{A})$ is observable;

ii $\mathbf{A}, \mathbf{B}_2)$ is stabilisable and $\mathbf{C}_2, \mathbf{A})$ is detectable;

iii $\mathbf{D}_{12}^* \begin{bmatrix} \mathbf{C}_1 & \mathbf{D}_{12} \end{bmatrix} = \begin{bmatrix} \mathbf{0} & \mathbf{I} \end{bmatrix}$

iv $\begin{bmatrix} \mathbf{B}_1 \\ \mathbf{D}_{21} \end{bmatrix} \mathbf{D}_{21}^* = \begin{bmatrix} \mathbf{0} \\ \mathbf{I} \end{bmatrix}$

The closed loop transfer function from $\mathbf{w}$ to $\mathbf{z}$ is found through the lower linear fractional transformation (LFT), $\mathbf{z} = \mathbf{T}_{zw}\mathbf{w} = F_l(\mathbf{G}, \mathbf{K})\mathbf{w}$. A lower linear fractional transformation is

$$F_l(\mathbf{G}, \mathbf{K}) = \mathbf{G}_{11} + \mathbf{G}_{12}\mathbf{K}(\mathbf{I} - \mathbf{G}_{22}\mathbf{K})^{-1}\mathbf{G}_{21} \tag{A.2.2}$$

We will focus on the sub-optimal problem, as there is not much benefit in finding truly optimal controllers over controllers that are close in the norm sense. So we are interested in finding a controller that ensures that $||\mathbf{T}_{zw}||_\infty <$

γ, with $\gamma > \gamma_{\min}$, where $\gamma_{\min}$ is the optimal H_∞ norm of $\mathbf{T}_{zw}$. For a given γ, we have the following theorem:

Theorem 1: State space solution to H_∞ sub-optimal control problem *There exists an admissable controller $\boldsymbol{K}(s)$ such that $||\boldsymbol{T}_{zw}||_\infty < \gamma$ if and only if the following three conditions hold:*

i $\mathbf{X}_\infty \geq 0$ *is a stabilising solution to the algebraic Riccati equation*

$$\mathbf{A}^T\mathbf{X}_\infty + \mathbf{X}_\infty\mathbf{A} + \mathbf{C}_1^T\mathbf{C}_1 + \mathbf{X}_\infty(\gamma^{-2}\mathbf{B}_1^T\mathbf{B}_1 - \mathbf{B}_2^T\mathbf{B}_2)\mathbf{X}_\infty = \mathbf{0} \tag{A.2.3}$$

ii $\mathbf{Y}_\infty \geq 0$ *is a stabilising solution to the algebraic Riccati equation*

$$\mathbf{A}\mathbf{Y}_\infty + \mathbf{Y}_\infty\mathbf{A}^T + \mathbf{B}_1\mathbf{B}_1^T + \mathbf{Y}_\infty(\gamma^{-2}\mathbf{C}_1^T\mathbf{C}_1 - \mathbf{C}_2^T\mathbf{C}_2)\mathbf{Y}_\infty = \mathbf{0} \tag{A.2.4}$$

iii $\rho(\mathbf{X}_\infty\mathbf{Y}_\infty) < \gamma^2$

where $\mathbf{X}_\infty \geq 0$ means $\mathbf{X}_\infty$ is positive semi-definite and $\rho(\mathbf{X}_\infty\mathbf{Y}_\infty)$ is the maximum spectral radius of $\mathbf{X}_\infty\mathbf{Y}_\infty$. Also, for $\mathbf{X}_\infty$ and $\mathbf{Y}_\infty$ to be the stabilising solutions, the matrices $[\mathbf{A}+(\gamma^{-2}\mathbf{B}_1\mathbf{B}_1^T-\mathbf{B}_2\mathbf{B}_2^T)\mathbf{X}_\infty]$ and $[\mathbf{A}+\mathbf{Y}_\infty(\gamma^{-2}\mathbf{C}_1^T\mathbf{C}_1-\mathbf{C}_2^T\mathbf{C}_2)]$ must be stable (Hurwitz). Furthermore, when these conditions hold, one such controller is

$$\mathbf{K}_{sub}(s) := \left[\begin{array}{c|c} \hat{\mathbf{A}}_\infty & -\mathbf{Z}_\infty\mathbf{L}_\infty \\ \hline \mathbf{F}_\infty & \mathbf{0} \end{array}\right] \tag{A.2.5}$$

where

$$\hat{\mathbf{A}}_\infty = \mathbf{A} + \gamma^{-2}\mathbf{B}_1\mathbf{B}_1^*\mathbf{X}_\infty + \mathbf{B}_2\mathbf{F}_\infty + \mathbf{Z}_\infty\mathbf{L}_\infty\mathbf{C}_2$$

$$\begin{aligned} \mathbf{F}_\infty &= -\mathbf{B}_2^*\mathbf{X}_\infty, \\ \mathbf{L}_\infty &= -\mathbf{Y}_\infty\mathbf{C}_2^*, \\ \mathbf{Z}_\infty &= (\mathbf{I} - \gamma^{-2}\mathbf{Y}_\infty\mathbf{X}_\infty)^{-1}. \end{aligned}$$

The proof of this theorem is given by Doyle et al [78]. Generally, a bisection algorithm is used to find the smallest value of γ that still allows the solutions to the Riccati equations to exist, to within some tolerance on γ.

Appendix B

Quadrotor and Suspended Payload Translational Model Coefficients

$$v_{xx} = \dot{x} - 2L\cos\theta_L\cos\phi_L\dot{\theta}_L + 2L\sin\theta_L\sin\phi_L\dot{\phi}_L \tag{B.0.1}$$

$$v_{xt} = L^2\cos^2\theta_L\cos^2\phi_L\dot{\theta}_L - \frac{1}{2}l^2\sin 2\theta_L\sin 2\phi_L\dot{\phi}_L \tag{B.0.2}$$

$$v_{xp} = L^2\sin^2\theta_L\sin^2\phi_L\dot{\phi}_L \tag{B.0.3}$$

$$v_{yy} = \dot{y} - 2L\cos\theta_L\cos\phi_L\dot{\phi}_L + 2L\sin\theta_L\sin\phi_L\dot{\theta}_L \tag{B.0.4}$$

$$v_{yp} = L^2\cos^2\theta_L\cos^2\phi_L\dot{\phi}_L - \frac{1}{2}l^2\sin 2\theta_L\sin 2\phi_L\dot{\theta}_L \tag{B.0.5}$$

$$v_{yt} = L^2\sin^2\theta_L\sin^2\phi_L\dot{\theta}_L \tag{B.0.6}$$

$$v_{zz} = \dot{z} - 2L\sin\theta_L\cos\phi_L\dot{\theta}_L - 2L\cos\theta_L\sin\phi_L\dot{\phi}_L \tag{B.0.7}$$

$$v_{zt} = L^2\sin^2\theta_L\cos^2\phi_L\dot{\theta}_L + \frac{1}{2}l^2\sin 2\theta_L\sin 2\phi_L\dot{\phi}_L \tag{B.0.8}$$

$$v_{zp} = L^2\cos^2\theta_L\sin^2\phi_L\dot{\phi}_L \tag{B.0.9}$$

Appendix C

Additional Modelling Information

The values used to model the SLADe quadrotor and suspended payload system are given in Table C.1. The data comes from Möller [72].

Table C.1: Plant Parameters

Parameter	**Symbol**	**Unit**	**Value**
Quadrotor mass	M_c	kg	9.00
X-Axis Moment of Inertia	I_{xx}	kg.m^2	0.61
Y-Axis Moment of Inertia	I_{yy}	kg.m^2	0.61
Z-Axis Moment of Inertia	I_{zz}	kg.m^2	1.06
Moment arm	d	m	0.408
Drag chord distance	r_D	m	0.18
Rotor lift to drag ratio	R_{LD}	ND	0.1
Drag area - North	A_x	m^2	0.50
Drag area - East	A_y	m^2	0.50
Drag area - Down	A_z	m^2	0.50
Drag coefficient	C_D	ND	1.0
Rotor time constant	τ	s	0.125
Nominal load mass	M_L	kg	3.50
Nominal cable length	L	m	1.50
Drag area - payload	A_L	m^2	0.125

The nonlinear simulation model contains sensor noise on the measurements. The sensor noise from the SLADe's sensor suite has been characterized during previous research by the Electronic System Laboratory. These sensor noise estimates have been used in Hardware-in-the-Loop simulations as well. The sensor noise parameters are presented in Table C.2. In this table, $\ddot{x}_B$, $\ddot{y}_B$, and $\ddot{z}_B$ are used to denote the acceleration measured by the accelerometer in the body-fixed x_B axis, y_B axis, and z_B axis respectively.

Table C.2: Gyroscope and GPS Measurement Noise Parameters in Simulation

Sensor	**Measurement**	**PSD**	**Block Sample Time (s)**
Roll Gyroscope	P	1.523×10^{-6}	0.02
Pitch Gyroscope	Q	1.523×10^{-6}	0.02
Yaw Gyroscope	R	1.523×10^{-6}	0.02
X Accelerometer	$\ddot{x}_B$	2×10^{-4}	0.02
Y Accelerometer	$\ddot{y}_B$	2×10^{-4}	0.02
Z Accelerometer	$\ddot{z}_B$	2×10^{-4}	0.02
GPS N Speed	$\dot{x}$	1.00×10^{-7}	0.002
GPS E Speed	$\dot{y}$	1.00×10^{-7}	0.002
GPS D Speed	$\dot{z}$	8.00×10^{-8}	0.002

Wind disturbances are approximated using the configuration shown in Figure C.1. The model incorporates wind gusts and constant wind. The value of the constant wind is summed with the wind gusts. The gusts are created by using a band-limited white noise (BLWN) block from the Simulink library, and using a low-pass filter with a cut-off frequency of 5 seconds to smooth the output. This creates a simple approximation of real wind disturbances.

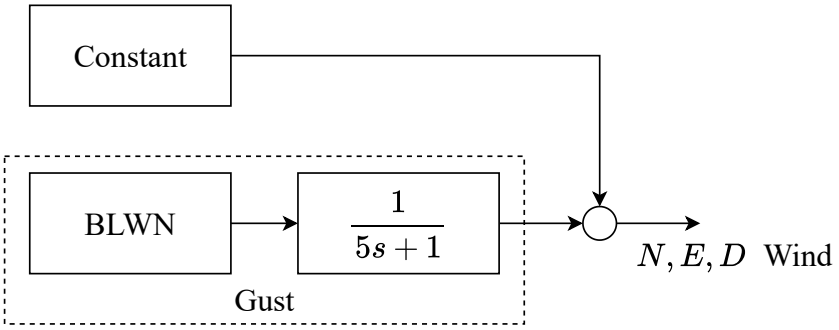

Figure C.1: Wind disturbance model

References

[1] Declan Bates and Ian Postlethwaite. *Robust multivariable control of aerospace systems*, volume 8. IOS Press, 2002.

[2] Sigurd Skogestad and Ian Postlethwaite. *Multivariable feedback control: analysis and design*, volume 2. Wiley New York, 2007.

[3] John Doyle. Guaranteed margins for LQG regulators. *IEEE Transactions on automatic Control*, 23(4):756–757, 1978.

[4] Richard A Hyde. *Hinf aerospace control design: a VSTOL flight application*. Springer Science & Business Media, 2013.

[5] Cameron C Taylor and Jacobus AA Engelbrecht. Acceleration-based control of a quadrotor with a swinging payload. In *Pattern Recognition Association of South Africa and Robotics and Mechatronics International Conference (PRASA-RobMech), 2016*, pages 1–8. IEEE, 2016.

[6] Glenn Vinnicombe. Robust design in the graph topology; a benchmark example. In *1992 American Control Conference*, pages 2063–2064. IEEE, 1992.

[7] Otto JM Smith. Posicast control of damped oscillatory systems. *Proceedings of the IRE*, 45(9):1249–1255, 1957.

[8] Neil C Singer. *Residual vibration reduction in computer controlled machines*. PhD thesis, Massachusetts Institute of Technology, 1988.

[9] GP Starr. Swing-free transport of suspended objects with a path-controlled robot manipulator. *ASME J. Dyn. Syst., Meas., Control*, 107(1):97–100, 1985.

[10] Gregory Starr, John Wood, and Ronald Lumia. Rapid transport of suspended payloads. In *Robotics and Automation, 2005. ICRA 2005. Proceedings of the 2005 IEEE International Conference on*, pages 1394–1399. IEEE, 2005.

[11] John T Betts. Survey of numerical methods for trajectory optimization. *Journal of Guidance, Control and Dynamics*, 21(2):193–207, 1998.

[12] Jacobus Adriaan Albertus Engelbrecht. *Automatic Flight Envelope Recovery for Large Transport Aircraft.* PhD thesis, Stellenbosch University, 2016.

[13] Johannes JK Engelbrecht and Jacobus AA Engelbrecht. Optimal attitude and flight vector recovery for large transport aircraft using sequential quadratic programming. In *Pattern Recognition Association of South Africa and Robotics and Mechatronics International Conference (PRASA-RobMech), 2016*, pages 1–7. IEEE, 2016.

[14] Paul T Boggs and Jon W Tolle. Sequential quadratic programming. *Acta numerica*, 4:1–51, 1995.

[15] Luigi S Cicolani and Gerd Kanning. Equations of motion of slung-load systems, including multilift systems, nasa, 1992. Technical report, NASA-TP-3280.

[16] Morten Bisgaard, Jan Dimon Bendtsen, and Anders La Cour-Harbo. Modeling of generic slung load system. *Journal of Guidance, Control, and Dynamics*, 32(2):573–585, 2009.

[17] Louis R Lucassen and Fred J Sterk. Dynamic stability analysis of a hovering helicopter with a sling load. *Journal of the American Helicopter Society*, 10(2):6–12, 1965.

[18] L Feaster, C Poli, and R Kirchhoff. Dynamics of a slung load. *Journal of Aircraft*, 14(2):115–121, 1977.

[19] Sabi J Asseo and Richard F Whitbeck. Control requirements for sling-load stabilization in heavy lift helicopters. *Journal of the American Helicopter Society*, 18(3):23–31, 1973.

[20] Narendra K Gupta and Arthur Earl Bryson. *Automatic Control of a Helicopter with a Hanging Load.* Department of Aeronautics and Astronautics, Stanford University, 1973.

[21] Narendra K Gupta and AE Bryson. Near-hover control of a helicopter with a hanging load. *Journal of Aircraft*, 13(3):217–222, 1976.

[22] Tuvya Ronen, A Bryson, Jr., and W Hindson. Dynamics of a helicopter with a sling load. In *13th Atmospheric Flight Mechanics Conference*, page 2288, 1985.

[23] Bellur Lakshminarayana Nagabhushan. *Systematic investigation of models of helicopter with a slung load.* PhD thesis, Virginia Tech, 1977.

[24] D Faille and AJJ van der Weiden. Robust regulation of a flying crane. In *Control Applications, 1995., Proceedings of the 4th IEEE Conference on*, pages 494–499. IEEE, 1995.

[25] Robert Mahony, Vijay Kumar, and Peter Corke. Multirotor aerial vehicles. *IEEE Robotics and Automation magazine*, 20(32), 2012.

[26] Morten Bisgaard, Anders la Cour-Harbo, and Jan Dimon Bendtsen. Adaptive control system for autonomous helicopter slung load operations. *Control Engineering Practice*, 18(7):800–811, 2010.

[27] Ivana Palunko and Rafael Fierro. Adaptive control of a quadrotor with dynamic changes in the center of gravity. *IFAC Proceedings Volumes*, 44(1):2626–2631, 2011.

[28] Ivana Palunko, Rafael Fierro, and Patricio Cruz. Trajectory generation for swing-free maneuvers of a quadrotor with suspended payload: A dynamic programming approach. In *Robotics and Automation (ICRA), 2012 IEEE International Conference on*, pages 2691–2697. IEEE, 2012.

[29] Ivana Palunko. *Agile load transportation systems using aerial robots*. PhD thesis, The University of New Mexico, 2013.

[30] Ivana Palunko, Aleksandra Faust, Patricio Cruz, Lydia Tapia, and Rafael Fierro. A reinforcement learning approach towards autonomous suspended load manipulation using aerial robots. In *Robotics and Automation (ICRA), 2013 IEEE International Conference on*, pages 4896–4901. IEEE, 2013.

[31] Paul EI Pounds, Daniel R Bersak, and Aaron M Dollar. Stability of small-scale UAV helicopters and quadrotors with added payload mass under PID control. *Autonomous Robots*, 33(1-2):129–142, 2012.

[32] Fátima Silva Leite. Geometric nonlinear control-an introduction. *Unpublished paper*, 2010.

[33] Farhad A Goodarzi, Daewon Lee, and Taeyoung Lee. Geometric stabilization of a quadrotor UAV with a payload connected by flexible cable. In *American Control Conference (ACC), 2014*, pages 4925–4930. IEEE, 2014.

[34] Farhad A Goodarzi and Taeyoung Lee. Dynamics and control of quadrotor UAVs transporting a rigid body connected via flexible cables. In *American Control Conference (ACC), 2015*, pages 4677–4682. IEEE, 2015.

[35] Farhad A Goodarzi. Autonomous aerial payload delivery with quadrotor using varying length cable. In *Advanced Mechatronic Systems*

(ICAMechS), 2016 International Conference on, pages 394–399. IEEE, 2016.

[36] Patricio J Cruz, Meeko Oishi, and Rafael Fierro. Lift of a cable-suspended load by a quadrotor: A hybrid system approach. In *American Control Conference (ACC), 2015*, pages 1887–1892. IEEE, 2015.

[37] Prasanth Kotaru, Guofan Wu, and Koushil Sreenath. Dynamics and control of a quadrotor with a payload suspended through an elastic cable. In *2017 American Control Conference (ACC)*, pages 3906–3913. IEEE, 2017.

[38] Taeyoung Lee. Geometric control of quadrotor uavs transporting a cable-suspended rigid body. *IEEE Transactions on Control Systems Technology*, 26(1):255–264, 2017.

[39] Kristian Klausen, Thor I Fossen, and Tor Arne Johansen. Nonlinear control of a multirotor UAV with suspended load. In *Unmanned Aircraft Systems (ICUAS), 2015 International Conference on*, pages 176–184. IEEE, 2015.

[40] Sara Sadr, S Ali A Moosavian, and Payam Zarafshan. Dynamics modeling and control of a quadrotor with swing load. *Journal of Robotics*, 2014, 2014.

[41] Marco M Nicotra, Emanuele Garone, Roberto Naldi, and Lorenzo Marconi. Nested saturation control of an UAV carrying a suspended load. In *American Control Conference (ACC), 2014*, pages 3585–3590. IEEE, 2014.

[42] ME Guerrero, DA Mercado, R Lozano, and CD García. Ida-pbc methodology for a quadrotor UAV transporting a cable-suspended payload. In *Unmanned Aircraft Systems (ICUAS), 2015 International Conference on*, pages 470–476. IEEE, 2015.

[43] Martijn Weijers. Minimum swing control of a UAV with a cable suspended load. Master's thesis, University of Twente, 2015.

[44] Amit Ailon and Shai Arogeti. On set-point control of a quadrotor-type helicopter with a suspended load. In *Control, Automation and Robotics (ICCAR), 2016 2nd International Conference on*, pages 194–199. IEEE, 2016.

[45] R Praveen Kumar Jain. Transportation of cable suspended load using unmanned aerial vehicles. Master's thesis, Delft University of Technology, 2015.

[46] Yaser Alothman, Wesam Jasim, and Dongbing Gu. Quad-rotor lifting-transporting cable-suspended payloads control. In *Automation and Computing (ICAC), 2015 21st International Conference on*, pages 1–6. IEEE, 2015.

[47] Yaser Alothman and Dongbing Gu. Quadrotor transporting cable-suspended load using iterative linear quadratic regulator (iLQR) optimal control. In *Computer Science and Electronic Engineering (CEEC), 2016 8th*, pages 168–173. IEEE, 2016.

[48] Mathieu Geisert and Nicolas Mansard. Trajectory generation for quadrotor based systems using numerical optimal control. In *Robotics and Automation (ICRA), 2016 IEEE International Conference on*, pages 2958–2964. IEEE, 2016.

[49] Daniel Mellinger, Alex Kushleyev, and Vijay Kumar. Mixed-integer quadratic program trajectory generation for heterogeneous quadrotor teams. In *Robotics and Automation (ICRA), 2012 IEEE International Conference on*, pages 477–483. IEEE, 2012.

[50] Thibaut Raharijaona and François Bateman. Robust control for an off-centered quadrotor. In *Control & Automation (MED), 2011 19th Mediterranean Conference on*, pages 1253–1258. IEEE, 2011.

[51] Taeyoung Lee, Melvin Leok, and N Harris McClamroch. Nonlinear robust tracking control of a quadrotor UAV on SE (3). *Asian Journal of Control*, 15(2):391–408, 2013.

[52] Yu Xu and Changfei Tong. Quantitative feedback control of a quadrotor. In *Industrial Electronics (ISIE), 2012 IEEE International Symposium on*, pages 1309–1314. IEEE, 2012.

[53] Matt Rich, Nicola Elia, and Phillip Jones. Design and implementation of an hinfinity controller for a quadrotor helicopter. In *Control & Automation (MED), 2013 21st Mediterranean Conference on*, pages 1189–1198. IEEE, 2013.

[54] Duncan McFarlane and Keith Glover. A loop-shaping design procedure using hinfinity synthesis. *IEEE transactions on automatic control*, 37(6):759–769, 1992.

[55] Aykut C Satici, Hasan Poonawala, and Mark W Spong. Robust optimal control of quadrotor UAVs. *IEEE Access*, 1:79–93, 2013.

[56] Markus Windolf, Nils Götzen, and Michael Morlock. Systematic accuracy and precision analysis of video motion capturing systems, exemplified on the vicon-460 system. *Journal of biomechanics*, 41(12):2776–2780, 2008.

[57] Byung-Cheol Min, Ji-Hyeon Hong, and Eric T Matson. Adaptive robust control (arc) for an altitude control of a quadrotor type UAV carrying an unknown payloads. In *Control, Automation and Systems (ICCAS), 2011 11th International Conference on*, pages 1147–1151. IEEE, 2011.

[58] Shicong Dai, Taeyoung Lee, and Dennis S Bernstein. Adaptive control of a quadrotor UAV transporting a cable-suspended load with unknown mass. In *Decision and Control (CDC), 2014 IEEE 53rd Annual Conference on*, pages 6149–6154. IEEE, 2014.

[59] Hae-In Lee, Byung-Yoon Lee, Dong-Wan Yoo, Gun-Hee Moon, and Min-Jea Tahk. Dynamics modeling and robust controller design of the multi-UAV transportation system.

[60] Guilherme V Raffo and Marcelino M de Almeida. Nonlinear robust control of a quadrotor UAV for load transportation with swing improvement. In *American Control Conference (ACC), 2016*, pages 3156–3162. IEEE, 2016.

[61] Xu Zhou, Xiaoli Zhang, Jiucai Zhang, and Rui Liu. Stabilization and trajectory control of a quadrotor with uncertain suspended load. *arXiv preprint arXiv:1612.04324*, 2016.

[62] Stephen Boyd, Laurent El Ghaoui, Eric Feron, and Venkataramanan Balakrishnan. *Linear matrix inequalities in system and control theory*. SIAM, 1994.

[63] Constantine H Houpis, Steven J Rasmussen, and Mario Garcia-Sanz. *Quantitative feedback theory: fundamentals and applications*. CRC Press, 2005.

[64] Salah I Al Swailem. *Application of robust control in unmanned vehicle flight control system design*. PhD thesis, Cranfield University, 2004.

[65] SJ Williams and RA Hyde. A comparison of different h/spl infin methods in vstol flight control system design. In *American Control Conference, 1990*, pages 2508–2513. IEEE, 1990.

[66] Marco La Civita, George Papageorgiou, William C Messner, and Takeo Kanade. Design and flight testing of a gain-scheduled h/sub/spl infin//loop shaping controller for wide-envelope flight of a robotic helicopter. In *American Control Conference, 2003. Proceedings of the 2003*, volume 5, pages 4195–4200. IEEE, 2003.

[67] Isharaka Gunasinghe and Alexander Lanzon. A systematic weight synthesis procedure for performance optimisation in h_∞ loop shaping. In *Control Conference (ECC), 2007 European*, pages 223–228. IEEE, 2007.

[68] Mobolaji Osinuga, Sourav Patra, and Alexander Lanzon. Incorporating smoothness into weight optimization for h_∞ loop-shaping design. In *Control & Automation (MED), 2010 18th Mediterranean Conference on*, pages 856–861. IEEE, 2010.

[69] A Lanzon. Weight optimization in h_∞ problems. *Automatica*, 41:1201–1208, 2005.

[70] Yuyan Liu and Shiliang Zhou. Low order structured weight optimization for h_∞ loop shaping design procedure. In *Intelligent Control and Automation (WCICA), 2012 10th World Congress on*, pages 2257–2262. IEEE, 2012.

[71] Glenn Vinnicombe. Frequency domain uncertainty and the graph topology. *IEEE Transactions on Automatic Control*, 38(9):1371–1383, 1993.

[72] Paul Daniel Stefanus Moller. Automated landing of a quadrotor unmanned aerial vehicle on a translating platform. Master's thesis, Stellenbosch: Stellenbosch University, 2015.

[73] Kemin Zhou, John Comstock Doyle, Keith Glover, et al. *Robust and optimal control*, volume 40. Prentice Hall New Jersey, 1996.

[74] Kemin Zhou and John Comstock Doyle. *Essentials of robust control*, volume 104. Prentice Hall Upper Saddle River, NJ, 1998.

[75] Glenn Vinnicombe. *Uncertainty and Feedback: H [infinity] Loop-shaping and the [nu]-gap Metric*. World Scientific, 2001.

[76] DJ Hoyle, Richard A Hyde, and David JN Limebeer. An h/sub infinity/approach to two degree of freedom design. In *[1991] Proceedings of the 30th IEEE Conference on Decision and Control*, pages 1581–1585. IEEE, 1991.

[77] Ray E Bolz. *CRC handbook of tables for applied engineering science*. CRC press, 2019.

[78] John Doyle, Keith Glover, Pramod Khargonekar, and Bruce Francis. State-space solutions to standard h_2 and h_∞ control problems. In *1988 American Control Conference*, pages 1691–1696. IEEE, 1988.